Atomic layer deposition of strontium titanate : from material control to nanoscale devices

DOI:
[10.6100/IR776341](#)

Document status and date:
Published: 01/01/2014

Document Version:
Publisher's PDF, also known as Version of Record (includes final page, issue and volume numbers)

Please check the document version of this publication:

• A submitted manuscript is the version of the article upon submission and before peer-review. There can be important differences between the submitted version and the official published version of record. People interested in the research are advised to contact the author for the final version of the publication, or visit the DOI to the publisher's website.
• The final author version and the galley proof are versions of the publication after peer review.
• The final published version features the final layout of the paper including the volume, issue and page numbers.

[Link to publication](#)

Atomic Layer Deposition of Strontium Titanate

from material control to nanoscale devices

PROEFSCHRIFT

ter verkrijging van de graad van doctor aan de
Technische Universiteit Eindhoven, op gezag van de
rector magnificus, prof.dr.ir. C.J. van Duijn, voor een
commissie aangewezen door het College voor
Promoties, in het openbaar te verdedigen
op woensdag 27 augustus 2014 om 16.00 uur

door

Valentino Longo

geboren te Montebelluna, Italië

Dit proefschrift is goedgekeurd door de promotoren en de samenstelling van de promotiecommissie is als volgt:

voorzitter:	prof.dr. H.J.H. Clercx
1^e promotor:	prof.dr.ir. W.M.M. Kessels
2^e promotor:	prof.dr. F. Roozeboom
copromotor:	dr. M.A. Verheijen
leden:	prof.dr. J. Schmitz (UT)
	prof.dr. M. Leskelä (University of Helsinki)
	prof.dr. A. Fiore
adviseur:	dr. S. Hoffmann-Eifert (Forschungszentrum Jülich)

Contents

Chapter 1

General Introduction

1.1   Nanoscale Devices and Materials Control

The continuous downscaling in size in microelectronics manufacturing allows us to have more inexpensive and more powerful electronic devices each year. This is possible due to efforts in many research fields to keep up with Moore's Law which over the past decades has dictated a roadmap aiming at a number of integrated devices on the same chip area roughly doubling every two years [1]. Advances in the technological processing steps employed, such as photolithography, dry etching and the employment of new materials have enabled smaller feature sizes for many years. However, with the scaling approaching sub-20nm nodes many issues are brought up since various technologies find their final limitations in this range. For these reasons efforts are being made to find alternative solutions to continue with the roadmap envisioned by Moore's Law. In particular, innovative 3-D structures and more complex new materials are continuously introduced to achieve smaller and better performing nanoscale devices. The most prominent examples can be found in the complementary metal-oxide-semiconductor (CMOS) transistor and dynamic-random-access-memory (DRAM) technologies.

In CMOS manufacturing MOS field-effect transistor (MOSFET) scaling has been achieved over the last decade by new technologies and designs as illustrated in Figure 1.1 from Intel [2][3]. First, strained silicon channels were introduced to achieve higher electron mobility. Next, SiO_2 gate oxides were replaced by hafnium-based *high-k* oxides in the 45 nm node. The high relative permittivity (*k-value*) of this new gate dielectric al-
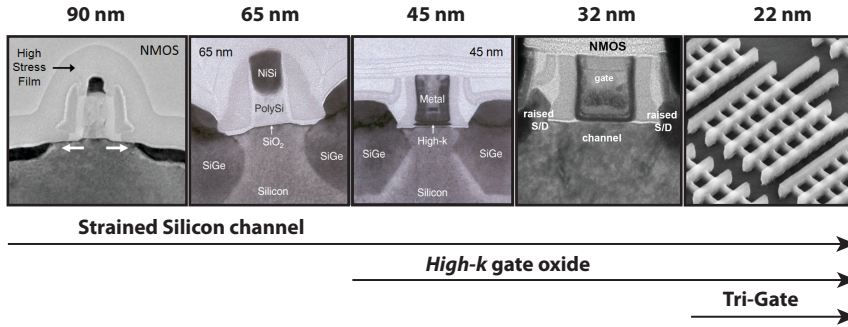
Figure 1.1: Illustration of the technological solutions implemented by Intel to keep up with Moore's Law for sub-100 nm nodes in CMOS technology [2][3].

lows further scaling with enough oxide thickness to suppress the tunneling current from the gate to the active channel. Recently, 3-D FinFET (or Tri-gate) transistors were introduced by Intel to overcome issues related to the 22 nm node [3]. For future nodes other technological solutions such as III-V semiconductors or nanowire-based channels are currently being investigated.

Figure 1.2.a shows the evolution in the design of the DRAM capacitor in a one-transistor-one-capacitor (*1T-1C*) DRAM cell to meet the requirements of the continuous downscaling [4]. Planar capacitor structures have been replaced over the years by semi-planar and, subsequently, by 3-D structures with increasing aspect ratios, such as trenches, crowns and pillars, to achieve sufficient capacitance values.

Also the electrode and dielectric materials have been replaced over the different technology nodes to improve the electrical performance. The capacitor electrodes were at first made of poly-Si but have now been replaced by more conductive TiN films. Even more effort has been spent to find new materials for the dielectric layer and to tailor its properties. Figure 1.2.b shows the cross-section of a $TiN/ZrO_2/Al_2O_3/ZrO_2/TiN$ metal-insulator-metal (MIM) capacitor employed nowadays in DRAM technology [5]. This figure clearly shows the complexity reached in the capacitor structure where multiple layers have to be deposited with excellent conformality over high aspect ratio structures. Furthermore, the three layers forming the capacitor dielectric in Figure 1.2.b have been chosen and designed to achieve a high permittivity value (due to the high-k material of polycrystalline ZrO_2) and low leakage current (due to the superior insulating properties of the amorphous Al_2O_3 interlayer). In this manner, a sufficient capacitance value could be maintained by employing high-k dielectrics, while keeping the leakage current below the required specifications for DRAM cells. To achieve such structure a thermal treat-
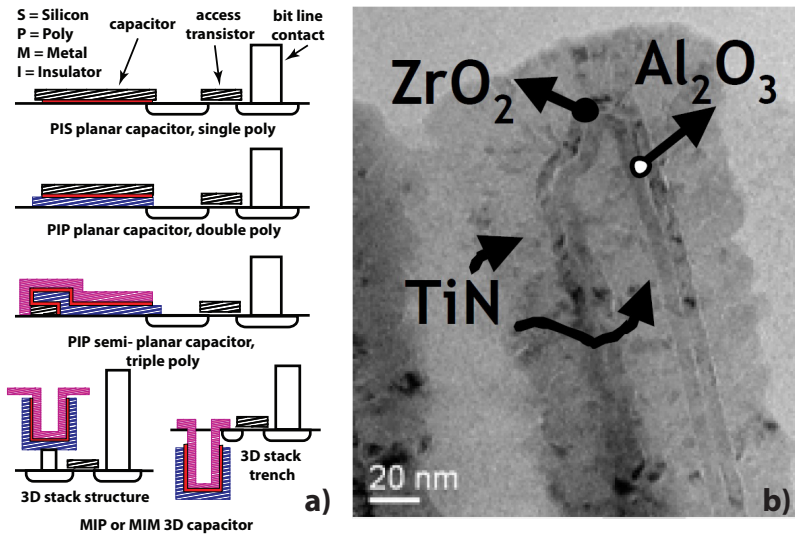
Figure 1.2: Evolution over the years of the capacitor design and of the material employed in a typical *1T-1C* DRAM cell (adapted from [4]) (a) and transmission electron microscopy cross-section of a $TiN/ZrO_2/Al_2O_3/ZrO_2/TiN$ MIM capacitor structure [5] (b).

ment is applied to guarantee the crystallization of the ZrO_2 films. However, the thermal budget has to be limited due to compatibility issues. In particular, relatively low temperatures should be used to avoid damage to the capacitor structure such as oxidation of the TiN electrodes and interdiffusion between the thin films that make up the MIM device.

This example shows how important it is to control the different films employed in advanced structures in terms of material properties. Furthermore, control over the thin films' dimensions is becoming more and more critical due the continuously thinner films employed and the good step coverage required on the 3-D structures illustrated above. For controlling all these film properties in the fabrication of electronic devices two main aspects have to be considered.

Firstly, the deposition process of the thin film itself. To achieve the required thickness and composition control of the thin film and a good step coverage (for deposition over non-planar structures) the most appropriate deposition technique and deposition conditions have to be chosen. Further control on material properties such as the crystalline phase and the morphology of the deposited film can also be achieved during deposition since these properties strongly depend on the deposition process and on the deposition

conditions. Moreover, the influence of the deposition process on the substrate/film interface and its compatibility with the other processing steps (i.e. the thermal budget employed) are additional parameters that one should take into account to select the deposition conditions.

Secondly, modification of the material properties can be achieved by pre-treatment of the substrate surface or by post-treatment of the film. Such treatments are employed to induce changes and to tailor the substrate/film interface and the film properties when these cannot be achieved by the deposition process alone. Furthermore, possible modifications to the film and interface properties induced by the steps following the film deposition in the process flowchart of the device have to be taken into account as well. For example, the employment of high thermal budgets or reactive compounds in the following processing steps can result in the damage of the film properties and therefore have to be avoided.

The ultimate control of the two abovementioned processing steps combined, i.e. the film deposition and the film/surface treatments, enables superior tuning of film and interface properties. This is essential to achieve the required performance of future nanoscale devices.

An example of such dual control of thin film material properties is presented in this thesis. In this work these two aspects were addressed by focusing on the control of the material properties of strontium titanate (STO, $Sr_xTi_yO_z$) thin films deposited by atomic layer deposition (ALD), an emerging technique in semiconductor processing. STO is an *ultrahigh-k* dielectric material ($k \approx 300$ for bulk STO) which finds application in memory technology as the dielectric material for next generation DRAM or as the resistive switching layer in MIM capacitors. An introductory description of the material properties of STO and of the memory concepts where STO thin films find application will be given in Chapter 2.

To tailor the STO material properties the ALD technique was chosen as the deposition process since it enables the required composition control of a ternary oxide, such as STO, and it also gives superior thickness control needed to achieve ultrathin (< 10 nm) STO films. The ability of ALD to control the growth and the material properties of thin films will be described in the next section.

As an additional step to achieve the required functionality of the STO thin films rapid thermal annealing, a thin film treatment, was applied. This film treatment is required to crystallize the amorphous as-deposited STO films to achieve the desired dielectric performance associated to the crystalline *perovskite* structure. Thus, the employment of such a thin film treatment step opens the possibility to further tailor the material properties of
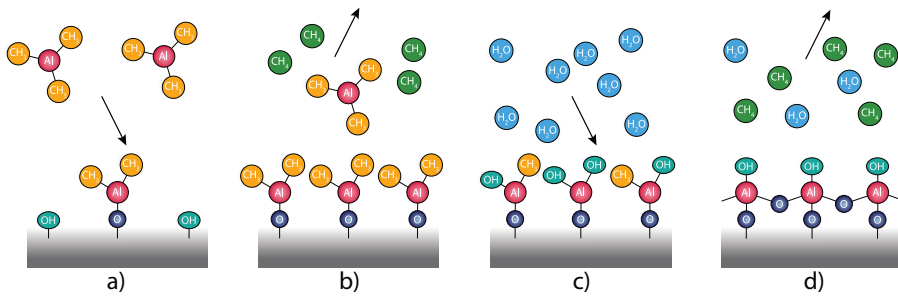
Figure 1.3: Schematic illustration of a cycle of the ALD process of Al_2O_3 where the co-reactant doses, TMA (a) and water (c) are separated by purge/pump steps (b) and (d).

the STO thin films which will influence the MIM device performance.

1.2 Controlling Thin Film Growth by Atomic Layer Deposition

Atomic layer deposition (ALD) is a vapor-phase technique for the synthesis of ultrathin films. ALD is based on the alternating dosing of precursors and co-reactant gases separated by purge or pump steps. Thus the thin films are grown in a *layer-by-layer* fashion due to the limited amount of a monolayer of precursor or gas that can either be adsorbed or react with the substrate surface in each dose step. Due to this characteristic ALD allows sub-nanometer thickness control, good uniformity and superior step coverage.

The reaction principle of ALD is illustrated in Figure 1.3 for the case of Al_2O_3. The ALD process for Al_2O_3 consists of the alternate dosing of $Al(CH_3)_3$, trimethylaluminum (TMA), precursor and H_2O. In the first half-cycle the TMA precursor vapor is dosed into the ALD reactor which then reacts with the -OH terminated sample surface. The TMA molecules are chemisorbed on the substrate surface via a ligand exchange reaction where the CH_3 precursor ligands and the hydroxyl groups present on the substrate surface react to form surface Al-O bonds and volatile CH_4 molecules. Due to the finite amount of -OH groups present on the substrate surface the number of TMA molecules that can be chemisorbed is self-limited. When the surface is saturated with the adsorbed precursor molecules the surface is -CH_3 terminated and no more TMA molecules can adsorb. A purge or a pump step is then used to remove the excess precursor and the by-products, in this case CH_4.

In the second half-cycle H_2O molecules are dosed and they react with the CH_3 ligands present on the surface. CH_4 molecules are again formed as by-product during this reaction and the CH_3 ligands on the surface are replaced by hydroxyl groups. Also this reaction is self-limiting due to finite amount of CH_3 ligands on the surface. When virtually all CH_3 ligands have reacted with the water molecules a purge or pump step is applied again to remove the volatile by-products. After one ALD cycle typically 0.1 nm Al_2O_3, i.e., a submonolayer of material has formed and the surface is once again -OH terminated. This increase in thickness achieved for each ALD cycle is called *growth-per-cycle* (GPC). The ALD cycle can be repeated to obtain the desired final film thickness.

Sufficient amounts of precursor and co-reactant species should be supplied to the surface to guarantee the saturation of the self-limited half-reactions. Generally, when this condition is met the same amount of material is deposited all over the substrate per unit surface including on high aspect ratio structures. Furthermore, purge or pump steps are used to avoid any reactions between the precursor vapor and the co-reactant in the vapor phase or on the surface. In this manner, an undesired chemical vapor deposition (CVD) component in the growth process is avoided. Thus one can achieve high-quality thin films with good uniformity over large deposition areas and superior conformality with respect to other deposition techniques such as CVD and physical vapor deposition (PVD) where the growth behavior is flux-dependent.

ALD gives superior thickness control but it also gives the possibility to precisely control the material properties and to achieve multi-component materials by controlling the ALD dosing sequence. Figure 1.4 shows three different ALD dosing sequences. The regular *AB* approach (a) is the one employed in the deposition of Al_2O_3 described above and consists of the dosing of two co-reactants separated by purging steps. The "multistep" approach comprises the addition of one or more co-reactants, in this case one co-reactant *C*, to the ALD cycle. This *ABC* or "multistep" approach (b) gives the possibility to further tune the material properties of the film which is being deposited. For example, in the deposition of Pt thin films at low temperature, where *A* is $Me_3(MeCp)Pt$ and *B* is an O_2 plasma, PtO_x is usually obtained. By introducing another step, *C*, in the ALD cycle consisting of an H_2 plasma, the PtO_x is reduced leading to pure Pt thin films [7]. Finally, in the "supercycle" approach (c) two ALD processes, *A1B1* and *A2B2*, are combined. This approach gives the possibility to tune the number of *A1B1* and *A2B2* cycles, *m* and *n*, respectively, in a supercycle. By tuning the *m/n* ratio it is usually possible to control the incorporation of each individual component hence, it is possible to control the composition of the entire compound. This approach can be used to grow accurately doped thin films. For example, to obtain Al-doped zinc oxide (ZnO:Al), ALD cycles of Al_2O_3
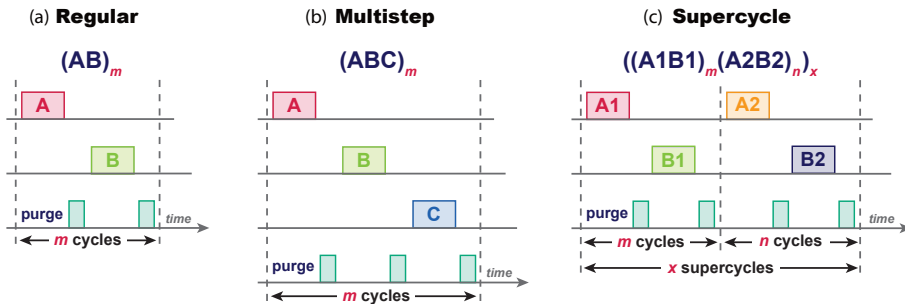
Figure 1.4: Schematic illustration of the "regular" ALD mode (a) and of more advanced ALD approaches: the "multistep" mode (b) and the "supercycle" mode (c). In the "multistep" approach (b) an additional co-reactant C is added to the ALD cycle and in the "supercycle" (c) approach cycles of two "regular" ALD processes are mixed (with a ratio = m/n) to obtain doping of a thin film or a multicomponent compound.

and ZnO are combined with the ratio between the two different cycles depending on the doping level targeted [8]. Another application of this approach is the deposition of multicomponent compounds such as ternary oxides where the ALD processes of two oxides are combined. This advantage of ALD will be the key feature in obtaining strontium titanate ($SrTiO_3$) thin films with different stoichiometries by combining TiO_2 and SrO ALD cycles with different ratios in an STO supercycle.

Furthermore, depending on the nature of the reactant activation during deposition, a distinction can be made between the different ALD processes, namely "thermal ALD" and "plasma-assisted ALD". When ALD reactions are purely thermally driven the ALD process is usually referred to as "thermal ALD". For example, in "thermal ALD" of metal oxides an H_2O vapor or O_2 gas is generally used in combination with a metal-precursor where the chemical reactions are driven only by the substrate temperature (150-350 °C). This is the case of the abovementioned example of ALD of Al_2O_3. In "plasma-assisted ALD", additional reactive and energetic species are created in a plasma and used as the co-reactant. By inducing a plasma discharge in a gas, electrons are accelerated in the generated electric fields and radicals, ions and photons are created upon collision of such electrons with the neutral gas species. The employment of these energetic species enhances the chemical reaction rates at the surface. This permits deposition at lower temperatures (in some cases down to room temperature) and the employment of precursors which are not reactive towards the regular co-reactant species employed in "thermal ALD" processes [6].

1.3 Controlling the Material Properties by Thin Film Treatment

After the deposition process the thin films do not always show the desired properties. In order to achieve the required film functionality more treatments can be applied to the thin films. In most cases this involves a thermal treatment or the use of a plasma. Such a treatment step is intended to modify the material and interface properties of the thin films. Examples of applications of such treatments are the removal of contaminants and defects, crystallization, densification of thin films and surface modification. Different approaches can be used to control the material properties. Pre-treatments can be applied to improve the properties of the interface between the substrate and the thin film and to influence the subsequent growth behavior and the properties of the film, while post-deposition treatments can be employed to modify the thin film properties as well as to enhance the interface properties. Furthermore, film treatments can be applied both *ex-situ* or *in-situ*. In-situ treatments are used to achieve the required film modification without vacuum break to remove the sample. This can enhance the film and interface properties since the specimen is not exposed to air, thus assuring a lower level of contaminants. Furthermore, this approach gives more processing flexibility.

Figure 1.5 shows an example of a process flow for the fabrication of a MIM capacitor. In this process flow both treatment and deposition steps are employed to obtain the MIM structure with the required properties. Examples of surface/film treatments which are commonly employed in such process flow are delineated in the process flow chart in the second column. In particular, a pre-treatment step can be used prior to the dielectric deposition to remove possible contamination on the bottom electrode surface for example by means of an oxygen plasma.

Such step can also be employed to affect the growth behavior of the following deposition step by changing the surface termination of the bottom electrode surface. Furthermore, annealing steps can be applied after the deposition steps of the dielectric and of the top electrode. In line with the study case presented in this thesis, the thermal annealing step after the dielectric deposition is employed to crystallize the dielectric film and to remove possible contaminants in the film. A cure anneal after the top electrode deposition is usually employed to improve the interface between the dielectric and the top electrode and to heal possible damages caused by the top electrode deposition to the dielectric layer.

With the aim of tailoring the properties of the device the most appropriate processing step has to be chosen for each of the manufacturing steps. For example in Figure 1.5 a
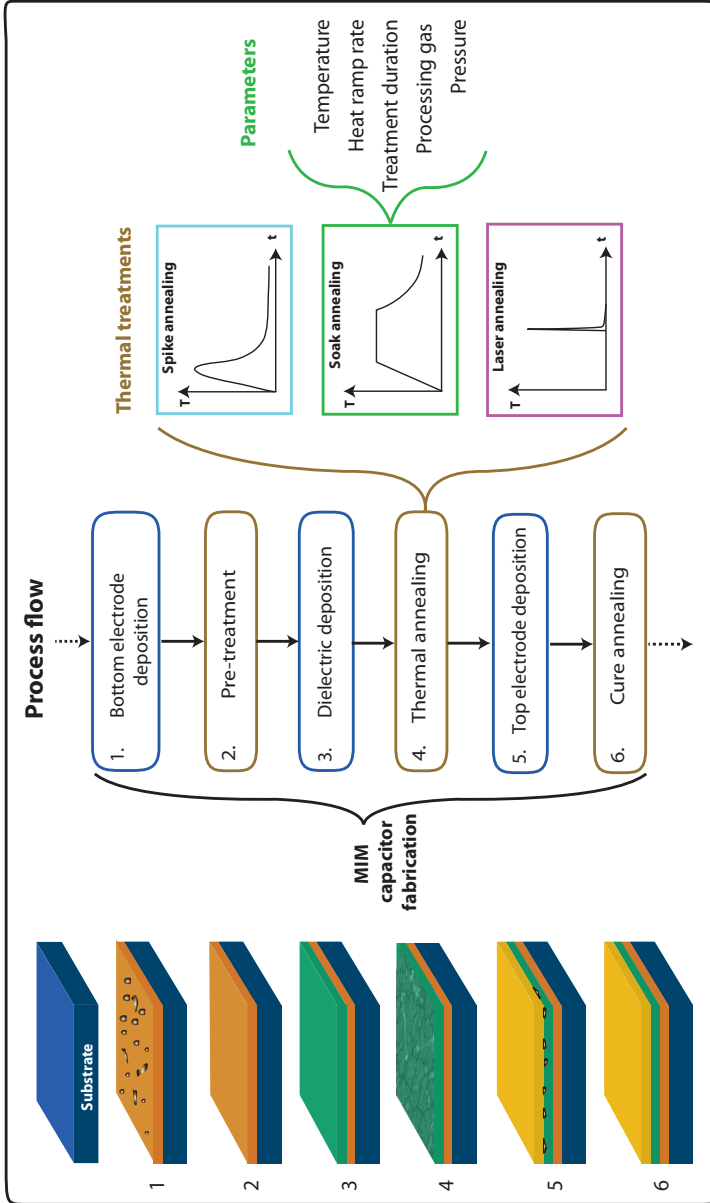
Figure 1.5: Example of a process flow for the fabrication of a MIM structure with deposition steps shown in the second column and delineated in blue and treatment steps in brown. The evolution of the stack is also illustrated. The choice of possible processes which can be employed in each step is exemplified for the thermal treatment step. Within each possible process a set of parameters can be tuned to optimize the process.

thermal annealing step is envisioned to crystallize the dielectric film. For this purpose different annealing approaches can be used (i.e. laser, soak and spike annealing) [9]. Furthermore, each annealing approach has specific parameters which can be tuned to further optimize the microstructure and the morphology of the crystallized film. Therefore, the final structure is the result of the tuning of each of these steps. Furthermore, such an example also shows how the final structure is the result of the interplay of all steps. For example, the properties of the bottom electrode are not influenced only by the deposition process itself but can be affected by the subsequent dielectric deposition and by the treatments employed. Thus, for tailoring the material properties of each thin film composing the MIM structure and, consequently, optimizing the performance of the device, the possible influence of each processing step on the overall structure has to be taken into account.

1.4   Aim of the Research Project

As introduced in the previous sections there is a high demand for new functional materials which have to be implemented in future nanoscale devices. This calls not only for the development of new processes for the preparation of thin films of such advanced materials but also for the control of the properties of such thin films to achieve the required functionality of the material. Essential here is the tailoring of the processing steps involved in the fabrication of a device such as the deposition processes and possible treatment steps. Moreover, the interactions between the processing steps have to be taken into account since the final structure and the properties of the thin films are the result of the interplay of these steps.

This thesis work addresses these aspects by focusing on the control and tailoring of the material properties of STO thin films. STO has been selected as a technological relevant example since its material properties and performance, as a dielectric or resistive switching material, strongly depends on the fabrication steps. Furthermore, as a perovskite STO represents a wide class of multicomponent oxides. Hence, the study presented in this thesis gives insight in the details of tailoring the properties of this material as well as other perovskite materials and ternary compounds. As introduced in the previous sections, control over the material properties of STO thin films is obtained by controlling both the deposition conditions and the treatment steps. The aim of this work is to the tailor the properties of STO thin films by means of these two processing steps to optimize the performance of STO-based MIM devices.

In this research project a plasma-assisted ALD process of STO thin films was first

developed and characterized. Issues such as the control of the thickness and the composition of STO by ALD have been addressed. In particular, the influence of the cycle ratio between SrO and TiO_2 ALD cycles in an STO ALD supercycle on the growth behavior and on the film composition has been studied. Here, spectroscopic ellipsometry was used to determine the stoichiometry and the crystallinity on the STO thin films. These findings will be presented in Chapter 4. Since the as-deposited STO thin films are amorphous and need to be crystallized by a post-deposition thermal treatment to obtain the required dielectric properties related to its perovskite structure, the crystallization behavior of STO thin films was studied in detail by transmission electron microscopy. Chapter 5 discusses the crystallization behavior of ALD STO thin films deposited on Si_3N_4 and Al_2O_3 focusing on the influence of film composition and thermal budget on the morphology and the microstructure of the crystallized films.

Since STO thin films are to be employed in MIM structures, the implementation of MIM layer stacks with Pt as the electrode and STO as the dielectric material, respectively, is discussed in Chapter 6. Both the crystallization behavior of STO when deposited on Pt and the influence of the thermal annealing step on the MIM structure is addressed.

Once the relation between the process conditions, film composition, morphology and microstructure had been established, it was possible to study the influence of these parameters on functional MIM devices where STO was employed either as the dielectric or resistive switching material. In this context Chapter 7 focuses on the electric performance of Pt/STO/Pt MIM capacitor structures. In particular, the influence of the STO film composition and morphology on the capacitor performance is discussed. Furthermore, Chapter 8 discusses the influence of parameters such as film composition and thickness and contact pad size on the resistive switching behavior of Pt/STO/TiN micro- and nanocrossbar test structures.

This thesis work was carried out at the Plasma and Material Processing (PMP) group of the Eindhoven University of Technology (TU/e) in The Netherlands. The combination of the extensive expertise on synthesis of materials by (plasma-assisted) ALD and of the wide available choice of characterization techniques and diagnostics makes the PMP group an unique research environment with the aim of controlling and tailoring the material properties of thin films at the nanoscale.

The thesis project was part of the "Enhance" Marie Curie initial training network project within the 7th Framework Programme (FP7/2007-2013) founded by the European Commission, which focused on the fabrication, integration and characterization of new materials. The results reported in Chapter 7 and 8 are the outcome of a close collaboration with the partners within the "Enhance" network at the Institute of Electronic Materials

(IEM) at the Peter Grünberg Institute at the Forschungszentrum Jülich, Germany.

1.5   Outline

This thesis is structured as follows:

- Chapter 2 describes the material properties of STO and the applications of STO thin films in nanoscale devices. Furthermore, a review of the state-of-the-art of ALD of STO is presented.

- Chapter 3 contains the experimental part. The experimental setups employed in this work for the ALD process of STO and for the rapid thermal annealing (RTA) of the thin films are described. The chapter also introduces the characterization techniques which have been extensively employed in this dissertation work with a particular focus on their application to determine the the material properties of STO thin films.

- Chapters 4 to 8 present the results obtained in this thesis work. These five chapters correspond to individual journal articles published or to be published in peer-reviewed journals and conference proceedings. A list of these publications is given at the end of this dissertation. Some of the chapters are presented with addenda to present relevant additional information not reported in the published articles.

- Chapter 9 describes the main conclusions and outlook of the work.

1.6   References

1. G. Moore, *Electronics*, 38, 8, (1965).
2. P. Packan, S. Akbar, M. Armstrong, D. Bergstrom, M. Brazier, H. Deshpande, K. Dev, G. Ding, T. Ghani, O. Golonzka, W. Han, J. He, R. Heussner, R. James, J. Jopling, C. Kenyon, S.H. Lee, M. Liu, S. Lodha, B. Mattis, A. Murthy, L. Neiberg, J. Neirynck, S. Pae, C. Parker, L. Pipes, J. Sebastian, J. Seiple, B. Sell, A. Sharma, S. Sivakumar, B. Song, A.St. Amour, K. Tone, T. Troeger, C. Weber, K. Zhang, Y. Luo and S. Natarajan, *IEDM Technology Digest*, 659, (2009).
3. M. Bohr, *IEDM Technology. Digest*, 11-1, (2011).
4. E. Gerritsen, N. Emonet, C. Caillat, N. Jourdan, M. Piazza, D. Fraboulet, B. Boeck, A. Berthelot, S. Smith and P. Mazoyer, *Solid-State Electronics*, 49, 1767 (2005).

5. D.S. Kil, H.S. Song, K.J. Lee, K. Hong, J.H. Kim, K.S. Park, S.J. Yeom, J.S. Roh, N.J. Kwak, H.C. Sohn, J.W. Kim and S.W. Park, VLSI Technology Digest, (2006).

6. H. Profijt, "Plasma-Surface Interaction in Plasma-Assisted Atomic Layer Deposition", PhD Thesis, Eindhoven University of Technology, (2012).

7. A. Mackus, "Atomic Layer Deposition of Platinum: from surface reactions to nanopatterning", PhD Thesis, Eindhoven University of Technology, (2013).

8. Y. Wu, P.M. Hermkens, B.W.H van de Loo, H.C.M Knoops, S.E. Potts, M.A. Verheijen, F. Roozeboom and W.M.M. Kessels, *J. Appl. Phys.*, 114(2), 024308, (2013).

9. F. Roozeboom, ed., "Advances in Rapid Thermal and Integrated Processing", Kluwer Academic Publishers, Dordrecht, The Netherlands, (1996).

Chapter 2

Strontium Titanate: Material Properties, Applications and Atomic Layer Deposition

---

The aim of this chapter is to introduce the reader to the material properties of strontium titanate (SrTiO$_3$, STO) and to the applications of ALD STO thin films studied in this thesis. With this goal, the *perovskite* crystal structure and material properties of STO will be presented in the first section. An overview of the deposition techniques which are commonly employed for the synthesis of STO thin films will also be given. The application of ALD STO thin films as the dielectric material in the dynamic random access memories (DRAM) and as the resistive switching material in resistive switching random access memories (ReRAM) will be discussed in section 2.2. Finally, in section 2.3 a review of the ALD processes of STO reported in the literature will be presented. The different approaches adopted in the literature to achieve ALD STO thin films with performance satisfying the requirements for sub-30 nm DRAM MIM capacitor technology will also be presented in this section.
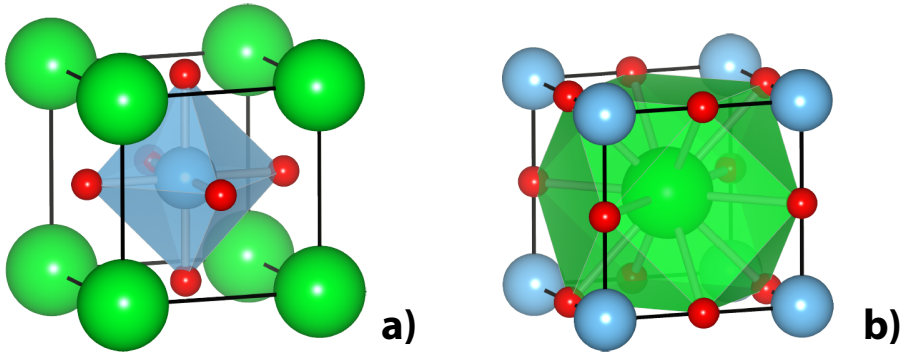
Figure 2.1: Representation of the cubic perovskite crystal structure of SrTiO$_3$ with the Ti-cations placed at the center (a) or at the corners (b) of the unit cell. Sr in green (large), Ti in blue (blue), and O in red (small).

2.1 Strontium Titanate: Crystal Structure, Material Properties and Deposition Techniques

Strontium titanate is a complex oxide material which belongs to a class of materials known as perovskites. Oxidic perovskite materials have the general unit formula *ABO$_3$*, where *A* and *B* are two different cations, with *A* being a larger cation than *B*. Two representations of the cubic perovskite crystalline structure of STO, belonging to the $Pm\bar{3}m$ space group, are presented in Figure 2.1.a and b. Ideal perovskites have a cubic crystalline structure with, in the representation in Figure 2.1.a, the large cations *A* (Sr) sitting at the corners of the cubic unit cell (0, 0, 0), *B* (Ti) cations sitting at the center of the cube (1/2, 1/2, 1/2) and oxygen anions placed at the face centered positions of the cube (1/2, 1/2, 0). In this crystal configuration, a Ti-atom at the center of the cubic unit cell, as represented in Figure 2.1.a, has a 6-fold octahedral coordination with the oxygen anions while a Sr-atom, when represented at the center of the unit cell as shown in Figure 2.1.b, has a 12-fold coordination and is surrounded by a cuboctahedron of oxygen anions.

At room temperature STO shows this cubic crystalline structure with a lattice parameter a = 3.905 Å. At $T \approx 105$ K, STO undergoes a second order phase transition and below this temperature STO exhibits a tetragonal structure with space group $I4/mcm$ [1,2]. This phase transition is associated with a rotation of the oxygen octahedra, with the octahedra of neighboring unit cells rotating in opposite directions [1,2]. STO is a so-called incipient ferroelectric [3] which remains in the paraelectric state down to nearly

CURVE	SAMPLE	$\vec{E}$ ∥	τ ∥	σ_{th} ∥
1	A	[110]		[110]
2	B	[110]		[110]
3	B	[1$\bar{1}$0]		[110]
4	A	[110]	[1$\bar{1}$0]	

Inset: $10^3/\varepsilon$, $\varepsilon = \dfrac{8.0 \times 10^4}{T - 35.5}$
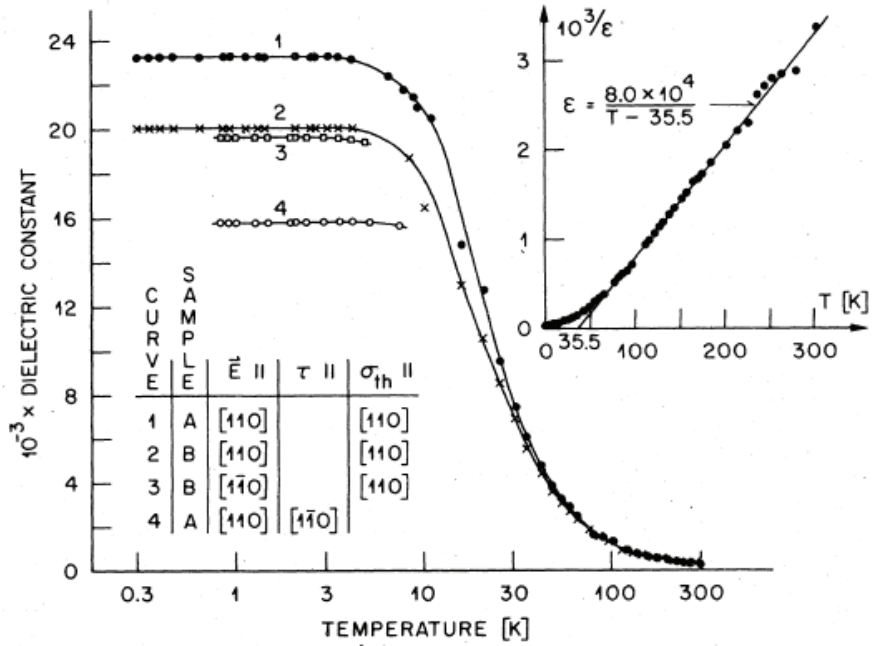
Figure 2.2: Dielectric constant of SrTiO$_3$ single crystals as a function of temperature. Taken from [4]. The inset figure plots the inverse of the dielectric constant as a function of temperature showing the Curie-Weiss behavior of SrTiO$_3$.

0 K [4]. The dielectric permittivity, ϵ, of single-crystalline STO follows a Curie-Weiss behavior:

$$\epsilon \propto \frac{1}{(T - T_{\mathrm{c}})}$$

with a Curie temperature T_c, for single-crystalline STO determined experimentally ≈ 35 K [4-6]. Figure 2.2 plots the dielectric function as a function of temperature for STO single domains [4]. For temperatures approaching $T = 0$ K, ϵ reaches values of the order of 2×10^4 depending on the crystallographic orientation in which the electric field is applied. Even if single crystalline STO is an incipient ferroelectric, strain, defects, doping and oxygen vacancies have proven to be able to increase the Curie temperature of STO. Therefore, STO films showing ferroelectric behavior can be achieved by inducing such imperfections in the crystalline structure. Reports in the literature can be found where STO thin films being ferroelectric at room temperature were achieved [7-9].

STO is a dielectric material which has an indirect and a direct band gap of 3.2 eV

and 3.4 eV, respectively [10,11]. The optical properties of single crystalline and of poly-crystalline STO thin films will be discussed in more detail in Chapter 4. At room temperature single-crystalline STO exhibits a permittivity value $\epsilon \approx 300$ [4]. This is related to the mobility of the Ti-cations with respect to the oxygen octahedral which is responsilbe for the strong ionic polarizabilty and the paraelectric phase [12]. Due to the non-linear polarizability, related to its paraelectricity, STO shows a non-linear dielectric behavior.

Although STO is regarded as an ultrahigh-k material, *n*-type semiconductor and even metallic behavior can be induced by oxygen vacancies which can act as an electron donor in $SrTiO_3$ [13-15]. As will be described in more detail in the section dedicated to the resistive switching application of STO thin films, the oxygen vacancies are responsible for the valence-change memory (VCM) behavior of STO. Oxygen vacancies can be induced by controlling the incorporation of oxygen during the deposition of STO thin films or by post-processing, i.e. annealing in reducing atmosphere. Furthermore, as in the case of resistive switching, oxygen vacancies in perovskites can be induced by applying an electrical field. Also doping by other cations, such as La and Nb, results in *n*-type semi-conducting behavior [13,14,16]. Nb-doped STO is a common conductive substrate which is used in the epitaxial growth of many perovskite materials with minimal lattice constant mismatch. Furthermore, another parameter which can affect the electrical properties of STO is the cation ratio [Sr]/([Sr]+[Ti]). The influence of this parameter on the dielectric performance of ALD STO thin films will be discussed in section 2.3.3 as well as in the following chapters.

Recently, STO has attracted a lot of attention due its interesting electronic properties. In particular, due to its ultrahigh-k value STO has been regarded as a possible dielectric material for gate oxides in metal-oxide-semiconductor field-effect transistor (MOSFet) structures [17,18] and, as will be described in section 2.2.1, as the insulating layer in MIM capacitors for memory applications. Furthermore, STO has recently been the focus of research in the field of oxide electronics. STO shows a minimal lattice mismatch with most of other perovskite oxides [19]. STO is therefore the preferred template for the preparation of oxide heterostructures which exhibit various properties and applications [19]. Perovskite oxides show properties such as high temperature superconductivity (cuprates), colossal magnetoresistance (manganites), ferroelectricity (titantes) and can be grown epitaxially on STO [20-22]. Moreover, in the last decade attention has been drawn on the properties of STO surfaces and of the interface that STO forms with other oxides. In literature various reports can be found on the 2-dimensional electron gas obtained at the STO/$LaAlO_3$ interface [23-28]. Moreover, reports have shown that STO is a topological insulator, meaning that the STO surfaces contains conducting electronic states in contrast

to the insulating "bulk" STO [29]. These peculiar properties make STO attractive for applications in various research fields.

Different reports can be found in the literature where deposition techniques such as pulsed laser deposition (PLD) [20,21,30], molecular beam epitaxy (MBE) [31-33], sputtering[17,22,34], sol-gel deposition [35,36], liquid phase deposition (LPD) [37] and chemical vapor deposition (CVD) [38-40] have been employed for the synthesis of STO thin films. Most of the efforts reported with the employment of such techniques are aimed to achieve high-k STO thin films with low dielectric losses. The main applications of STO thin films prepared with such techniques are in tunable microwave devices, due to the non-linear dielectric behavior of STO and its high tunability, and as an high-k oxide for MOS structures for different semiconductor substrates. Due to its lattice mismatch of only 1.7 % upon an in-plane 45 ° rotation with respect to Si [19,41], STO can be used as the buffer layer between the Si substrate and other functional perovskites [19]. For the epitaxial growth of STO thin films directly on Si MBE is the preferred technique [32,33] while the employment of PLD for this purpose is not well-established yet [30].

For the applications studied in this dissertation the abovementioned deposition techniques cannot guarantee the required step coverage over high aspect ratio structures. As introduced in Chapter 1, ALD is therefore the method of choice. The next section describes such applications where 3D topology are envisioned.

2.2   Applications of STO Thin Films Prepared by ALD

In this section an overview of the main potential industrial applications of ALD STO thin films will be given. In the first part the employment of STO as the dielectric material in MIM capacitors for future DRAM technology nodes is discussed. This discussion can be extended to other applications where STO is to be employed as the dielectric in capacitor structures. Furthermore, the physical limits of this technology and the need for new memory concepts in the near future will be addressed. In the second part, the application of STO thin films as the resistive switching material for ReRAM devices is discussed. Since the working principle of resistive switching (RS) is rather complex compared to that of DRAM (which is based on the charging and discharging of a capacitor) the RS phenomena will be introduced in more detail. The proposed mechanism as reported in the literature for the manifestation of such phenomena in the STO material will also be described. Furthermore, a brief description of the possible cell structure and memory architecture for ReRAM is given.
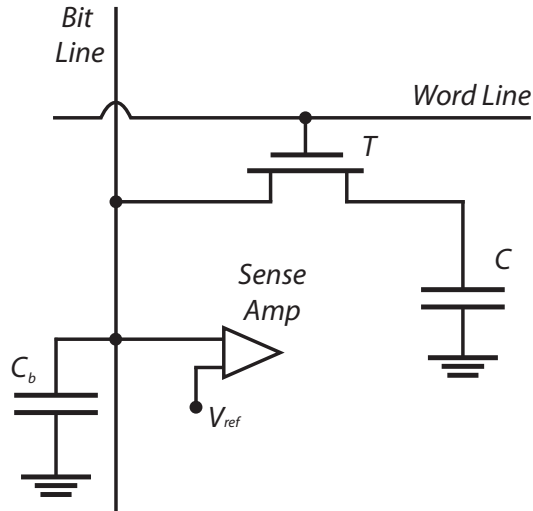
Figure 2.3: Schematic representation of a *1T-1C* DRAM cell. Such cell consists of a MOSFET transistor, *T*, and a capacitor, *C*. The digital information stored in C is sensed by the sense amplifier as a voltage change of the bit line due to a charge exchange between C and C_b (bit line capacitance) when the *T* is accessed.

2.2.1 Dynamic Random Access Memory

The dynamic random access memory (DRAM) is a volatile capacitor-based memory type which was introduced in the market in the early '70s [42]. This technology is based on a simple memory cell design which has guaranteed its success for many decades. The schematic representation of a DRAM cell is depicted in Figure 2.3. The cell consists of a capacitor, *C*, and a transistor, *T*, and is usually referred to as *1T-1C* DRAM cell. The gate contact of the transistor is connected to the *word line* while the *bit line* is connected to the capacitor via the transistor. A representative illustration of a today's *1T-1C* DRAM cell with a three-dimensional capacitor is shown in Figure 2.4.a [43].

The digital information, i.e. '0' or '1', consisting of the charge stored in the capacitor is accessed through the transistor *T*. During a reading operation, *T* is accessed and the stored charge is shared between the capacitor *C* and the capacitance of the bit line, C_b. This results in a (positive or negative) voltage change of the bit line which is sensed by the sense amplifier which determines the presence of a '0' or '1' in the accessed cell. The capacitance of each cell has to be sufficient to store enough charge to induce a sufficient change in voltage (~ 100 mV) to be sensed. The DRAM is a volatile memory since the
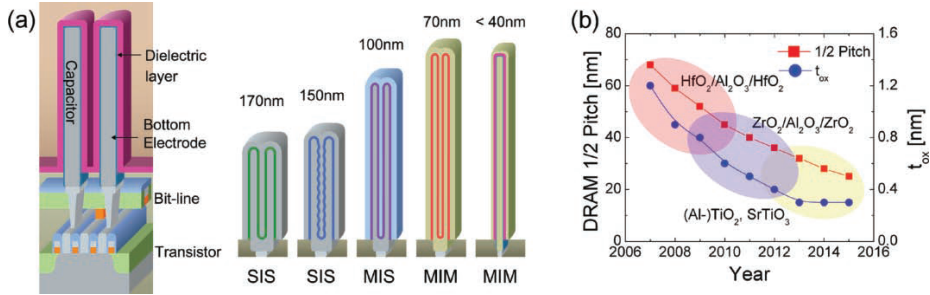
Figure 2.4: Illustration of a today's *1T-1C* DRAM cell and evolution of the capacitor geometry over the technology nodes (a). ITRS trends of the feature size and equivalent oxide thickness (t_{ox}, EOT) over the years and proposed possible dielectric material solutions to fulfill such requirements (b). Taken from [43].

charge stored in the capacitor cannot be kept indefinitely due to leakage and relaxation currents. Therefore, the cell has to be designed to be able to retain the digital information within a certain threshold for an amount of time (retention time) correspondent to the interval between two *refresh* operations. Due to this constraint the leakage current has to be limited to ~ 1 fA per cell.

The architecture of the *1T-1C* cell have been continuously upgraded over the years to keep up with scaling dictated by Moore's Law as already introduced in Chapter 1. One of the most important issues encountered with scaling is the capacitance value of each cell which has to be kept constant over the technological nodes ($\sim$ 20-25 fF) [44]. For this reason three-dimensional capacitors have been used with their aspect ratio increasing over the technological nodes to compensate for the decreasing cell area. With the same objective, materials with increasing permittivity have been used as the dielectric layer. Furthermore, transition from semiconductor to metal (*S* and *M*, respectively in Figure 2.4.a) electrodes have been accomplished over the technological nodes. As shown in Figure 2.4.a, with scaling reaching feature sizes below 40 nm, capacitors with a multi-structured bottom electrode have to be avoided since there is not sufficient space to accommodate both the dielectric film and the inner top electrode. The only capacitor structure which can be achieved on such reduced cell area consists of a singular pillar where the metal electrodes and the dielectric material should be deposited with excellent step coverage to form the MIM structure. The height of the capacitor pillars is limited by the mechanical stability, therefore new ultrahigh-k materials are the escape route to keep the capacitance constant while decreasing the device area. The employment of materials

with higher permittivity comes along with a reduced band gap [45]. Therefore, in future nodes TiN electrodes might not meet the DRAM requirements in terms of leakage current due to their limited work function. Recent reports in the literature have evidenced that high work function metals such as Ru or RuO_2 will have to be employed as the electrode material to increase the barrier height at the metal/dielectric interface [46]. The choice of materials for the dielectric layer in future DRAM MIM capacitors is limited due to the many requirements which have to be fulfilled. Details on the requirements for DRAM technology nodes and possible material solutions are reported by the ITRS roadmap [44,47]. In particular, to meet the requirements for 3x nm nodes the dielectric material should have a permittivity value above 50-60 and an *equivalent oxide thickness* (EOT) below 0.5 nm [44,47]. To achieve such ultrahigh-k values, crystalline materials have to employed which usually require an additional thermal treatment step in the manufacturing process to obtain this crystallinity. Due to compatibility issues between the processing steps the material choice is limited to materials having crystallization temperatures below 600 °C [48]. Furthermore, with writing times in the order of 1 ns the selected dielectric material has to show a stable permittivity with frequencies up to the GHz regime. Finally, the selected material has to show chemical and thermal stability, to guarantee the lifetime of the device, and also be compatible with standard semiconductor manufacturing processing.

As depicted in Figure 2.4.b the choice of dielectric materials satisfying these requirements is restricted to TiO_2 based material, especially Al-doped rutile TiO_2 (ATO) and perovskite materials, such as STO [47]. ATO thin films show an higher interfacial Schottky barrier height with respect to undoped TiO_2 enabling MIM devices with an EOT = 0.5 fulfilling the leakage current requirements for DRAM [43]. It has been proposed that ATO might be employed in future DRAM to fill the gap between the current $ZrO_2/Al_2O_3/ZrO_2$ (ZAZ) dielectric and future nodes where materials with higher permittivity must be used [43]. STO has been identified as the preferred candidate for the dielectric material in future DRAM MIM capacitors. An up-to-date review of the processes and performance of ALD of STO will be presented in section 2.3.

Despite its success which lasted for more than four decades, the DRAM technology is approaching its final technological limits. In particular with the feature size F approaching the 20 nm node space will be very limited to accommodate all the layers that make up the MIM capacitor while keeping the material properties of the layers within the DRAM requirements. Figure 2.5 shows a schematic representation of pedestal MIM capacitors with an ultimate cell area of $4F^2$ ($2F$ for the bit line and $2F$ for the word line; for a detailed description of a DRAM cell design the reader is referred to [49]). In this
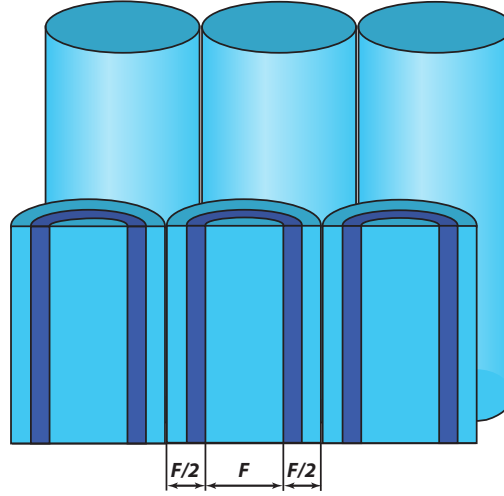
Figure 2.5: Representation of pillar capacitors with a DRAM cell area of $4F^2$. The inner bottom electrodes consist of vertical pillars with diameter F. In this configuration the dielectric film (dark) and the top electrode film are limited to a total thickness to $F/2$.

case the bottom electrode consists of a pillar with a diameter equal to F (limited by the technology) and the dielectric and top electrode films must have a total thickness of $F/2$ (common top electrode). This means that for $F = 20$ nm the dielectric and the top electrode films combined will have a total thickness of 10 nm. Thinner metallic electrodes will have higher resistance due to enhanced electron scattering which limits the access times of the cell. Furthermore, reducing the dielectric thickness results in increased leakage currents which is detrimental for the DRAM cell performance.

For these reasons alternative solutions are being investigated to find new memory concepts for the future [50]. In the next section a new non-volatile memory concept for which the STO thin films studied in this work have also been tested will be introduced.

2.2.2   Resistive Switching Random Access Memory

The resistive switching (RS) phenomenon consists of a sudden change in the resistance of a dielectric material upon the application of an electric field or a current to the dielectric itself. Generally, such a change in resistance is reversible and non-volatile. These characteristics are the bases for resistive-switching random access memories (ReRAM or RRAM) where the digital information stored in a cell consists of the *resistance-state* of the dielectric layer. Such resistance-state is set by applying a certain voltage to the
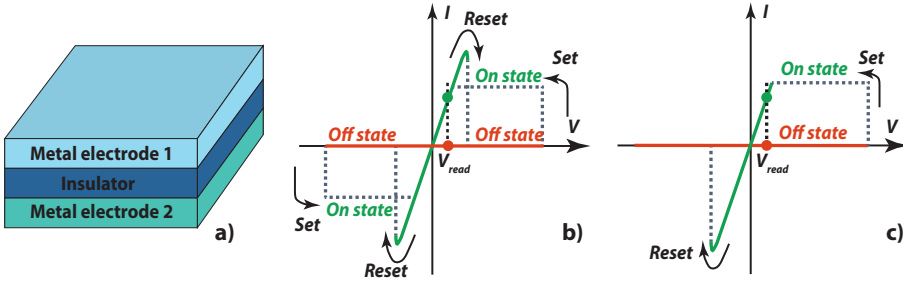
Figure 2.6: MIM structure employed in RS memories where the RS material is sandwiched between two metal electrodes (a). Schematic representation on the unipolar (b) and bipolar (c) switching *I-V* curves.

cell. During the *read* operation, a non-destructive voltage (or current) can be applied to determine the resistance state of the cell. A ReRAM cell usually consists of a metal-insulator-metal structure (MIM) with the insulator being the RS layer as shown in Figure 2.6.a. Different materials can be employed as the RS layer. In particular this phenomenon has been reported for a wide range of metal oxides, for chalcogenides, other ionic solids as well as organic compounds [51,52].

Two different types of RS behavior, *unipolar* and *bipolar*, can be identified and their representative *I-V* characteristics are shown in Figure 2.6.b and c, respectively. In the unipolar switching (Figure 2.6.b) the dielectric layer can be switched between a highly resistive state (*off-state*) and a low resistance state (*on-state*) by applying a voltage with the same polarity. In the bipolar switching (Figure 2.6.c) the resistive state of the dielectric layer is switched between the two states by applying voltages of opposite polarities. For example, if the device is set in the on-state by a positive voltage, a negative voltage has to be applied to reset the device in the off-state. Most of the abovementioned materials can be switched in both unipolar and bipolar modes depending on the symmetry and electrode materials employed in the MIM device design and on the voltage/current applied [52-56]. In both cases, the device is set on the on-state or off-state during a *write* operation by applying a *Set* or *Reset* voltage, respectively, in order to store the digital information (see Figure 2.6.b and c). During a *read* operation a small voltage is applied, V_{read} in Figure 2.6.b and c, to determine the resistive state of the cell without altering it.

Usually, an initial *electroforming* process is required in order for the insulating layer to exhibit RS properties [49,51,52]. The electroforming process generally consists in applying to the insulating layer higher voltages/currents for longer times compared to the

working parameters employed during the normal RS process. During this treatment the insulating layer undergoes a soft-breakdown which results in the formation of a conductive path that is responsible for the switching process. To avoid a hard-breakdown of the insulating layer and to control the properties of the conductive path a *current compliance* is used during electroforming. This consists in limiting the current flowing throw a device to a set amount. Typically, the conductive path obtained during the electroforming process consists of a so-called *filament* generated across the dielectric. In this case, the low resistance state, R_{on}, is in principle independent of the area of the MIM device since the resistance of the filament is much lower compared to the surrounding unperturbed dielectric. In this scenario, the device area can be scaled to enhance the ratio between the resistance in the off-state (R_{off}) and on-state (R_{on}) since R_{off} increases with smaller device feature size. However, RS showing a dependence of R_{on} on the device area has also been reported [57,58]. This is related to a homogenous RS phenomenon which involves changes in the whole film or in the interface between the dielectric and the metal electrodes. In this case, the RS phenomenon is related to a field-induced change in the Schottky-barrier or tunnel barrier height at one of the electrode/dielectric interfaces [49]. As will be shown later for the case of STO, the coexistence of a filamentary and homogenous switching has been reported. Furthermore, in between these two extreme cases, filamentary and homogenous switching, there are other types of RS such as multifilament or inhomogeneous (or localized) interface-type switching [49].

Two main aspects are responsible for the processes which leads to a RS event: the electric field applied to the RS material and the Joule heating due to the high current densities [52]. In general, the electric field and Joule heating are present in all kinds of RS, however, their importance is highly dependent on the device structure and RS mechanism. Yang et al. proposed a classification of the different switching processes for metal oxides depending on the relative importance of the electric field or Joule heating [52]. In their report, the authors showed that the electric field plays a key role in bipolar switching while for unipolar switching Joule heating is more important. Other important parameters which determine the switching behavior and the associated conduction mechanism are the gradients in temperature, electric field and composition. For a more detailed description of the influence of these parameters on the RS the reader is referred to reference [52].

Different switching mechanisms can be distinguished depending mainly on the RS material and electrode material(s) employed in the fabrication of the MIM device and on the electroforming process. Although the mechanisms at the microscopic level of the RS are still under debate, a classification of the main switching phenomena is given here-

after with a brief description for each one. For a more detailed description the reader is referred to reference [49].

Three main kinds of RS memory have been distinguished:

- The electrochemical metallization memory (ECM), also called conductive bridge (CB) or programmable metallization cell (PCM): In this case the MIM structure is usually composed of one electrochemically active metal electrode (usually Ag or Cu), a chemically inert metal electrode and an ion conductive insulating layer in between. This kind of memory exhibits a bipolar switching behavior. Ions of the electrochemically active electrode drift towards the inert electrode to form a "metallic bridge" in the insulator reaching both electrodes (on-state). This metallic filament is disrupted by applying a reverse electric field, hence causing drift of the electrochemically active ions in the opposite direction (off-state) [59,60].

- The thermochemical memory (TCM): For this kind of memory the RS material usually consists of a metal oxide which shows higher resistivity in the highest oxidized state. The two metal electrodes are usually composed of one and the same material as asymmetry in the cell structure is not needed for TCM memory [52]. In this kind of memory the RS shows a unipolar behavior and thermochemical processes are dominant. During the electroforming process a conductive filament consisting of reduced oxide is formed in a thermoelectric breakdown setting the device in the on-state. During the Reset operation, Joule heating due to the high current density in the filament results in temperature gradients. This leads to changes in stoichiometry and the subsequent rupture of the filament leading to the off-state [61].

- The valence change memory (VCM): This is the type of memory which will be addressed in Chapter 8. Since this is the RS mechanism mainly observed in STO it will be described in more in detail here.

In the VCM usually an asymmetric MIM structure is employed with one of the two electrodes being ion-conducting. This kind of memory exhibits a bipolar switching. Many variants of this kind of memory are known but in order to remain consistent with the electronic properties of the material studied in this work, STO, and with the kind of RS behavior presented in Chapter 8, the case of a filamentary VCM for a dielectric with n-type behavior is presented hereafter. In the case illustrated in Figure 2.7, the STO is sandwiched between a Pt and a TiN electrode, with the TiN being the ion-conductive electrode able to accommodate the oxygen anions due to its high oxygen affinity. In this
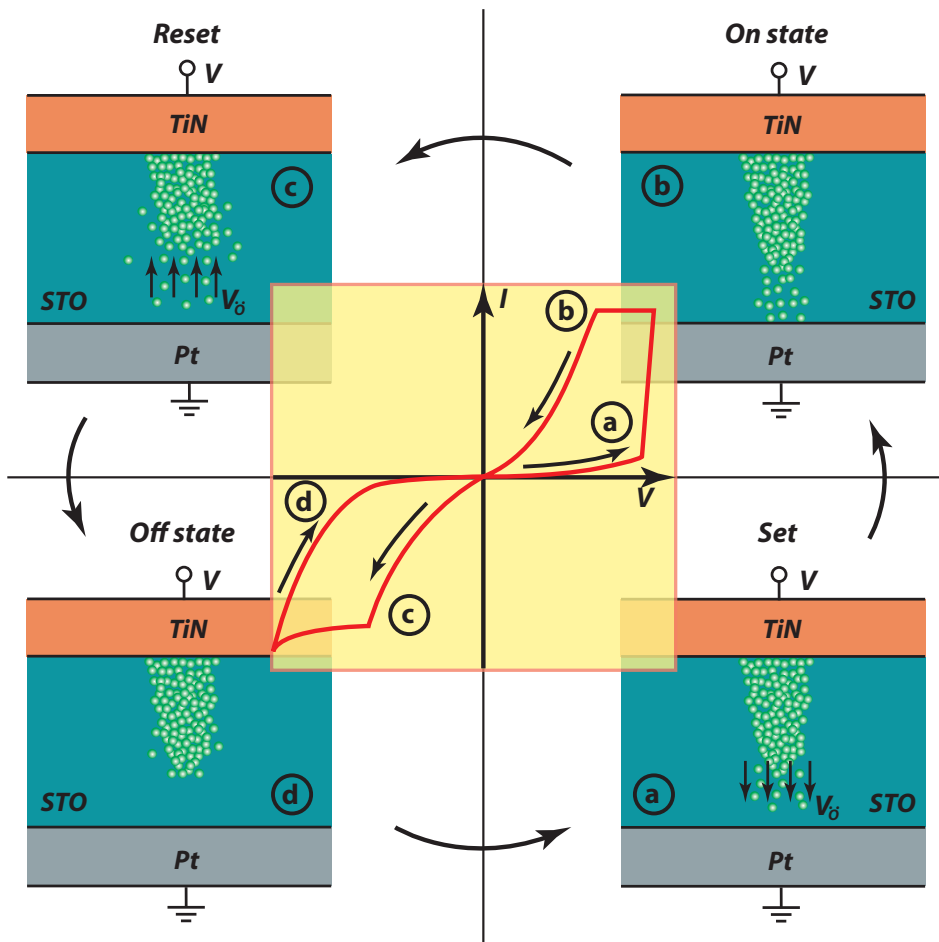
Figure 2.7: Schematic illustration of the working principle of a STO-based VCM MIM cell with Pt and TiN electrodes. During Set operations a positive voltage is applied to the TiN electrode and oxygen vacancies ($V_{\ddot{o}}$) are attracted to the Pt electrode (a), thus forming a filamentary conductive path which results in a sudden decrease of the resistance. The device is then in the on-state (b). During a Reset operation a negative voltage is applied to the TiN electrode (c). The oxygen vacancies are repelled from the Pt resulting in the dissolution of the filament at the Pt/STO interface, thus resetting the device in the off-state (d).
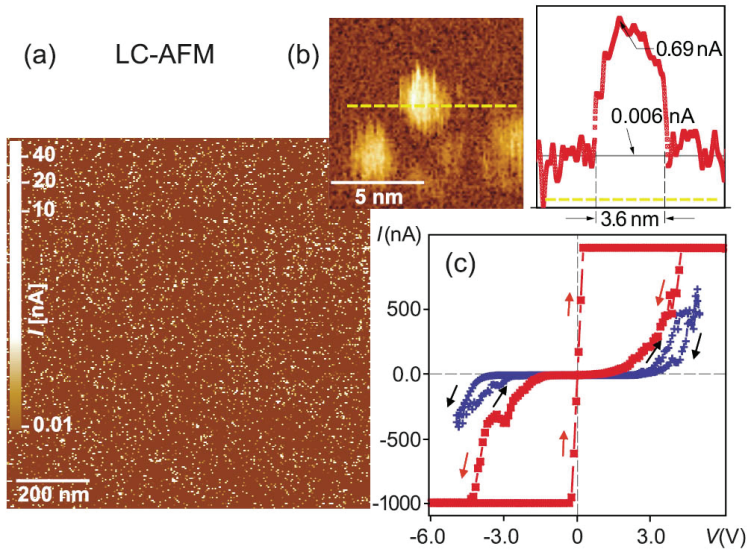
Figure 2.8: Local conductive atomic force microscopy (LC-AFM) scan of an STO(10 nm)/SrRuO₃ structure obtained with a Pt/Ir coated AFM tip (a). Higher resolution LC-AFM scan and current values over a conductive filament (b). Resistive switching *I-V* curves of two different filaments with current compliance of 600 nA (blue) and 1 μA (red) leading to non-linear and linear behavior, respectively (c). Taken from [62].

scenario, a filament consisting of reduced STO (high concentration of oxygen vacancies, $V_{\ddot{o}}$) obtained after electroforming of the device, is responsible for the resulting RS. Usually after forming, the device is reset to the off-state by applying a sufficient voltage with opposite polarity with respect to the forming voltage. Figure 2.7.a shows the filament during the Set operation where a positive voltage is applied to the TiN electrode. Oxygen vacancies are therefore attracted to the Pt electrode. Due to the local reduction process the height and width of the barrier at the STO/Pt interface are lowered and a sudden increase in current is achieved. The device is therefore in the on-state (Figure2.7.b). In Reset operations (Figure2.7.c) a voltage with opposite polarity is applied (negative voltage applied to the TiN electrode). The oxygen vacancies are repelled from the Pt electrode resulting in the progressive dissolution of the conductive filament and the re-oxidation of the STO in the proximity of the Pt electrode. When the filament is disrupted the device is in the off-state (Figure2.7.d) characterized by lower current values.

The description of the switching process just given is rather simplified. In fact, since the RS mechanism is related to the movement of oxygen vacancies, temperature plays a

crucial role in the switching kinetics. In particular, the drift of the ions responsible for the formation and rupture of the filament is strongly temperature dependent. During Set and Reset operations, the velocity of the oxygen vacancies depends on the local electric field and temperature gradients which are constantly changing due to the evolution of the conductivity and the geometry of the filament. This complicates the full understanding and simulations of the RS kinetics. The strong influence of the temperature on the RS mechanism can also be understood in the case of metal oxide, where, typically both VCM and TCM can occur. As mentioned above, thermal heating enhances the motion of oxygen vacancies, however due to temperature gradients motion of ions is achieved not only perpendicular to the electrode surface. Therefore, depending on the amount of heat (hence, the amount of current) also thermally-driven disruption of the filament can take place. This is the reason why for many oxides both VCM and TCM, and therefore bipolar and unipolar switching, respectively, can be achieved by employing different values of leakage compliance [49]. The coexistence of VCM and TCM has been reported for STO thin films. It was proposed that the coexistence of these two RS modes is related to a different conduction mechanism with a homogenous interface-type VCM bipolar behavior and a filamentary TCM unipolar behavior [55,56].

Usually, in VCM the off-state does not show a linear behavior due to the presence of a Schottky contact between the metal and the dielectric. The linearity of the *I-V* curve in the on-state is dependent on the nature of the conducting path responsible for the switching. In particular, if the conducting path in the on-state makes an ohmic contact with both electrodes, a linear *I-V* dependence will be present. On the other hand, the on-state will exhibit a non-linear behavior if a residual Schottky or tunnel barrier is still present at the metal/insulator interface. The electroforming process and the current compliances employed during RS are of fundamental importance on determining the linearity of the on-state behavior. Figure 2.8 shows local conductive atomic force microscopy (LC-AFM) results from the literature obtained for STO(10 nm)/SrRuO$_3$ employing at Pt/Ir coated AFM tip [62]. As it can be seen many conductive filaments were formed while scanning the sample area (Figure2.8.a). Such filaments with a 2-4 nm diameter showed higher conductivity compared to the surrounding matrix (Figure 2.8.b). In this report it was shown how the current compliance employed during Set operations strongly influences the linearity of the conduction in the on-state [62]. Figure 2.8.c shows that by using a current compliance of 600 nA a non-linear *I-V* behavior was achieved (blue curve), while by increasing the compliance to 1 μA a linear *I-V* behavior was obtained (red curve). It was suggested that this difference in *I-V* behavior was due to the different nature of the filaments. Only by applying a sufficient current flow the filament was completely re-
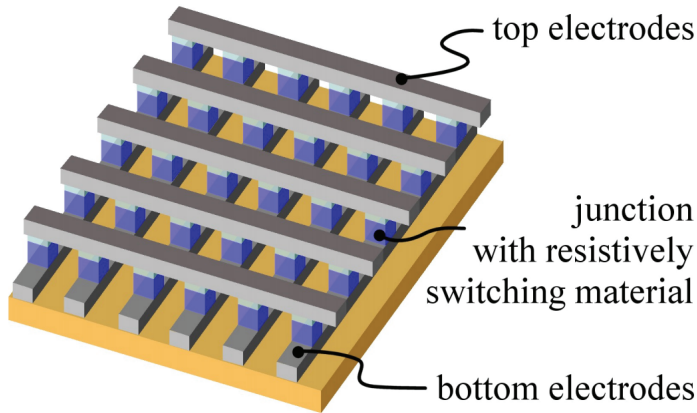
Figure 2.9: Schematic illustration of the nano-crossbar design. Taken from [63].

duced resulting in an ohmic contact at both metal interfaces, while for the lower current compliance the filament remained partially semiconducting resulting in a non-linear *I-V* curve [62].

For the design of the ReRAM cells the employment of nano-crossbar structures is envisioned. The design of a nanocrossabr is shown in Figure 2.9 [63]. and consists of two metallic lines positioned perpendicular to each other corresponding to the bottom and top electrode. The resistive swithcing material is placed in between these two electrode at their cross-point. Considering an array consisting of many bottom and top electrode lines, each cross-point consists in a resistive switching memory cell. With this design, high integration density can be achieved with each memory cell consisting of a $4F^2$ two-terminal passive element. Micro and nano-crossbar devices were employed in this work to study the RS behavior of ALD STO thin films (see Chapter 8). ALD was the preferred technique to deposit STO to obtain conformal deposition over the bottom electrode bars. For a more detailed description of the nano-crossbar design, and possible architectures the reader is referred to [64].

2.3 ALD of STO: Precursors, Processes and Material Properties

For the applications presented in the previous section STO thin films have to be deposited on structures with 3D topology. For this reason ALD is the technique of choice to be employed for the deposition of STO thin films. Most of the research presented in the

literature on the preparation of STO thin films by ALD focuses on the performance of STO as the dielectric layer in MIM capacitors for DRAM applications. A review of the precursors employed, ALD processes, thin film properties and dielectric performance of STO thin films deposited by ALD is reported hereafter.

The first paper reported in the literature concerning ALD of STO was published in 1999 by Vehkamäki et al. [65]. Since then, the interest in the development of new ALD processes of STO was raised due to the increased attention on STO as a possible high-k dielectric material for future DRAM nodes. An up-to-date list of the publication on ALD of STO reported in the literature is reported in Table 2.1 which lists the year of publication, precursors, co-reactants and the deposition temperatures employed.

2.3.1 Strontium and Titanium Precursors for ALD of STO

When selecting a precursor(s) for the development of an ALD process, generally, the following requirements have to be fulfilled:

- Volatility: the precursor needs to have a sufficient vapor pressure (typically a few mTorr) at the temperature at which it is kept in order to obtain a sufficient precursor delivery to the reactor at reasonable dosing times.

- Reactivity: the precursor should be reactive towards the surface groups involved in the ALD process and also towards the co-reactant employed in order to achieve film growth.

- Stability: the precursor needs to be chemically stable at the deposition temperatures used in order to avoid spontaneous decomposition, a condition that could lead to undesired reactions and CVD-like growth.

- Availability: for mass production the precursor elements (e.g. Sr, Ti) should be abundantly present in the Earth's crust. This is the case for both Sr (0.036 %) and (Ti 0.66 %). Also, the processes for the synthesis of the precursors need to be well established.

Another issue concerning the choice of the precursors is that for the deposition of a ternary compound such as STO both, Ti and Sr in this case, precursors need to be stable at the selected substrate temperature. Furthermore, the ALD processes for the single binary oxides, in this case TiO_2 and SrO, have to be chemically compatible with each other. The precursor choice for the development of ALD processes of STO thin films is limited due to the scarcity of precursors for alkaline rare earth metals. Until recently

the choice of ALD Sr precursors was limited to β-diketonates, such as $Sr(thd)_2$ (thd = 2,2,6,6-tetramethyl-3.5-heptanedione, also referred to as tmhd or dipivaloylmethane (DPM)), which are successful precursors for metallorganic-chemical-vapor-deposition (MOCVD) of $SrTiO_3$ [66]. However, these precursors show low volatility and relatively high temperatures (> 300 °C) are usually required due to the limited reactivity towards water and oxygen gas [66,67]. Furthermore, when O_3 is used as the oxidizing agent in combination of Sr β-diketonates the resulting films contain mainly $SrCO_3$ [68]. With the employment of a (H_2O or O_2) plasma the growth of SrO and STO films is possible with β-diketonates precursors at relatively low temperatures 250 - 280 °C achieving mostly carbonate-free films [69-71].

Cyclopentadienyl-based (Cp-based) precursors for Sr were first developed at the University of Helsinki and the first report of their utilization as a precursor for ALD of STO thin films dates back to 1999 [65]. However, the precursor employed in that work, $Sr(^iPr_3Cp)_2$, has not been widely available for years until the interest in such precursors increased since STO was considered as the most prominent candidate for the high-k dielectric material in MIM capacitors in future DRAM nodes. Recently, Cp-based Sr precursors have been made available by chemical suppliers [72] and most of the papers published in the literature since then report the employment of such Cp-based Sr precursors. This family of precursors shows good reactivity toward ozone and oxygen plasmas [72]. Cp-based Sr precursors also exhibit an improved thermal stability and higher volatility compared to the β-diketonates which makes them more suitable as ALD precursors [72]. In this thesis work the HyperSr™ precursor, namely bis(tri-isopropylcyclopentadienyl) strontium with the 1,2-dimethoxyethane adduct ($Sr(^iPr_3Cp)_2(DME)$), from Air Liquide has been employed as the Sr precursor.

The choice for the Ti precursor has not been as limited as for the Sr case but some issues can be brought up when an ALD TiO_2 process has to be combined with an SrO process to obtain STO. For example Ti halides, such as $TiCl_4$, which are commonly used in ALD for the deposition of TiO_2 and TiN, have to be avoided due to their reactivity toward Sr [67]. Consequently, Ti alkoxides have first received much attention as Ti precursors for ALD of STO. The first published papers on ALD of STO reported the use of $Ti(O^iPr)_4$ [65,66,68-71,73-78], which is a well-known precursor for the ALD process of TiO_2. However, Ti alkoxides have a relatively limited thermal stability which makes them incompatible to thermal ALD processes concurrently with Sr β-diketonates which need higher temperatures to be reactive with common oxidizing sources. Nevertheless, due to its relatively high volatility $Ti(O^iPr)_4$ has been successfully used in depositing STO by ALD in combination with Sr β-diketonates and oxygen plasma or water plasma [69-

71,73,75-78] or in combination with Sr Cp-based precursors and water [65,66,79]. Also Ti(OMe)$_4$ has been widely used in ALD of STO, in combination with Sr Cp-based precursors and water, due to its increased thermal stability compared to Ti(O^{i}Pr)$_4$. However, Ti alkoxides cannot be employed at high substrate temperatures (> 300 - 350 °C) due to their limited stability. In order to achieve in-situ crystallization employing a seed-layer (see section 3.3) higher temperatures ($\sim$ 400 °C) have to be used. For this reason, Ti precursors with increased thermal stability such as Ti(^{i}OPr$_2$)(thd)$_2$ and Ti(^{t}BuO)$_2$(thd)$_2$ have been employed [43,80-84]. Furthermore, Ti Cp-based precursors have been developed to achieve a wide ALD temperature window [43,72,84-86]. One of this type of precursors, namely (pentamethylcyclopentadienyl)trimethoxy-titanium, Ti(CpMe$_5$)(OMe)$_3$ (Ti-Star, Air Liquide) has been employed in this work and can be employed as ALD precursor at temperatures as high as 400 °C.

2.3.2 ALD of STO: different approaches to thin film growth

To obtain a ternary oxide such as STO by ALD the most common approach is to combine the two ALD processes of the single binary oxides, in the case of STO SrO and TiO$_2$, by mixing them to obtain an STO ALD supercycle (see Figure 1.4.c). The incorporation of each of the two binary oxides and hence the two different cations should depend on the relative number of ALD cycles of each of the two oxides in the ALD supercycle of the ternary oxide and on the GPC of the binary processes. However, the growth behavior is ruled by the surface chemistry which changes every time the process switches between TiO$_2$ and SrO ALD cycles. The surface reactions are determined by the precursors and the oxidizing source employed in each of the two binary oxide ALD processes. When TiO$_2$ is grown on SrO (or vice versa) the growth behavior is usually different compared to when TiO$_2$ (SrO) ALD cycles are executed on a TiO$_2$ (SrO) surface. This usually affects the GPC of the binary oxides when switching between SrO and TiO$_2$ ALD cycles. Consequently, this results in the enhanced (or reduced) incorporation of one of the two components. For example, it has been reported that when employing Ti(^{t}BuO)$_2$(thd)$_2$ the maximum [Ti]/([Ti]+[Sr]) ratio obtained in the films, irrespective of the ratio between SrO and TiO$_2$ ALD cycles, was 0.20 [43]. This was imputed to the steric hindrance of the precursor. For these reasons, when developing an ALD STO process based on mixing cycles of ALD processes established for the preparation of TiO$_2$ and SrO, the growth behavior has to be investigated to establish the relation between the (SrO)/(TiO$_2$) ALD cycle ratio and the achievable STO composition (see Chapter 4).

Table 2.1: Up-to-date overview of the reports on ALD of STO in the literature. For each paper the Ti precursor(s), Sr precursor(s), oxidizing agent(s) and deposition temperature(s) employed are listed in the corresponding columns. Also the "ALD approach" used in each report and the year of publication is given. Cp = cyclopentadienyl, DME = dimethoxyethane, Et = ethyl, Me = methyl, ^{i}Pr = isopropyl, ^{t}Bu = tertiary butyl, thd = 2,2,6,6-tetramethyl-3,5-heptanedionate, THF = tetrahydrofuran.

Ti precursor	Sr precursor	Oxygen source	Deposition temperature (°C)	ALD approach	Year of publication	Reference
Ti(O^{i}Pr)$_4$	Sr(^{i}Pr$_3$Cp)$_2$(THF)	H$_2$O	250-325	supercycle	1999	Vehkamäki et al. [65]
Ti(^{i}Pr$_3$Cp)$_2$(THF)	Sr(^{i}Pr$_3$Cp)$_2$(THF)	H$_2$O	250-325	supercycle	2001	Vehkamäki et al. [66]
Ti(O^{i}Pr)$_4$	Sr(thd)$_2$	O$_2$ plasma	150-275	supercycle	2002	Kil et al. [69]
Ti(O^{i}Pr)$_4$	Sr(thd)$_2$	O$_2$ plasma	250-350	mixed precursors	2002	Lee et al. [70]
Ti(O^{i}Pr)$_4$	Sr(thd)$_2$	O$_3$, H$_2$O	290, 325	supercycle	2003	Kosola et al. [68]
Ti(O^{i}Pr)$_4$	Sr(thd)$_2$	H$_2$O plasma	250	supercycle	2005	Lee et al. [71]
Ti(O^{i}Pr)$_4$	Sr(thd)$_2$	H$_2$O plasma	250	supercycle	2005	Kwon et al. [73]
Ti(O^{i}Pr)$_4$	Sr(thd)$_2$	/	300	supercycle	2006	Bhaskar et al. [74]
Ti(O^{i}Pr)$_4$	Sr(thd)$_2$	H$_2$O, H$_2$O plasma	190-270	supercycle	2007	Kwon et al. [75]
Ti(O^{i}Pr)$_4$	Sr(thd)$_2$	O$_2$ plasma	225	supercycle	2007	Ahn et al. [76]
Ti(O^{i}Pr)$_4$	Sr(thd)$_2$	O$_2$ plasma	225	supercycle	2007	Kim et al. [77]
Ti(O^{i}Pr)$_4$	Sr(thd)$_2$	O$_2$ plasma	225	supercycle	2008	Ahn et al. [78]
Ti(thd)$_2$(O^{i}Pr)$_2$	Sr(thd)$_2$	H$_2$O	370	supercycle	2008	Lee et al. [80]
Ti(thd)$_2$(O^{i}Pr)$_2$	Sr(thd)$_2$	H$_2$O	370	supercycle	2008	Lee et al. [81]
Ti(OMe)$_4$	Sr(^{t}Bu$_3$Cp)$_2$	H$_2$O	250-300	supercycle	2008	Menou et al. [91]
Ti(Me$_5$Cp)(OMe)$_3$, Prime-Ti	Sr(^{i}Pr$_3$Cp)$_2$	H$_2$O, O$_3$	275	supercycle	2008	Katamreddy et al. [72]
Ti(OMe)$_4$	Sr(^{t}Bu$_3$Cp)$_2$	H$_2$O	250	supercycle	2009	Menou et al. [88]

Table 2.1 *Continued.*

Ti precursor	Sr precursor	Oxygen source	Deposition temperature ($^\circ$C)	ALD approach	Year of pubblication	Reference
$Ti(thd)_2(O^iPr)_2$	$Sr(thd)_2$	H_2O	370	supercycle	2009	Lee et al. [82]
$Ti(OMe)_4$	$Sr(^iBu_3Cp)_2$	H_2O	250	supercycle	2010	Pawlak et al. [89]
$Ti(OMe)_4$	$Sr(^iBu_3Cp)_2$	H_2O	250	supercycle	2010	Pawlak et al. [92]
$Ti(OMe)_4$	$Sr(^iBu_3Cp)_2$	H_2O	250	supercycle	2010	Popovici et al. [67]
$Ti(thd)_2(^iOPr)_2$, $Ti(^iOPr)_4$, $Ti(^iBuO)_2(thd)_2$	$Sr(thd)_2$	H_2O, O_3	370	supercycle	2010	Kim et al. [43]
$Ti(OMe)_4$	$Sr(^iBu_3Cp)_2$	H_2O	250	supercycle	2010	Menou et al. [94]
$Ti(OMe)_4$	$Sr(^iBu_3Cp)_2$	H_2O	250	supercycle	2011	Kim et al. [46]
$Ti(OMe)_4$	$Sr(^iBu_3Cp)_2$	H_2O	250	supercycle	2011	Pawlak et al. [93]
$Ti(OMe)_4$, $Ti(Me_5Cp)(OMe)_3$	$Sr(^iBu_3Cp)_2$	H_2O, O_3	250, 370	supercycle	2011	Popovici et al. [85]
$Ti(OMe)_4$	$Sr(^iBu_3Cp)_2$	H_2O	250	supercycle	2011	Popovici et al. [90]
$Ti(thd)_2(O^iPr)_2$	$Sr(^iPr_3Cp)_2$	H_2O, O_3	370	supercycle	2011	Lee et al. [83]
$Ti(Me_5Cp)(OMe)_3$	$Sr(^iPr_3Cp)_2(DME)$ (HyperSr)	O_2 plasma	250	supercycle	2011	Langereis et al. [86]
$Ti(NEtMe)_4$ (TEMATi)	$Sr(^iPr_3Cp)_2$ (AbsoluteSr)	O_3	300	superlattice	2011	Riedel et al. [87]
$Ti(thd)_2(O^iPr)_2$	$Sr(^iPr_3Cp)_2$	H_2O, O_3	370	supercycle	2012	Lee et al. [95]
$Ti(OMe)_4$	$Sr(^iBu_3Cp)_2$	O_3	250	supercycle	2012	Blomberg et al. [96]
$Ti(OMe)_4$	$Sr(^iBu_3Cp)_2$	O_3	250	supercycle	2012	Lukosious et al. [97]
$Ti(O^iPr)_4$	$Sr(^iPr_3Cp)_2$	H_2O	250	supercycle	2013	McDaniel et al. [79]
$Ti(Me_5Cp)(OMe)_3$, $Ti(thd)_2(O^iPr)_2$	$Sr(^iPr_3Cp)_2$	H_2O, O_3	370	supercycle	2013	Lee et al. [84]
$Ti(Me_5Cp)(OMe)_3$	$Sr(^iPr_3Cp)_2(DME)$ (HyperSr)	O_2 plasma	250-350	supercycle	2011	Longo et al. This work

Most of the reports in the literature regarding ALD of STO are based on the super-cycle approach (see the "ALD approach" column in Table 2.1). However, a few other papers have been published where more singular methods have been used to obtain STO thin films by ALD.

Riedel et al. reported the preparation of STO thin films by depositing TiO_2/SrO superlattices using ALD and then applying a thermal annealing step [87]. During the annealing step the mixing of the two oxides is achieved by thermal diffusion and with the proper thermal budget applied full crystallization of the STO thin films is achieved. Using this approach the composition of the STO thin films is determined by the relative amount of TiO_2 and SrO that have been incorporated in the superlattice stack [87].

Another approach found in the literature consists of dosing the Sr and Ti precursors at the same time [70]. Lee et al. reported on an ALD process for STO thin films where the Sr and Ti precursors were dissolved in tetrahydrofuran to form two separate solutions. The solution were then evaporated and dosed in the reactor chamber simultaneously. The GPC of this process showed a saturation behavior with increasing dosing of the solution of the precursors. Furthermore, for the solution concentration employed close-to-stoichiometric STO thin films were achieved [70]. However, this approach does not give the same process flexibility as in the supercycle approach since the composition of the films cannot be tuned by simply changing the ratio between SrO and TiO_2 ALD cycles.

2.3.3 ALD of STO: Different Approaches to Optimize STO Thin Film Properties

To avoid thermal decomposition of the precursors and consequently a CVD growth component, relatively low temperatures ($< 400\,^\circ$C) have to be employed during ALD processing of STO. As a consequence the as-deposited STO thin films are usually in the amorphous state. To achieve the ultrahigh-k values needed to obtain high density capacitance values the films need to be crystallized into the perovskite crystal structure. The most problematic issue encountered during the crystallization of STO thin films is that when a post-deposition annealing step is employed, cracks and voids are formed, due to film densification and shrinkage, especially at the grain boundaries. These have been reported to serve as leakage paths for currents which is detrimental for the MIM devices where an STO thin film is implemented as the dielectric layer [43,75,80-82,85,88,89,Chapter 7]. Different research groups have tried to find solutions to this problem with the common aim of containing the leakage current below the requirements

for MIM capacitors for DRAM technology (1×10^{-8} A cm^{-2} at 1 V) while keeping an ultrahigh-k value of the thin film. In particular, most of the reports in the literature on this matter have been published by the Interuniversity Microelectronics Centre, imec, in Belgium and by the group Prof. C. S. Hwang at the Seoul National University, Korea.

In their first reports of ALD of STO the imec authors focused on the deposition of STO thin films on TiN substrates to characterize the process and to the determine the STO thin film dielectric properties. They employed a Cp-based Sr precursor, Sr(^{t}Bu$_3$Cp)$_2$, Ti(OMe)$_4$ as the Ti precursor and water vapor to deposit the STO thin film with the supercycle approach achieving various film stoichiometries [67,88,91]. In these first reports single STO thin films were deposited and then crystallized by post-deposition rapid thermal annealing (RTA). It was shown that the highest permittivity was achieved for the stoichiometric STO thin films. By increasing the Sr-content the crystalline thin film showed a decrease in k-value, however, the leakage current was also decreased which is beneficial for the MIM capacitor performance [67,88,91]. Furthermore, it was shown that all compositions obtained (0.45 < [Sr]/([Sr]+[Ti]) < 0.67) could be crystallized into the perovskite structure with an increased cell parameter for the Sr-rich films suggesting that the excess Sr may be dissolved in the STO [67,88,91]. However, the crystallization temperature was not independent of the composition with the lowest value obtained for stoichiometric STO ($\sim$ 540 °C). Sr-rich films could be crystallized with slightly higher temperature even for highly non-stoichiometric STO ([Sr]/([Sr]+[Ti]) = 0.67), while the crystallization temperature increased in a more abrupt fashion for Ti-rich films [67,88,91]. Further research carried out by the imec group focused on determining the impact of the crystallization behavior of the STO thin films on the electric properties of TiN/STO/TiN MIM stacks [88-90]. It was shown that the stoichiometric STO thin films crystallized by an RTA step at 600 °C showed nano-cracks at the grain boundaries resulting in relatively high leakage current densities. The Sr-rich films however showed a more compact morphology after crystallization with a reduced average grain size ($\sim$ 50 nm) which resulted in a decreased leakage current [89]. Yet, the k-value was reduced from $\sim$ 210 for the stoichiometric STO thin films to $\sim$ 60 for Sr-rich ones ([Sr]/([Sr]+[Ti]) = 0.62) resulting in higher equivalent oxide thickness (EOT) [88]. To obtain both an ultrahigh-k value and low leakage current the imec group developed a new approach, illustrated in Figure 2.10. In this approach a TiO$_2$ interlayer is first deposited on the bottom electrode (RuO$_x$/Ru/TiN) substrate before the Sr-rich STO deposition (Figure 2.10 (a)) [46,92,93]. During the RTA step the thin film showed a crystallization behavior comparable to the Sr-rich film with no cracks formation (Figure 2.10 (d)). Furthermore, during the thermal treatment Ti atoms diffuse from the TiO$_2$ interlayer in the STO, thus
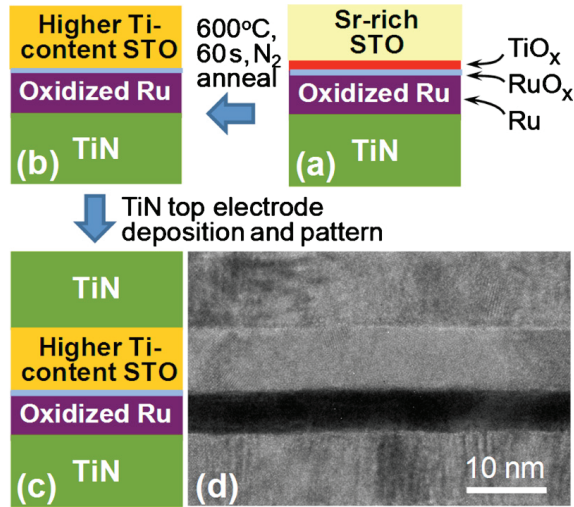
Figure 2.10: Illustration of the MIM stack sequence adopted by the imec group to reduce the leakage current. A thin TiO_x layer is placed between the RuO_x bottom electrode and the Sr-rich STO film (a). During the RTA step the TiO_x and STO films intermix (b) to achieve a close-to-stoichiometric STO film with superior dielectric properties (c). A cross-section transmission electron microscopy image of the final stack is shown in (d). Taken from [93].

compensating the off-stoichiometry of the Sr-rich film (Figure 2.10 (b)). Research was carried out to determine the optimal thickness of the TiO_2 interlayer to achieve the lowest EOT [46,92,93]. Pawlak et al. employed this TiO_2 interlayer in combination with a RuO_x/Ru bottom electrode (Ru prepared by ALD on TiN substrates). The use of a RuO_x thin layer (obtained by oxidizing the ALD Ru bottom electrode) was essential in achieving the best electrical performance. It was proposed that during the RTA step the RuO_x thin layer avoids oxygen scavenging from the STO film (i.e. oxidation of the TiN or Ru electrode) which results in oxygen vacancies in the STO and, consequently, in electron traps which are detrimental for the leakage current [92,93]. The employment of such a thin RuO_x layer, serving as an oxygen reservoir during RTA, results in improved insulating properties of the STO film. The contribution of the high work function of the Ru metal electrode, the employment of the RuO_x and TiO_2 interlayers resulted in leakage current values as low as $\sim 1 \times 10^{-7}$ A cm^{-2} for an EOT = 0.4 nm, which is the record value reported so far in the literature [93].

In other publications the imec group also reported on the seed-layer approach which consists of first depositing an ultra-thin STO film (3 - 5 nm) and then crystallizing it

by RTA before the STO main layer deposition [85,90,94]. In particular, it was reported that when a crystalline Sr-rich seed layer was employed this serves as a template during crystallization (by post-deposition annealing) leading to crack-free films with reduced grain size [90]. Furthermore, Menou et al. reported on the influence of a 5 nm seed layer (stoichiometric STO) on the crystallization temperature. It was shown that by using the crystalline seed the crystallization temperature was decreased to $420\,°C$ which is $100\,°C$ less than that for a single STO film with similar thickness ($\sim 520\,°C$) [94]. In-situ crystallization was also achieved by the imec group employing a crystalline seed layer and Ti-Star ($Ti(Me_5Cp)(OMe)_3$) as the Ti precursor which shows an enhanced thermal stability (up to $\sim 400\,°C$) [85]. Employing a 3 nm Sr-rich crystalline seed layer and then depositing on top a stoichiometric STO main layer (10 nm) at $370\,°C$, Popovici et al. showed that the STO film was crystalline in the as-deposited state and showing suppressed crack formation [85]. However, the electrical measurement of Pt/STO/TiN stacks evidenced that the in-situ crystallized STO showed higher leakage current compared to the STO thin film crystallized by post-deposition RTA on a crystalline seed-layer. This was ascribed to the incorporation of carbon impurities in the in-situ crystallized STO caused by the high deposition temperature [85].

A particular effort in optimizing the STO thin film properties employing a crystalline seed-layer has been carried out by the group of Prof. Hwang at the Seoul National University, Korea. The first papers on ALD of STO published by this group focused on the developing an ALD process of STO employing $Sr(thd)_2$, $Ti(O^iPr)_4$ and a remote H_2O plasma to obtain conformal thin STO thin films over contact holes both in terms of thickness and composition [71,73]. It was shown that despite the fact that the $Sr(thd)_2$ precursor starts decomposing at $\sim 200\,°C$ it was possible to achieve excellent thickness conformality and composition uniformity at a deposition temperature of $250\,°C$ (see Figure 2.11). This was achieved by keeping the Sr precursor bubbler at $180\,°C$, thus avoiding the oligomerization of the precursor and, consequently, widening the ALD window of the process to higher temperature [71,73]. The seed-layer approach was then employed to try to reduce the high leakage values due to the cracks obtained after a post-deposition annealing [75]. By employing the same precursors and H_2O vapor, a 5 nm seed was deposited at $250\,°C$ and then annealed at $650\,°C$. The main STO layer (15 nm) was then deposited under the same process conditions [75]. The crystallization of the main layer by post-deposition annealing was possible at temperature as low as $400\,°C$ due to the seed-layer which supplies nucleation sites for the crystallization process. The formation of cracks was reduced with the seed-layer approach [75]. However, shrinkage of the main layer remains dependent on the main layer deposition temperature and was still
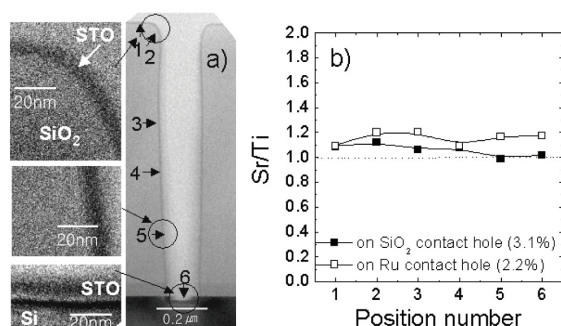
Figure 2.11: (a) Cross-sectional TEM images of a STO film deposited by plasma-assisted ALD on a SiO$_2$ contact hole (aspect ratio 1:8) and (b) elemental composition over the SiO$_2$ and Ru contact holes. Taken from Kwon et al. [73].

evident after the annealing step. This resulted in relatively high leakage currents [75]. To improve the electric properties of the STO thin films a process to obtain in-situ crystalliz-ation was developed. Lee et al. employed Ti(thd)$_2$(O^{i}Pr)$_2$ as the Ti precursor which has an increased thermal stability ($\sim 400\,°$C) compared to the previously employed Ti(O^{i}Pr)$_4$ ($\sim 280\,°$C) [80-82]. Consequently, they could extend the ALD temperature window up to 390 °C. ALD of STO employing such Ti precursor, Sr(thd)$_2$ and H$_2$O carried out at 370 °C resulted in amorphous films without using a crystalline seed layer. These films exhibited reduced shrinkage and crack formation upon post deposition annealing thus yielding improved dielectric performance compared to the results presented previously [43,80-82]. When a crystalline seed-layer (3 - 5 nm) was employed, in-situ crystalliz-ation was achieved by depositing the main layer (~ 10 nm) at 370 °C. The crystalline film obtained with this approach showed a small grain size (< 50 nm) [80-82]. The tem-perature of the RTA step employed to crystallize the seed-layer proved to be a critical parameter to obtain in-situ crystallization of the main layer. In particular, when high temperatures were employed (> 700 °C) the oxidation of the Ru bottom electrode and the formation of strontium ruthenate (SRO) phases resulted in a seed layer which led to a partial crystallization of the main layer [80,82]. By crystallizing the seed-layer at 650 - 700 °C optimal leakage current densities of the in-situ crystallized STO film were achieved ($\sim 1\times10^{-7}$ A cm^{-2} at 0.8 V for an EOT = 0.72 nm) [81].

In order to achieve an ALD process for STO with a GPC compatible with mass production Lee et al. used the Sr(^{i}Pr$_3$Cp)$_2$ precursor, which exhibits higher GPC com-pared to the previously employed Sr(thd)$_2$ [43,81]. The authors reported that even if the Sr(^{i}Pr$_3$Cp)$_2$ precursor starts decomposing at $\sim 320\,°$C it was possible to extend the

ALD window of the STO ALD process by selecting the optimum ALD sequence of the precursors and of the oxidizing sources. It was demonstrated that by using H_2O as the oxidizing source for the $Ti(thd)_2(O^iPr)_2$ and ozone for $Sr(^iPr_3Cp)_2$ it was possible to deposit STO thin films in a genuine ALD mode up to $370\,°C$ with a seven-fold higher GPC compared to their previous work [83]. However, they reported that for such a combination of precursors the composition of the STO thin films was not reproducible due to an in-situ oxidation and subsequent reduction of the Ru substrate. This resulted in an excessive supply of oxygen atoms and consequent CVD-like growth of the SrO layer at the onset on the growth [83,84]. To overcome this issue, a thin (≤ 5 nm) TiO_2 or Al_2O_3 interlayer was employed to prevent this substrate/film interaction thus, achieving a better composition control [83,95]. Despite the fact that the TiO_2 interlayer has a lower permittivity value which increases the total EOT of the dielectric stack, improved leakage current performance was achieved ($\sim 3\times10^{-8}$ A cm^{-2} at 0.8 V for an EOT = 0.57 nm) [83]. In their latest published work, Lee et al. reported that the increased Sr incorporation at the substrate/film could be avoided by employing the $Ti(Me_5Cp)(OMe)_3$ precursor [84]. The enhanced CVD-like growth behavior shown by this precursor in the early stages of the deposition was beneficial in preventing the increased Sr incorporation early on in the deposition process. Consequently, the TiO_2 or Al_2O_3 interlayer could be removed and lower EOT values could be achieved [84]. With this approach the authors achieved excellent dielectric properties (8×10^{-8} A cm^{-2} at 0.8 V for an EOT = 0.43 nm) [84].

The group of Prof. Hwang is the only one which has also reported results in the literature concerning the conformality of ALD STO thin films over high aspect ratio structures. Kwon et al. showed excellent thickness conformality and composition uniformity, for a contact hole with aspect ratio 1:8 as shown in figure 2.11 [73]. Remarkably, these results were obtained when a remote H_2O plasma was employed as the oxygen source showing the possibility of achieving excellent conformality by using a plasma-assisted ALD process [73]. In another report, Lee et al. showed excellent thickness and composition conformality (~ 95 %) of the STO thin films deposited by thermal ALD at $370\,°C$ over a contact hole with aspect ratio 1:10 (see figure 2.12) [84]. This result suggests that the film was grown in self-limited ALD fashion even for this relatively high deposition temperature [83].

The other reports pubblished in the literature by other research groups on ALD of STO which are not reviewed here are also listed on Table 2.1. It should be noted that the research reported in this thesis is the continuation of the work iniated by Langereis et al. [86] at the Plasma and Material Processing group of the Applied Physics department of
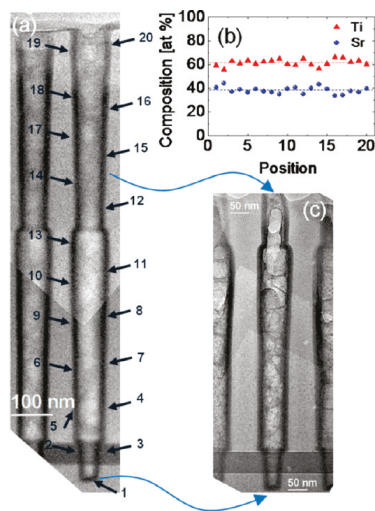
Figure 2.12: Cross-sectional TEM images of an STO film deposited at $370\,^{\circ}\text{C}$ on a contact hole with aspect ratio 1:10 (a,c) and energy dispersive spectroscopy elemental compositional profile along the contact hole. Taken from [84].

the University of Eindhoven.

2.4   References

1. R.A. Cowley, *Phil. Trans. R. Soc. Lond. A*, 354, 2799 (1996).

2. S.A. Hayward, E.K.H. Salje, *Phase Transit.*, 68, 501 (1999).

3. J. Hemberger, P. Lunkenheimer, R. Viana, R. Böhmer and A. Loidl, *Phys. Rev. B*, 52, 13159 (1995).

4. K.A. Müller and H. Burkard, *Phys. Rev. B*, 19, 3593 (1979).

5. K.A. Müller, W. Berlinger and E. Tosatti, *Zeitschrift fur Physik B*, 84, 277 (1991).

6. J. Dec, W. Kleemann and B. Westwanski, *J. Phys.: Condens. Matter.*, 11, L379 (1999).

7. Y.S. Kim, D.J. Kim, T.H. Kim and T.W. Noh, *Appl. Phys. Lett.*, 91, 042908 (2007).

8. J.H. Haeni, P. Irvin, W. Chang, R. Uecker, P. Reiche, Y.L. Li, S. Choudhury, W. Tian, M.E. Hawley, B. Craigo, A.K. Tagantsev, X.Q. Pan, S.K. Streiffer, L.Q. Chen, S.W. Kirchoefer, J. Levy and D.G. Schlom, *Nature*, 430, 758 (2004).

9. M.P. Warusawithana, C. Cen, C.R. Sleasman, J.C. Woicik, Y. Li, L.F. Kourkoutis, J.A. Klug, H. Li, P. Ryan, L.P. Wang, M. Bedzyk, D.A. Muller, L.Q. Chen, J. Levy and D.G. Schlom, *Science*, 324, 367 (2009).

10. S. Zollner, A.A. Demkov, R. Liu, P.L. Fejes, R.B. Gregory, P. Alluri, J.A. Curless, Z. Yu, J. Ramdani, R. Droopad, T.E. Tiwald, J.N. Hilfiker and J.A. Woollam, *J. Vac. Sci. Technol., B*, 18, 2242 (2000).

11. M. Cardona, *Phys. Rev.*, 140, A651 (1965).

12. C. Kittel, "Introduction to Solid State Physics", 8th Ed., Wiley, (2005).

13. O.N. Tufte and P.W. Chapman, *Phys. Rev.*, 155, 796 (1967).

14. H. P. R. Frederikse and W. R. Hosler, *Phys. Rev.*, 161, 822 (1967).

15. D.A. Muller, N. Nakagawa, A. Ohtomo, J.L. Grazul, and H.Y. Hwang, *Nature*, 430, 657 (2004).

16. J. Son, P. Moetakef, B. Jalan, O. Bierwagen, N.J. Wright, R. Engel-Herbert and S. Stemmer, *Nature Materials*, 9, 482 (2010).

17. T.J. Park, J.H. Kim, J.H. Jang, J. Lee, S.W. Lee, S.Y. Lee, H.S. Jung and C.S. Hwang, *J. Electrochem. Soc.*, 156(9), G129 (2009).

18. K. Eisenbeiser, J.M. Finder, Z. Yu, J. Ramdani, J.A. Curless, J.A. Hallmark, R. Droopad, W.J. Ooms, L. Salem, S. Bradshaw and C.D. Overgaard, *Appl. Phys. Lett.*, 76, 1324 (2000).

19. S.H. Baek and C.B. Eom, *Acta Mater.*, 61, 2734, (2013).

20. I. Pallecchi, G. Grassano, D. Marre', L. Pellegrino, M. Putti and A.S. Siri, *Appl. Phys. Lett.*, 78, 2244 (2001).

21. D. Marre', A. Tumino, E. Bellingeri, I. Pallecchi, L. Pellegrino and A.S. Siri, *J. Phys. D: Appl. Phys.*, 36, 896 (2003).

22. H.Y. Lee, C.H. Hsu, Y.W. Hsieh and H.J. Liu, *Thin Solid Films*, 469, 327 (2004).

23. H.Y. Hwang, Y. Iwasa, M. Kawasaki, B. Keimer, N. Nagaosa and Y. Tokura, *Nature Mater.*, 11, 103 (2012).

24. H.W. Jang, D.A. Felker, C.W. Bark, Y. Wang, M.K. Niranjan, C.T. Nelson, Y. Zhang, D. Su, C.M. Folkman, S.H. Baek, S. Lee, K. Janicka, Y. Zhu, X.Q. Pan, D.D. Fong, E.Y. Tsymbal, M.S. Rzchowski and C.B. Eom, *Science*, 331, 886 (2011).

25. C. Cen, S. Thiel, J. Mannhart and J. Levy, *Science*, 323, 1026 (2009).

26. J. Mannhart, D.H.A. Blank, H.Y. Hwang, A.J. Millis and J.M. Triscone, *MRS Bulletin*, 33, 1027 (2008).

27. A.D. Caviglia, S. Gariglio, N. Reyren, D. Jaccard, T. Schneider, M. Gabay, S. Thiel, G. Hammerl, J. Mannhart and J.M. Triscone, *Nature*, 456, 624 (2008).

28. A. Ohtomo and H.Y. Hwang, *Nature*, 427, 423 (2004).

29. A.F. Santander-Syro, O. Copie, T. Kondo, F. Fortuna, S. Pailhe's, R. Weht, X.G. Qiu, F. Bertran, A. Nicolaou, A. Taleb-Ibrahimi, P. Le Fe've, G. Herranz, M. Bibes, N. Reyren, Y. Apertet, P. Lecoeur, A. Barthe'le'my and M.J. Rozenberg, *Nature*, 469, 189 (2011).

30. M. Spreitzer, R. Egoavil, J. Verbeeck, D.H.A. Blanka and G. Rijnders, *J. Mater. Chem. C*, 1, 5216 (2013).

31. F. Yang, K.J. Jin, H.B. Lu, M. He and G.Z. Yang, *J. Phys. D: Appl. Phys.*, 42, 045116 (2009).

32. R. McKee, F. Walker and M. Chisholm, *Phys. Rev. Lett.*, 81, 3014 (1998).

33. T. Tsurumi, T. Suzuki, M. Yamane and M. Daimon, *Jpn. J. Appl. Phys.*, 33, 5192 (1994).

34. S. Schmelzer, D. Bräuhaus, S. Hoffmann-Eifert, P. Meuffels, U. Böttger, L. Oberbeck, P. Reinig, U. Schröder, and R. Waser, *Appl. Phys. Lett.*, 97, 132907 (2010).

35. U. Selvaraj, A.V. Prasadarao, S. Komarneni and R. Roy, *Mat. Lett.*, 23, 123 (1995).

36. D. Bao, X. Yao, N. Wakiya, K. Shinozaki and N. Mizutani, *Appl. Phys. Lett.*, 79, 3767 (2001).

37. M.K. Lee, H.C. Lee and Z.H. Lee, *Jpn. J. Appl. Phys.*, 46, 5116 (2007).

38. C.S. Kang, C.S. Hwang, H.J Cho, B.T. Lee, S.O. Park, J.W. Kim, H. Horii, S.I Lee, Y.B. Koh and M.Y. Lee, *Jpn. J. Appl. Phys.*, 35, 4890 (1996).

39. Z. Wang, T. Yasuda, S. Hatatani and S. Oda, *Jpn. J. Appl. Phys.*, 38, 6817 (1999).

40. D. Kon, K. Hashiba, T. Kawashima and Y. Akiyama, *ECS Trans.*, 25, 333 (2009).

41. H. Mori and H. Ishiwara, *Jpn. J. Appl. Phys.*, 30, L1415 (1991).

42. R. H. Dennard, *U.S. Patent*, (1968).

43. S.K. Kim, S.W. Lee, J.H. Han, B. Lee, S. Han and C.S. Hwang, *Adv. Funct. Mater.*, 20, 2989 (2010).

44. http://www.itrs.net/Links/2012ITRS/Home2012.htm.

45. J. Robertson, *Solid State Electron.*, 49, 283 (2005).

46. M.S. Kim, M. Popovici, J. Swerts, M.A. Pawlak, K. Tomida, B. Kaczer, K. Opsomer, M. Schaekers, H. Tielens, C. Vrancken, S. van Elshocht, I. Debusschere, L. Altimime and J.A. Kittl, *IMW, 2011 3rd IEEE International*, (2011).

47. http://www.itrs.net/Links/2013ITRS/Home2013.htm updated version.

48. S. van Elshocht, C. Adelmann, S. Clima, G. Pourtois, T. Conard, A. Delabie, A. Franquet, P. Lehnen, J. Meersschaut, N. Menou, M. Popovici, O. Richard, T. Schram, X.P. Wang, A. Hardy, D. Dewulf, M.K. Van Bael, P. Lehnen, T. Blomberg, D. Pierreux, J. Swerts, J.W. Maes, D.J. Wouters, S. De Gendt and J.A. Kittl, *J. Vac. Sci. Technol., B*, 27, 209 (2009).

49. S. Hong, *IEDM 2010, Technical Digest*, (2010).

50. R. Waser, ed., "Nanoelectronics and Information Technology", 3rd Ed., Wiley, (2012).

51. R. Waser and M. Aono, *Nature Mater.*, 6, 833 (2007).

52. J.J. Yang, D.B. Strukov and D.R. Stewart, *Nature Nanotech.*, 8, 13 (2013).

53. L. Goux, J.G. Lisoni, M. Jurczak, D.J. Wouters, L. Courtade and Ch. Muller, *J. Appl. Phys.*, 107, 024512 (2010).

54. D.S. Jeong, H. Schroeder and R. Waser, *Electrochem. Solid-State Lett.*, 10, G51 (2007).

55. X. Sun, G. Li, X. Zhang, L. Ding and W. Zhang, *J. Phys. D: Appl. Phys.*, 44, 125404 (2011).

56. M.H. Tang, Z.P. Wang, J.C. Li, Z.Q. Zeng, X.L Xu, G.Y Wang, L.B Zhang, Y.G. Xiao, S.B Yang, B.Jiang and J. He, *Semicond. Sci. Technol.*, 26, 075019 (2011).

57. A. Sawa, *Mater. Today*, 11, 28 (2008).

58. R. Meyer, L. Schloss, J. Brewer, R. Lambertson, W. Kinney, J. Sanchez and D. Rinerson, *Proc. NVMTS*, 54 (2008).

59. I. Valov, R. Waser, J.R. Jameson and M.N. Kozicki, *Nanotechnology*, 22, 254003 (2011).

60. T. Tsuruoka, K. Terabe, T. Hasegawa and M. Aono, *Nanotechnology*, 21, 425205 (2010).

61. D. Ielmini, R. Bruchhausb and R. Waser, *Phase Transit.*,84, 570, (2011).

62. K. Szot, R. Dittmann, W. Speier and R. Waser, *Phys. Stat. Sol. (RRL)*, 1, R86 (2007).

63. C. Nauenheim, C. Kügeler, A. Rüdiger, R. Waser, A. Flocke and T.G. Noll, *Nanotechnology, 2008. NANO '08. 8th IEEE Conference on*, 464 (2008).

64. C. Kügeler, R. Rosezin, E. Linn, R. Bruchhaus and R. Waser, *Appl. Phys. A - Mater. Sci. Process.*, 102, 791 (2011).

65. M. Vehkamäki, T. Hatanpää, T. Hänninen, M. Ritala, M. Leskelä, *Electrochem. Solid-State Lett.*, 2, 504 (1999).

66. M. Vehkamäki, T. Hänninen, M. Ritala, M. ä, T. Sajavaara, E. Rauhala and J. Keinonen, *Chem. Vap. Deposition*, 7, 75 (2001).

67. M. Popovici, S. van Elshocht, N. Menou, J. Swerts, D. Pierreux, A. Delabie, B. Brijs, T. Conard, K. Opsomer, J.W. Maes, D.J. Wouters and J.A. Kittl, *J. Electrochem. Soc.*, 157, G1 (2010).

68. A. Kosola, M. Putkonen, L.S. Johansson and L. Niinisto, *Appl. Surf. Sci.*, 211, 102 (2003).

69. D.S. Kil, J.M. Lee, and J.S. Roh, *Chem. Vap. Deposition*, 8, 195 (2002).

70. J.H. Lee, Y.J. Cho, Y.S. Min, D.Kim, and S.W. Rhee, *J. Vac. Sci. Technol. A*, 20, 1828 (2002).

71. S.W. Lee, O.S. Kwon, and C.S. Hwang,*Microelectron. Eng.*, 80, 158 (2005).

72. R. Katamreddy, V. Omarjee, B. Feist, C. Dussarrat, M. Singh and C. Takoudis, *ECS Trans.*, 16, 487 (2008).

73. O.S. Kwon, S.K. Kim, M. Cho, C.S. Hwang and J. Jeong, *J. Electrochem. Soc.*, 152, C229 (2005).

74. S. Bhaskar, D. Allgeyer and J.A. Smythe, *Appl. Phys. Lett.*, 89, 254103 (2006).

75. O.S. Kwon, S.W. Lee, J.H. Han and C.S. Hwang, *J. Electrochem. Soc.*, 154, G127 (2007).

76. J.H Ahn, J.Y Kim, S.W. Kang, J.H. Kim and J.S. Roh, *Appl. Phys. Lett.*, 91, 062910 (2007).

77. J.Y. Kim, J.H. Ahn, S.W. Kang, J.H. Kim and J.S. Roh, *Appl. Phys. Lett.*, 91, 092910 (2007).

78. J.H. Ahn, S.W. Kang, J.Y. Kim, J.H. Kim and J.S. Roh, *J. Electrochem. Soc.*, 155, G185 (2008).

79. M.D. McDaniel, A. Posadas, T.Q. Ngo, A. Dhamdhere, D.J. Smith, A.A. Demkov and J.G. Ekerdt, *J. Vac. Sci. Technol. A*, 31, 01A136 (2013).

80. S.W. Lee, J.H. Han, O.S. Kwon and C.S. Hwang, *J. Electrochem. Soc.*, 155, G253 (2008).

81. S.W. Lee, O.S. Kwon, J.H. Han and C.S. Hwang, *Appl. Phys. Lett.*, 92, 222903 (2008).

82. S.W. Lee, J.H. Han and C.S. Hwang, *ECS Trans.*, 19, 685 (2009).

83. S.W. Lee, J.H. Han, S. Han, W. Lee, J.H. Jang, M. Seo, S.K. Kim, C. Dussarrat, J. Gatineau, Y.S. Min and C.S. Hwang, *Chem. Mater.*, 23, 2227 (2011).

84. W. Lee, J.H. Han, W. Jeon, Y.W. Yoo, S.W. Lee, S.K. Kim, C.H. Ko, C. Lansalot-Matras and C.S. Hwang, *Chem. Mater.*, 25 , 953 (2013).

85. M. Popovici, K. Tomida, J. Swerts, P. Favia, A. Delabie, H. Bender, C. Adelmann, H. Tielens, B. Brijs, B. Kaczer, M.A. Pawlak, M.S. Kim, L. Altimime, S. van Elshocht and J. A. Kittl, *Phys. Stat. Sol. A*, 208, 1920 (2011).

86. E. Langereis, R. Roijmans, F. Roozeboom, M.C.M. van de Sanden and W.M.M. Kessels, *J. Electrochem. Soc.*, 158, G34, (2011).

87. S. Riedel, J. Neidhardt, S. Jansen, L. Wilde, J. Sundqvist, E. Erben, S. Teichert and A. Michaelis, *J. Appl. Phys.*, 109, 094101 (2011).

88. N. Menou, M. Popovici, S. Clima, K. Opsomer, W. Polspoel, B. Kaczer, G. Rampelberg, K. Tomida, M.A. Pawlak, C. Detavernier, D. Pierreux, J. Swerts, J.W. Maes, D. Manger, M. Badylevich, V.V. Afanas'ev, T. Conard, P. Favia, H. Bender, B. Brijs, W. Vandervorst, S. van Elshocht, G. Pourtois, D.J. Wouters, S. Biesemans and J.A. Kittl, *J. Appl. Phys.*, 106, 094101 (2009).

89. M.A. Pawlak, B. Kaczer, M.S. Kim, M. Popovici, K. Tomida, J. Swerts, K. Opsomer, W. Polspoel, P. Favia, C. Vrancken, C. Demeurisse, W.C. Wang, V. V. Afanas'ev, W. Vandervorst, H. Bender, I. Debusschere, L. Altimime and J. A. Kittl, *Appl. Phys. Lett.*, 97, 162906 (2010).

90. M. Popovici, S. van Elshocht, N. Menou, P. Favia, H. Bender, E. Rosseel, J. Swerts, C. Adelmann, C. Vrancken, A. Moussa, H. Tielens, K. Tomida, M.A. Pawlak, B. Kaczer, G. Schoofs, W. Vandervorst, D.J. Wouters and J.A. Kittl, *J. Vac. Sci. Technol. B*, 29, 01A304 (2011).

91. N. Menou, X.P. Wang, B. Kaczer, W. Polspoel, M. Popovici, K. Opsomer, M.A. Pawlak, W. Knaepen, C. Detavernier, T. Blomberg, D. Pierreux, J. Swerts, J.W. Maes, P. Favia, H. Bender, B. Brijs, W. Vandervorst, S. van Elshocht, D.J. Wouters, S. Biesemans and J.A. Kittl, *IEDM 2008, Technical Digest*, 929 (2008).

92. M.A. Pawlak, M. Popovici, J. Swerts, K. Tomida, M.S. Kim, B. Kaczer, K. Opsomer, M. Schaekers, P. Favia, H. Bender, C. Vrancken, B. Govoreanu, C. Demeurisse, W.C. Wang, V.V. Afanas'ev, I. Debusschere, L. Altimime and J.A. Kittl, *IEDM* 2010.

93. M.A. Pawlak, B. Kaczer, M.S. Kim, M. Popovici, J. Swerts, W.C. Wang, K. Opsomer, P. Favia, K. Tomida, A. Belmonte, B. Govoreanu, C. Vrancken, C. Demeurisse, H. Bender, V.V. Afanas'ev, I. Debusschere, L. Altimime and J.A. Kittl, *Appl. Phys. Lett.*, 98, 182902 (2011).

94. N. Menou, M. Popovici, K. Opsomer, B. Kaczer, M.A. Pawlak, C. Adelmann, A. Franquet, P. Favia, H. Bender, C. Detavernier, S. Van Elshocht, D.J. Wouters, S. Biesemans and J.A. Kittl, *Jpn. J. Appl. Phys.*, 49, 04DD01 (2010).

95. W. Lee, J.H. Han, S.W. Lee, S. Han, W.J. Jeon and C.S. Hwang, *J. Mater. Chem.*, 22, 15037 (2012).

96. T. Blomberg, J. Anttila, S. Haukka, M. Tuominen, M. Lukosius, Ch. Wenger and T. Saukkonen, *Thin Solid Films*, 520, 6535 (2012).

97. M. Lukosius, Ch. Wenger, T. Blomberg, A. Abrutis, G. Lupina, P.K. Baumann and G. Ruhle, *ECS J. Solid State Sci. Technol.*, 1, N1 (2012).

Chapter 3

Experimental Equipment and Characterization of STO Thin Films

In this chapter, the experimental equipment used for the ALD and for the rapid thermal annealing (RTA) processing of the STO thin films will be described. A short description of the RTA working principle will also be given. Furthermore, four techniques which have been extensively used in this work to characterize the structure and the composition of the STO thin films will be introduced. These are: Spectroscopic Ellipsometry (SE), X-ray Photoelectron Spectroscopy (XPS), X-ray Diffraction (XRD) and Transmission Electron Microscopy (TEM). In particular, SE has been used to determine the thickness and optical constants of the STO films. Furthermore, as it will be discussed in Chapter 4, this technique has proven to be an non-intrusive and fast method to determine the cation stoichiometry and the crystallinity of the STO films. XPS has been used to determine the STO film composition and to confirm the cation stoichiometry values obtained by SE measurements. Moreover, XPS depth profiling analysis has been used to determine the elemental concentrations and possible phase segregations throughout the STO films and to investigate the interfaces between STO and the other thin films comprising the film stacks analyzed in this work. XRD measurements were used to determine the crystalline phase and possible texture of the STO films. Finally, TEM was employed to study the crystallization behavior of STO thin films. Several TEM techniques were utilized and these will be briefly described in this chapter. A description of these techniques, with a particular focus on their application on the characterization of STO films, will be given.
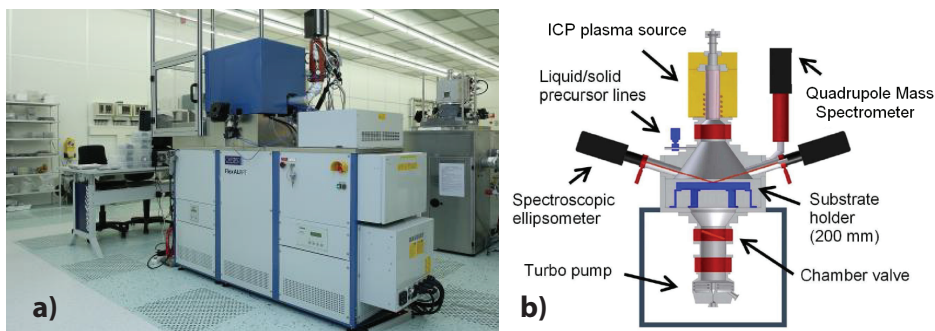
Figure 3.1: Picture (a) and schematic illustration (b) of the Oxford Instruments'
FlexAL™ ALD reactor employed in this thesis work.

3.1   ALD Equipment

The experimental equipment employed in this work for the deposition of the STO films
(and Pt) by ALD is an Oxford Instruments' FlexAL™reactor. A picture and a schem-
atic of this reactor are shown in Figure 3.1.a and 3.1.b, respectively. The reactor can
accommodate wafers with diameter up to 200 mm and it has a load-lock chamber for
loading and unloading the samples without the need of venting the main reactor cham-
ber. Both the load-lock and the main reactor chamber are equipped with turbomolecular
pumps. The base pressure in the reactor chamber is typically in the order of 10^{-7} Torr.
However, during processing the pressure in the reactor is in the order of a few tens mTorr.

The delivery of the precursor is achieved through dedicated ALD valves (Swagelok®)
which can close and open in a few ms. Such valves are placed close to the reactor cham-
ber and are connected through stainless steel delivery lines to the precursor canisters
which are stored in heated pods. Usually, the temperature of the delivery lines is 20-
30 °C higher than the temperature of the pods in order to avoid condensation of the
precursor vapors in the lines. The delivery of a precursor to the reactor chamber can
be achieved either by simply opening the ALD valve connected to the relative delivery
line, and therefore drawing the precursor vapor, or by "bubbling". The latter consists of
"bubbling" an inert gas (i.e. Ar) through the liquid precursor and, therefore, delivering
a mixture of the precursor vapor and the inert gas to the reactor. This method usually
guarantees a more stable and reliable delivery over time and, for this reason, it was the
method of choice employed in this work. For the preparation of the STO films presented
in this thesis the substrate was usually treated by an oxygen plasma (generally 1 minute)
prior to deposition in order to remove surface contamination and the ALD process was

then started by first dosing the Sr-precursor.

The FlexAL^{TM}reactor employed in this work can accomodate four different chemical precursors in four separated pods. Separate inlets and delivery lines are used for each precursor. Furthermore, various co-reactant sources are available such as water and ozone (through an ozone generator). Furthermore, the reactor is equipped with a remote inductively coupled (ICP) plasma generator placed above the main reactor chamber. This source consists of a cylindrical inductor coil wrapped around an Al_2O_3 discharge tube. The plasma generated in such source is usually referred as "remote plasma" since the plasma source is not placed in the close vicinity of the substrate and the substrate is not involved in the generation of the plasma. Various gases are available for the generation of the plasma in this setup (i.e. Ar, O_2, N_2, H_2, NH_3, SF_6). In this work a remote O_2 plasma was used as the oxidizing agent. For a detail description of the ion flux and energies, photon flux, electron density and temperature in this setup the reader is referred to reference [1].

The substrate holder can be set to temperature values up to $400\,°C$. However, due to the low pressure in the reactor the actual temperature of the heated samples is 20-25 % lower (in $°C$) as confirmed by calibration measurements. The reactor walls are usually heated (up to $120\,°C$) during deposition to avoid condensation of the precursors and of the co-reactants employed (i.e. water) and to guarantee reasonable purge times.

This setup is equipped with dedicated ports and windows for in-situ characterization of the ALD processes. For example, as depicted in Figure 3.1.b, quadrupole mass spectrometry (QMS) and spectroscopic ellipsometry (SE) measurements can be performed during the deposition of thin films. The employment of in-situ characterization techniques enables the monitoring and the control of the deposition process and, therefore, allows a deeper understanding of the growth mechanism.

For the preparation of STO and Pt thin films in this reactor the *growth-per-cycle* of the different processes (SrO, TiO_2, STO and Pt) were monitored by in-situ and ex-situ SE to confirm the reproducibility of the depositions. Furthermore, the composition of the STO films was also monitored by SE with the same aim. It should be noted that the reactor walls need to be conditioned by performing a few hundred ALD cycle of the desidered process in order to obtain reproducibile results when switching between different processes in the reactor. This was for example the case for the preparation of the Pt/STO/Pt stacks studied in Chapter 6.

Another aspect which should be noted is the limited temperature at which the Hyper-Sr precursor could be heated. Since the reactor walls cannot be heated above $120\,°C$, the temperature of the delivery lines and of the precursor pod of the Hyper-Sr precursor
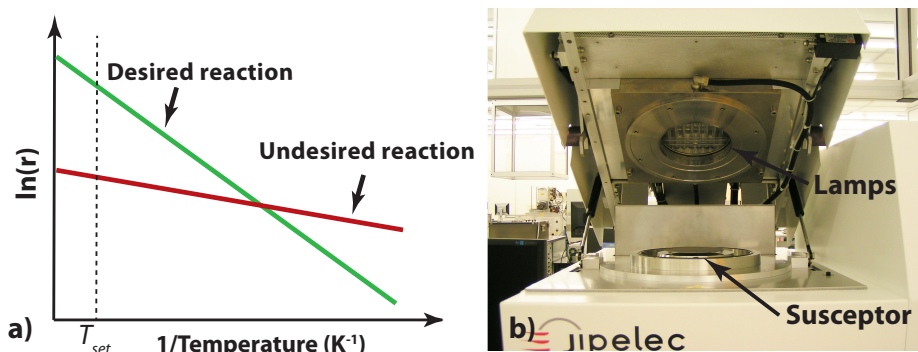
Figure 3.2: Arrhenius plot of the rates of a desired process, for which a thermal treatment is employed, and of a representative undesired reaction (a). By rapidly ramping up to T_{set} the desired reaction rate will be accelerated while suppressing any of the undesired reaction rate. Picture of the Jipelec Jetfirst equipment employed in this work for the RTA of STO thin films (b). The lamps and the susceptor are indicated.

were kept at $150\,°C$ and $120\,°C$, respectively, in order to avoid condensation and clogging. This resulted in a ALD dosing time of the Hyper-Sr precursor of 15 s. However, this dosing time could be probably reduced if higher temperature could be employed.

3.2   Rapid Thermal Annealing Equipment

Rapid thermal annealing (RTA) is a thermal treatment widely used in the semiconductor industry. It involves the short-time radiative heating of a sample, usually, by means of infrared lamps (tungsten-halogen) with ramp rates up to $100\,°C/s$. Due to the radiative heating, during RTA the sample is not in thermal equilibrium with the flowing gas ambient which is introduced at lower temperature. Furthermore, the RTA equipment itself is not intentionally heated (cold wall). In contrast, during furnace annealing heating of the sample is achieved through resistive heaters. In this configuration, the sample is heated through convection and it is in (semi-)equilibium with the gas ambient and the furnace walls (hot walls). In semiconductor manufacturing RTA has taken over furnace annealing due to the reduced treatment durations, hence, reduced thermal budget necessary to achieve the same thermally-activated process. This can greatly reduce non-intended side-reactions related to the prolonged heating of the sample. This concept is illustrated in Figure 3.2.a where the Arrhenius plots of two different processes are shown. The desired reaction is the thermally-activated process for which the thermal treatment step is inten-

ded (e.g. crystallization of amorphous films) while the undesired reaction consists in one or more unwanted side-reactions (e.g. inter-diffusion between different films, dopant diffusion, etc.). To activate the desired reaction more selectively a certain thermal budget must be applied, for example by reaching and keeping the sample at a desired temperature, T_{set} for a certain amount of time. Undesired effects can be reduced by rapidly ramping the sample temperature to T_{set} for which the desired reaction has a much higher rate, r, than the undesired reactions. However, in furnace annealing, where the furnces are usually large multi-wafer (batch) reactors, the temperature ramp time is significant (up to 30 minutes) due to the large amount of heat required to bring the entire system (gas ambient and walls) to the required temperature. This leads to pronounced unwanted reactions compared to RTA. RTA is therefore preferred in a variety of semiconductor processes such as activation of dopants, the repair of damages from ion implantation, removal of contaminants and the modification of thin films and interface properties [2].

Figure 3.2.b shows a picture of one of the RTA reactors employed in this thesis work (Jipelec Jetfirst 100). The susceptor which serves as the substrate holder and the infrared lamps are indicated in the figure. In this work RTA has been employed to crystallize the amorphous as-deposited STO thin films into the perovskite structure and to tailor their crystallization process. In particular, heat ramps in the range of 55-60 °C/s have been employed to quickly reach the required crystallization temperature (550-700 °C, see Chapter 5). After reaching the required value, the temperature is kept constant for a certain amount of time before the sample is radiatively (i.e. exponentially) cooled down to room temperature. This temperature profile is that of the "soak" annealing shown in Figure 1.5. In this study annealing times up to 10 minutes have been employed to study the crystallization process of STO thin films. This is rather long compared to standard RTA treatment duration employed in semiconductor manifucaturing. Yet, the term RTA will still be used to describe the radiative annealing employed in this work.

3.3 Spectroscopic Ellipsometry

Spectroscopic ellipsometry (SE) is an optical technique which can be employed to determine the thickness and the optical properties of thin films [3]. The working principle is illustrated in Figure 3.3. A light source is used to shine polarized light (linearly polarized in Figure 3.3) onto the sample at an angle θ with respect to the sample surface normal, set to maximize the sensitivity of the measurement (typically 70-80 ° for Si substrates). With the polarization of the incident light known, the changes in polarization upon reflection on the sample can be measured by a detector. For example linear polarization
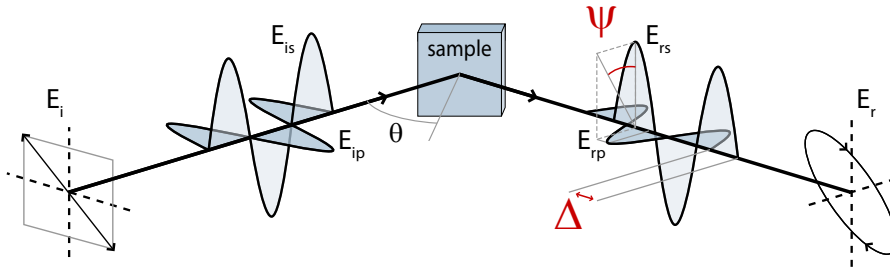
Figure 3.3: Schematic illustration of the working principle of spectroscopic ellipsometry. Polarized light is incident onto the sample at an angle θ with respect to the surface normal. Changes in light polarization are measured upon reflection on the sample as the ellipsometric angles Ψ and Δ.

can be achieved for the incident light by a fixed polarizer, while for determining the polarization of the reflected light a rotating polarizer (analyzer) can be used. In particular, the ellipsometric angles, Ψ and Δ can be measured in this way. Ψ and Δ represent the amplitude ratio and the phase difference of p-polarized and s-polarized light upon reflection, respectively. These two parameters are measured over the spectral range of the optical system (usually in the visible/UV range). For the data analysis of spectroscopic ellipsometry data, a model comprising the thicknesses and optical constants of the layers constituting the examined sample is used. The thickness and the optical properties of the thin film of interest are then obtained through a fitting procedure to minimize the error between the measured Ψ and Δ values and those calculated with the model. From a SE measurement the dielectric function or the complex refractive index of a thin film can be determined. As will be shown in Chapter 4, from the dielectric function information such as the refractive index, the optical band gap and the band structure of the thin film material can be derived.

To determine the thickness and the dielectric function of the STO thin films studied in this work a two-step procedure was employed.

First, the ellipsometric angles were fitted by employing a so-called *Cauchy* model for the optical constants of STO. The Cauchy model is generally used for semi-transparent films in their transparency range (e.g. below the band gap). Therefore, the absorption coefficient, k, or the imaginary part of the dielectric function, ϵ_2, are equal to zero in this range, while the dispersion of the refractive index, n, is expressed by:
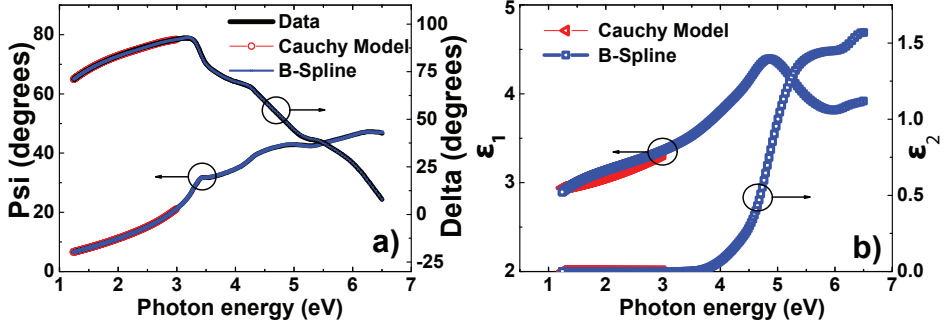
$$n(\lambda) = A + B/\lambda^2 + C/\lambda^4 + ...$$

Figure 3.4: Experimental Ψ and Δ values from a spectroscopic ellipsometry measurement of a STO thin film deposited on Si (a). The experimental data are compared with Ψ and Δ values obtained using a Cauchy model or a B-spline parameterization for the STO thin film (a). Dielectric functions, ϵ_1 and ϵ_2, obtained by the Cauchy model and by the B-spline parameterization for the STO thin film (b).

where A, B and C are the fitting parameters used during data analysis and λ is the light wavelength. In this work, a Cauchy model was used up to photon energies of 3 eV (STO band gap > 3 eV).

Secondly, the fit was extended to the entire spectral range of the measurement (in this work, 1.25-6.5 eV) employing a B-spline or Basis-spline parameterization. This procedure consists of parameterizing the dielectric function by a recursive set of polynomial splines. Therefore, during data analysis the optical constants are determined by using as fitting parameters the polynomial coefficients of the B-splines. Furthermore, the optical constants of a film can be ensured to remain physically relevant since with B-splines Kramers-Kronig consistency can be guaranteed. This also reduces the number of fitting parameters by 50% since the real part of the dielectric function, ϵ_1, can be calculated from the imaginary part, ϵ_2, through a Kramers-Kronig transformation. For a more detailed description of B-spline parameterization the reader is referred to [4,5].

Figure 3.4.a shows the fit results of the two-step process employed in the determination of the thickness and dielectric function of an amorphous STO thin film deposited on Si. The figure shows the data for the ellipsometric angles Ψ and Δ as measured and as fitted with a Cauchy model and a B-spline parameterization. In both cases, a Si/native oxide/STO/air stack model was employed. It can be seen that both the Cauchy model and B-spline parameterization fitting procedures give Ψ and Δ which properly describe the experimental values. Figure 3.4.b shows the dielectric function as determined by employing the Cauchy model and the B-spline parameterization. As mentioned above,

ϵ_2 was kept equal to zero for the fit with the Cauchy model. The slight difference in ϵ_1 between the two models is related to the more accurate and physical representation of the dielectric function by the B-spline parameterization since Kramers-Kronig consistency is not guaranteed by the Cauchy model.

In this thesis work this fitting procedure has been widely used to determine the thickness and the dielectric function of amorphous and crystalline STO thin films. Furthermore, SE has been used to determine the stoichiometry of STO amorphous films as will be described in Chapter 4.

3.4   X-ray Photoelectron Spectroscopy

X-ray photoelectron spectroscopy (XPS) is a surface-sensitive characterization technique for quantitative elemental composition and chemical analysis. In XPS, the examined specimen is irradiated by an X-ray beam and electrons are photoemitted from the sample. Considering the mean free path length of electrons, photoemitted electrons can escape the sample without loss of kinetic energy (due to scattering) only from the region of < 10 nm below the surface. Hence, the surface sensitivity of XPS. The electrons which escape from the sample surface are collected and their kinetic energy is measured. The kinetic energy E_K depends on the binding energy E_B in their bond-state and on the energy, $h\nu$, of the X-ray radiation. In particular,

$$E_B = h\nu - E_K - \phi$$

where ϕ is the so-called spectrometer work function. The binding energy is specific to the orbital and the atom from which the electron is photoemitted. Therefore, it is possible to determine the elemental composition of a sample. Moreover, quantitative analysis can be performed since the amount of detected electrons for a certain binding energy is proportional to the presence of a certain element in the sample. The binding energy of the photoemitted electrons is dependent on the chemical environment and on the oxidation state. Therefore, with XPS it is also possible to distinguish between different compounds representing different chemical environments. The quantitative elemental analysis is performed by determining the relative intensities of the peaks corresponding to the different elements present in the examined specimen. In particular, the intensity of a peak (usually the peak area) is divided by the sensitivity factor (SF) corresponding to the element and orbital of the peak, to quantify the presence of such element. This quantification gives the relative intensities of the detected elements (i.e. atomic percentages).

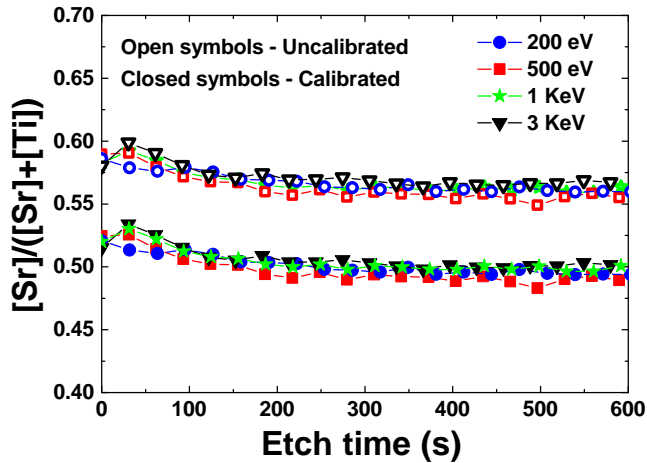In this work XPS has been mainly used to determine the elemental composition of

Figure 3.5: [Sr]/([Sr]+[Ti]) ratio as a function of etch time of a stoichiometric single-crystalline STO sample with calibrated and uncalibrated sensitivity factors and different Ar ion energies.

the STO thin films. In particular, the cation ratio [Sr]/([Sr]+[Ti]) and the presence of contaminants, such as carbon, have been determined by XPS.

In addition to conventional XPS, *depth profiling* was performed to determine the elemental composition throughout the film and any possible side-reaction at the substrate/film interface (i.e. interdiffusion). To carry out a depth profile Ar^+ ions are accelerated by an ion gun ($\sim$ 100-5000 eV) and focused on the spot ($\sim$ 50-500 μm^2) where the XPS analysis is performed. In this way a layer of material is etched off the sample surface, with the amount of material removed being dependent on the kinetic energy and the flux of ions. After each etch step an XPS analysis is performed to obtain compositional data points as a function of depth in the film.

To determine the elemental composition of the STO films the SF values for the Sr3d, Ti2p and O1s were first calibrated. With this aim, XPS analysis was carried out on a single-crystalline STO sample (20 x 20 mm^2, Crystal GmbH). Depth profile analysis of the single-crystalline STO was performed to remove surface contamination and to determine if undesired preferential etching (i.e. selective etching of different elements) takes place during Ar ion exposure. Figure 3.5 shows the cation ratio [Sr]/([Sr]+[Ti]) for the uncalibrated (i.e. software database values) and calibrated SF as a function of etch time for the single-crystalline STO sample. For the calibration of the SF, values guaranteeing a [Sr]/([Sr]+[Ti]) $\approx$ 0.50 throughout the depth profile were used. The
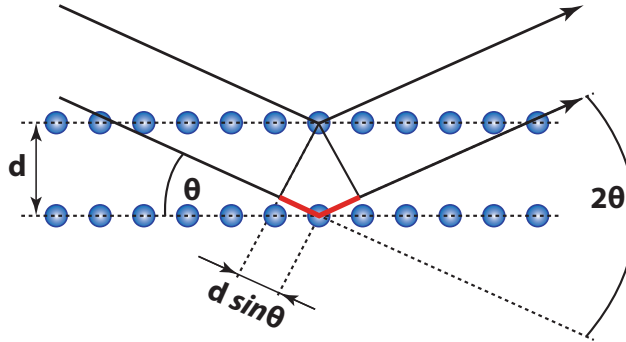
Figure 3.6: Representative illustration of a set of lattice planes hit by X-rays. The difference in distance covered by the two X-rays reflected by the top and bottom lattice planes is indicated in red. θ is the angle of incidence of the X-ray radiation and d the spacing between the lattice planes.

[Sr]/([Sr]+[Ti]) was also independent of the Ar ion energy employed. The sensitivity factors calibrated for the single-crystalline STO proved to be also accurate for the amorphous as-deposited ALD STO thin films, as confirmed by Rutherford backscattering spectrometry analysis (see Table 4.1).

3.5 X-ray Diffraction

X-ray diffraction (XRD) is a characterization technique employed to determine the crystalline structure of a sample. This technique is based on the detection of constructive interference of X-rays elastically scattered from the examined specimen. With this aim, the examined sample is exposed to a coherent X-ray radiation beam which, depending on the microstructure of the sample, is diffracted in specific directions. By moving an X-ray detector it is possible to determine the directions of the diffracted beams and their intensities to form a diffraction spectrum. Figure 3.6 shows a schematic illustration of the condition that has to be met to achieve constructive interference from a set of lattice planes. In this figure, an X-ray beam hits the sample with an incident angle θ. As can be seen, the X-ray reflected from the lower lattice plane traverses a longer distance compared to the X-ray reflected from the top lattice plane. The difference between the distance covered by the two X-rays is highlighted in red in Figure 3.6. This amounts to $2dsin\theta$, where θ is the angle of incidence of the X-ray beam and d is the spacing between the two lattice planes. If this difference in distance is equal to a multiple of the
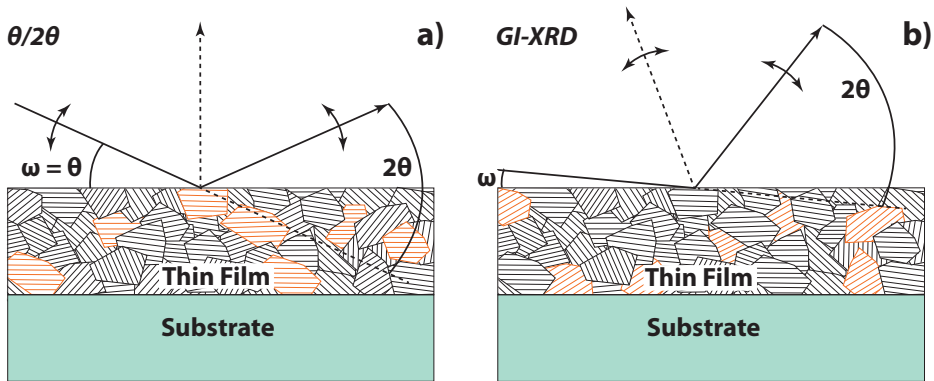
Figure 3.7: Schematic illustration of the $\theta/2\theta$ (a) and grazing incidence XRD (GI-XRD) (b) configurations. In the $\theta/2\theta$ configuration $\omega = \theta$, while in GI-XRD ω is fixed to small values ($< 2°$). The bisectors are represented by the dashed arrows. In both configurations the grains of a non-textured polycrystalline sample which can give raise to diffraction are highlighted in red.

wavelength of the X-ray radiation (1.54 Å when using a Cu K$_\alpha$ source), constructive interference between the two X-rays will occur. This condition for interference is referred to as *Bragg's law* and is described by the following equation:

$$2dsin(\theta) = n\lambda$$

For each crystal structure, the characteristic spacing d_{hkl} between planes for a generic set of lattice planes identified by the so-called Miller's indices h,k,l can be used in the above formula. In this way the condition for the detection of interference from such set of planes is met.

In a so-called $\theta/2\theta$ scan measurements both the incident X-ray beam and the detector make an angle θ with respect to the sample surface as shown in Figure 3.7.a. By scanning over a range of 2θ values during the measurement, various sets of lattice planes can produce constructive interference for different θ values. In this measurement configuration only the lattice planes oriented parallel to the sample surface of a randomly oriented polycrystalline sample will contribute to the diffraction spectra, as shown in Figure 3.7.a. Since the penetration depth of Cu K$_\alpha$ X-rays is usually in the range of 10-100 μm, for thin films with thicknesses in the nanometer range a strong contribution of the substrate on the diffraction spectra is usually an issue [6]. For this reason another measurement configuration should be employed to gain more information on the crystalline structure
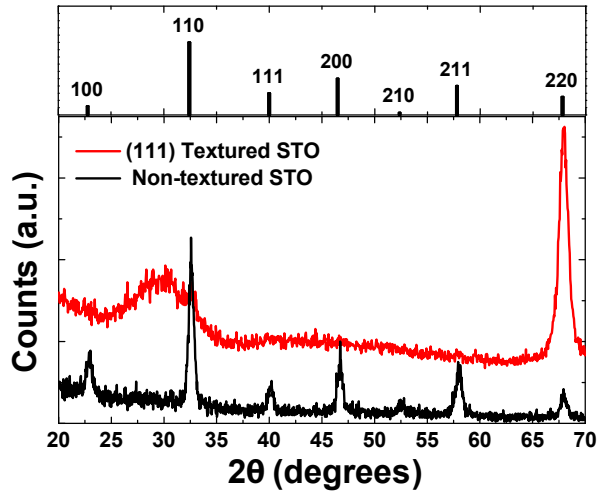
Figure 3.8: GI-XRD spectra of a (111) textured and non-textured STO thin films. The powder reference spectrum for perovskite STO is included as a reference.

of a thin film minimizing the substrate contribution. This configuration, called *grazing-incidence XRD*, will be described in the next section.

3.5.1   Grazing-Incidence XRD

In grazing-incidence XRD (GI-XRD) the X-ray beam hits the sample with a very low incident angle, ω (usually $< 2\,°$) which, however, must be larger than the so-called *critical angle*, characteristic of the material under analysis, to avoid total reflection. The angle of incidence is fixed and a diffraction spectrum is collected by moving the detector along the 2θ circle as shown in Figure 3.7.b. The maximum path length that an X-ray can travel in the thin film before reaching the substrate is $t/sin(\omega)$, where t is the thickness of the examined film. By decreasing ω to such low values, the length of the X-ray path in the film can be increased to values much larger than the film thickness. This strongly decreases the intensity of X-rays reaching the substrate and, therefore, its contribution to the signal. Furthermore, due to the assymetry of the GI-XRD measurement, the reflection component is eliminated, thus, the background is reduced. This results in an increased signal-to-noise ratio of the diffraction peaks corresponding to the thin film. Due to the thickness of the STO thin films studied in this work (12-30 nm) GI-XRD has been widely employed in the determination of their crystalline phase.

As shown in Figure 3.7.b, the bisector between the incident and reflected X-ray is

not perpendicular to the sample surface as in the case of a $\theta/2\theta$ scan. The lattice planes giving raise to diffraction are those perpendicular to such bisector and are highlighted in Figure 3.7.b. In the GI-XRD configuration the direction of the bisector is constantly changing due to the fixed incidence angle. Therefore, by scanning over the 2θ range during the measurement, lattice planes having different orientations with respect to the surface normal are brought into diffraction conditions. For a non-textured polycrystalline film where grains are randomly oriented, the diffraction pattern as measured by GI-XRD will in principle reproduce the ratio between the peaks as in the reference powder spectrum, since for any 2θ value corresponding to a diffraction peak, there will be corresponding lattice planes perpendicular to the bisector. However, for a textured film the orientation of the crystallites is not randomly distributed. In this case, the crystalline grains are present in one or more preferred orientations with respect to the sample surface. In case of a $\theta/2\theta$ scan as discussed above, the presence of such texture(s) can be easily recognizable. Since the XRD peaks in the $\theta/2\theta$ configuration originate from the planes perpendicular to the surface, if a set of lattice planes is preferentially parallel to sample surface, its peak intensity is strongly increased while the other peaks will be reduced. However, during the GI-XRD measurement of a textured film, for the 2θ value corresponding to the diffraction of a certain set of planes, such lattice planes are not necessarily perpendicular to the bisector corresponding to that 2θ value. Hence, the lattice planes will not be accessible and the corresponding diffraction peak will not be detected. The absence of intensity of this specific reflection acquired at a specific off-normal bisector angle cannot directly be related to a specific preferential orientation of lattice planes parallel to the substrate surface. Thus, GI-XRD measurements of textured thin films can be rather difficult to interpret and further XRD analysis is usually needed to determine the crystalline phase and preferred orientation of the thin film.

Figure 3.8 shows GI-XRD spectra of a randomly oriented and a (111) textured STO film. It can be clearly seen that the randomly oriented film replicates the peak ratio of the reference powder spectrum of perovskite STO. The GI-XRD of the textured film shows only the (220) peak. As will be also explained in Chapter 7, the angle between the <111> orientation (which is perpendicular to the sample surface) and the <220> orientation is 35.26°. Therefore, for $2\theta = 67.8°$ ((220) diffraction peak) and for the angle of incidence used in these measurements, $\omega = 0.324°$, the bisector presents an offset of only 1.684° with respect to the <220> direction. Due to the width of the orientation distribution function (ODF), (220) planes could still be accessible and result in the (220) peak seen in the GI-XRD spectra in Figure 3.8. For the other perovskite crystallographic orientations, the angle offset that they form with the bisector when 2θ satisfies Bragg's law for such
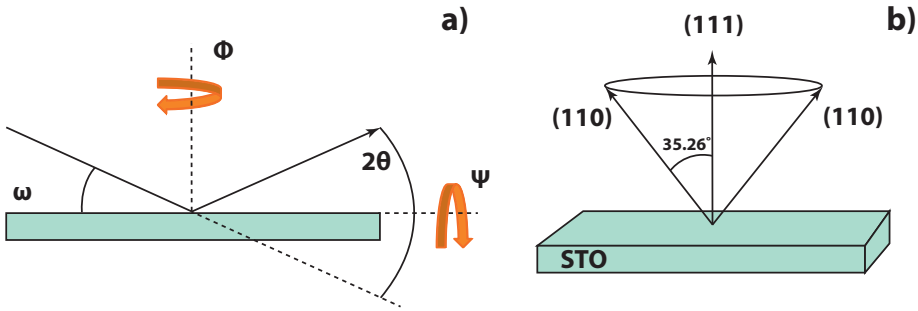
Figure 3.9: Schematic illustration of texture XRD analysis measurements where the angles ψ and ϕ are varied (a) and representation of a (111) *fiber textured* STO film.

orientations, makes it not possible to detect the relative diffraction peaks.

3.5.2   Ψ-Scan Measurement

In order to confirm the texture and determine the ODF of a thin film XRD measurement can be performed where the angles Ψ and Φ (Figure 3.9.a) are varied. During this measurement the angle of incidence (ω), and 2θ are fixed and set to satisfy Bragg's condition for a specific set of lattice planes. In this manner, the diffraction intensity corresponding to that set of lattice planes is detected while scanning Ψ and/or Φ. If texture is present in the examined thin film the lattice planes are aligned along specific directions. By scanning over Ψ and Φ during the XRD measurement it is possible to detect the presence of diffraction peaks along such directions and determine the orientation distribution for that specific set of planes, hence, the texture of a sample. By combining Ψ and Φ scans a so-called *pole figure* is obtained. The reader is addressed to reference [6] for a more detailed description on texture analysis. In the case of a thin film presenting *fiber texture*, where a certain set of lattice planes is oriented parallel to the substrate (i.e. textured in the *out-of-plane* direction and randomly oriented in the *in-plane* directions), Ψ scans may be sufficient to determine the film texture. In fact, in this case the diffraction intensity is independent of Φ.

For fiber textured STO thin films with the <111> direction perpendicular to the sample surface ((111) planes parallel to the sample surface), the <110> direction will be oriented with an offset of $35.26\,^\circ$ with respect to the surface normal (Figure 3.9.b). Since Pt and STO both present a cubic crystalline structure with similar lattice parameters, the (110) peak was chosen for the Ψ scan of STO/Pt structures since it is not an

allowed reflection for Pt. Therefore, by fixing $2\theta = 32.42°$ (and $\omega = 16.21°$) and tilting the sample by varying Ψ during the measurement, the (110) peak should be detected for $\Psi = \pm 35.26°$.

Figure 7.4 shows Ψ scans of fiber textured STO films where peaks at $\approx \pm 35°$ were detected. The assumption of fiber textured films is corroborated by the symmetry of the scan shown in Figure 7.4 where the peaks at $\pm 35°$ had comparable intensities. In the case of a textured film having both an out-of-plane texture, i.e. the <111> direction aligned along the surface normal, as well as an in-plane preferential orientation, the (110) peak should show a 3-fold symmetry. Therefore, the presence of diffraction peaks for the same positive and negative values of Ψ would not be possible.

3.6 Transmission Electron Microscopy

Transmission electron microscopy (TEM) is a microscopy technique which employs electrons with a high kinetic energy (up to 300 keV) to obtain a high-resolution image of a sample. In TEM, the highly energetic electron beam is transmitted through a sample, therefore, only ultra-thin samples (< 100-200 nm) can be examined by TEM. Since different TEM modes and imaging techniques can be employed, various types of information can be gained. In the following sections the TEM imaging techniques employed in this work will be briefly introduced and their application to the imaging of STO thin films will be described. Furthermore, electron diffraction (ED), a technique which makes use of the electron beam of the TEM to determine the crystal structure and orientation of one or more crystals in a sample, will also be introduced. For the analysis of STO thin films by TEM and ED the films were deposited on thin (≈ 15 nm) Si_3N_4 membranes which are transparent to the electron beam. Furthermore, cross-sectional TEM analysis was also performed on a thin (50-100 nm) lamella taken from a Pt/STO/Pt film stack prepared by ALD (see Chapter 6). The preparation of this thin lamella was performed using a Focused Ion Beam (FIB).

3.6.1 Bright-Field and Dark-Field TEM

The working principles of the imaging TEM mode, which is used in both bright-field (BF)-TEM and dark-field (DF)-TEM imaging, is illustrated in Figure 3.10.c. In this configuration the electron beam is collimated by a set of condenser lenses before reaching the sample. After passing through the sample the electron beam can be diffracted. Therefore, not only the transmitted electron beam (direct beam) is present but also a series of
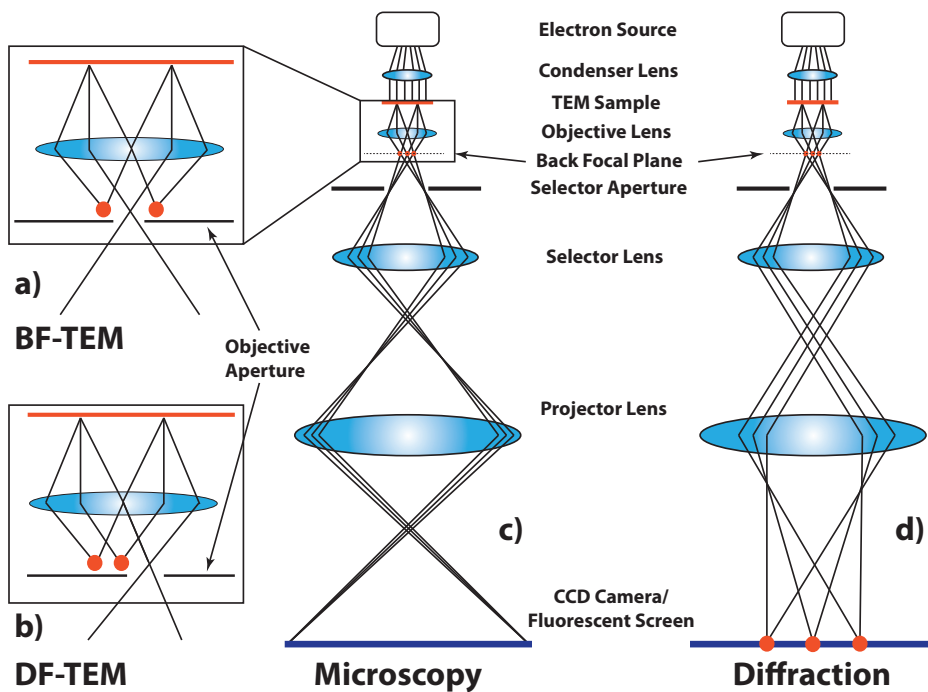
Figure 3.10: Schematic illustration of the positions of the objective aperture used to select the direct beam (a) or a diffracted beam (b) in order to obtain BF-TEM or DF-TEM images, respectively, and TEM configurations for the imaging (c) and diffraction mode (d).

diffracted beams. These beams are then condensed by the objective lenses. In the back focal plane, the primary and diffracted beams are spatially separated, forming the electron diffraction pattern. The objective aperture (3.10.a and b) can be inserted in the back focal plane to choose the beam which will form the image. Projector lenses are then used to highly magnify the image which is then projected on a fluorescent screen and recorded by a CCD camera. The difference between BF and DF-TEM consists of the different beam(s) selected by the objective aperture in the back focal plane. In particular, in BF-TEM (3.10.a) the direct beam is selected while in DF-TEM (3.10.b) one or more diffracted beams are chosen by moving the objective aperture in the back focal plane of the objective lenses. However, in both cases the resulting image is a projection of a selected region of the sample.

Since in BF-TEM the image is formed by the transmitted primary beam, the contrast is determined by the amount of electrons which passes through the sample. Therefore, regions with a higher average atomic number (Z) or thicker regions of the sample will result in a darker contrast compared to thinner regions or with atoms with lower Z. Furthermore, the contrast depends on the crystalline structure of the sample. In BF-TEM a crystal which is oriented in a strongly diffracting orientation with respect to the incoming electron beam will result in the image as a darker region. Upon tilting the sample away from this strongly diffracting orientation, the crystal will appear brighter in the resulting BF-TEM image. In the case of a randomly oriented polycrystalline thin film the contrast of each single grain in BF-TEM will depend on its own crystallographic orientation with respect to the electron beam. Therefore, differently oriented grains will display different grey scales in the images despite the fact that the same material and thickness is uniformly present all over the examined region.

In DF-TEM the objective aperture is positioned in such way that a diffracted beam is selected to form the image. Therefore, only regions of the sample which contribute to that specific diffracted beam will give raise to brightness in the image. Usually, only regions (i.e. crystalline grains) of the sample having the same crystallographic orientation will show as brighter regions in DF-TEM images. Therefore, this technique can be employed to resolve single-crystalline grains or to identify grains with the same crystallographic orientation.

The differences in contrast between BF-TEM and DF-TEM just described can be understood from the images of the Pt/STO/Pt lamella studied in Chapter 6. Figure 6.3.a and b show BF and DF-TEM images of the lamella, respectively. In the BF-TEM image (Figure 6.3.a) the contrast is dominated by the differences in composition of the three layers (Pt or STO) resulting therefore in electron density contrast. However, DF-TEM
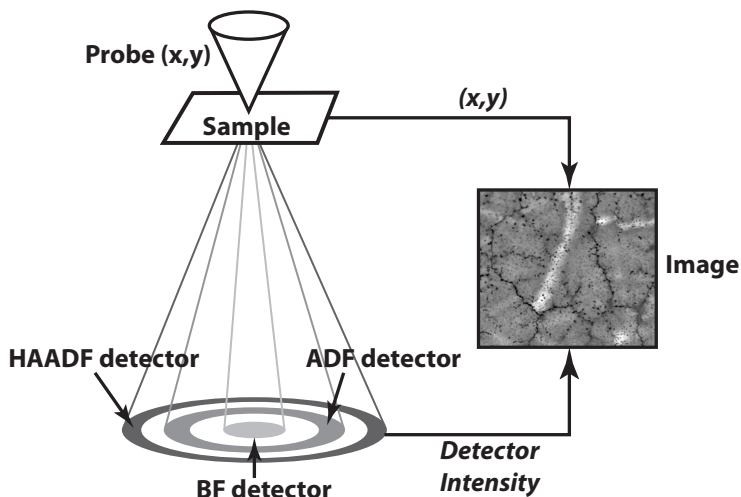
Figure 3.11: Schematic illustration of the working principle of scanning TEM imaging (STEM). The focused electron beam (probe) is rastered over the selected region of the sample and electrons are collected by BF, annular DF (ADF) and high-angle annular DF (HAADF) detectors to construct the image.

images of the same lamella region revealed other features of the sample. The light contrast regions in the Pt layers in Figure 6.3.b correspond to single Pt grains. Therefore, differences in average grain size of the two Pt films could be identified. Furthermore, the STO grain indicated by the arrow in Figure 6.3.a could be identified in DF-TEM by tilting of the lamella and therefore bringing the grain in a strongly diffracting orientation with respect to the electron beam.

3.6.2   High-Angle Annular Dark Field Scanning TEM

High-Angle Annular Dark Field Scanning TEM (HAADF-STEM) is a technique mainly used to obtain images of a sample providing Z (atomic number) contrast. While for BF-TEM and DF-TEM the images are formed as a projection of the sample, in STEM techniques the sample is scanned by a focused electron beam. The working principle of STEM is shown in Figure 3.11. The electron beam is focused on a narrow spot of the sample and after passing through it, electrons are collected by the detector(s). By scanning the focused electron beam on the sample and assigning the detected number of electrons to each (x,y) scanning position a STEM image is formed.

Both BF and DF detectors can be used in STEM. In particular, the circular BF de-
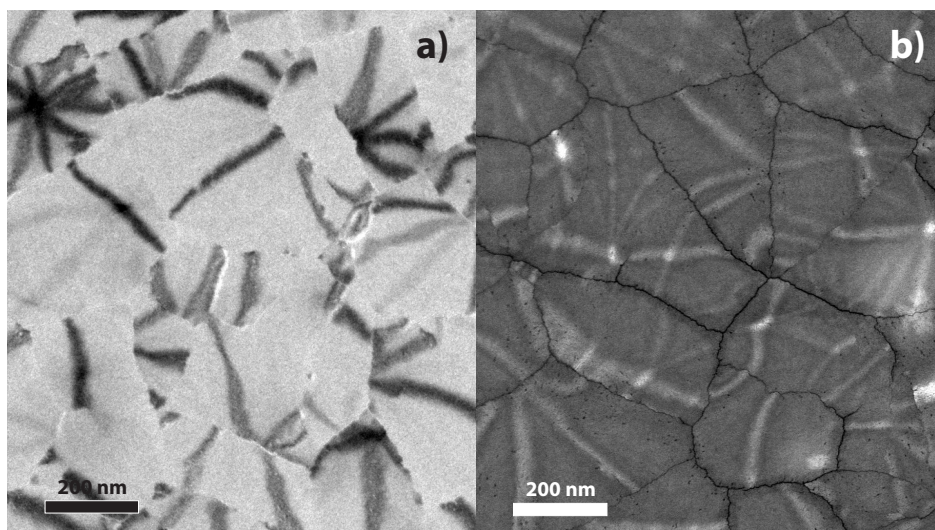
Figure 3.12: BF-TEM (a) and HAADF-STEM (b) images of a crystallized STO thin film.

tector is positioned in order to collect the primary beam while annular DF (ADF) detectors are positioned in order to collect electrons diffracted and scattered by the sample (Figure 3.11). The advantage of using ADF-STEM compared to DF-TEM is that many more electrons are collected by an annular detector compared to the number of electrons passing through the objective aperture. Furthermore, by removing the BF-STEM detector during ADF-STEM, the direct beam can be collected by an electron energy loss spectroscopy (EELS) detector to simultaneously acquire images as well as spectral information.

For HAADF imaging an annular DF detector is placed at a high angle with respect to the direct beam in order to collect electrons scattered (and diffracted) by the sample. Z contrast generally dominates HAADF images since the angular distribution of the scattered electrons strongly depends on the atomic number of the atom from which they are incoherently scattered. Moreover, the amount of scattered electrons from a location on the sample depends also on the local density (e.g. film thickness). In the optical plane where the HAADF detector is placed the diffraction pattern is formed. By changing the magnification of the diffraction pattern in this plane, hence, the camera length (defined as the effective distance between the sample and the optical plane where the detector is placed), the portion of the diffraction pattern which falls on the HAADF detector can be changed. In particular, for short camera lengths (i.e. low magnification) the image is

dominated by density and Z contrast while for longer camera lengths (i.e. higher magnification) also diffraction contrast can be visualized in the image. In Chapter 5 and 6 an intermediate camera length was employed, hence, both density and diffraction contrast were imaged.

Figure 3.12.a and b show a BF-TEM and a HAADF-STEM image of the same crystallized STO thin film, respectively. While for the BF-TEM image the contrast is dominated by diffraction, visualizing the strongly diffracting star-shapes characteristic of *transrotational* crystals (see addendum of Chapter 5), the HAADF image gave a clearer morphological contrast. In particular, with HAADF-STEM imaging it was possible to clearly identify the cracks at the grain boundaries but also nano-voids (few nanometers in diameter) within single grains (see also Figure 5.4).

3.6.3   Electron Diffraction

Apart from the imaging techniques described above, a TEM microscope also offers the possibility to perform diffraction analysis on the sample in order to gain information on its microstructure and crystallinity. Electron diffraction (ED) analysis can be performed in the TEM configuration shown in Figure 3.10.d. Similarly to BF and DF-TEM, the collimated electron beam passes through the sample to form a diffraction pattern in the back focal plane. However, during ED the magnetic lenses positioned below the sample are used to project the diffraction pattern on the screen (and on the CCD camera) instead of creating a projected image of the sample. Similarly to the case of XRD, where X-ray diffraction patterns are collected, in ED the diffraction pattern caused by Bragg scattered electrons, can be used to determine the microstructure of the sample. In the case of a polycrystalline sample the diffraction pattern is formed by diffraction rings which correspond to different sets of lattice planes, while ED of a single crystal will result in localized diffraction spots. The distance of the diffraction ring (or spot) to the centre of the pattern is characteristic for the probed interplanar distance, in analogy to the 2θ angle in XRD spectra. Furthermore, information on the texture of thin films can be gained.

Figure 6.5.a and b show ED images of an ALD Pt thin film before and after a RTA step. While for the as-deposited film (Figure 6.5.a) all Pt diffraction rings characteristic for the Pt crystal structure were detected, indicating a mostly randomly oriented nature of the grains, the annealed film showed enhanced intensity for some diffraction rings while some other diffraction rings disappeared. This indicates that recrystallization occurred after the annealing step, leading to a textured film. Furthermore, the fact the diffraction rings of the annealed sample are discontinuous suggests that a larger average grain size is

achieved after RTA, as the sampled area corresponding to the ED pattern is only several tens of μm^2, allowing only a limited number of crystals to contribute to this pattern.

Electron diffraction and XRD apply the same basic principle for detecting crystallographic information. In the present study, these techniques are both used because of their complementary nature: XRD has a much higher precision in determining lattice parameters and provides an average over a large sampled volume, while the strength of ED is the possibility to locally probe both crystal structure and orientation (distribution) and to directly correlate this information to high magnification image information.

3.7   References

1. H. Profijt, "Plasma-Surface Interaction in Plasma-Assisted Atomic Layer Deposition", PhD Thesis, Eindhoven University of Technology, (2012).

2. F. Roozeboom, ed., "Advances in Rapid Thermal and Integrated Processing", Kluwer Academic Publishers, Dordrecht, The Netherlands, (1996).

3. H. Fujiwara, "Spectroscopic Ellipsometry Principles and Applications", Wiley, (2007).

4. B. Johs and J.S. Hale, *Phys. Status Solidi A*, 205, 715 (2008).

5. J.W. Weber, T.A.R. Hansen, M.C.M. van de Sanden and R. Engeln, *J. Appl. Phys.*, 106, 123503 (2009).

6. M. Birkholz, "Thin Film Analysis by X-Ray Scattering", Wiley, (2006).

Chapter 4

Plasma-Assisted Atomic Layer Deposition of SrTiO$_3$: Stoichiometry and Crystallinity Studied by Spectroscopic Ellipsometry*

Abstract   Strontium titanate (SrTiO$_3$, STO) films were deposited by plasma-assisted ALD using cyclopentadienyl-based Sr- and Ti-precursors with O$_2$ plasma as the oxidizing agent. Spectroscopic ellipsometry (SE) was employed to determine the thickness and the optical properties of the layers. As determined from Rutherford backscattering spectrometry (RBS), [Sr]/([Sr]+[Ti]) ratios ranging from 0.42 to 0.68 were achieved for 30-40 nm thick films by tuning the [SrO]/[TiO$_2$] ALD cycle ratio. Films deposited at 250 °C were amorphous and required post-deposition annealing to crystallize into the ultrahigh-k perovskite structure. The crystallinity of the films after rapid thermal annealing strongly depended on the film composition as observed by X-ray diffraction measurements. Using RBS data for a set of as-deposited samples, an optical constant library was built to determine the film stoichiometry from SE directly for the amorphous as-deposited films. After rapid thermal annealing the crystalline phase could be determined from the position of critical points of the measured dielectric function and the estimation of the stoichiometry was also possible for crystallized layers. These results open up a new way to use SE as a *real-time* characterization method to monitor and tune the STO film composition and crystallinity.

4.1   Introduction

Strontium titanate (SrTiO$_3$, STO) is a perovskite material which has attracted considerable attention in recent years due to its various properties. Stoichiometric SrTiO$_3$ is a dielectric material, however oxygen vacancies and doping can be used to obtain semiconductive and conductive STO [1-3]. Furthermore, STO shows other interesting properties such as paraelecriticity and ferroelectricity, also when deposited as a thin film [4,5]. Resistive switching behavior has been reported for metal-insulator-metal (MIM) structures where STO was employed as the dielectric material [6]. However, among all STO properties, its ultrahigh permittivity value (theoretically k $\approx$ 300) has attracted most interest. For next generation dynamic random access memories (DRAM), high-density MIM trench capacitors having an equivalent oxide thickness (EOT) < 0.4 nm and a low leakage current are needed [7]. To meet such requirements ultrahigh-k dielectric layers (k >100) need to be deposited conformally over high aspect-ratio structures. Furthermore, the processing temperature has to be < 600 °C due to process integration constraints [8]. For these reasons STO appears to be the favorite candidate as dielectric material due to its high permittivity and its relatively low crystallization temperature ($\approx$ 550 °C). To deposit STO thin films over high aspect ratio structures, atomic layer deposition (ALD) is the method of choice since its characteristic *layer-by-layer* growth results into high-quality layers and excellent step coverage. A common approach to deposit ternary oxides by ALD consists in alternating ALD cycles of the binary oxides, with a certain ratio, to obtain the desired material [9-14]. In this way, not only the thickness, but also the film composition can be precisely controlled by ALD.

To achieve the required ultrahigh-k values, STO films must be crystallized into the perovskite structure by post-deposition thermal annealing or they have to be deposited at relatively high temperatures on crystalline seed layers [15-19]. The stoichiometry of the STO films strongly affects the crystallization temperature, crystalline microstructure after annealing and the dielectric constant [20]. Recent developments on ALD of STO showed that Sr-rich films have a smaller grain size after annealing resulting in lower leakage current values [19,21]. For these reasons monitoring the stoichiometry and crystallinity of STO films is necessary to tune the processing conditions such that the requirements for the application envisioned are met.

In this work, we report on the plasma-assisted ALD of STO films from cyclopentadienyl-based precursors for both, TiO$_2$ and SrO. The oxidizing agent was an O$_2$ plasma generated in a remote inductively coupled plasma (ICP) source. In our previous work, STO films were deposited with the same precursors in a home-built reactor [22]. In

this work the process was scaled-up in a commercial Oxford Instruments FlexAL™ tool which can accommodate wafers up to 200 mm in diameter. It was demonstrated that the film stoichiometry is related to the [SrO]/[TiO$_2$] ALD cycle ratio. Using X-ray diffraction (XRD) and Rutherford backscattering spectrometry (RBS) data as a cross-reference it was shown that it is possible to probe directly the stoichiometry and crystallinity of thin STO films by spectroscopic ellipsometry (SE). In addition, we present a pragmatic approach to determine the stoichiometry of amorphous STO films by means of an optical constant library that was built with the CompleteEASE® software (J.A. Woollam). Since SE measurements can also be taken in-situ this could provide a means for monitoring the film properties during processing.

4.2   Experimental Details

The STO thin films were deposited in an Oxford Instruments' FlexAL™ reactor on 100 and 200 mm Si (100) wafers with native oxide. This reactor was upgraded during this experimental work, leading to slightly different results before and after the upgrade. Hereafter, we will indicate the system before the upgrade as FlexAL-A and after the upgrade as FlexAL-B. The precursors employed were Ti-Star, (pentamethylcyclopentadienyl)-trimethoxy-titanium, CpMe$_5$Ti(OMe)$_3$ and Hyper-Sr, bis(tri-isopropylcyclopentadienyl)-strontium with the 1,2-dimethoxyethane adduct, Sr(iPr$_3$Cp)$_2$DME, both from Air Liquide. Since the Ti-Star precursor is not reactive towards H$_2$O in an ALD process, an O$_2$ (>99.999 % purity) plasma generated by an inductively coupled plasma (ICP) source was used as the oxidizing agent. The precursors were stored in stainless steel canisters heated to 70 °C and 120 °C for Ti-Star and Hyper-Sr, respectively. For both precursors, the delivery to the deposition chamber was achieved with a 100 sccm Ar (>99.999 % purity) bubbling flow. The delivery lines were kept at a temperature 30 °C higher than the precursor canisters to avoid condensation and clogging. As confirmed by calibration measurements, the actual sample temperature is lower than the set value (by 20-25 % in °C). We will hereafter report this set value and refer to it as "set temperature".

Rapid thermal annealing (RTA) for 10 minutes in flowing N$_2$ was employed to crystallize the STO layers into the perovskite structure using an AST SHS100 system. The crystalline phase of the films was determined by grazing incidence X-ray diffraction (GI-XRD) at an incidence angle of 0.5 ° with respect to the substrate plane. X-ray diffractometry was performed using a Panalytical X'Pert PRO MRD employing Cu K$_\alpha$ (1.54 Å) radiation.

The thickness and the dielectric function of the films were measured in the spectral

range 1.25-6.5 eV with an M2000D spectroscopic ellipsometer from J.A. Woollam. The measurements were performed ex-situ on a goniometric stage for measurements under variable angles. Acquisition and fitting of the ellipsometry data were performed with the CompleteEASE® 4.64 software (J.A. Woollam). For the fitting of the SE data a model comprising the Si substrate, native oxide and deposited film were used. The thickness of the native oxide was determined with a Cauchy model before the STO deposition. With the film deposited, the data were first fitted using a Cauchy model in the transparent region of the STO layers (< 3 eV), from which the thickness of the film was extracted. The fit was then extended to the entire measured spectral range using a B-spline parameterization. This means representing a dielectric function with a spline curve defined as a linear combination of Basis-splines (B-splines). B-splines are a recursion set of polynomial splines that can ensure Kramers-Kronig consistency and reduce the number of fitting parameters [23,24]. This method was chosen due to its versatility to accurately parameterize the dielectric functions of STO films having different stoichiometries. Furthermore, the library that was built in CompleteEASE® makes also use of the B-spline parameterization.

Rutherford backscattering spectroscopy (RBS) was used to determine the elemental composition and atomic areal densities of the films using 2 MeV $4He^+$ ions (AccTec BV, The Netherlands). X-ray photoelectron spectroscopy measurements were also performed on a Thermo Scientific K-Alpha KA1066 spectrometer using monochromatic Al K_α X-ray radiation ($h\nu$ = 1486.6 eV). Photoelectrons were collected at a take-off angle of 60 °. A 400 μm diameter X-ray spot was used in the analysis and the samples were neutralized using an electron flood gun to correct for differential or non-uniform charging. For cross-referencing the atomic composition from XPS measurements, a stoichiometric $SrTiO_3$ substrate (20 mm x 20 mm, Crystal GmbH) was measured and the sensitivity factors for the Sr3d, Ti2p and O1s peaks were tuned accordingly to obtain stoichiometric $SrTiO_3$ from the detected relative amounts of the single elements. This procedure was executed after surface contamination removal by Ar^+ ion (500 eV) sputtering. Ar^+ ion sputtering was also employed for depth profiling of the stoichiometric STO sample to exclude the possibility of preferential sputtering. The analysis confirmed that the sensitivity factors were accurate throughout the depth profile.

4.3 Results and Discussion

4.3.1 Plasma-Assisted ALD of TiO$_2$ and SrO

The deposition processes of the individual binary oxides, TiO$_2$ and SrO, were first developed to determine the *growth-per-cycle* (GPC), the appropriate purge times and the saturation behavior for both the precursor doses and the O$_2$ plasma exposure in the FlexAL-A reactor. For the TiO$_2$ process a dosing time of 2 s for the Ti-Star precursor and an exposure time of 8 s for the O$_2$ plasma were required to achieve saturation. For the SrO process the Hyper-Sr precursor dosing time and the exposure time of O$_2$ plasma were 15 s and 8 s, respectively. Purge times required to avoid any CVD-like growth, were 2 s and 10 s after the Ti- and Sr-precursor step, respectively. After the O$_2$ plasma, the purge step times were 2 s and 15 s for the TiO$_2$ or SrO process, respectively. With these settings saturation was reached for both processes at a set temperature of 250 °C. The GPC, as determined by SE, was 0.036 and 0.11 nm/cycle for TiO$_2$ and SrO, respectively. These values deviate from those reported previously by Langereis et al. for the home-built ALD-I reactor [22], in which the GPC for TiO$_2$ and SrO were 0.054 and 0.051 nm/cycle, respectively. Differences in GPC between these two setups have previously been reported for plasma-assisted ALD process of Ta$_2$O$_5$ [25], and were ascribed to the differences in the reactor designs. Differences in precursor delivery and plasma source design can result in different radical and ion fluxes in the two reactors [25]. The value recorded in this work for the GPC of SrO is, however, in good agreement with a GPC of ≈ 0.1 nm/cycle reported for Hyper-Sr and O$_3$, and 0.11 nm/cycle for Hyper-Sr and H$_2$O [26]. In one of the first reports on ALD of STO, the GPC for the SrO process using Sr(C$_5$^{i}PrH$_2$)$_2$ (Hyper-Sr without the DME adduct) and H$_2$O was also 0.11 nm/cycle [9]. The GPC of TiO$_2$ is comparable to those reported in the literature, with values ranging from 0.022 nm/cycle [27] to ≈ 0.03 nm/cycle [26] for the combination of Ti-Star and O$_3$. These values show the variation in GPC reported in the literature for ALD processes employing the same precursors but developed in different equipment, showing the sensitivity of ALD processes to the varying reactor design and experimental conditions.

4.3.2 Plasma-Assisted ALD of STO

ALD of STO was achieved by combining ALD cycles of the two binary oxides to obtain one STO supercycle. In this way an STO supercycle is composed of x SrO cycles and y TiO$_2$ cycles and the [SrO]/[TiO$_2$] ALD cycle ratio is defined as x/y. The STO films were deposited with various ALD [SrO]/[TiO$_2$] cycle ratios in the FlexAL-A reactor at a
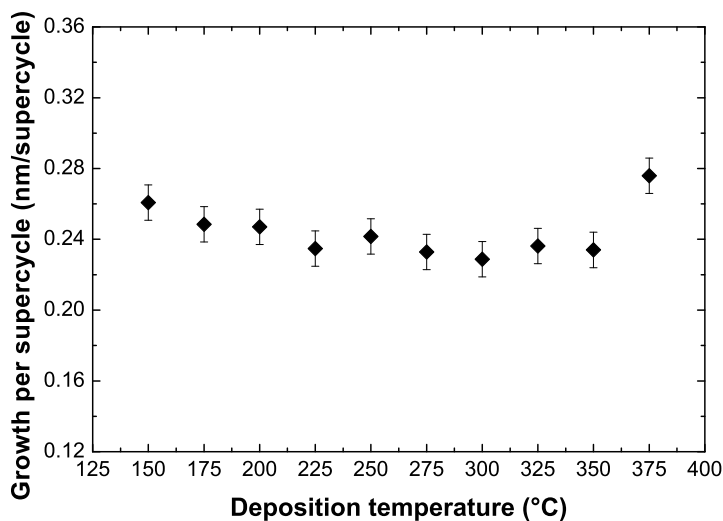
Figure 4.1: Temperature dependence of the growth per supercycle of STO films deposited with a [SrO]/[TiO$_2$] ALD cycle ratio of 1:3 in the FlexAL-B reactor.

set temperature of 250 °C. Two different approaches to combine the binary oxides were employed. The first consisted in executing the SrO cycles followed by the TiO$_2$ cycles (indicated hereafter as *"consecutive"* or simply by *"2:5"*), e.g. a supercycle with cycle ratio [SrO]/[TiO$_2$] = 2:5 corresponds to 2 cycles SrO followed by 5 TiO$_2$ cycles. The other approach consisted of intermixing the TiO$_2$ and SrO cycles (indicated hereafter with the notation *"2:5 mixed"*), e.g. a supercycle with cycle ratio [SrO]/[TiO2] = 2:5 corresponding to the sequence 1 SrO, 2 TiO$_2$, 1 SrO and 3 TiO$_2$ cycles.

The ALD temperature window of the STO process was also investigated. For this purpose films were deposited in the FlexAL-B reactor with a [SrO]/[TiO$_2$] cycle ratio 1:3. The growth per supercycle, obtained by dividing the total thickness of the film by the number of STO supercycles, (Figure 4.1) was nearly constant from 150 °C to 350 °C. A slight decrease in growth with increased temperature is most likely due to desorption of surface groups and/or to densification of the film at higher temperatures. At a set temperature of 375 °C a higher growth per supercycle was observed as well as an enhanced non-uniformity and higher Sr-concentration in the layers, suggesting the decomposition of the Hyper-Sr precursor. The difference between the decomposition temperature of the Hyper-Sr precursor (300 °C) reported by Katamreddy et al. [26] and our data is most likely due to the difference between the set and the actual wafer temperature.

Table 4.1: Influence of the [SrO]/[TiO$_2$] ALD cycle ratio on the elemental composition of STO films determined by RBS. The relative errors in the atomic density are 3% for Sr, Ti, and O. Also the [Sr]/([Sr]+[Ti]) content ratios obtained from XPS measurements are listed. The relative errors in the [Sr]/([Sr]+[Ti]) ratios from RBS and XPS are 6% and 5% respectively. The thickness of the films was determined by ex-situ SE. The error in thickness is $\pm$ 0.5 nm.

[SrO]/[TiO$_2$] ALD cycle ratio	Thickness (nm)	Sr atomic density (10^{22} at/cm^3)	Ti atomic density (10^{22} at/cm^3)	O atomic density (10^{22} at/cm^3)	[Sr]/([Sr]+[Ti]) content from RBS	[Sr]/([Sr]+[Ti]) content from XPS
2:10	31.4	1.06	1.46	4.36	0.42	0.43
2:9	32.6	1.16	1.24	4.39	0.48	0.49
2:8	29.4	1.21	1.16	4.41	0.51	0.52
1:4	30.5	1.31	1.06	4.10	0.55	0.56
1:3	35.1	1.33	0.78	4.27	0.63	0.63
2:4	40.5	1.42	0.67	4.35	0.68	0.68
2:5 mixed *	30.1	1.18	1.12	4.22	0.51	0.51

4.3.3 Film Composition and Cation Incorporation

RBS measurements were performed to determine the composition of the STO films and to establish a relation between the stoichiometry of the film and the [SrO]/[TiO$_2$] cycle ratio. XPS measurements were performed on the same set of samples after surface contamination removal by Ar$^+$ ions sputtering. XPS composition analysis results were in excellent agreement with the RBS results (Table 4.1). These measurements confirmed that by changing the [SrO]/[TiO$_2$] cycle ratio different compositions could indeed be deposited. The [Sr]/([Sr]+[Ti]) ratio for the examined films ranged from 0.42 to 0.68. Near-stoichiometric values of 0.51 for [SrO]/[TiO$_2$] cycle ratios 2:8 and 2:5 "mixed", were obtained for the FlexAL-A and the FlexAL-B reactors, respectively. The difference in the ALD cycle ratio yielding stoichiometric STO can be attributed to a slightly decreased GPC of the SrO process after the upgrade of the reactor. In general, the SrO process seemed to be very sensitive to the reactor conditions.

The relation between the film growth and the cation incorporation was investigated. Figure 4.2 shows the [Sr]/([Sr]+[Ti]) content ratio calculated from the RBS data reported in Table 4.1. The horizontal axis was weighted taking into account the two different GPC values for the single processes. In this way the expected Sr-content is represented by a straight line connecting the two extremes corresponding to the two binary processes. The

---

*Film deposited in the FlexAL-B reactor. In the "mixed" approach TiO$_2$ and SrO ALD cycles were intermixed (i.e. the [SrO]/[TiO$_2$] ALD cycle ratio = 2:5 mixed corresponds to the sequence 1 SrO, 2 TiO$_2$, 1 SrO and 3 TiO$_2$ cycles).
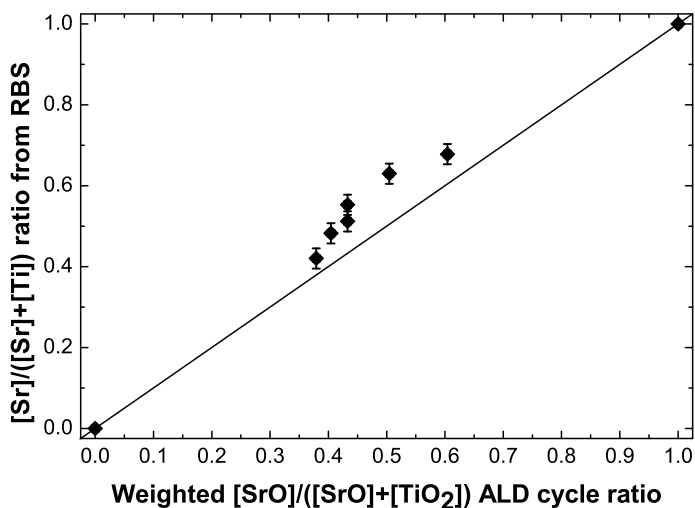
Figure 4.2: [Sr]/([Sr]+[Ti]) content ratio as extracted from the RBS measurements. The [SrO]/([SrO]+[TiO$_2$]) ALD cycle ratio (horizontal axis) was weighted by the GPC values of the individual SrO and TiO$_2$ processes. The straight line represents the expected Sr-content, based on the GPC of the binary oxides and the ALD cycle ratio.

Sr-content resulting from RBS analysis was higher than expected, thus suggesting an enhanced incorporation of Sr cations into the film. Furthermore, when films were deposited with the same [SrO]/[TiO$_2$] cycle ratio but with different cycle sequences, the Sr-content was higher when single SrO cycles were intercalated between TiO$_2$ cycles, i.e. in the mixed approach. This is evident for cycle ratios 1:4 and 2:8, where the [Sr]/([Sr]+[Ti]) content ratio was 0.55 and 0.51, respectively. This implies that SrO growth is slightly enhanced by the underlying TiO$_2$ surface. Earlier, we already reported that the deposition of SrO could be enhanced after TiO$_2$ ALD cycles, resulting also in a higher Sr-content than simply expected from the cycle ratio [22]. A strong dependency of the metal cation on the ligand removal and on the hydroxylation of the surface during the precursor and oxidizing steps was found for different ternary oxide compounds deposited by ALD from β-diketonate precursors [28]. The concentration of -OH groups on the surface is therefore dependent on the previous reactant step and thus influences the number of precursor molecules that react with the surface in the following dosing step.

Taking into account that not only the [SrO]/[TiO$_2$] ALD cycle ratio but also the sequence in which the precursors are dosed influences the cation incorporation, it is possible to precisely tune the film composition both by adjusting the cycle ratio as well as
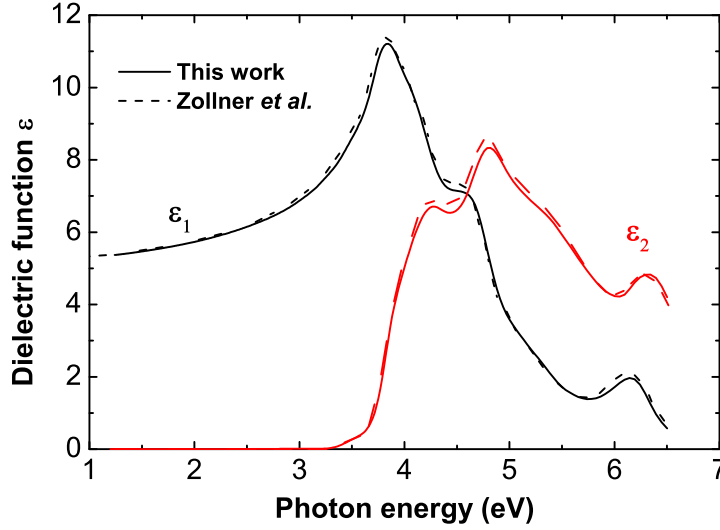
Figure 4.3: Dielectric function of bulk stoichiometric SrTiO$_3$ (100) measured by spectroscopic ellipsometry in this work (solid line) and from Zollner et al. (dashed line) [29].

by choosing the cycle sequence in an STO supercycle.

4.3.4   Optical Properties of STO

The optical properties of crystalline bulk STO have been investigated by various techniques such as valence electron energy-loss spectroscopy, vacuum ultraviolet spectroscopy, reflectivity and spectroscopic ellipsometry measurements [29,30]. Studies have been also reported on the optical properties of thin crystalline STO films [29]. Zollner et al. extracted the dielectric function of bulk STO from spectroscopic ellipsometry measurements in the spectral range 0.74-8.7 eV [29]. In this work we performed SE measurements on an STO (100) bulk sample. Figure 4.3 shows the dielectric function of the STO from our measurement and it is compared to the results from Zollner et al. showing an excellent agreement. In their work, the so-called critical points related to interband optical transitions were identified from the dielectric function and assigned to the electronic band structure of crystalline STO. For this purpose the electronic structure was calculated within the local-density approximation (LDA). Other works can be found in the literature on the calculation of the electronic structure and density of states (DOS) of STO using different approximations [29-31]. Independently of the approximation used for the *ab initio* calculation, all authors reported that the top valence bands are related

to O2p orbitals and that the lowest conduction bands consist of Ti3d orbitals. Sr-related bands were found at higher energies. Calculations also predicted that crystalline STO has an indirect and direct band gap. The calculated band gap values can vary depending on the approximation used and can be corrected to reproduce the experimental band gap [29]. These calculation results are in agreement with optical measurements where the indirect and direct band gap values were reported to be 3.2 eV and 3.4 eV respectively [29,33]. The critical points in the dielectric function at 3.8, 4.3, 4.8 and 6.2 eV reported by Zollner et al. were then assigned to transitions from the O2p valence bands to Ti3d conduction bands. Features in the dielectric function in the spectral range 7-9 eV were assigned to Sr5d orbitals and sp-antibonding orbitals [29]. As a result of its critical point structure, STO, as evident in Figure 4.3, has its maximum in the real part of the dielectric function, ϵ_1, at 3.9 eV. This feature is a fingerprint of the crystallinity of STO and, as will be shown below, can be used to discriminate between amorphous and crystalline thin films. Regarding the optical properties of amorphous STO, calculations of the band structure and its relation to the dielectric function, cannot be found in literature to our knowledge. In the next sections we will show how the dielectric function of both amorphous and crystalline layers is affected by the film stoichiometry. Also the influence of the film thickness on the dielectric function will be discussed.

4.3.5 Spectroscopic Ellipsometry Measurements of Amorphous STO Films

The dielectric functions, ϵ_1 (real part) and ϵ_2 (imaginary part), of the TiO_2 and SrO films, as well as those of STO films deposited in the FlexAL-A reactor with different $[SrO]/[TiO_2]$ cycle ratios were measured by spectroscopic ellipsometry. Figure 4.4 shows the dielectric functions of the as-deposited STO films for which RBS was performed. The dielectric functions of TiO_2 and SrO films are given for comparison. The optical band gaps of the two binary oxides, $\sim$ 3.3 eV for TiO_2 and > 5 eV for SrO, were in good agreement with the values reported in the literature [34,35]. Figure 4.4 shows that the dielectric functions of the as-deposited STO films are all distributed in a logical compositional order, and lie between the dielectric functions of TiO_2 and SrO indicating that mixtures of the two binary oxides were deposited in the amorphous phase. The values for the refractive index n (at 1.96 eV) of all STO films deposited in the FlexAL-A reactor with different $[SrO]/[TiO_2]$ cycle ratios are shown in Figure 4.5.a and were obtained from the dielectric function values through the relations:

$$\epsilon_1 = n^2 - k^2$$

$$\epsilon_2 = 2nk$$

where k is the extinction coefficient. Values are distributed between those of the two binary oxides (also shown) and n increases when the relative number of TiO_2 cycles increases. Values of n for the near-to-stoichiometric STO films deposited in this work were 1.88 and 1.89 for the FlexAL-A and FlexAL-B reactors, respectively ([Sr]/([Sr]+[Ti]) ratio of 0.51). These values are in agreement with our previous work, where the film with [Sr]/([Sr]+[Ti]) ratio of 0.52 had $n = 1.91$ [22], and with literature results, where as-deposited stoichiometric STO films ([Sr]/([Sr]+[Ti]) = 0.5) with $n = 1.86$ were obtained from $Sr(tBu_3Cp)_2$ and $Ti(OMe)_4$ [36].

The indirect band gap values, E_g, for the STO films were determined by plotting $(\alpha h\nu n)^{1/2}$ versus the photon energy, where $\alpha = 4\pi k/\lambda$ is the absorption coefficient, n and k are the real and imaginary part of the complex refractive index, and $h\nu$ is the incident photon energy. The linear part of this function above the transparent region is fitted with a straight line. The band gap value corresponds to the intercept value of this line with the horizontal axis [37,38]. This procedure for the determination of E_g is illustrated in the inset of Figure 4.5.b for a film deposited with a [SrO]/[TiO_2] ALD cycle ratio of 2:8. The band gap values are plotted in Figure 4.5.b and a decrease in E_g is evident with increased relative number of TiO_2 cycles. The refractive index and band gap values are plotted in Figure 4.6.a and 4.6.b, respectively, as a function of the [Sr]/([Sr]+[Ti]) ratio for samples which were analyzed by RBS. The figure clearly shows that the film composition can also be estimated by probing the refractive index and/or the band gap of the deposited film. A distinction can be made between samples deposited with the mixed and consecutive approach in Figure 4.5. For the mixed approach SrO cycles were always intercalated in between TiO_2 cycles while in the consecutive approach the SrO cycles were deposited before the TiO_2 cycles. The assumption for enhanced strontium incorporation on a TiO_2-terminated surface was corroborated by these results, where STO films deposited with the mixed approach showed a lower refractive index and a higher band gap. This confirms our observation that SrO deposition is slightly enhanced in the mixed growth mode.

The results confirm that the dielectric function of STO is strongly related to the film stoichiometry. Optically determined parameters, such as refractive index and band gap, can be used to determine the [Sr]/([Sr]+[Ti]) ratio of amorphous STO films. For this purpose, RBS results were used to determine the relation between the optical properties and the elemental composition of a set of samples with different stoichiometries. Once this was done the [Sr]/([Sr]+[Ti]) ratio can be directly derived from the SE data.

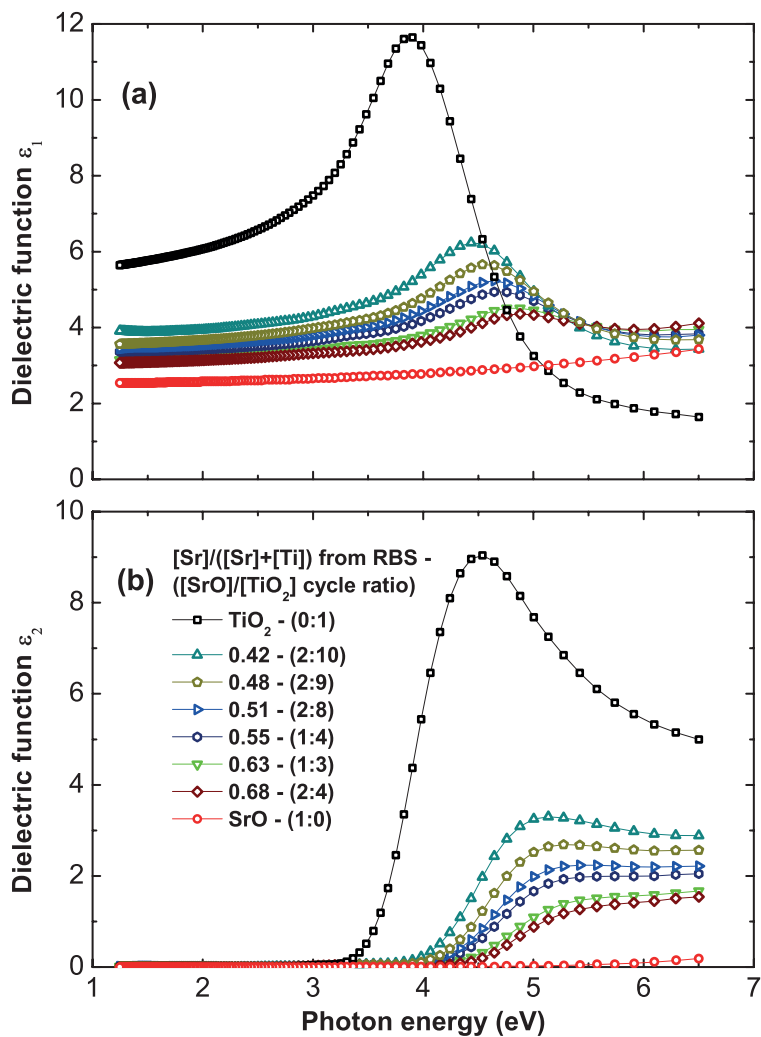For the determination of the film composition directly from the ellipsometry data, the

Figure 4.4: Real and imaginary part of the dielectric functions ϵ_1 (a) and ϵ_2 (b),respectively, of as-deposited TiO_2, SrO and of STO films. The corresponding [Sr]/([Sr]+[Ti]) content ratio from RBS and [SrO]/[TiO_2] cycle ratio are indicated for the STO films.
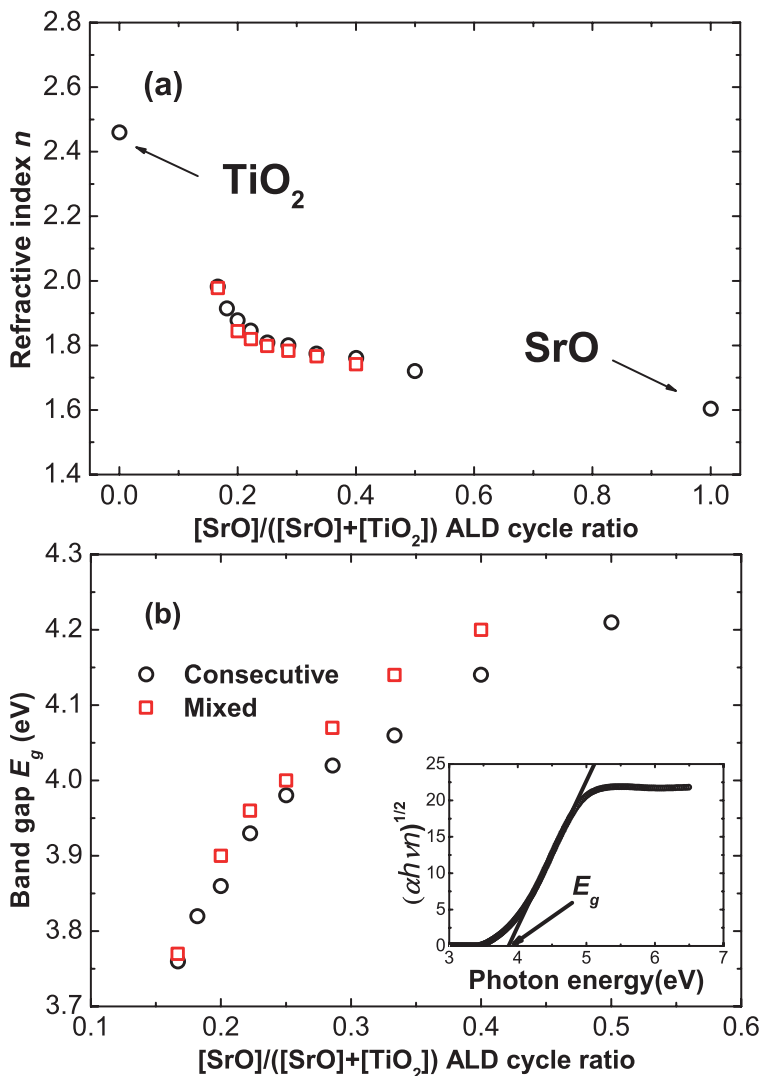
Figure 4.5: Refractive index, *n*, at 1.96 eV (a) and bandgap, E_g, (b) for STO films deposited with different [SrO]/[TiO₂] cycle ratios. The results are plotted versus [SrO]/([SrO]+[TiO₂]) cycle ratio. Both consecutive (SrO cycles followed by TiO₂ cycles in an STO supercycle) (circles), and mixed (SrO and TiO₂ cycles intermixed in an STO supercycle) (squares) approaches were employed for the depositions. Refractive index values are also shown for TiO₂ and SrO. The inset shows how the bandgap E_g is obtained by plotting $(\alpha h \nu n)^{1/2}$ as a function of the photon energy and by extrapolation of the linear part of the curve.
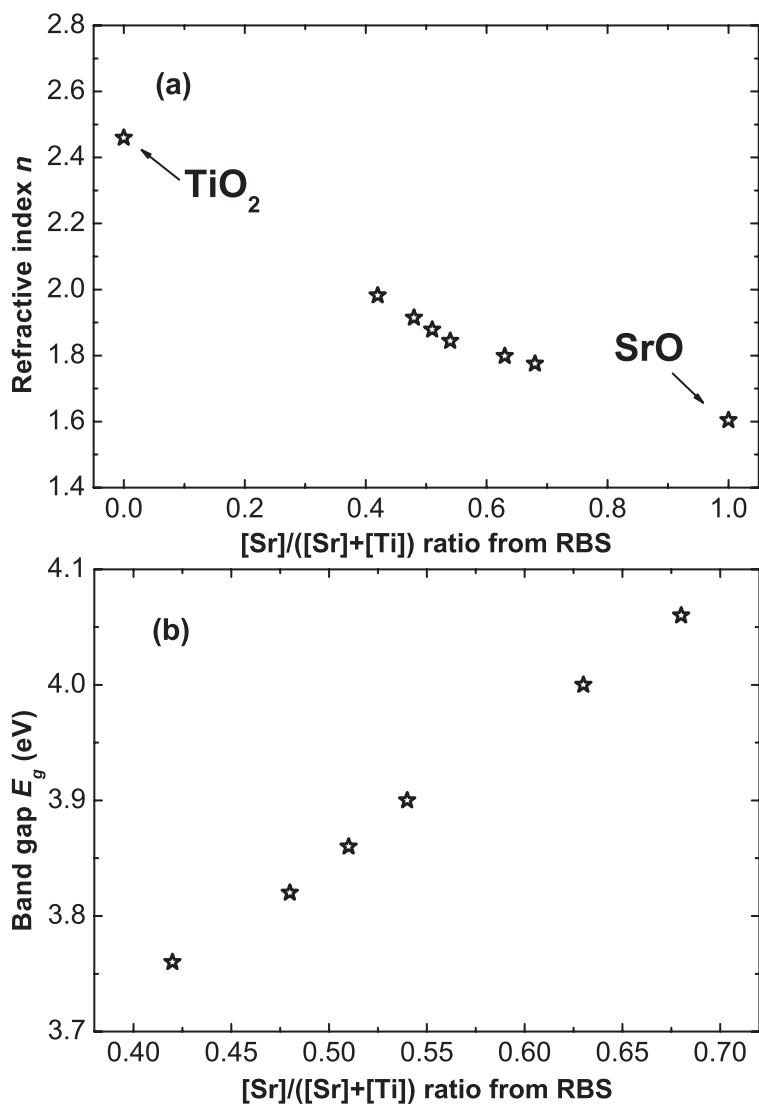
Figure 4.6: Refractive index, n, at 1.96 eV (a) and bandgap, E_g, (b) for STO films deposited with different [SrO]/[TiO$_2$] cycle ratio versus [Sr]/([Sr]+[Ti]) content ratio from RBS measurements. Refractive index values are also shown for TiO$_2$ and SrO.

CompleteEASE® software (J.A. Woollam) offers the possibility to build composition- or temperature-dependent B-spline-based optical constant libraries. A set of dielectric functions parameterized by B-splines corresponding to samples of known compositions (or temperatures), are loaded into the software by the user. The library is then built by interpolating these dielectric functions. The interpolation is based on the critical point shifting algorithm described by Snyder et al. for $Al_xGa_{1-x}As$ optical constants [39], where the dielectric function of a film with unknown composition is estimated by shifting the closest two dielectric functions of known compositions in energy to align their critical points. The unknown composition is then determined by taking a weighted average of the two dielectric functions of known composition. For this purpose, CompleteEASE® makes use of polynomials to shift the reference dielectric functions in energy accordingly to their known composition. In contrast to the approach by Snyder et al., who calculated the wavelength shifts to accurately align the critical points of the reference dielectric functions, the CompleteEASE® software calculates polynomials using a non-linear regression fit to minimize the error between two adjacent reference spectra when shifted in energy to the average of the two known compositions (called hereafter "mid-point composition"). Snyder et al. used a linear interpolation for the wavelength shift algorithm for $Al_xGa_{1-x}As$ optical constants [39]. Parameters such as the resolution (i.e. the B-spline node spacing) and the maximum degree of the polynomials should be optimized accordingly to the case to obtain the best results. In our case, the library was built using the B-spline parameterization of the dielectric functions of the films for which RBS was performed ([Sr]/([Sr]+[Ti]) from 0.42 to 0.68). Here, we used a resolution of 0.05 eV, and for the calculation of the polynomials the reference spectra were shifted by a constant (polynomial degree of 0 for the wavelength) and linearly interpolated for the calculation of the composition (polynomial degree of 1 for the composition). The absence of sharp features in the dielectric function of amorphous STO makes it possible to keep the degree of the polynomials low. Higher polynomial degrees can result in interpolation artifacts due to the algorithm. In our case, increasing the degree of the polynomials resulted in higher values of the shifts. Since the dielectric function of the mid-point composition is calculated as a weighted average of the two shifted adjacent dielectric functions of known compositions, high values of shifts resulted in misalignment of the transparent region of the two shifted spectra. This led to small non-zero values absorption below the band gap for the interpolated spectra. Figure 4.7 displays the B-spline parameterized dielectric functions of STO of known compositions (solid lines) and of the mid-point compositions calculated by the CompleteEASE® library (dashed lines), showing the accuracy of the algorithm. Also a library including the dielectric function of TiO_2 and SrO
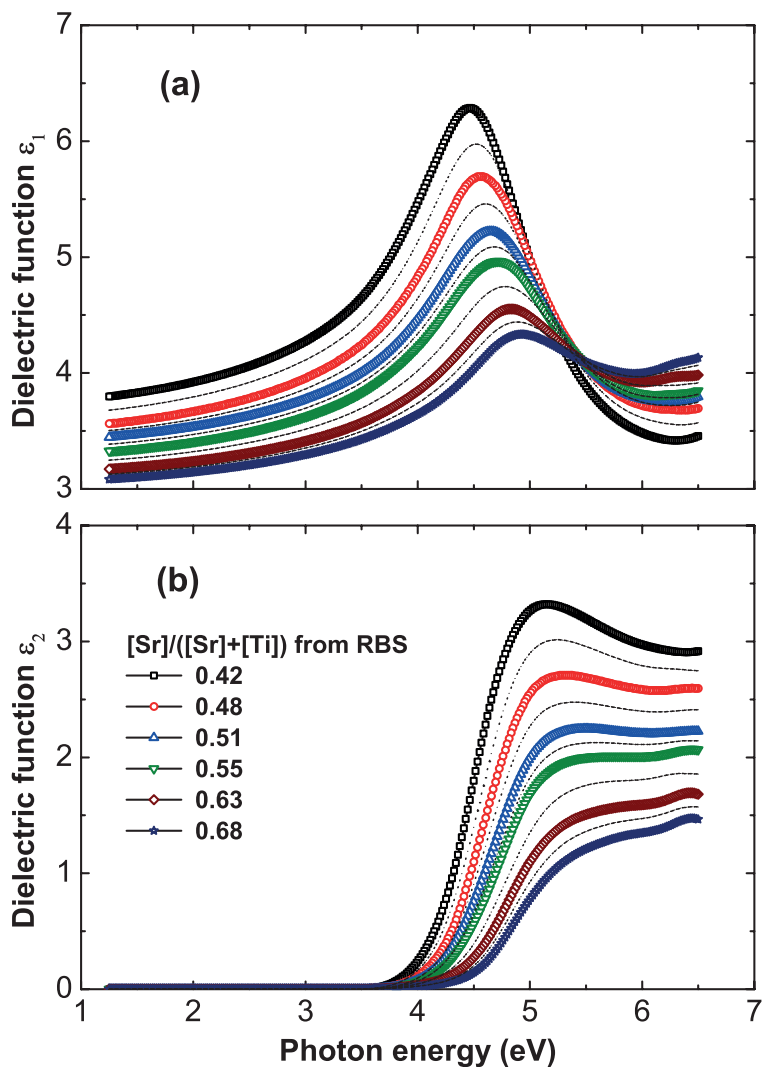
Figure 4.7: B-spline parameterized dielectric functions of STO films measured by RBS (symbols), and of "mid-point compositions" (average compositions between two adjacent known compositions) calculated by the optical constants library in CompleteEASE (dotted lines).

has been built. However, the difference in composition between the dielectric functions of STO films which are the richest in Ti- and Sr- as measured by RBS and the dielectric functions of TiO_2 and SrO is much larger than the difference between the single dielectric functions of the STO layers (Figure 4.4). The accuracy of the library depends on the difference between the dielectric function of known compositions and a poor fit was therefore obtained for layers having [Sr]/([Sr]+[Ti]) < 0.42 or > 0.68. Consequently, more dielectric functions of known compositions are required to have an accurate library also in these ranges. Once the library is built, the ellipsometry data from an as-deposited STO layer with unknown composition can be modeled using only the thickness and the [Sr]/([Sr]+[Ti]) ratio as fit parameters. To test the accuracy of the optical constant library, samples deposited with different [SrO]/[TiO_2] cycle ratios were measured by XPS and by SE. The SE data were fitted using this library, and the extracted [Sr]/([Sr]+[Ti]) ratio from SE and XPS were compared. For all samples measured (with 0.42 < [Sr]/([Sr]+[Ti]) < 0.68) the difference in [Sr]/([Sr]+[Ti]) ratio obtained from SE and XPS was < ± 0.02, confirming the accuracy of the optical constant library.

4.3.6 Spectroscopic Ellipsometry and XRD Measurements of Annealed STO Films

STO films deposited with different [SrO]/[TiO_2] cycle ratios were annealed in flowing N_2 atmosphere to achieve crystallization. After an RTA of 10 minutes at 600 °C, samples were measured by GI-XRD to determine their crystallinity. GI-XRD spectra of STO films with different compositions are given in Figure 4.8. Diffraction peaks corresponding to the cubic perovskite structure are clearly observed for films with [Sr]/([Sr]+[Ti]) ratio ranging from 0.48 to 0.63. The relative intensities of the diffraction peaks were comparable to the powder reference standards [40], indicating that there is no preferred crystal orientation. The intensity of the peaks decreased as the composition deviated from the stoichiometric value evidencing that a more pronounced crystallization is achieved for more stoichiometric films. Films deposited with [SrO]/[TiO_2] cycle ratios 2:3 and 2:10 were found to be mainly amorphous, suggesting that for Sr-rich and Ti-rich compositions a higher thermal budget is required for crystallization or that full crystallization into the perovskite structure is not achievable for such compositions. When comparing the spectra of the films with [Sr]/([Sr]+[Ti]) ratios 0.63 and 0.42 it is evident that Sr-rich films are more easily crystallized than Ti-rich films. This is in good agreement with the results of Menou et al. who reported higher crystallization temperatures for Ti-rich films [19]. Figure 4.9.a shows ϵ_1 as determined by SE for films that were also analyzed by GI-XRD.
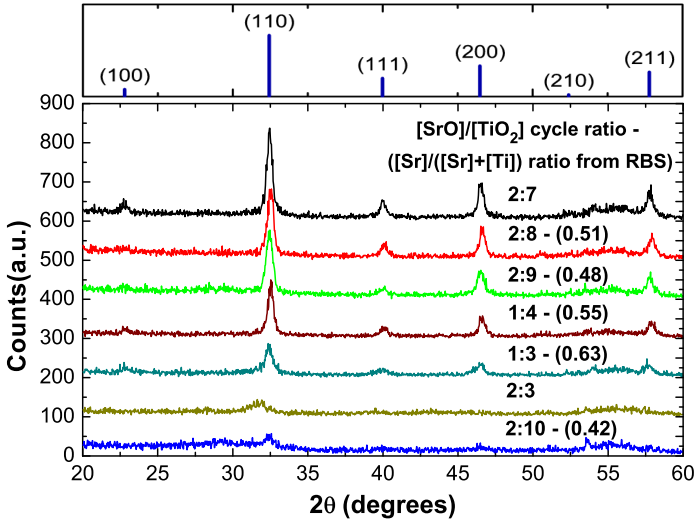
Figure 4.8: GI-XRD spectra of STO films after RTA at $600\,^{\circ}$C for 10 minutes in N_2. The corresponding [SrO]/[TiO$_2$] cycle ratio and [Sr]/[Sr]+[Ti] content ratio from RBS (when available) are indicated. The powder diffraction spectrum for crystalline STO is plotted as a reference [40].

Figure 4.9.b displays the real part of the dielectric function (ϵ_1) for bulk STO and crystalline STO films of 10 and 20 nm deposited by pulsed laser deposition as a reference [29]. As discussed above, the critical points of crystalline perovskite STO at low energies ($<$ 7 eV) are related to transitions from the O2p valence bands to the Ti3d conduction bands [29] and they result in a maximum in ϵ_1 at $\sim$ 4 eV. The presence of this maximum was clearly observed to coincide with the appearance of the diffraction peaks in the GI-XRD spectra. Films deposited with a [SrO]/[TiO$_2$] cycle ratio of 2:3 and 2:10 showed a peak at higher energies indicating an incomplete crystallization process. Comparing the dielectric functions of the as-deposited films (Figure 4.4.a) and of the annealed samples (Figure 4.9.a) a transition in ϵ_1 can be noticed. This suggests that after RTA these films are partially crystalline. This hypothesis is corroborated by GI-XRD that revealed weaker peaks for these films.

The intensity of the peak at $\sim$ 4 eV in ϵ_1 can also be used to estimate the stoichiometry of the crystallized films. As evident from Figure 4.9.a, the intensity of this peak is maximum for the more stoichiometric film ([SrO]/[TiO$_2$] = 2:8) and decreases gradually when deviating from the stoichiometric composition. This demonstrates that SE can be used to estimate the crystallinity of the STO films as well as the stoichiometry
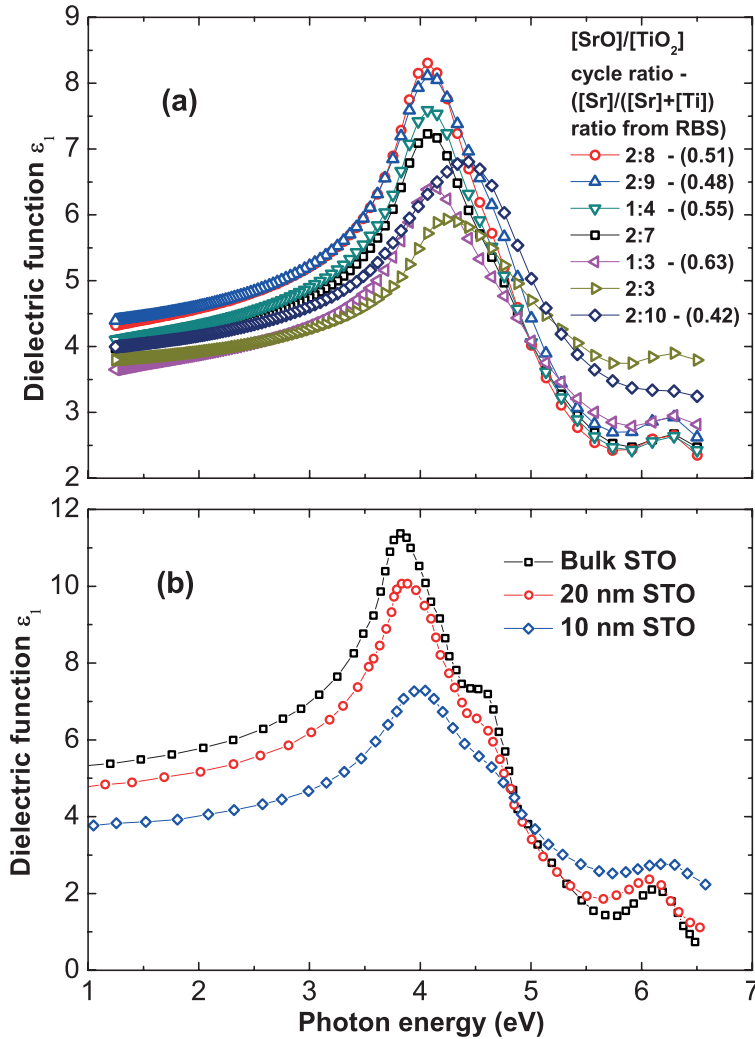
Figure 4.9: Real part (ϵ_1) of the dielectric function of STO films. Data of deposited films after RTA at 600 °C for 10 minutes in N_2 (a). Reference data from literature (b), ϵ_1 of bulk STO and of crystalline 10 nm, 20 nm STO films prepared by pulsed laser deposition [29].
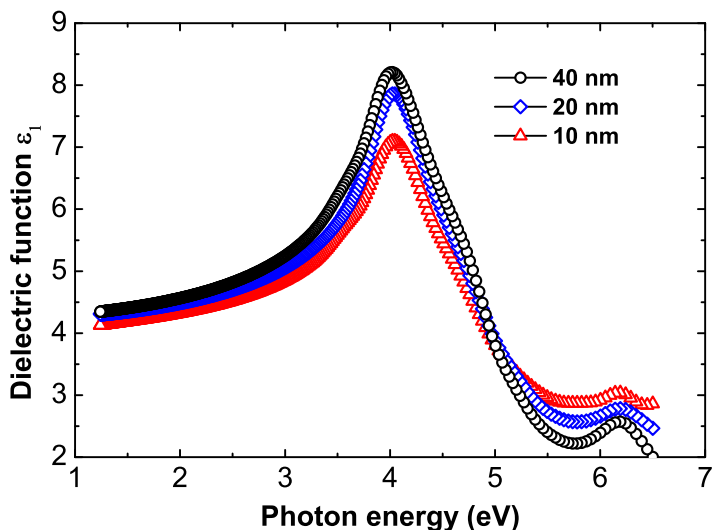
Figure 4.10: Real part (ϵ_1) of the dielectric functions of STO films with different thicknesses. Films were deposited with a [SrO]/[TiO$_2$] ALD cycle ratio of 1:3 in the FlexAL-B reactor.

of both as-deposited and crystallized films.

4.3.7   Film Thickness Influence on Dielectric Function

Films with different thicknesses (10-40 nm), deposited at 250 °C with a [SrO]/[TiO$_2$] cycle ratio 1:3 in the FlexAL-B reactor, were annealed at 650 °C for 10 min. The real parts of the dielectric functions of these layers are shown in Figure 4.10. Compared to the real part of the dielectric function of bulk STO the peaks are broadened and the amplitude is reduced. Furthermore, thinner films showed lower amplitudes of ϵ_1 and decreased refractive indices at 1.96 eV (2.35, 2.13, 2.12 and 2.08 respectively for bulk, 40 nm, 20 nm and 10 nm thick STO). This is an important consideration to take into account when comparing the dielectric function of thin films to estimate their composition. To establish an accurate relation between dielectric function and stoichiometry, layers with the same thickness should be used. In this work all layers were $\sim$ 30 nm in thickness. A similar trend for STO films deposited on Si was also reported by Zollner et al. [29] as illustrated in Figure 4.9.b. The broadening of the peaks at the critical points compared to the reference dielectric function of bulk STO was ascribed to the polycrystalline structure and defects in the film [29]. The decrease in refractive index films can be explained by

the more prominent influence of the low refractive index interfacial oxide (formed at the Si/STO interface) on the dielectric function of thinner STO films. The influence of the interfacial oxide is also increased upon annealing the STO films. XPS depth profiles (not reported here) showed Si diffusion into the STO film after the annealing step leading to silicate formation. This could also explain the lower amplitude of ϵ_1 for crystalline STO reported in this work ($\sim$ 30 nm thick, Figure 4.9.a and 4.10) compared to the one reported by Zollner et al. (20 nm thick STO, Figure 4.9.b) [29]. In the latter case the STO films deposited by pulsed laser deposition (PLD) were crystalline as-deposited and did not require an annealing step. This probably limits the formation of silicates, thus yielding a better quality interface between the STO and the Si substrate.

4.4   Conclusions

Strontium titanate films were deposited by plasma-assisted ALD from Ti-Star [(penta-methyl-cyclopentadienyl)trimethoxy-titanium], Hyper-Sr [bis(tri-isopropylcyclopentadie-nyl)-strontium-DME] and O_2 plasma. The ALD temperature window for this process was found to be between 150 °C to 350 °C. RBS analysis confirmed that the stoi-chiometry of the STO film is determined by the ALD cycle ratio employed and that the Sr-content is higher than expected from the [SrO]/[TiO$_2$] ALD cycle ratio. This was imputed to a slightly enhanced growth of SrO on a TiO$_2$ surface. Spectroscopic ellip-sometry was employed to determine the dielectric functions of the STO films in the as-deposited state and after RTA. Using an optical constants library, built in the SE software (CompleteEASE®), it was proven possible to determine the composition of amorph-ous STO thin films from the ellipsometric angles using RBS measurements as a cross-reference for the Sr and Ti content in the compositional range examined ([Sr]/([Sr]+[Ti]) from 0.42 to 0.68). It was also demonstrated how the composition of as-deposited films can be derived from the refractive index and band gap values. GI-XRD was employed to determine the crystallinity of the layers after RTA in N_2 for 10 minutes at 600 °C. Dif-fraction peaks corresponding to the cubic perovskite structure were observed for films with [Sr]/([Sr]+[Ti]) ratio ranging from 0.48 to 0.63. SE analysis of annealed films evid-enced also that only films appearing as crystalline from GI-XRD measurements, showed also a pronounced peak at $\sim$ 4 eV in the real part of the dielectric function (ϵ_1). This im-plies that SE, in addition to being an in-situ film growth monitoring tool, is an effective technique to determine the crystallinity of STO films and also to probe the stoichiometry of as-deposited and crystalline STO films.

Acknowledgments

4.5   Addendum: Conformality over 3D Structures

A first attempt to determine the conformality (step coverage) of the STO thin films was performed on 3D structures. Figure A.4.1.a shows a cross-section of a sample with tripod structures. On the tripods a ~ 50 nm thick (at the top of the tripods) STO thin film and a ~ 500 nm thick poly-Si film were deposited. The STO was deposited by plasma-assisted ALD and the poly-Si by low-pressure chemical vapor deposition (LPCVD). The height of the tripods and the interspace between the tripods were ~ 12 μm and ~ 2.3 μm, respectively, while the width of a tripod was ~ 1.1 μm (see Figure A.4.1.a). Therefore, the aspect ratio of this structure is ~ 5 (2.3 μm:12 μm). A top view of the tripod sample showing the direction in which the sample was sectioned is shown in Figure A.4.1.b while also the structure of the tripods before poly-Si deposition is schematically indicated. Figures A.4.1.c-f show the thickness of the STO thin film at different locations on the tripod structure. The STO film thickness was ~ 46 nm and ~ 33 nm at the top and the bottom of the side-wall of the tripods, respectively. Therefore, the conformality of the STO film on these structures was estimated to be ~ 70 %. SEM analysis on trenches with aspect ratios up to 15 revealed a conformality of ~ 50 %. It should be noted that the deposition conditions were not optimized for this purpose, in particular the dose and the purge times were only simply doubled compared to the values for planar substrates. In a recent work from Knoops et al. [41] it was shown how the recombination of radicals on the trench walls can have an influence on the step coverage of films deposited by plasma-assisted ALD. The thickness profiles of our STO films over the trench structures suggest that this process is recombination-limited [41] and optimization of the plasma conditions and exposure could improve the step coverage. However, also the diffusion of the precursors down the trench could be a limiting factor for the step coverage. Therefore, also the delivery of the precursors should be optimized.
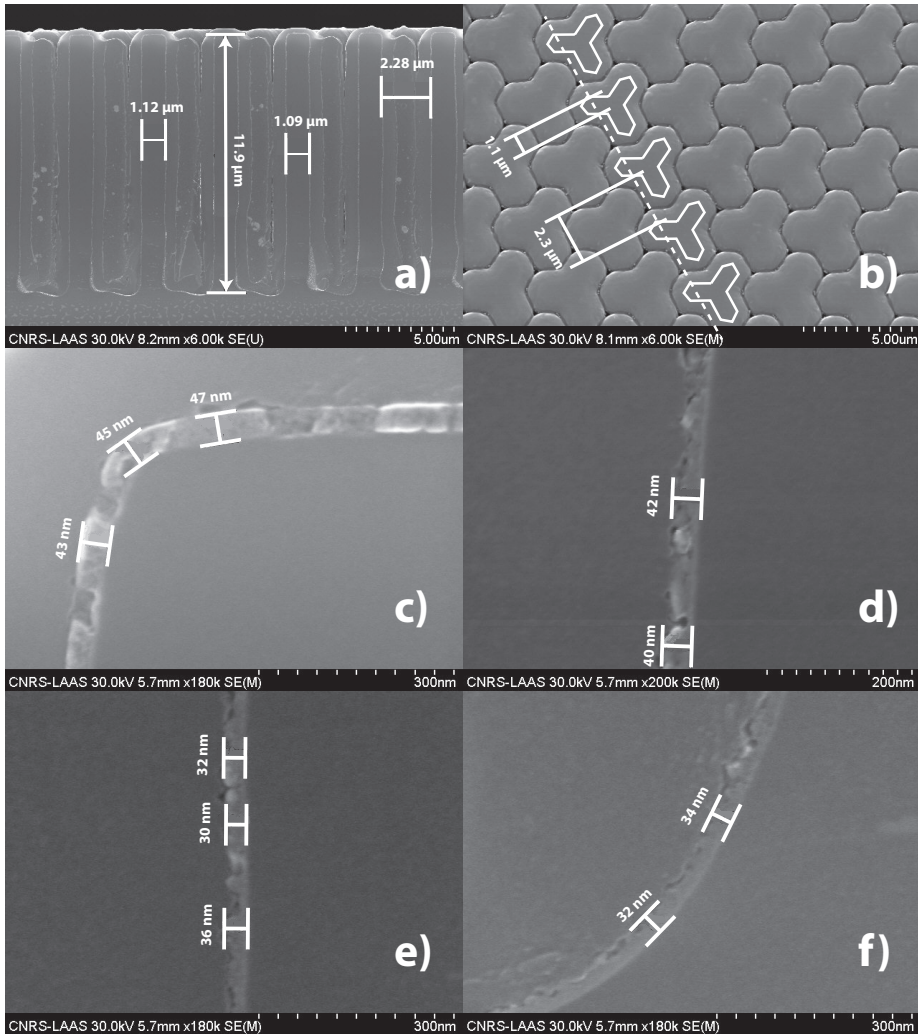
Figure A.4.1: SEM images of the tripods onto which an ALD STO thin film (~ 50 nm) and a thick poly-Si film (~ 500 nm) have been deposited. (a) Cross-section in which the depth ($\sim 12 \ \mu m$) and the width ($\sim 2.3 \ \mu m$) of the interspace between the tripods as well as the width of a tripod ($\sim 1.2 \ \mu m$) have been indicated. (b) Top-view of the tripods in which the direction of the sectioning of the sample and the structure of the tripods before the poly-Si film have been indicated. SEM images of the STO thickness profile at different depths (the thickness is indicated at various locations) over a side-wall of a tripod: (c) top of the tripod, (d) 2 μm deep, (e) 8 μm deep and (f) bottom of the tripod (12 μm deep).

4.6   References

1. O.N. Tufte and P.W. Chapman, *Phys. Rev.*, 155, 796 (1967).

2. T. Zhao, H.B. Lu, F. Chen, S.Y. Dai, G.Z. Yang and Z.H. Chen, *J. Cryst. Growth*, 212, 451 (2000).

3. N. Shanthi and D.D. Sarma, *Phys. Rev. B*, 57, 2153 (1998).

4. F.M. Pontes, E.J.H. Lee, E.R. Leite, E. Longo and J.A. Varela, *J. of Mat. Sci.*, 35, 4783 (2000).

5. R. Wordenweber, E. Hollmann, M. Ali, J. Schubert, G. Pickartz and T.K. Lee, *J. Eur. Ceram. Soc.*, 27, 2899 (2007).

6. D.H. Choi, D. Lee, H. Sim, M. Chang, and H.S. Hwang, *Appl. Phys. Lett.*, 88, 082904 (2006).

7. http://www.itrs.net/reports.html-2011 updated version.

8. S. van Elshocht, C. Adelmann, S. Clima, G. Pourtois, T. Conard, A. Delabie, A. Franquet, P. Lehnen, J. Meersschaut, N. Menou, M. Popovici, O. Richard, T. Schram, X.P. Wang, A. Hardy, D. Dewulf, M.K. Van Bael, P. Lehnen, T. Blomberg, D. Pierreux, J. Swerts, J.W. Maes, D.J. Wouters, S. De Gendt and J.A. Kittl, *J. Vac. Sci. Technol., B*, 27, 209 (2009).

9. M. Vehkamäki, T. Hanninen, M. Ritala, M. Leskelä, T. Sajavaara, E. Rauhala and J. Keinonen, *Chem. Vap. Deposition* , 7, 75 (2001).

10. M. Popovici, S. van Elshocht, N. Menou, J. Swerts, D. Pierreux, A. Delabie, B. Brijs, T. Conard, K. Opsomer, J.W. Maes, D.J. Wouters and J. A. Kittl, *J. Electrochem. Soc.*, 157, G1 (2010).

11. M. Vehkamäki, T. Hatanpaa, T. Hanninen, M. Ritala and M. Leskelä, *Electrochem. Solid-State Lett.*, 2, 504 (1999).

12. O.S. Kwon, S.K. Kim, M. Cho, C.S. Hwang and J. Jeong, *J. Electrochem. Soc.*, 152, C229 (2005).

13. A. Kosola, M. Putkonen, L.S. Johansson and L. Niinisto, *Appl. Surf. Sci.*, 211, 102 (2003).

14. J.H. Ahn, S.W. Kang, J.Y. Kim, J.H. Kim and J.S. Roh, *J. Electrochem. Soc.*, 155, G185 (2008).

15. S.W. Lee, J.H. Han, O.S. Kwon and C.S. Hwang, *J. Electrochem. Soc.*, 155, G253 (2008).

16. O.S. Kwon, S.W. Lee, J.H. Han and C.S. Hwang, *J. Electrochem. Soc.*, 154, G127 (2007).

17. S.W. Lee, O.S. Kwon, J.H. Han and C.S. Hwang, *Appl. Phys. Lett.*, 92, 222903 (2008).

18. N. Menou, M. Popovici, K. Opsomer, B. Kaczer, M.A. Pawlak, C. Adelmann, A. Franquet, P. Favia, H. Bender, C. Detavernier, S. van Elshocht, D.J. Wouters, S. Biesemans and J.A. Kittl, *Jap. J. Appl. Phys.*, 49, 04DD01 (2010).

19. N. Menou, X.P. Wang, B. Kaczer, W. Polspoel, M. Popovici, K. Opsomer, M.A. Pawlak, W. Knaepen, C. Detavernier, T. Blomberg, D. Pierreux, J. Swerts, J.W. Maes, P. Favia, H. Bender, B. Brijs, W. Vandervorst, S. van Elshocht, D.J. Wouters, S. Biesemans and J.A. Kittl, *IEDM 2008, Technical Digest*, 929 (2008).

20. N. Menou, M. Popovici, S. Clima, K. Opsomer, W. Polspoel, B. Kaczer, G. Rampelberg, K. Tomida, M.A. Pawlak, C. Detavernier, D. Pierreux, J. Swerts, J.W. Maes, D. Manger, M. Badylevich, V.V. Afanas'ev, T. Conard, P. Favia, H. Bender, B. Brijs, W. Vandervorst, S. van Elshocht, G. Pourtois, D.J. Wouters, S. Biesemans and J.A. Kittl, *J. Appl. Phys.*, 106, 094101 (2009).

21. M.A. Pawlak, M. Popovici, J. Swerts, K. Tomida, M.S. Kim, B. Kaczer, K. Opsomer, M. Schaekers, P. Favia, H. Bender, C. Vrancken, B. Govoreanu, C. Demeurisse, W.C. Wang, V.V. Afanas'ev, I. Debusschere, L. Altimime and J.A. Kittl, *IEDM 2010, Technical Digest* (2010).

22. E. Langereis, R. Roijmans, F. Roozeboom, M.C.M. van de Sanden and W.M.M. Kessels, *J. Electrochem. Soc.*, 158, G34, (2011).

23. B. Johs and J.S. Hale, *Phys. Status Solidi A*, 205, 715 (2008).

24. J.W. Weber, T.A.R. Hansen, M.C.M. van de Sanden and R. Engeln, *J. Appl. Phys.*, 106, 123503 (2009).

25. S.E. Potts, W. Keuning, E. Langereis, G. Dingemans, M.C.M. van de Sanden and W.M.M. Kessels, *J. Electrochem. Soc.*, 157, 66 (2010).

26. R. Katamreddy, V. Omarjee, B. Feist, C. Dussarrat, M. Singh and C. Takoudis, *ECS Trans.*, 16, 487 (2008).

27. M. Rose, J. Niinisto, P. Michalowski, L. Gerlich, L. Wilde, I. Endler and J.W. Bartha, *J. Phys. Chem. C*, 113, 21825 (2009).

28. S.D. Elliott and O. Nilsen, *ECS Trans.*, 41, 175 (2011).

29. S. Zollner, A.A. Demkov, R. Liu, P.L. Fejes, R.B. Gregory, P. Alluri, J.A. Curless, Z. Yu, J. Ramdani, R. Droopad, T.E. Tiwald, J.N. Hilfiker and J.A. Woollam, *J. Vac. Sci. Technol., B*, 18, 2242 (2000).

30. K. van Benthem, C. Elsasser and R.H. French, *J. Appl. Phys.*, 90, 6156 (2001).

31. R. Ahuja, O. Eriksson and B. Johansson, *J. Appl. Phys.*, 90, 1854 (2001).

32. S.D. Gou and B.G. Liu, *J. Appl. Phys.*, 110, 073525 (2011).

33. M. Cardona, *Phys. Rev.*, 140, A651 (1965).

34. S.K. Kim, W.D. Kim, K.M. Kim, C.S. Hwang and J. Jeong, *Appl. Phys. Lett.*, 85, 4112 (2004).

35. R.J. Kearney, M. Cottini, E. Grilli and G. Baldini, *Phys. Status Solidi B*, 64, 49 (1974).

36. M. Popovici, K. Tomida, J. Swerts, P. Favia, A. Delabie, H. Bender, C. Adelmann, H. Tielens, B. Brijs, B. Kaczer, M.A. Pawlak, M.S. Kim, L. Altimime, S. van Elshocht and J. A. Kittl, *Phys. Status Solidi A*, 208, 1920 (2011).

37. O. Fursenko, J. Bauer, G. Lupina, P. Dudek, M. Lukosius, C. Wenger and P. Zaumseil, *Thin Solid Films*, 520, 4532 (2012).

38. M. Di, E. Bersch, A.C. Diebold, S. Consiglio, R.D. Clark, G.J. Leusink and T. Kaack, *J. Vac. Sci. Technol., A*, 29, 041001-1 (2011).

39. P.G. Snyder, J.A. Woollam, S.A. Alterovitz and B. Johs, *J. Appl. Phys.*, 68, 5925 (1990).

40. Powder Diffraction File, Card No 35-0734, International Center for Diffraction Data, Newton Square, PA.

41. H.C.M. Knoops, E. Langereis, M.C.M. van de Sanden and W.M.M. Kessels, *J. Electrochem. Soc.*, 157, G241 (2010).

Chapter 5

Crystallization Study by Transmission Electron Microscopy of SrTiO$_3$ Thin Films Prepared by Plasma-Assisted ALD*

Abstract   The crystallization behavior of thin strontium titanate (SrTiO$_3$, STO) films with $\approx$ 15 nm thickness was studied by Transmission Electron Microscopy (TEM). Amorphous STO films with [Sr]/([Sr]+[Ti]) ratio ranging from 0.50 to 0.63 were deposited at 350 °C by plasma-assisted ALD and subsequently treated by rapid thermal annealing in flowing N$_2$ for crystallization. Different temperatures and annealing durations were employed to fully characterize the crystallization process. TEM analysis showed that *transrotational* crystals were formed and evidenced the influence of the STO composition and of the thermal budget applied on the grain size, crack and void formation. In particular, Sr-rich layers ([Sr]/([Sr]+[Ti] $\geq$ 0.59) showed a finer crystalline structure which was imputed to a higher nucleation probability at the onset of the crystallization process. Crystallization into the perovskite structure was confirmed for all the film compositions studied. By tuning the STO composition and the thermal budget of the annealing step it was demonstrated that it is possible to control the microstructure of the crystallized film as a further step in optimizing the STO film properties.

5.1 Introduction

Strontium titanate (SrTiO$_3$, STO) has received a lot of attention due to its properties that are related to its perovskite crystal structures. Among these, ferro-electricity, para-electricity, resistive-switching behavior and oxygen sensing have been reported for thin STO layers deposited by various techniques, such as physical vapor deposition (PVD), chemical vapor deposition (CVD) and pulsed laser deposition (PLD) [1-9]. Furthermore STO is an ultrahigh-k material with a theoretical k-value $\approx$ 300 for bulk STO. This property combined with a good thermal stability and relatively low crystallization temperature makes STO the dielectric material of choice for next generation dynamic random access memories (DRAM) [10-12]. STO high-k dielectric films have been deposited by ALD, especially since the application in deep trenches in silicon wafers calls for extremely conformal layers in such 3D structures. As ALD is the preferred technology of choice, the thermal budget used during the deposition needs to be limited to prevent decomposition of the metal-organic precursors typically employed. At low deposition temperatures the as-deposited STO films are amorphous and a thermal treatment is required to crystallize the films afterwards in order to obtain STO with the high dielectric constant targeted. Crystallization into the perovskite structure is achieved also for non-stoichiometric STO thin films. It has been shown that excess Sr is accommodated in the crystalline STO in a solid solution and it is only expelled out of the STO grains during high temperature annealing (> 700 °C) [13,14]. Increasing the Sr-content results in lower k-values compared to the stoichiometric films [15-17]. However, Sr-rich layers are to be used in next generation DRAM due to their superior dielectric properties and microstructure leading, amongst others, to lower leakage currents [10,11].

The thermal budget applied during annealing as well as specific parameters such as film composition and thickness are of crucial importance as they determine the crystallization behavior and the consequent final microstructure and electrical properties of the crystallized STO films. Crystallization of the film leads to in-plane and out-of-plane densification of the film. Because of the in-plane directional crystal growth, densification will eventually lead to void formation. Depending on the density of nuclei, the growth morphology and rate, voids will be either homogeneously distributed or concentrated at the grain boundaries, the latter leading to networks of so-called "nano-cracks" [14]. These lower density regions are detrimental if the STO is employed as a dielectric material. The cracks at the grain boundaries can be either formed due to densification caused by solid-state diffusion or to tensile stress between grains [13,14]. Recent studies showed that, when crystallized, Sr-rich layers ([Sr]/([Sr]+[Ti]) = 0.62) develop a

smaller grain size than stoichiometric films. This finer microstructure results in reduced crack formation, thus improved leakage current performance and dielectric properties [10-13,18]. This example shows the importance of resolving the correct process and temperature window to obtain the desired film properties for the specific application targeted. In recent literature, TEM studies have been published on STO films deposited by ALD and crystallized by rapid thermal annealing (RTA) with the aim of determining the STO microstructure and its relation to electrical properties [13,14,18,19]. However, to date a comprehensive study has not been reported on the relation between film composition, thermal budget and the crystalline microstructure of thin STO films. Since STO thin films are likely candidates for the above-mentioned applications, an in-depth understanding of their crystallization behavior will be vital.

In this work, we report on the crystallization behavior of STO thin films deposited by plasma-assisted ALD. The microstructure of the thin crystallized films was studied by TEM. To investigate the eventual influence of the underlying surface on the crystallization behavior, the 15 nm thin STO films were deposited at $350\,^{\circ}C$ both on bare Si_3N_4 and on Al_2O_3-coated Si_3N_4 TEM windows. These two materials show good diffusion barrier properties and remain in the amorphous state for the annealing temperatures employed in this work. This makes them both suitable for TEM imaging. Furthermore, Al_2O_3 is commonly used as a leakage current barrier layer in capacitor structures such as the one employed in DRAM technology [20]. Films with different compositions were treated by RTA. Different annealing temperatures and durations were applied to characterize the successive steps in the nucleation and crystallization. TEM analysis revealed that the temperature, the anneal duration and the film composition influence the final microstructure of the crystalline STO films. In particular it was shown that by accurately choosing the above mentioned parameters it is possible to control the average size and the morphology of the grains.

5.2 Experimental Details

STO thin films of nominal 15 nm thickness were deposited in an Oxford Instruments FlexAL™ thermal and plasma ALD reactor. The layers were deposited by plasma-assisted ALD at a temperature set at $350\,^{\circ}C$. The precursors employed were Ti-Star, (pentamethyl-cyclopentadienyl)trimethoxy-titanium, $CpMe_5Ti(OMe)_3$, and Hyper-Sr, bis-(tri-isopropyl-cyclopentadienyl)strontium with 1,2-dimethoxyethane adduct, $Sr(^iPr_3Cp)_2$-DME, both from AirLiquide. An O_2 (> 99.999 % purity) plasma generated by an inductively coupled plasma (ICP) source was used as the oxidizing agent. STO was obtained by

Table 5.1: [SrO]/[TiO$_2$] ALD cycle ratio, thickness and [Sr]/([Sr]+[Ti]) ratio of the STO films analyzed by TEM. The thickness and the [Sr]/([Sr]+[Ti]) ratio of the films in the as-deposited state were determined from spectroscopic ellipsometry experiments [22]. The errors in thickness and in the [Sr]/([Sr]+[Ti]) ratio are $\pm$ 0.50 nm and $\pm$ 0.03, respectively.

[SrO]/[TiO$_2$] ALD cycle ratio	Thickness (nm)	[Sr]/([Sr]+[Ti]) ratio
1:3	15.8	0.50
2:5 mixed *	15.4	0.53
1:2	14.9	0.59
2:3	15	0.63

mixing ALD cycles of the binary oxides TiO$_2$ and SrO. The details of the ALD process are reported elsewhere [21,22]. Films were deposited employing different [SrO]/[TiO$_2$] ALD cycle ratios to obtain different film compositions [21,22]. Silicon substrates were placed adjacent to the TEM windows (13 nm Si$_3$N$_4$ membranes) inside the reactor chamber during the depositions to allow ex-situ spectroscopic ellipsometry (SE) measurements (M2000D, J.A. Woollam, 1.25-6.5 eV). The elemental composition was extracted from the ellipsometry data by means of an optical constant library which was calibrated by means of Rutherford backscattering experiments [21]. The [SrO]/[TiO$_2$] ALD cycle ratios, the thicknesses in the as-deposited state and the [Sr]/([Sr]+[Ti]) ratios of the films examined in this study are listed in Table 5.1.

RTA in flowing N$_2$ was performed in an AST SHS100 system at temperatures ranging from 550 °C to 650 °C to crystallize the STO films. To determine the influence of the annealing duration, RTA was conducted for different dwell times for samples having the same STO layer deposited. For this purpose, the duration of the initial temperature ramp to reach the set RTA temperature was kept constant for samples annealed at the same temperature (10 s for 550 °C, 15 s for 600 °C and 650 °C), only the dwell time for the set temperature was varied. TEM studies were performed using a TECNAI F30ST TEM operated at 300 kV. Both Bright-Field TEM (BF-TEM) and High Angle Annular Dark-Field Scanning TEM (HAADF-STEM) modes were employed to characterize the samples. X-ray diffractometry (XRD) was performed on a Panalytical X'Pert PRO MRD employing Cu Kα (0.154 nm) radiation to determine the crystalline phase of the annealed films. Atomic Force Microscopy (AFM) was employed to study the surface morphology. AFM scans were performed using a NT-MDT Solver P47 microscope. Samples were scanned in tapping mode using a TiN coated Si tip (NSG10/TiN, NT-MDT).

---

*In the *"mixed"* approach TiO$_2$ and SrO ALD cycles were intermixed (i.e. the [SrO]/[TiO$_2$] ALD cycle ratio = 2:5 mixed corresponds to the sequence 1 SrO, 2 TiO$_2$, 1 SrO and 3 TiO$_2$ cycles [21,22].

5.3   Results and Discussion

Figures 5.1.a-c show Bright Field-TEM (BF-TEM) images of STO films on Si_3N_4 windows with [Sr]/([Sr]+[Ti]) = 0.53 annealed at $550\,^\circ$C for different times. The sample annealed for 1 minute was mainly amorphous containing only a low density of nuclei that can be recognized as darker dots in Figure 5.1.a. Upon annealing the film for 5 minutes, many crystals have formed in the amorphous matrix. Each crystal has its origin in a single-crystalline nucleus that grows due to solid state crystallization expanding in the amorphous matrix. The different sizes of the crystals can be explained by a crystallization process with a constant growth rate, where new nuclei are continuously formed during the crystallization process. After 10 minutes the layer was still not completely crystallized due to the slow crystal growth rate (< 0.1 μm/min) obtained under these conditions. In our study we can distinguish between two crystallization regimes: *nucleation-dominated* and *growth-dominated*. In the first, the nucleation probability is high, leading to a high density of small crystals that are limited in their lateral growth by the proximity of other nuclei, resulting in a small average crystal size upon full crystallization. In the latter, the nucleation probability is low and the crystallization process is dominated by growth of a low density of crystals, leading to a large crystal size upon full crystallization. A similar distinction of the two crystallization regimes can be found in the literature for phase change materials [23]. In case of the above mentioned $550\,^\circ$C anneal and [Sr]/([Sr]+[Ti]) = 0.53, the crystallization is growth-dominated rather than nucleation-dominated, resulting in an average grain size of 1 μm once the layer is fully crystallized.

Figures 5.1.d-f show BF-TEM images of STO thin films on Si_3N_4 windows having [Sr]/([Sr]+[Ti]) = 0.59 annealed at $550\,^\circ$C for different times. For this increased Sr-content in the STO film more nuclei can be observed for the sample annealed for 1 minute. This indicates that Sr-rich layers have a higher nucleation probability than the more stoichiometric ones. In addition, Sr-rich films exhibit a higher growth rate for the crystallites, resulting in a fully crystallized film already for an annealing time of 5 minutes. A further increase to 10 minutes did not result in remarkable morphological changes. The higher density of nuclei, compared to the film with [Sr]/([Sr]+[Ti]) = 0.53, resulted in a final smaller average grain size ($\sim$ 0.5 μm). The STO film with [Sr]/([Sr]+[Ti]) = 0.63 (data not shown) was also fully crystalline after a 5 minutes anneal at $550\,^\circ$C and showed an even smaller grain size (< 0.2 μm) while the STO film with [Sr]/([Sr]+[Ti]) = 0.50 (data not shown) was fully amorphous after 1 minute RTA at $550\,^\circ$C thus showing the lowest nucleation probability among the four compositions.
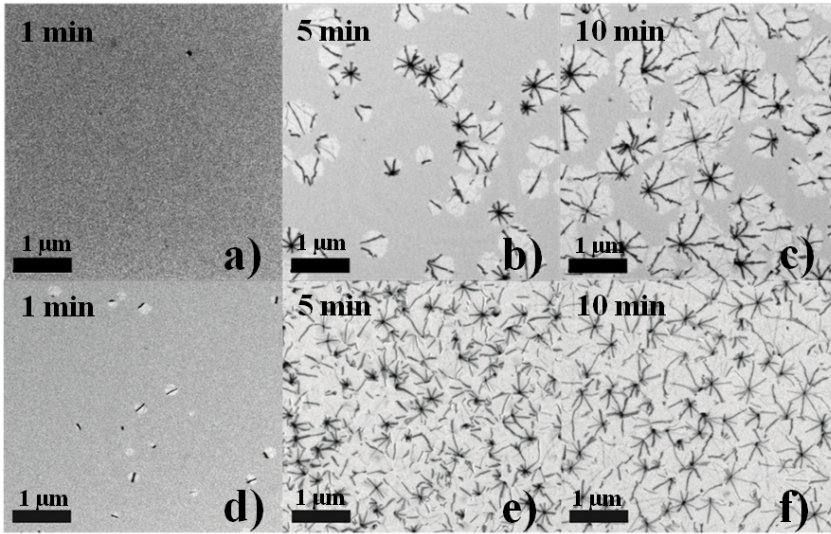
Figure 5.1: BF-TEM images of STO films on Si_3N_4 windows with $[Sr]/([Sr]+[Ti]) =$ 0.53 (a-c) and $[Sr]/([Sr]+[Ti]) = 0.59$ (d-f) after RTA at $550\,^{\circ}C$ for different annealing times as indicated in the figure.

Similar results were obtained for the STO films deposited on the Al_2O_3-coated windows.

The star-shaped patterns of varying diffraction contrast that can be recognized in the reported BF-TEM images are an indication of bending of the lattice planes within a single crystal. The term *transrotational* crystals was introduced by Kosolov et al. to describe this particular crystalline structure, since the lattice planes are not only replicated or *translated* but also *rotated* during crystal growth [24]. While grains in polycrystalline thin films give a uniform contrast in TEM imaging depending on their crystal orientation, transrotational crystals show contrast patterns due to the lateral variation in crystal orientation. The internal lattice plane bending is due to stress induced by the amorphous-to-crystalline transformation and film densification [23,24]. In the work of Kooi et al. it was proposed that, during crystal growth, new crystal planes nucleate at the top interface and the crystal front is characterized by a thickness profile with the crystallized region being thinner than the surrounding amorphous matrix. With the crystal expanding the crystal front advances and these newly formed crystal planes are "pushed down", resulting in internal lattice bending [23]. This hypothesis is consistent with the SE measurements performed before and after full crystallization of the STO films where a thickness reduction of $\sim 15\,\%$ was recorded upon crystallization. Figure 5.2.a shows an AFM topography image of an STO film with $[Sr]/([Sr]+[Ti]) = 0.53$ annealed at $550\,^{\circ}C$ for 5

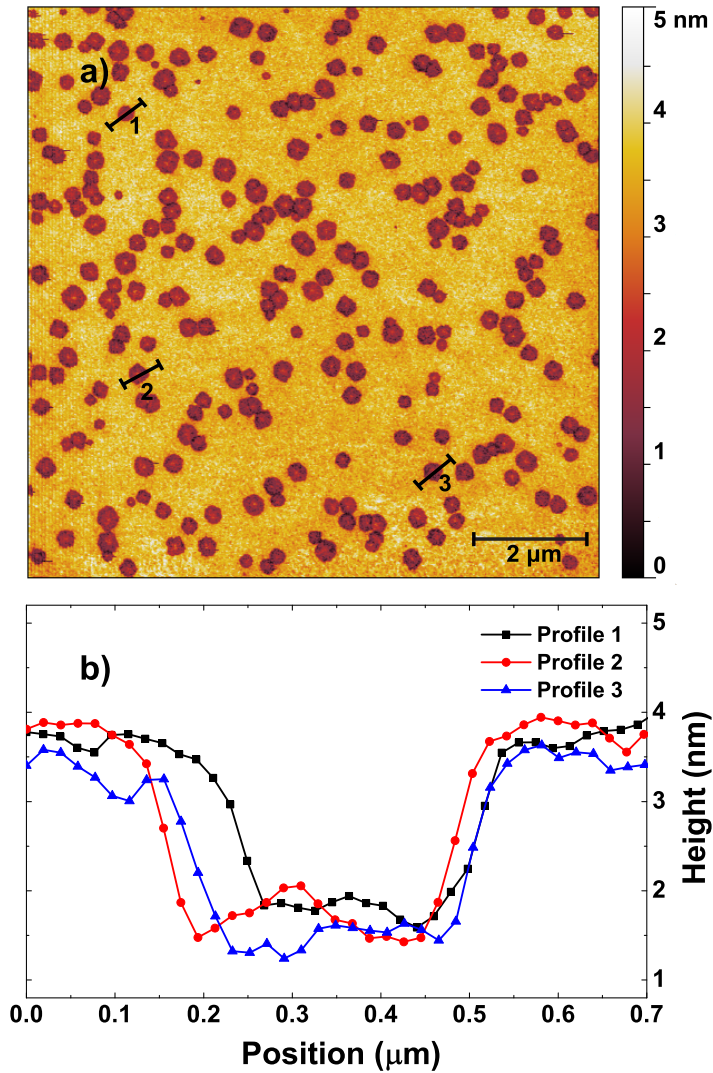**Figure 5.2:** 10 $\mu m \times$ 10 μm AFM scan of a STO film deposited on a bare Si_3N_4 TEM window with [Sr]/([Sr]+[Ti]) = 0.53 after RTA at 550 °C for 5 minutes (a) and height profiles along the three different developing crystals indicated in the AFM image (b).

minutes. In Figure 5.2.a the developing transrotational crystals are visible as disk-shaped regions with a diameter of ~ 300 nm and with a decreased thickness compared to the amorphous regions. Grain size and distribution are in excellent agreement with TEM images of samples with the same processing conditions (Figure 5.1.b). Figure 5.2.b displays the height profile along three different paths marked in Figure 5.2.a, each one crossing different single developing crystallites. The thickness difference between the crystallized and the amorphous STO is in the range of 2-2.5 nm, which is in good agreement with the decrease in thickness detected by SE. These measurements are also in good agreement with the model proposed by Kooi et al. where a thickness gradient is assumed at the crystal front [23].

The star-shaped bending contours show mainly a 3-fold or a 4-fold symmetry corresponding to specific crystallographic orientations. In particular, the centre of the star corresponds to a zone axis and the symmetry of the branches depends on the orientation of the zone axis. In particular a <001> and a <111> zone axis will show a 4-fold or a 3-fold symmetry, respectively. In this configuration, the crystal planes nearly perpendicular to the film surface giving rise to the bending contours are the planes oriented perpendicular to the orientation of the zone axis. Favia et al. performed nano-beam diffraction (NBD) on the centre and on the branches of stars with 4-fold symmetries that formed after crystallization of thin STO films [25]. Their analysis evidenced that the centre of the star corresponds to a <001> zone axis. NBD performed on the branches of the star showed diffraction patterns displaying periodicity in only one in-plane direction, implying that the bending contour contrast along a branch of the star originates from only one set of crystal planes.

Figures 5.3.a-d and 5.3.e-h show High Angle Annular Dark-Field Scanning TEM (HAADF-STEM) images of STO films with different [Sr]/([Sr]+[Ti]) ratios deposited on Al_2O_3-coated and bare Si_3N_4 windows, respectively, annealed by RTA at $600\,^{\circ}C$ for 1 minute. For these studies, HAADF-STEM imaging was preferred over BF-TEM imaging because of the excellent visibility of low-density regions (voids, nano-cracks). Instead of using a low camera length creating pure Z (atomic number) contrast, an intermediate camera length was selected to visualize both density differences as well as diffraction contrast. All layers were completely crystalline except for the STO film with [Sr]/([Sr]+[Ti]) = 0.50 deposited on Si_3N_4. A slightly lower nucleation probability was found for layers deposited on bare windows. Independently of the substrate, the microstructure of the crystallized films was found to have the same trend depending on the film composition. In particular, an increased Sr-content resulted in a smaller grain size, similar to the results obtained at $550\,^{\circ}C$ (Figure 5.1.e-f). This suggests that also
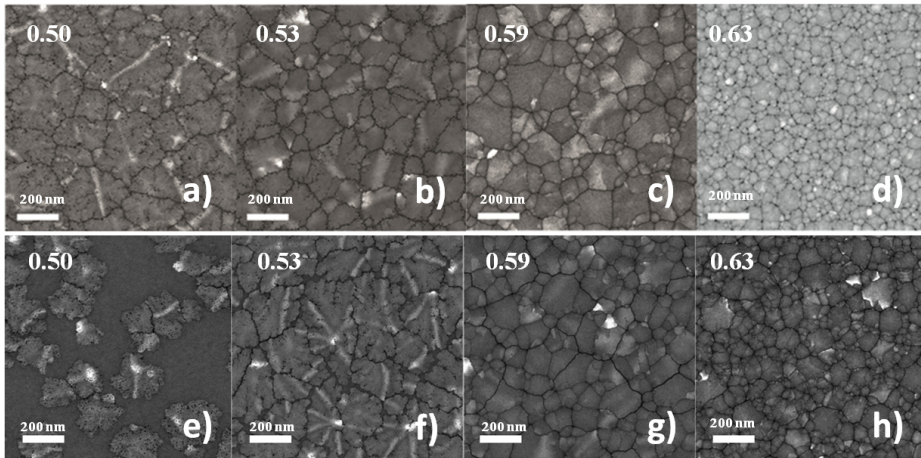
Figure 5.3: HAADF-STEM images of STO films with [Sr]/([Sr]+[Ti]) ratios ranging between 0.50 and 0.63 deposited on Al_2O_3-coated (a-d) and bare Si_3N_4 (e-h) TEM windows and annealed by RTA at $600\,^\circ$C for 1 minute.

for annealing at $600\,^\circ$C Sr-rich layers show a higher nucleation probability. Both the average size and the morphology of the crystallites changed with composition. For near-stoichiometric compositions ([Sr]/([Sr]+[Ti]) = 0.50, 0.53) (Figures 5.3.a-b, 5.3.e-f) the grains have a dendritic morphology with voids situated predominantly between the merging dendritic branches. The crystals have formed trans-rotationally with visible bending contours (white lines). For [Sr]/([Sr]+[Ti]) = 0.59 (Figures 5.3.c, 5.3.g), the crystallites showed a more regular shape. In addition, the bending contours within the grains are broader compared those which were visible for the more stoichiometric STO films, implying a reduced curvature of the crystal lattice. Kolosov et al., and Kooi et al. reported reduced internal bending for higher crystal growth rates [23,24]. This indicates that Sr-rich STO shows a higher nucleation probability as well as an increased crystal growth rate. For films with the highest Sr-content ([Sr]/([Sr]+[Ti]) = 0.63, (Figures 5.3.d and 5.3.h) the average grain size is further decreased and the bending contours related to the transrotational structure are no longer present.

Figure 5.4.a-d shows high magnification HAADF-STEM images of the samples with different compositions deposited on Al_2O_3-coated windows (cf. Figures 5.3.a-d). For near-stoichiometric films ([Sr]/([Sr]+[Ti]) = 0.50, 0.53) nano-cracks were formed at the grain boundaries and voids (black dots) with a diameter of a few nanometers were found within the crystals. For increased Sr-content ([Sr]/([Sr]+[Ti]) = 0.59) the voids were only
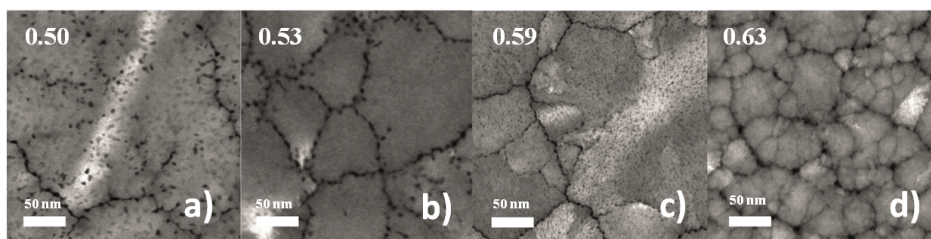
Figure 5.4: High magnification HAADF-STEM images of STO films with [Sr]/([Sr]+[Ti]) ratios ranging between 0.50 and 0.63 deposited on Al_2O_3-coated TEM windows and annealed by RTA at $600\,^\circ$C for 1 minute.
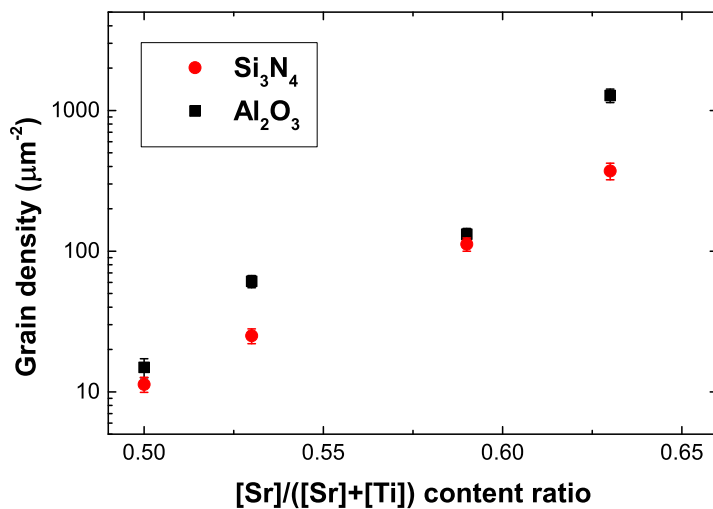

Figure 5.5: Grain density of STO films deposited on bare Si_3N_4 and Al_2O_3-coated TEM windows with different [Sr]/([Sr]+[Ti]) content ratios after RTA for 1 minute at $600\,^\circ$C.

present at the grain boundaries while small pores (> 1 nm) within the grain appeared. The film with [Sr]/([Sr]+[Ti]) = 0.63 showed a similar microstructure with voids formed between clusters of grains with even smaller average size. These higher resolution images also revealed changes in the structure of the grain boundaries. Well defined single grains separated by nano-cracks could be identified for near-stoichiometric layers. The films with increased Sr-content are characterized by clusters of closely packed crystals separated by voids.

Figure 5.5 shows the grain density of STO films deposited on the bare and Al_2O_3-coated Si_3N_4 TEM windows upon a 1 minute RTA anneal at 600 °C. For both substrates the trend was similar: an exponential increase in grain density as a function of Sr-content was found in the compositional range studied. As shown in Figure 5.3, this increase in grain density is due to a transition from growth-dominated to nucleation-dominated in the crystallization process when the Sr-content is increased. On both substrates an average grain size of $\sim$ 50 nm was found for the films with a [Sr]/([Sr]+[Ti]) ratio of 0.63. This is in good agreement with literature results for STO layers with [Sr]/([Sr]+[Ti]) = 0.62 deposited on TiN [13,14]. Apart from the film on Si_3N_4 with [Sr]/([Sr]+[Ti]) = 0.50 (50 % crystalline) all samples were fully crystalline after 1 minute RTA.

Figure 5.6.a shows the influence of the RTA temperature on the grain for STO films with [Sr]/([Sr]+[Ti]) = 0.53. Higher anneal temperatures lead to an increased nucleation probability and, consequently a higher grain density. In particular, the annealing temperature range from 550 °C to 650 °C results in a difference of more than two orders of magnitude in the grain density. It should be noted that an RTA of 1 minute at 550 °C only yields a low degree of crystallinity, as shown in Fig. 1.a. Figure 5.6.b shows the evolution of the grain density over annealing time for the RTA at 550 °C. A grain density of $\sim$ 3 μm^{-2} was achieved for both substrates after 10 minutes leading to nearly fully crystallized layers (Fig. 1.c). This grain density is nearly one order of magnitude lower as compared to higher temperature anneals illustrating the difference between the growth-dominated crystallization process at 550 °C and the nucleation-dominated crystallization at higher annealing temperatures.

GI-XRD was performed on STO films with [Sr]/([Sr]+[Ti]) = 0.53 and 0.63 deposited on Si samples coated with 20 nm Al_2O_3 to determine the crystalline structure after RTA. This substrate was used since GI-XRD on TEM windows was not possible due to size restrictions. The GI-XRD spectra of STO film after RTA with different thermal budgets with [Sr]/([Sr]+[Ti]) = 0.53 and 0.63 are shown in Figure 5.7.b and 5.7.c. The STO film with [Sr]/([Sr]+[Ti]) = 0.53 annealed at 550 °C for 1 minute was amorphous. Increasing the RTA time to 10 minutes resulted in the full crystallization of the layer. This is in
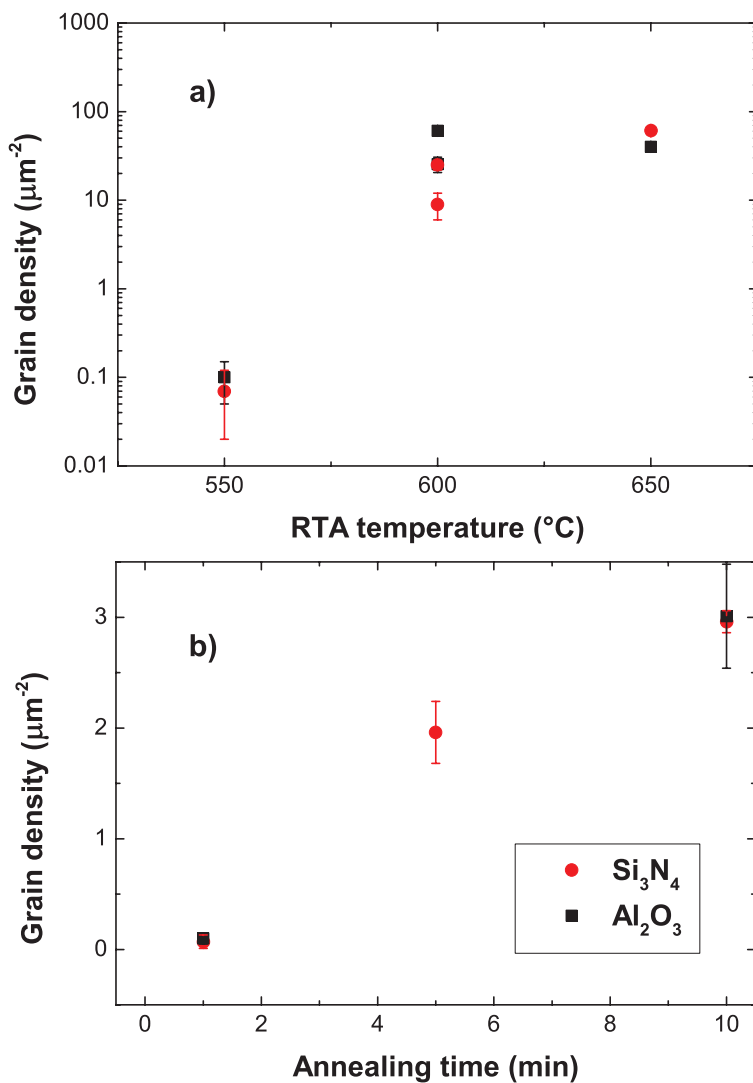
Figure 5.6: Grain density of STO films with [Sr]/([Sr]+[Ti]) = 0.53 on bare and Al_2O_3-coated Si_3N_4 TEM windows after RTA for 1 minute at annealing temperatures ranging from $550\,^{\circ}$C to $650\,^{\circ}$C (a) and its evolution over annealing time for the RTA at $550\,^{\circ}$C (b).

agreement with the TEM results reported above (Figure 5.1.a-c) where only a few nuclei were formed at this temperature after 1 minute RTA. The film with [Sr]/([Sr]+[Ti]) = 0.63 was fully crystalline after 1 min RTA at 550 °C. This confirms that for higher Sr-content a higher degree of crystallization is achieved compared to the more stoichiometric STO films. No remarkable difference was found between the GI-XRD spectra of the Sr-rich films for the different thermal budgets applied. This suggests that for this composition, the film is rapidly crystallized and a comparable microstructure is achieved due to a high nucleation probability at both temperatures.

Regardless of the film composition, only diffraction peaks corresponding to the STO perovskite structure were detected [26]. For the film with [Sr]/([Sr]+[Ti]) = 0.63 the diffraction peaks shifted to lower angles. This suggests that, for the annealing temperatures employed in this work, the excess of Sr is not segregating, but accommodated in the perovskite structure resulting in an expansion of the unit cell parameter. Menou et al. reported a similar shift of the diffraction peaks due to increased Sr-content in the STO film [13]. In the same work, it was also shown that no Ruddlesden-Popper phases were observed for annealing temperature up to 700 °C [13]. It was suggested that the excess Sr was in solution in the perovskite structure and that the Sr was only expelled out of the grains for high annealing temperatures (> 700 °C).

5.4 Conclusions

The influence of the thermal budget applied during rapid thermal annealing and of the elemental composition on the crystallization behavior of thin STO films deposited by plasma-assisted ALD was investigated. The grain size and crystallite density strongly depend on the film composition in the compositional range examined (([Sr]/([Sr]+[Ti]) from 0.50 to 0.63) with a decreasing grain size achieved when more Sr is incorporated in the layer. This was imputed to the higher nucleation probability for Sr-rich layers. This trend was found to be independent of the substrate used (Si_3N_4 or Al_2O_3). The nucleation probability appears to exhibit a stronger temperature dependency than the crystal growth rate, leading to a higher grain density, i.e. smaller grain size, at higher annealing temperatures. Furthermore, the microstructure of the films and the distribution of the voids within one single crystal and of nano-cracks at the grain boundaries were found to be dependent on the film stoichiometry. Nearly stoichiometric films ([Sr]/([Sr]+[Ti]) = 0.50, 0.53) showed transrotational crystals with voids formed within the single grains and nano-cracks at the grain boundaries. The bending of the lattice planes was reduced for higher Sr-contents due to the higher crystal growth rate. Increasing the Sr-content
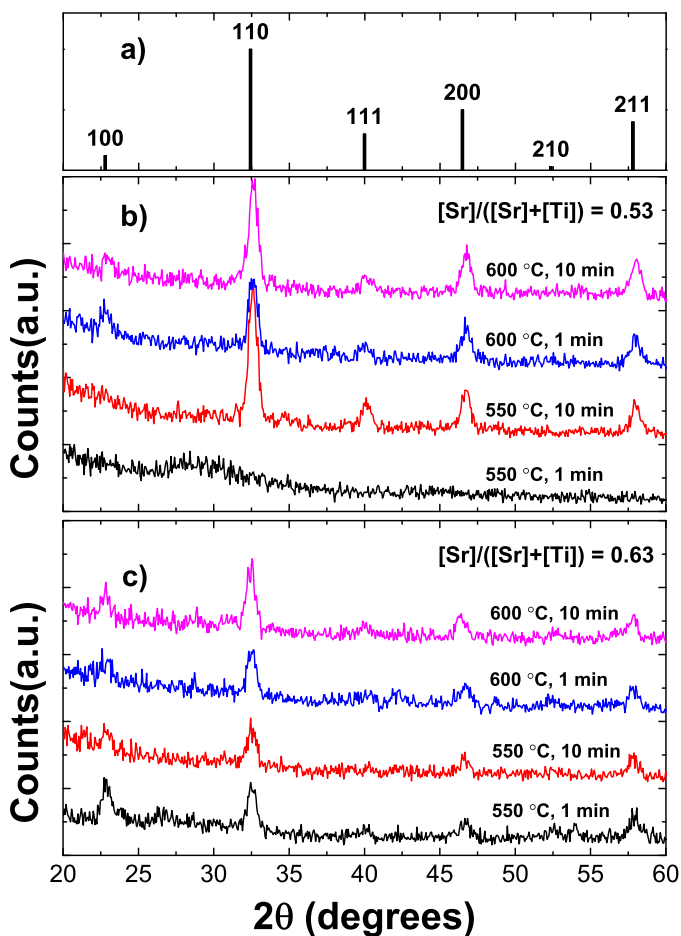
Figure 5.7: The diffraction spectrum for the SrTiO$_3$ perovskite structure [26] reported as a reference (a) for the GI-XRD spectra of STO films with [Sr]/([Sr]+[Ti])=0.53 (b) and 0.63 (c) deposited on 20 nm Al$_2$O$_3$/Si samples after RTA at 550 °C and 600 °C for 1 and 10 minutes.

resulted in a smaller size of the pores formed within one single crystallite (< 1 nm for ([Sr]/([Sr]+[Ti]) = 0.59 and 0.63) and in a more compact microstructure. We demonstrated that by choosing the thermal budget applied during the annealing step as well as the film composition it is possible to change the grain size, crystallites morphology and the distribution of voids and cracks. With these insights, these parameters can be tailored to obtain the microstructure which is most suitable for the specific application in which the STO film is used.

Acknowledgments

5.5   Addendum: Transrotational Crystals

The star-shaped patterns identified in the STO thin films after RTA at $550\,^\circ$C reported in the BF-TEM images in Figure 5.1 are characteristic of the transrotational structure. They were first identified and studied by Kosolov et al. for thin Fe_2O_3 films [24]. Later, more materials were found exhibiting this morphology, such as the GeSbTe alloys used in phase change recording media and in phase change memories [23].

These star patterns consist of a center of the "star" corresponding to a certain crystallographic zone axis and star branches representing the symmetry of this axis oriented parallel to the electron beam, as will be explained in more detail below. As explained in Chapter 3, the contrast in BF-TEM images is dependent on the orientation of the crystal with respect to the electron beam. A perfect crystal will display one grey-scale in the TEM image over its entire projected area. Imperfections in the crystal, such as bending of the lattice, will yield variations in contrast. The branches in the star-shaped patterns are caused by local variations in crystallographic orientation. They are also known as bending contours (BC), being an indication of local bending of the lattice.

As mentioned above in this chapter, the contraction term transrotational was introduced by Kosolov et al. to describe both the translation and the rotation of the crystal
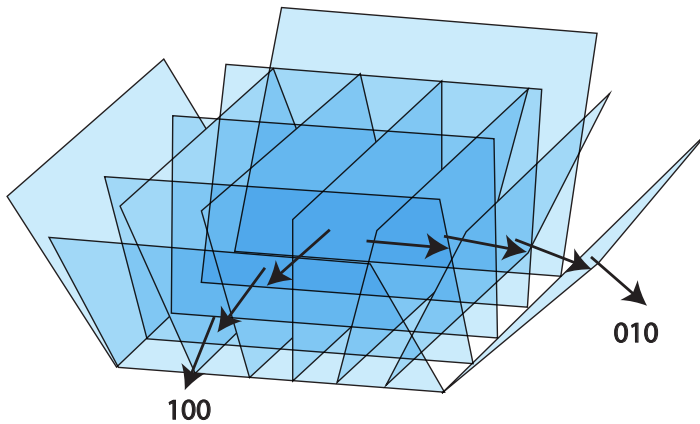
Figure A.5.1: Visual representation of the <100> and <010> lattice planes of an STO crystal in a transrotational crystal.

planes during the crystal growth [24]. A visual representation of crystal transrotation is shown in Figure A.5.1 where the bending of the <100> and <010> lattice planes of an STO crystal is illustrated.

The internal lattice plane bending is introduced during film densification upon the solid-state crystallization of layers deposited in the amorphous state. The abovementioned model of Kooi et al. proposes an explanation for the formation of such a crystalline structure and is shown in Figure A.5.2 [23]. Due to the increase in density upon the amorphous-crystalline phase transformation, the film thickness is reduced into the direction perpendicular to the film surface, (i.e. the only one in which the film is not constrained). This is illustrated by the thickness profile in Figure A.5.2.a. The initial situation, with a crystallized region with lattice planes oriented parallel to the film/substrate interface, is shown in Figure A.5.2.a. At the crystal front, the densification has not come to full completion, leaving room available for nucleation at the top interface (Fig. A.5.2.b). With the crystal front advancing, these newly formed planes are bent due to the shrinkage in the vertical direction (Fig. A.5.2.c). This model is in agreement with results from the literature [28-30] where nucleation was proven to occur at the top interface instead of at the film/Si_3N_4 interface.

The star-shaped patterns arise from the various symmetry operations (n-fold rotation axes, mirror planes) present in the cubic STO crystal structure. Thus the symmetry of the pattern will depend on the orientation of a crystal with respect to the electron beam. For example, a <001> zone axis will yield a 4-fold symmetry while a <111> zone axis will
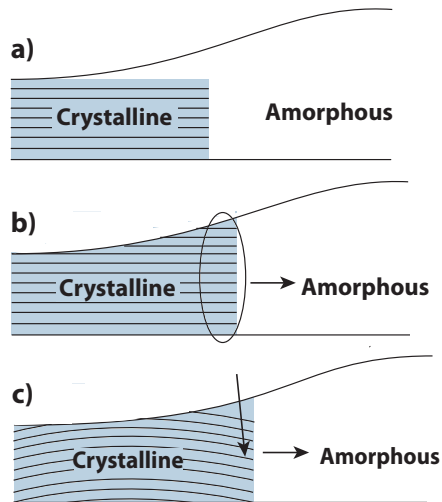
Figure A.5.2: Representation of the mechanism responsible for the formation of transro-
tational crystals, adapted from ref. [23]. A thickness profile is present at the crystalline-
amorphous interface (a). New lattice planes nucleate at the top surface (b) and are then
"pushed" down by densification of the film upon amorphous-crystalline transition (c).
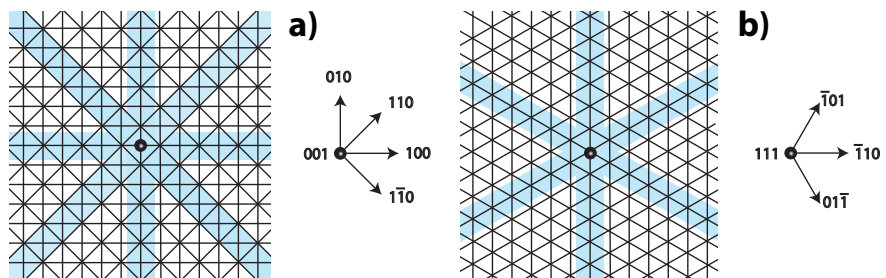
Figure A.5.3: Representation of lattice planes perpendicular to the sample surface for
<001> (a) and <111> (b) oriented crystals. The upward arrows represent the crystallo-
graphic axis parallel to the electron beam. The lattice planes parallel to these zone axes
are highlighted to evidence the crystal symmetries.

Figure A.5.4: BF-TEM top view images of a <100> STO crystallite with transrotational structure at two slightly different orientations of the sample before (a) and after (b) tilting of the sample over 1 $^{\circ}$.

result in a 3-fold symmetry. As the TEM images of the STO films are acquired in top view, the crystallographic axis parallel to the surface normal det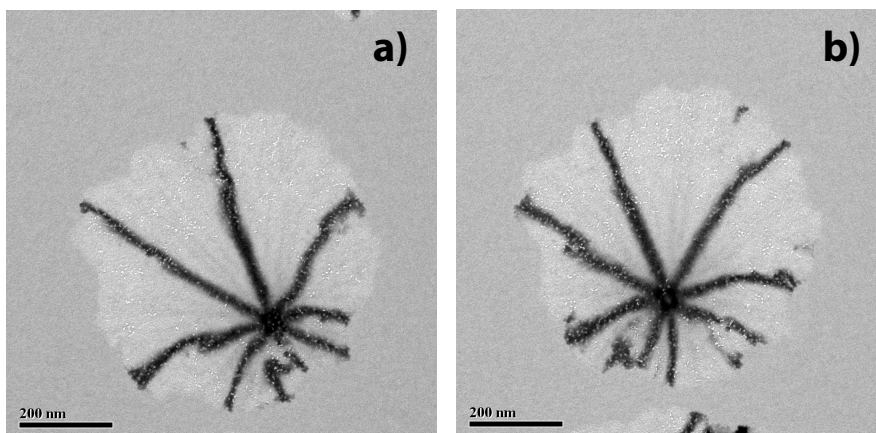ermines the symmetry of the star-shaped pattern. Figures A.5.3.a and b show two representative cases corresponding to crystals having their <001> and <111> zone axes parallel to the surface normal. A schematic "top view" of the set of lattice planes perpendicular to the sample surface is shown. The arrows point out of the film plane represent the zone axes.

To imagine the transrotational structure observed in the STO films, one can think of deforming the patterns in Figure A.5.3 by keeping the central axis fixed and "bending" all lattice planes away from this away from this central axis. As explained above, areas will appear dark in a BF-TEM image when the crystal locally is in a strongly diffracting orientation. This requirement is fulfilled when lattice planes are oriented parallel to the electron beam. In the centre of the patterns in Figure A.5.3, this requirement is fulfilled for several sets of lattice planes, resulting in the dark, central spot in the star-shaped pattern. In addition, the transrotational crystal contains zones in which one set of lattice planes 'crosses' the zone axis (i.e. one set of planes is still parallel to the electron beam), as highlighted in Figure A.5.3, while the other sets of lattice planes are tilted. As Bragg's law is satisfied for a set of planes 'crossing' the zone axis, a dark line will appear in the BF-TEM image. Adding up all these diffracting sets of planes results in the patterns evidenced in Figure A.5.3.

As mentioned above, the star patterns in Figure 5.1 contain a center of the "star" corresponding to a zone axis and, for STO, 6 or 8 star branches representing the symmetry of the crystallographic axis oriented parallel to the electron beam. By tilting the sample, the original centre of the pattern will no longer be parallel to the electron beam. However, another position in the crystal will now be oriented parallel to the electron beam and, as a result, the star-shaped pattern will move accordingly in the TEM image. Figure A.5.4.a and b show BF-TEM top view images of an STO crystallite, embedded in the surrounding amorphous matrix, before and after tilting of the sample, respectively, over $1°$. As explained, by tilting of the sample the zone axis and the star-shaped pattern have shifted. In particular, the star-shape pattern is conserved with the same 4-fold symmetry and with the star branches aligned along the same directions before and after tilting. Measuring the shift of this centre as a function of sample tilt allows for a quantitative analysis of the crystal curvature.

Finally, the influence of the crystal growth rate on the transrotational crystal structure is discussed. It has been reported that for lower crystal growth rates the bending of the lattice planes is increased [23,24]. The reason for this phenomenon can be understood by referring to the above mentioned model proposed by Kooi et al. Assuming that the nucleation of new planes at the top surface is a constant in time, for fast crystal growth the density of such planes is decreased since the crystal front is advancing faster upon decreasing the time for new planes to nucleate. For these conditions the tilt of the lattice planes is then less pronounced. This is in agreement with our results where STO films crystallized by RTA at $550°$ (Figure 5.1) showed sharp star-patterns, while for RTA at $600°$ (Figure 5.3) these patterns appeared broadened indicating a lower degree of internal bending due the faster crystal growth rate at higher temperatures. Furthermore, Sr-rich STO films, which showed higher nucleation probability and higher crystal growth rates than more stoichiometric films, grew with a less pronounced tilt of the lattice planes compared to more stoichiometric films annealed at the same conditions.

5.6   References

1. R. Wödenweber, E. Hollmann, M. Ali, J. Schubert, G. Pickartz and T.K. Lee, *J. Eur. Ceram. Soc.*, 27, 2899 (2007).

2. Y.S. Kim, D.J. Kim, T.H. Kim, T.W. Noh, J.S. Choi, B.H. Park and J.G. Yoon, *Appl. Phys. Lett.*, 91, 042908 (2007).

3. D. Marré, A. Tumino, E. Bellingeri, I. Pallecchi, L. Pellegrino and A.S. Siri, *J Phys. D Appl. Phys.*, 36, 896 (2003).

4. F.M. Pontes, E.J.H. Lee, E.R. Leite and E. Longo, *J. Mater. Sci.*, 35, 4783 (2000).

5. R. Muenstermann, T. Menke, R. Dittmann, S. Mi, C.L. Jia, D. Park and J. Mayer, *J. Appl. Phys.*, 108, 124504 (2010).

6. K. Szot, R. Dittmann, W. Speier and R. Waser, *Phys. Status Solidi RRL*, 1, R86 (2007).

7. X. B. Yan, Y. D. Xia, H.N. Xu, X. Gao, H.T. Li, R. Li, J. Yin and Z.G. Liu, *Appl. Phys. Lett.*, 97, 112101 (2010).

8. T. Hara and T. Ishiguro, *J. Ceram. Soc. Jpn.*, 118, 300 (2010).

9. T. Hara and T. Ishiguro, *Sensor. Actuat. B- Chem.*, 136, 489 (2009).

10. M.S. Kim, M. Popovici, J. Swerts, M.A. Pawlak, K. Tomida, B. Kaczer, K. Opsomer, M. Schaekers, H. Tielens, C. Vrancken, S. van Elshocht, I. Debusschere, L. Altimime and J. A. Kittl,

11. 3rd IEEE International Memory Workshop (2011).

12. M.A. Pawlak, M. Popovici, J. Swerts, K. Tomida, M.S. Kim, B. Kaczer, K. Opsomer, M. Schaekers, P. Favia, H. Bender, C. Vrancken, B. Govoreanu, C. Demeurisse, W.C. Wang, V.V. Afanas'ev, I. Debusschere, L. Altimime and J.A. Kittl, *IEDM* 2010.

13. M.A. Pawlak, B. Kaczer, M.S. Kim, M. Popovici, J. Swerts, W.C. Wang, K. Opsomer, P. Favia, K. Tomida, A. Belmonte, B. Govoreanu, C. Vrancken, C. Demeurisse, H. Bender, V.V. Afanas'ev, I. Debusschere, L. Altimime and J.A. Kittl, *Appl. Phys. Lett.*, 98, 182902 (2011).

14. N. Menou, M. Popovici, S. Clima, K. Opsomer, W. Polspoel, B. Kaczer, G. Rampelberg, K. Tomida, M.A. Pawlak, C. Detavernier, D. Pierreux, J. Swerts, J.W. Maes, D. Manger, M. Badylevich, V.V. Afanas'ev, T. Conard, P. Favia, H. Bender, B. Brijs, W. Vandervorst, S. van Elshocht, G. Pourtois, D.J. Wouters, S. Biesemans and J.A. Kittl, *J. Appl. Phys.*, 106, 094101 (2009).

15. M.A. Pawlak, B. Kaczer, M.S. Kim, M. Popovici, K. Tomida, J. Swerts, K. Opsomer, W. Polspoel, P. Favia, C. Vrancken, C. Demeurisse, W.C. Wang, V. V. Afanas'ev, W. Vandervorst, H. Bender, I. Debusschere, L. Altimime and J. A. Kittl, *Appl. Phys. Lett.*, 97, 162906 (2010).

16. S. Clima, G. Pourtois, N. Menou, M. Popovici, A. Rothschild, B. Kaczer, S. van Elshocht, X.P. Wang, J. Swerts, D. Pierreux, S. De Gendt, D.J. Wouters and J.A. Kittl, *Microelectron. Eng.*, 86, 1936 (2009).

17. S.K. Kim, S.W. Lee, J.H. Han, B. Lee, S. Han and C.S. Hwang, *Adv. Func. Mat.*, 20, 2989 (2010).

18. M. Popovici, S. van Elshocht, N. Menou, J. Swerts, D. Pierreux, A. Delabie, B. Brijs, T. Conard, K. Opsomer, J.W. Maes, D.J. Wouters and J. A. Kittl, *J. Electrochem. Soc.*, 157, G1 (2010).

19. M. Popovici, S. van Elshocht, N. Menou, P. Favia, H. Bender, E. Rosseel, J. Swerts, C. Adelmann, C. Vrancken, A. Moussa, H. Tielens, K. Tomida, M.A. Pawlak, B. Kaczer, G. Schoofs, W. Vandervorst, D.J. Wouters and J.A. Kittl, *J. Vac. Sci. Technol. B*, 29, 01A304 (2011).

20. P. Favia, M. Popovici, G. Eneman, G. Wang, M.B. Gonzalez, E. Simoen, N. Menou and H. Bender, *ECS Trans.*, 33(11), 205 (2010).

21. J.A. Kittl, K. Opsomer, M. Popovici, N. Menou, B. Kaczer, X.P. Wang, C. Adelmann, M.A. Pawlak, K. Tomida, A. Rothschild, B. Govoreanu, R. Degraeve, M. Schaekers, M. Zahid, A. Delabie, J. Meersschaut, W. Polspoel, S. Clima, G. Pourtois, W. Knaepen, C. Detavernier, V.V. Afanas'ev, T. Blomberg, D. Pierreux, J. Swerts, P. Fischer, J.W. Maes, D. Manger, W. Vandervorst, T. Conard, A. Franquet, P. Favia, H. Bender, B. Brijs, S. van Elshocht, M. Jurczak, J. van Houdt and D.J. Wouters, *Microelectron. Eng.*, 86, 1789 (2009).

22. V. Longo, N. Leick, F. Roozeboom and W.M.M. Kessels, *ECS J. Solid State Sci. Technol.*, 2(1), N15 (2013).

23. V. Longo, N. Leick, F. Roozeboom and W.M.M. Kessels, *ECS Trans.*, 41(2), 63 (2011).

24. B.J. Kooi and J.T. De Hosson, *J. Appl. Phys.*, 95, 4714 (2004).

25. V.Y. Kolosov and A.R. Thölén, *Acta Mater.*, 48, 1829 (2000).

26. P. Favia, M.B. Gonzales, E. Simoen, P. Verheyen, D. Klenov and H. Bender, *J. Electrochem. Soc.*, 158, H438 (2011).

27. Powder Diffraction File, Card No 35-0734, International Centre for Diffraction Data, Newton Square, PA.

28. B.J. Kooi, W.M.G. Groot and J.T. De Hosson, *J. Appl. Phys.*, 95, 924 (2003).

29. T.H. Jeong, M.R. Kim, H. Seo, S.J. Kim and S.Y. Kim, *J. Appl. Phys.*, 86, 774 (1999).

30. N. Ohshima, *J. Appl. Phys.*, 79, 8357 (1996).

Chapter 6

ALD of SrTiO$_3$ and Pt for Pt/SrTiO$_3$/Pt MIM structures: Growth and Crystallization study[*]

Abstract   Metal-insulator-metal (MIM) structures with ultrahigh-k strontium titanate films (SrTiO$_3$, STO) and Pt as the dielectric and electrode material, respectively, have been prepared by ALD. The MIM structures were prepared with near-stoichiometric and Sr-rich ([Sr]/([Sr]+[Ti]) = 0.54 and 0.63, respectively) with a thickness of 15 nm. The influence of the rapid thermal annealing step at 600 °C in flowing N$_2$, required to crystallize the STO, on the crystalline microstructure of the Pt bottom electrode and of the STO films has been investigated. Transmission electron microscopy and electron diffraction analysis evidenced that the morphology of the Pt bottom electrode is influenced by thermal treatment. Locally, an epitaxial relation between the <111> textured Pt and the STO film could be found. However, X-ray and electron diffraction analysis showed that the STO crystalline grains were mainly randomly oriented. Top view TEM analysis revealed that the near-stoichiometric STO thin films deposited on Pt have a crystallization behavior comparable to those deposited on Al$_2$O$_3$, with nano-crack formation at the grain boundaries and an average grain size of $\sim$ 100 nm.

6.1   Introduction

Metal-insulator-metal (MIM) structures form the basic building block of the state-of-the-art capacitors used in many applications in the electronics industry. For example, MIM devices are employed in the dynamic-random access memories (DRAM) technology as the memory element and in the back-end of line integration as decoupling or analog-to digital conversion capacitors. Furthermore, the implementation of resistive switching devices is also based on MIM structures with the insulating film being the active resistive element. For implementation of MIM capacitors with high capacitance densities the employment of ultrahigh-k dielectric materials is envisioned. Strontium titanate (SrTiO$_3$, STO) is a dielectric material which exhibits many interesting properties due to its perovskite crystalline structure (i.e. ferroelectricity, paraelectricity, restive switching behavior, etc.). Among these, its ultrahigh-k value ($\approx$ 300 for the bulk material) makes STO one of the favorite candidates for the dielectric material in next generation DRAM [1-3]. Atomic layer deposition (ALD) is the method of choice for the deposition of both the conductive electrode and the dielectric material in the aforementioned applications since conformal layers over high aspect ratio structures with extreme thickness control will be required to reach sufficiently high capacitance densities. When deposited by ALD, STO thin films are amorphous and require a thermal annealing step to achieve ultrahigh-k values. Usually, for the electrode material, high work function materials such as Pt and Ru are investigated to contain the leakage current through the STO film by increasing the potential barrier at the metal-dielectric interface [4-10]. In particular, better leakage current performance was obtained for Pt than for other electrode materials employed in DRAM manufacturing such as TiN [11]. For further optimization of the performance of MIM structures it is crucial to investigate the microstructural transformation that both materials, dielectric and metal electrode, undergo during the manufacturing steps. In particular, the thermal annealing step required to crystallize the amorphous STO into ultrahigh-k perovskite films can also affect the underlying metallic film and influence the crystallization behavior of the STO itself. In our previous work we addressed the influence of the cation composition and of the thermal budget on the crystallization behavior of STO films deposited on Al$_2$O$_3$ and Si$_3$N$_4$ [12]. In this work, we have fabricated full MIM Pt/STO/Pt structures by ALD with the aim to study the influence of a functional Pt bottom electrode layer on the crystallization process of STO as well as the influence of the thermal annealing on the electrode itself. In particular, we have addressed the differences in texture of the bottom Pt before and after the thermal annealing treatment and the relation between the crystalline microstructure of the Pt and the STO film. The presen-

ted results are also compared with our previous results obtained for STO deposited on Al_2O_3. This work is of interest for applications where the implementation of STO films sandwiched between Pt electrodes is envisioned as well as for other applications where a Pt film is employed underneath an STO thin film, e.g. in non-symmetric MIM structures for resistive switching applications.

6.2   Experimental details

The Pt films of 20 nm thickness were prepared by plasma-assisted ALD at 300 °C on thermally grown SiO_2 (450 nm)/Si substrates, in an Oxford Instruments FlexAL™ ALD reactor, employing methylcyclopentadienyl-trimethylplatinum ($MeCpPtMe_3$) and an O_2 plasma [13-15]. Pt films of 13 nm in thickness were also deposited under the same conditions on Si_3N_4 membranes for TEM analysis. STO thin films with a nominal thickness of 15 nm were deposited by plasma-assisted ALD, in the same ALD reactor, at 350 °C on the Pt-coated substrates. Cyclopentadienyl-based precursors, namely Ti-Star, (pentamethylcyclopentadienyl)-trimethoxy-titanium, $CpMe_5Ti(OMe)_3$ and Hyper-Sr, bis(tri-isopropylcyclopentadienyl)-strontium with 1,2-dimethoxyethane adduct, Sr-$(^iPr_3Cp)_2DME$, both from Air Liquide, were combined with an O_2 plasma for the SrO and TiO_2 ALD processes. The STO films were deposited by mixing SrO and TiO_2 ALD cycles. In this study, two STO compositions (near-stoichiometric and Sr-rich) were prepared by tuning the $[SrO]/[TiO_2]$ ALD cycle ratio [16]. To obtain full MIM structures, the top Pt electrode layer ($\sim$ 20 nm) was deposited by thermal ALD at 300 °C from $MeCpPtMe_3$ and O_2 gas [15]. In this case, thermal ALD was preferred over the plasma-assisted process to avoid any damage to the crystalline STO films. The thickness of the Pt and STO films was determined by spectroscopic ellipsometry (SE) (M2000D, J.A. Wool-lam, 1.25-6.5 eV) [16]. The elemental composition of the STO films was also extracted from the SE data by means of an optical constant library which was calibrated by means of Rutherford backscattering experiments [16]. The $[SrO]/[TiO_2]$ ALD cycle ratios, film thicknesses and $[Sr]/([Sr]+[Ti])$ ratios of the STO films examined in this study are listed in Table 6.1. The STO/Pt stacks were annealed, before the top Pt film deposition, by rapid thermal annealing (RTA in a JetFirst100 system from Jipelec) at 600 °C in flowing N_2 with annealing times ranging from 1 to 10 minutes to crystallize the STO films into the perovskite structure.

TEM studies were performed using a TECNAI F30ST TEM operated at 300 kV. Both Bright-Field (BF) TEM and Dark-Field (DF) TEM modes were employed to characterize the samples. For cross-sectional TEM analysis the MIM structures were coated
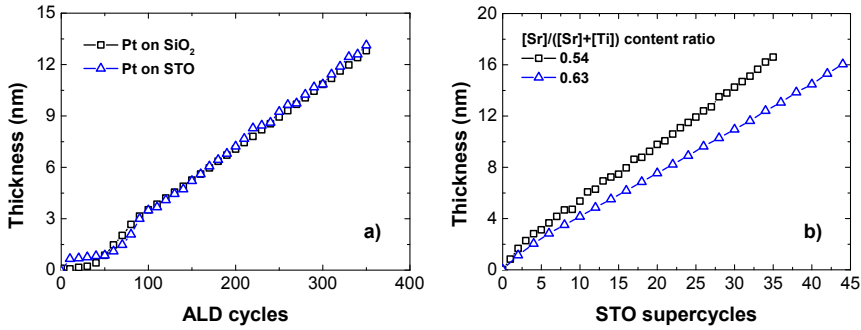
Figure 6.1: Thickness evolution as a function of number of ALD cycles as measured by in-situ SE of Pt on STO and on SiO_2 (a) and of STO ($[Sr]/([Sr]+[Ti]) = 0.54$ and 0.63) on Pt-coated substrates prepared by ALD (b). For the deposition of Pt and STO films plasma-assisted ALD was employed.

by ALD with a 50 nm Al_2O_3 protective layer. Electron diffraction (ED) was employed to determine the crystalline microstructure of the analysed films. X-ray photoelectron spectroscopy (XPS) depth profiles of the STO/Pt layer stacks and of the complete MIM structures were performed on a Thermo Scientific K-Alpha KA1066 spectrometer using monochromatic Al K_α X-ray radiation ($h\nu = 1486.6$ eV). A 400 μm diameter X-ray spot was used in the analysis and photoelectrons were collected at a take-off angle of $60\,^\circ$. The samples were neutralized using an electron flood gun to correct for differential or non-uniform charging. An Ar^+ ion beam (500 eV) was used to etch the samples for depth profile analysis. Grazing-incidence X-ray diffraction (GI-XRD) measurements were performed to determine the crystallinity of the STO films on a Panalytical X'Pert PRO MRD employing Cu K_α radiation.

6.3   Results and discussion

The ALD growth behavior of STO on Pt and that of Pt on STO were investigated by means of in-situ SE. Figure 6.1.a shows the evolution of thickness with the number of ALD cycles of Pt films deposited by plasma-assisted ALD on STO and on SiO_2. The growth behavior of Pt on SiO_2 is included as a reference. The Pt film growth showed a nucleation delay of ~ 50 cycles and a growth-per-cycle (GPC) ≈ 0.04 nm/cycle for both substrates. These results are consistent with previous results from our group on plasma-assisted ALD of Pt [13-15]. The evolution of the thickness of near-stoichiometric

Table 6.1: [SrO]/[TiO$_2$] ALD cycle ratio, thickness and [Sr]/([Sr]+[Ti]) ratio of the STO films. The thickness of the films and the [Sr]/([Sr]+[Ti]) ratio were determined from spectroscopic ellipsometry [16]. The errors in thickness and in the [Sr]/([Sr]+[Ti]) ratio are $\pm$ 0.50 nm and $\pm$ 0.03, respectively.

[SrO]/[TiO$_2$] ALD cycle ratio	Thickness (nm)	[Sr]/([Sr]+[Ti]) ratio
2:5 mixed *	15.4	0.53
2:3	15	0.63

([Sr]/([Sr]+[Ti]) = 0.54) and Sr-rich ([Sr]/([Sr]+[Ti]) = 0.63) STO thin films was monitored by in-situ SE on Pt-coated substrates prepared by plasma-assisted ALD (Figure 6.1.b). The thickness evolution of the STO films showed a linear behavior with no nucleation delay. The difference in GPC between the two STO compositions is due to the different amount of total TiO$_2$ and SrO ALD cycles in an STO supercycle. The STO films deposited had thicknesses and compositions values (cf. Table 6.1) comparable to those reported in our previous work for STO films deposited on Al$_2$O$_3$ and Si$_3$N$_4$ [12].

Figure 6.2 shows the XPS depth profiles of insulator-metal (IM) STO/Pt stacks (Pt deposited by ALD on SiO$_2$) with as-deposited STO (a,b) and of full MIM Pt/STO/Pt structures with crystallized STO after RTA at 600 °C for 10 minutes (c,d), for the two STO compositions studied. The composition of the films was uniform throughout the layers and showed no remarkable changes after the RTA step. The small C-content ($\sim$ 3% for near-stoichiometric STO, and $\sim$ 5% for Sr-rich STO) in the amorphous STO layers in the IM stacks can be attributed to the deposition process and the adsorption of carbonaceous species. This contamination was completely removed after the RTA treatment. As can be seen the required time to etch the STO film during XPS depth profiling was reduced once the films were annealed. This is consistent with a $\sim$ 15% thickness reduction due to the STO crystallization [12,16]. The interfaces between the STO and Pt were sharp and did not suffer from interdiffusion or phase segregation upon thermal treatment.

A lamella for cross-sectional TEM analysis was prepared from the MIM Pt/STO/Pt structure grown with the Sr-rich STO composition as reported in Figure 6.2.d. Figure 6.3 shows BF-TEM (a) and DF-TEM (b) images of this structure. The three films in the Pt (19nm)/STO (15 nm)/Pt (19 nm) structure can be identified as well as the underlying SiO$_2$ substrate and the Al$_2$O$_3$ protective layer deposited on top of the MIM stack. In DF-TEM imaging, the bright regions corresponds to crystals oriented in a strongly dif-

---

*SrO and TiO$_2$ ALD cycles mixed as much as possible. [SrO]/[TiO$_2$] ALD cycle ratio 2:5 mixed corresponds to the following ALD cycle sequence: 1SrO, 2 TiO$_2$, 1 SrO, 3 TiO$_2$ [16].
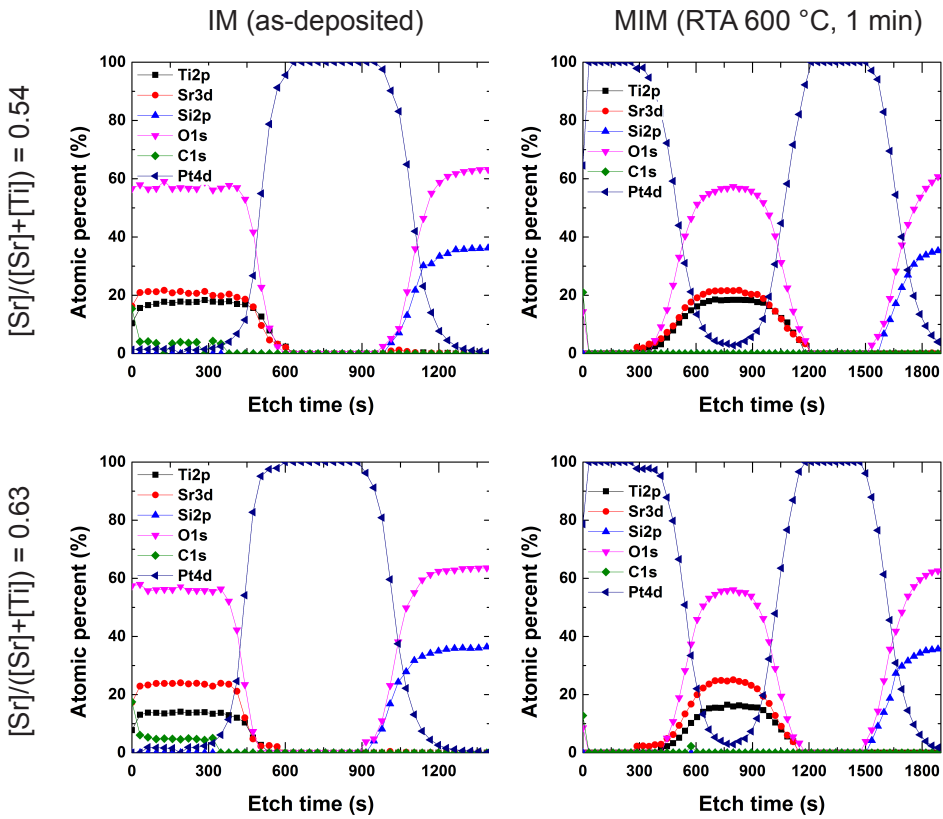
Figure 6.2: XPS depth profiles of as-deposited STO on Pt (([Sr]/([Sr]+[Ti]) = 0.54 (a) and 0.63) (b)) and of MIM Pt/STO/Pt structures with STO films ([Sr]/([Sr]+[Ti]) = 0.54 (c) and 0.63 (d)) crystallized by RTA at 600 °C for 10 minutes.
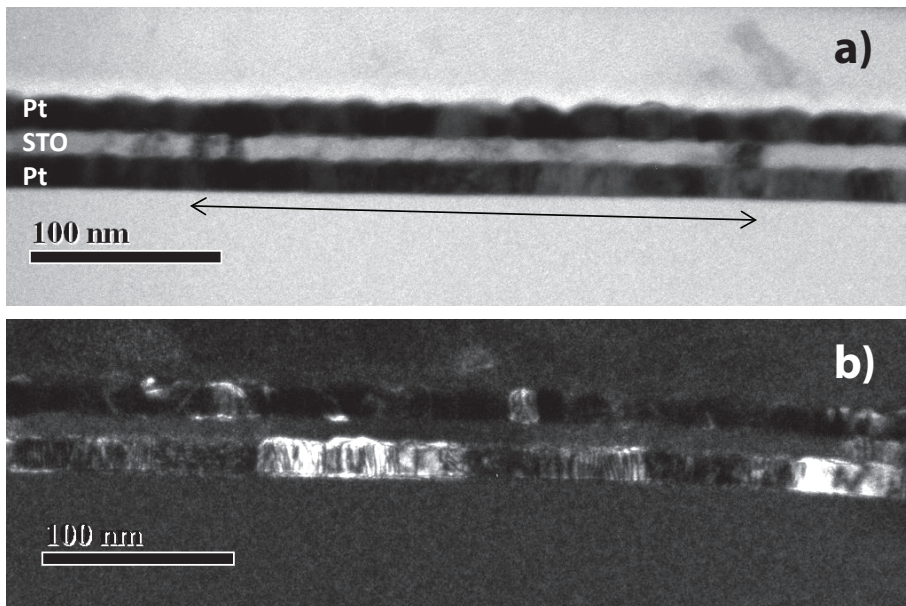
Figure 6.3: Bright field TEM (a) and dark-field TEM cross-sectional images of a MIM Pt/STO/Pt structure ([Sr]/([Sr]+[Ti]) = 0.63). The arrow in (a) indicates the length of an STO crystal. The inhomogeneous contrast is due to its transrotational structure. Figure b displays the difference in Pt grain size for the lower and upper layer. The RTA step (10 minutes at 600 °C) was performed before the top Pt film deposition.

fracting orientation with respect to the electron beam, thus providing an easy route to visualize grain sizes. One prominent difference between the grain size of the bottom and top Pt films can be noticed. In particular the bottom Pt film had a much larger grain size compared to the top one. This is due to solid state recrystallization of the Pt film during the RTA step needed to crystallize the STO film. TEM top view images (not shown here) evidenced that a 13 nm Pt film had an average grain size of $\sim$ 10 nm in the as-deposited state and a grain size of 100-200 nm after RTA at 600 °C for 1 minute.

The Pt top electrode in the MIM structure did not undergo any thermal treatment and a few single grains with $\sim$ 10 nm lateral dimension can be identified in Figure 6.3.b, in agreement with the results from top view TEM analysis. Furthermore, a 300 nm STO grain could be identified in Figure 6.3.a as evidenced by the arrow in the image. Figure 6.4.a shows a high resolution BF-TEM image of the same MIM structure. The STO layer was fully crystalline. Fast Fourier transform (FFT) patterns acquired from selected
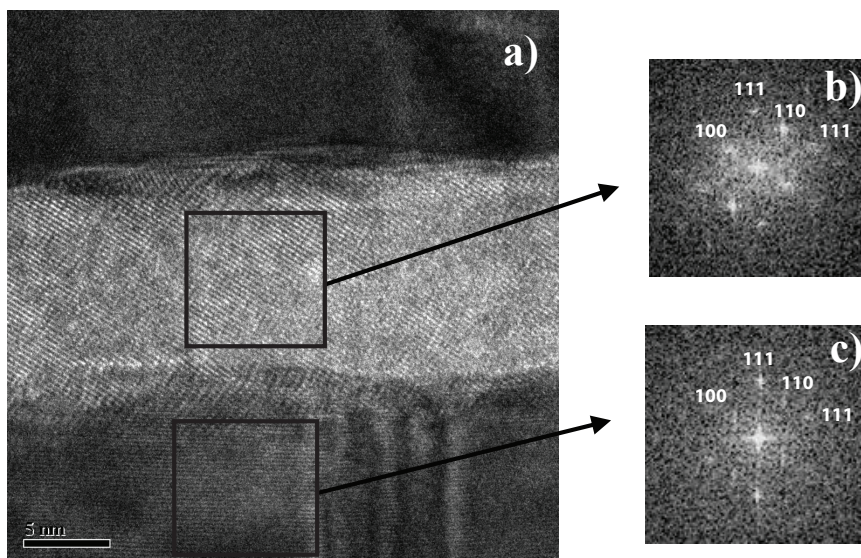
Figure 6.4: (a) High resolution bright-field TEM image of the MIM Pt/STO/Pt structure as shown in Figure 6.3, and Fast Fourier Transform images of selected areas of the image corresponding to the STO film (b) and to the bottom Pt film (c).

areas within the STO and the Pt layer are displayed in Figures 6.4.b and c, respectively. These FFT patterns revealed an epitaxial relation between the two layers, as the <111> orientations of the lower Pt layer and the STO layer were aligned. This epitaxial relation could only be detected locally because of the transrotational nature of the STO crystal [12,17-18]. In addition, it was not observed for the other STO crystals in the 20 μm wide transparent area of the TEM sample.

Figures 6.5.a and b show the electron diffraction (ED) patterns of a 13 nm Pt layer deposited by plasma-assisted ALD in the as-deposited state and after RTA at 600 $^\circ$C for 1 minute, respectively. The pattern of the as-deposited Pt film shows a set of diffraction rings representing all allowed reflections of Pt. This pattern of continuous rings is consistent with a polycrystalline film with a small average grain size ($\sim$ 10 nm as determined from top view TEM analysis). Analysis of the absolute intensities of the rings yields information about an onset to texture of the film, as is usually derived from the intensities of peaks in XRD spectra. Alternatively, ED pattern analysis as a function of tilt of the sample with respect to the electron beam was performed (not shown here). This analysis
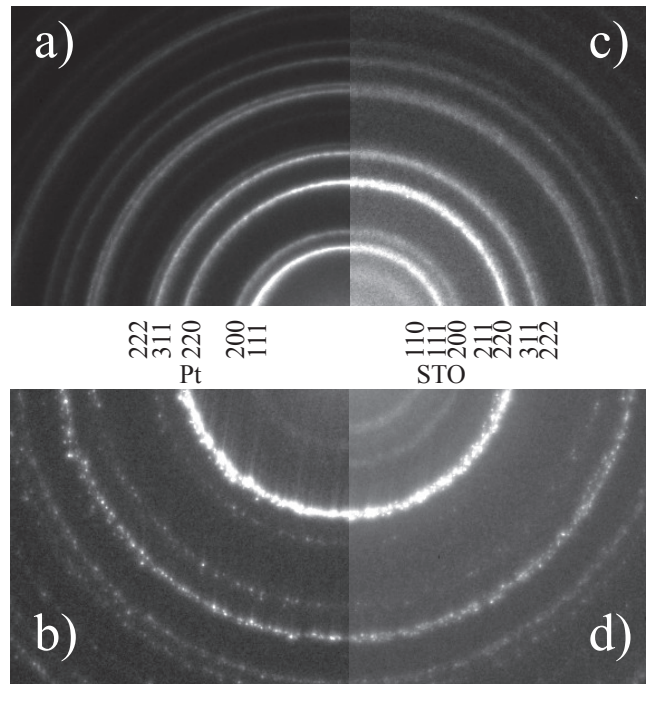
Figure 6.5: Electron diffraction patterns of a 13 nm Pt film deposited by plasma-assisted ALD in the as-deposited state (a) and after RTA at 600 °C for 1 minute (b) and of a stack of Pt (13 nm)/STO (15 nm, [Sr]/([Sr]+[Ti]) = 0.54)) prepared by plasma-assisted ALD, as-deposited (c), and after RTA at 600 °C for 1 minute (d). Allowed reflections for Pt and STO are indicated.

revealed the presence of arc segments of increased intensities over the still continuous rings, indicating an onset to <111> texture for this film. After the RTA step, the ED analysis showed interrupted ring patterns due to the increased Pt grain size. Furthermore, the virtual absence of the (111), (002) and (311) rings and the increased intensity of the (220) ring indicated a pronounced <111> texture of the Pt film after annealing.

Figures 6.5.c and d show the ED patterns of an STO (15 nm, [Sr]/([Sr]+[Ti]) = 0.54)/Pt (13 nm) stack before and after RTA at 600 °C for 1 minute, respectively. The ring pattern of the as-deposited stack was comparable to that of the as-deposited Pt film. Due to the amorphous STO layer the Pt diffraction rings appeared slightly blurred and a diffuse ring representing amorphous STO was detected at the expected location of the (110)
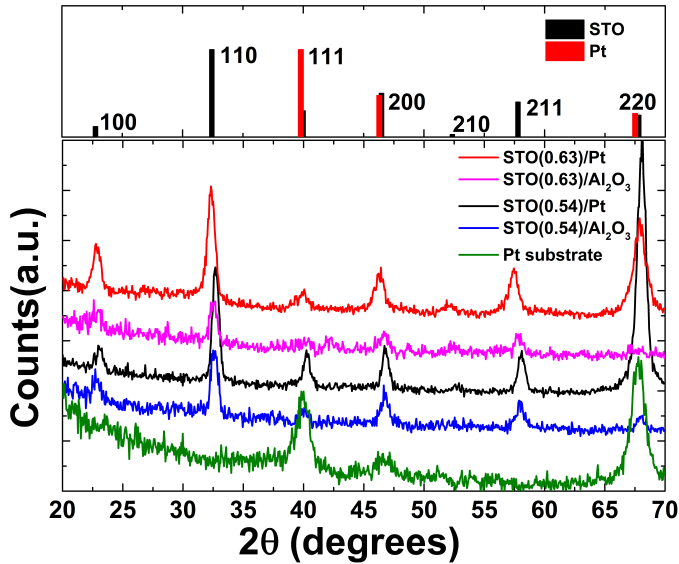
Figure 6.6: GI-XRD patterns of STO films with [Sr]/([Sr]+[Ti]) = 0.54 and 0.63 grown on Pt and on Al_2O_3 [12] after RTA at $600\,^{\circ}C$ for 1 minute. The GI-XRD of the Pt substrate is included as a reference.

STO ring. The ring pattern of the STO/Pt stack after RTA step suggests that the Pt layer underneath the STO film behaved similarly to the Pt-only film upon RTA: an increase in grain size and enhanced development of <111> texture. The ED pattern also confirmed that the STO was crystallized during the RTA step as evidenced by the presence of the (110) and (200) STO diffraction rings. The other allowed STO reflections were either not detected due to their expected limited intensity or due to their overlap with the Pt reflections. The pattern of continuous diffraction rings corresponding to the crystalline STO film remained unchanged upon tilting of the sample indicating that the degree of texture of the STO was limited or even zero (i.e. STO grains randomly oriented). This confirms that the aforementioned epitaxial relation detected in the cross-sectional TEM analysis is just a local phenomenon and does not represent the crystalline structure across the entire STO/Pt stack.

Figure 6.6 shows the GI-XRD patterns of the STO/Pt stacks fabricated with the 15 nm thick near-stoichiometric and Sr-rich STO films after RTA at $600\,^{\circ}C$ for 1 minute. The GI-XRD pattern of STO films (with equal thickness, composition and annealing conditions) deposited on Al_2O_3 (12) and of the bare as-deposited Pt-coated substrate are included for comparison. The crystallized STO films on Pt showed diffraction spectra
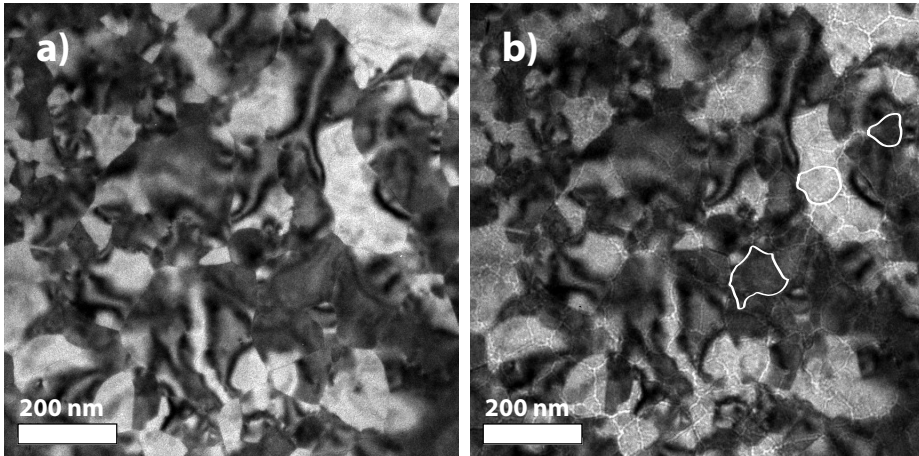
Figure 6.7: In-focus (a) and under-focused (b) BF-TEM top view images of an STO ([Sr]/([Sr]+[Ti]) = 0.54)/Pt stack after RTA at 600 °C for 1 minute. Three STO grains have been highlighted in image b).

comparable to those of crystallized STO films on Al_2O_3. The higher intensity for the 220 peak can be imputed either to a contribution of the textured <111> Pt film (as seen in Figure 6.5.b and in the reference GI-XRD Pt pattern) or to a slightly preferred <111> orientation of the STO film. The shift towards lower 2θ angles of the STO diffraction peaks for Sr-rich film is ascribed to an increase of the lattice parameter due to the non-stoichiometry of this film [12].

Figure 6.7 shows top view BF-TEM images of an STO ([Sr]/([Sr]+[Ti]) = 0.54))/Pt stack deposited on a Si_3N_4 TEM window. Imaging the grain size of the Pt and STO layers separately is not straightforward in top-view imaging, as TEM is an imaging technique, projecting the contrast of both layers on top of each other. In-focus imaging (a) predominantly displayed the size and lattice bending of the Pt grains, because of the larger diffraction contrast of the Pt layer. Under-focus imaging of the same area (b) was intentionally used to enhance the contrast of the STO layer, displaying the nano-cracks at the grain boundaries, visible as light contrast surrounding each STO grain (the boundaries of three STO grains have been highlighted for clarity) and the voids within the STO grains (visible as points with light contrast within one STO grain). It is evident that the Pt had a large grain size (> 100 nm), consistent with the conclusion drawn from ED analysis. The top view TEM analysis also confirmed that the near-stoichiometric STO film was fully crystallized after 1 minute RTA at 600 °C, with an average grain size of $\sim$ 100 nm in

agreement with our previous results for STO films deposited on Al_2O_3 with equivalent STO composition and thermal treatment procedure [12]. We note that top view TEM analysis of Sr-rich STO films on Pt has not been performed yet. However, changes in the microstructure and morphology are expected for increased Sr-content as previously reported for STO films on Al_2O_3 substrate [12].

6.4   Conclusions

The preparation of Pt/STO/Pt MIM structures by ALD was discussed. The ALD processes for Pt deposited on STO and for STO deposited on Pt showed no differences in growth behavior compared to STO and Pt deposited on SiO_2 and Al_2O_3 reference substrates. The effects of the RTA step, needed to crystallize the STO films, on the morphology and texture of the bottom Pt electrode and on the crystallization behavior of the STO films were also studied. TEM and ED analysis showed that the Pt bottom electrode experiences an increase in average grain size from $\sim$ 10 nm to > 100 nm during the RTA treatment at 600 °C, due to solid state re-crystallization. The as-deposited Pt layer showed an onset to a <111> texture which after the RTA step led to a strong <111> texture of the Pt film. TEM and ED analysis of the STO/Pt stack showed that the STO film is crystalline after the RTA step and that the STO film does not affect the re-crystallization process of the underlying Pt film. Cross-sectional TEM analysis of the MIM structure showed a local epitaxial relation between the Pt and the STO. However, the STO films were mainly randomly oriented as confirmed by GI-XRD and ED measurements. Furthermore, it was shown that, it was possible to visualize both the Pt and STO grains by focus or under-focusing during top view TEM image acquisition. Finally, TEM top view analysis indicated that the near-stoichiometric STO film ([Sr]/([Sr]+[Ti]) = 0.54) on Pt exhibits a crystallization behavior close to the one previously observed for STO films deposited on Al_2O_3, with comparable grain size and nano-crack formation at the grain boundaries.

Acknowledgments

6.5   References

1. M.S. Kim, M. Popovici, J. Swerts, M.A. Pawlak, K. Tomida, B. Kaczer, K. Opsomer, M. Schaekers, H. Tielens, C. Vrancken, S. van Elshocht, I. Debusschere, L. Altimime and J.A. Kittl, *3rd IEEE International Memory Workshop*, (2011).

2. M.A. Pawlak, M. Popovici, J. Swerts, K. Tomida, M.S. Kim, B. Kaczer, K. Opsomer, M. Schaekers, P. Favia, H. Bender, C. Vrancken, B. Govoreanu, C. Demeurisse, W.C. Wang, V.V. Afanas'ev, I. Debusschere, L. Altimime and J.A. Kittl, *IEDM 2010, Technical Digest*, (2010).

3. M.A. Pawlak, B. Kaczer, M.S. Kim, M. Popovici, J. Swerts, W.C. Wang, K. Opsomer, P. Favia, K. Tomida, A. Belmonte, B. Govoreanu, C. Vrancken, C. Demeurisse, H. Bender, V.V. Afanas'ev, I. Debusschere, L. Altimime and J.A. Kittl, *Appl. Phys. Lett.*, 98, 182902 (2011).

4. W. Lee, O.S. Kwon, J.H. Han and C. S. Hwang, *Appl. Phys. Lett.*, 92, 222903 (2008).

5. O.S. Kwon, S.W. Lee, J.H. Han and C. S. Hwang, *J. Electrochem. Soc.*, 154, G127 (2007).

6. W. Lee, J.H. Han, W. Jeon, Y.W. Yoo, S.W. Lee, S.K. Kim, C.H. Ko, C. Lansalot-Matras and C.S. Hwang, *Chem. Mater.*, 25, 953 (2013).

7. S.W. Lee, J.H. Han, S. Han, W. Lee, J.H. Jang, M. Seo, S.K. Kim, C. Dussarrat, J. Gatineau, Y.S. Min and C. S. Hwang, *Chem. Mater.*, 23, 2227 (2011).

8. O.S. Kwon, S.K. Kim, M. Cho, C.S. Hwang and J. Jeong, *J. Electrochem. Soc.*, 152, C229 (2005).

9. S.W. Lee, J.H. Han, O.S. Kwon and C. S. Hwang, *J. Electrochem. Soc.*, 155, G253 (2008).

10. T. Blomberg, J. Anttila, S. Haukka, M. Tuominen, M. Lukosius, C. Wenger and T. Saukkonen, *Thin Solid Films*, 520, 6535 (2012).

11. M. Lukosius, T. Blomberg, D. Walczyk, G. Ruhl and C. Wenger, *IOP Conference Series-Materials Science and Engineering*, 41, 012015 (2012).

12. V. Longo, M.A. Verheijen, F. Roozeboom and W.M.M. Kessels, *J. Solid State Sci. Technol.*, 2, N120 (2013).

13. L. Baker, A.S. Cavanagh, D. Seghete, S.M. George, A.J.M. Mackus, W.M.M. Kessels, Z.Y. Liu and T. Wagner, *J. Appl. Phys.*, 109, 084333 (2011).

14. H.C.M. Knoops, A.J.M. Mackus, M.E. Donders, M.C.M. van de Sanden, P.H.L. Notten and W.M.M. Kessels, *Electrochem. Solid-State Lett.*, 12, G34 (2009).

15. H.C.M. Knoops, A.J.M. Mackus, M.E. Donders, M.C.M. van de Sanden, P.H.L. Notten and W.M.M. Kessels, *ECS Trans.*, 16, 209 (2008).

16. V. Longo, N. Leick, F. Roozeboom and W.M.M. Kessels, *J. Solid State Sci. Technol.*, 2, N15 (2013).

17. V.Y. Kolosov and A.R. Thölén, *Acta Mater.*, 48, 1829 (2000).

18. B.J. Kooi and J.T. De Hosson, *J. Appl. Phys.*, 95, 4714 (2004).

Chapter 7

Influence of Stoichiometry on the Performance of MIM Capacitors from Plasma-assisted ALD Sr$_x$Ti$_y$O$_z$[*]

Abstract   Strontium titanate, Sr$_x$Ti$_y$O$_z$ (STO), thin films with various cation stoichiometries were deposited by plasma-assisted atomic layer deposition (ALD) using cyclopentadienyl-based metal precursors and oxygen plasma as counter-reactant. [Sr]/([Sr]+[Ti]) compositions ranging from 0.46 to 0.57 were obtained by changing the [SrO]/[TiO$_2$] ALD cycle ratios. As-deposited 15-30 nm thick Sr$_x$Ti$_y$O$_z$ films prepared at 350 °C on Pt-coated silicon substrates were amorphous. Post-annealing at 600-650 °C for 10 min under N$_2$ gas resulted in a crystallization into the perovskite phase. Stoichiometric STO and Sr-rich STO films exhibited a certain degree of (111) texture while the Ti-rich STO films showed a lower degree of crystallization. Crystallized layers exhibited a smaller band gap E$_g$ than amorphous ones, while within the stoichiometry series the value of E$_g$ increased with increasing Sr-content. Within the stoichiometry series Pt/STO/Pt structures with Sr-rich STO films showed the lowest leakage current densities. At 1.0 V values of about 2×10^{-8} and 5×10^{-6} Acm^{-2} were obtained for the as-deposited and the annealed films, respectively. Highest capacitance density was obtained for 15 nm polycrystalline stoichiometric SrTiO$_3$ films resulting in a capacitor equivalent thickness CET of about 0.7 nm. Pt/Sr$_x$Ti$_y$O$_z$/Pt capacitors with the STO being in amorphous state exhibited a positive voltage nonlinearity factor α of about 400 ppm V^{-2}, while the negative α-values for crystallized films showed a systematic variation with the stoichiometry, the degree of crystallization and the thickness of the STO layer. This demonstrates

that a broad performance range of MIM capacitors is accessible by controlling the stoichiometry and the degree of crystallization of plasma-assisted ALD $Sr_xTi_yO_z$ thin films.

7.1   Introduction

Strontium titanate ($SrTiO_3$, STO) is a high-k dielectric material which is of considerable interest for application in microelectronics due to its high charge storage capacity, good insulating properties, and chemical stability even in direct contact to silicon. Therefore, STO thin films are being investigated for nearly any kind of charged based devices, like for example as gate oxides in high-k field effect transistors [1], and as capacitive layers in dynamic random access memories (DRAM) [2-5] and in metal-insulator-metal (MIM) capacitors used in analog circuits for decoupling, signal mixing, and for analog-to-digital conversion [6-9]. Following the trends in miniaturization and component size reduction also passive components such as decoupling capacitors are meant to be integrated on-chip. According to the International Technology Roadmap for Semiconductors (ITRS) [10] capacitance densities of about C/A > 10 nF mm^{-2} will be required in combination with a low quadratic voltage coefficient of capacitance of about α < 100 ppm V^{-2}. For dielectric films in the storage cells of future generation DRAM devices, an aggressive scaling of the capacitor equivalent thickness down to CET < 0.5 nm is required, while leakage current densities at 1.0 V should not exceed $\sim 1 \times 10^{-8}$ A cm^{-2}.

A comprehensive compilation of the scaling characteristics of DRAM cells is provided in a recent review by Schroeder et al. [11]. A key difference between analog devices compared to memories is that for the latter highly conformal deposition techniques are mandatory in order to be compatible with the very high aspect ratios of DRAM capacitors used in today's production while the high-k oxide layer thicknesses are geometrically constrained to a few nanometers [4]. Atomic layer deposition (ALD) has been identified as the most promising technique to fulfill the challenging conformality and thickness control requirements. Substantial efforts have been undertaken by research groups worldwide to develop suitable ALD processes for high-k $SrTiO_3$ thin films [12-18]. Mostly, a post-deposition annealing at about 600 °C is required for a crystallization of the as-deposited films. Further analyses on integrated MIM structures revealed that the performance of the capacitors is strongly influenced by the ALD processing and annealing conditions which basically affect the crystal structure and morphology of the $SrTiO_3$ crystals [16]. Additionally, the stoichiometry [Sr]/([Sr]+[Ti]) ratio of the as-deposited amorphous ALD films strongly affects the crystallization behavior and as a consequence the physical and electrical properties of the MIM capacitors [18, 19].

In our work, a plasma-assisted ALD process for the growth of state-of-the-art $SrTiO_3$ thin films on platinum coated silicon substrates was utilized for a systematic study of the influences of the films' crystal structure and stoichiometry on their optical proper-

ties as well as on the electrical performance of Pt/$Sr_xTi_yO_z$/Pt capacitors. In addition to leakage current properties and CET values, also the influence of film thickness and stoichiometry on the capacitance nonlinearity was determined which is beyond the content of publications [8, 20] that recently appeared.

7.2   Experimental

$Sr_xTi_yO_z$ thin films with thickness ranging from 15 to 30 nm (see Table 7.1) were deposited at 350 °C on 1×1/2 inch^2 Pt (100 nm)/ZrO_2 (20 nm)/SiO_2 (400 nm)/Si (100) substrates by means of plasma-assisted ALD in an Oxford Instruments FlexAL reactor. The layers were deposited employing cyclopentadienyl-based precursors, namely, Ti-Star, (pentamethylcyclopenta-dienyl)tri-methoxytitanium, $CpMe_5Ti(OMe)_3$, and Hyper-Sr, bis(tri-isopropylcyclopentadienyl) strontium with 1,2-dimethoxy-ethane adduct, Sr-($^iPr_3Cp)_2$DME, both from AirLiquide. The O_2 plasma used as a co-reactant was generated in a remote inductively coupled plasma (ICP) source. For the determination of the thickness, the band gap, and the optical properties of the films, ex-situ spectroscopic ellipsometry (SE) measurements were performed (M2000D, J.A. Woollam, 1.25-6.5 eV). The composition of the STO films was estimated from the optical properties determined by SE employing a library calibrated by Rutherford back scattering measurements [17]. For cross-checking the [Sr]/([Sr]+[Ti]) values obtained from SE, X-ray photoelectron spectroscopy (XPS) measurements were performed on a Thermo Scientific K-Alpha KA1066 spectrometer using monochromatic Al K_α X-ray radiation (hν = 1486.6 eV). Photoelectrons were collected at a take-off angle of 60 °. A 400 μm diameter X-ray spot was used in the analysis and the samples were neutralized using an electron flood gun to correct for differential or nonuniform charging. The sensitivity factors for the Sr3d, Ti2p, and O1s peaks were calibrated on a stoichiometric $SrTiO_3$ target as previously reported [17]. For studying the structural properties of the perovskite films, rapid thermal annealing (RTA) of the films at 600 and 650 °C in flowing N_2 gas at atmospheric pressure was employed. Structural properties were studied by X-ray diffractometry (XRD) using a Panalytical X'Pert PRO MRD employing Cu K_α (1.54 Å) radiation. Both Psi and grazing-incidence XRD (GI-XRD) scans were performed on the samples. The electrical properties of Pt/STO/Pt capacitors were studied for $Sr_xTi_yO_z$ films of about 30 and 15 nm in thickness both in the as-deposited amorphous state and after annealing at 600 °C for 10 min in N_2. Top Pt electrode contacts with a pad diameter of 60 μm were deposited by means of e-beam evaporation and lift-off process after conventional photolithography. The Pt bottom electrodes were contacted by etching of the oxide, using reactive ion beam

Table 7.1: Influence of the [SrO]/[TiO$_2$] ALD cycle ratio on the elemental composi-
tion of about 30 and 15 nm thick amorphous STO films. The [Sr]/([Sr]+[Ti]) content
ratios were determined by SE and cross-checked by XPS. The relative errors in the
[Sr]/([Sr]+[Ti]) ratios from SE and XPS are ± 0.03 and ± 0.02, respectively. The thick-
ness of the films was determined by ex-situ SE. The error in thickness is ± 0.5 nm.

[SrO]/[TiO$_2$] ALD cycle ratio	Thickness (nm)	[Sr]/([Sr]+[Ti]) ratio from SE	[Sr]/([Sr]+[Ti]) ratio from XPS
1:4	27.6	0.46	0.46
	15.1		
1:3	29.9	0.50	0.50
	14.9		
1:2	31.7	0.57	0.58
	15.4		

etching (RIBE 300, Oxford Instruments). Current-voltage characteristics were obtained
using a programmed Keithley 2611 System Source Meter. Capacitance-voltage meas-
urements at room temperature were performed with a Hewlett Packard 4284A Precision
LCR Meter applying 100 kHz signals with amplitude of 50 mV.

7.3   Results on Film Composition, Structural, and Op-
tical Properties

7.3.1   Spectroscopic Ellipsometry and X-ray Photoelectron Spectro-
scopy

The Sr$_x$Ti$_y$O$_z$ thin films were deposited by intermixing TiO$_2$ and SrO ALD cycles. By
tuning the ratio between the cycles the stoichiometry of the films was varied. The
[SrO]/[TiO$_2$] cycle ratio used for the examined STO films, the thickness, and the com-
position measured by SE are listed in Table 7.1. The [Sr]/([Sr]+[Ti]) ratios obtained from
XPS analysis are included as a crosscheck. They are in excellent agreement with the val-
ues obtained from the SE optical constant library [17].

Figure 7.1 shows the dielectric functions (ϵ_1 and ϵ_2) of the ∼30 nm thick Sr$_x$Ti$_y$O$_z$
films in the as-deposited state (a and b) and after RTA at 650 °C for 10 min (c and
d). For the as-deposited films the dielectric functions show an increase in magnitude of
both ϵ_1 and ϵ_2 with increasing Ti-content which is in agreement with our previous res-
ults [17]. After the RTA step a change in the dielectric function of the stoichiometric
([Sr]/([Sr]+[Ti]) = 0.50) and the Sr-rich (0.57) films was observed, while no remarkable
changes are visible for the Ti-rich film (0.46).
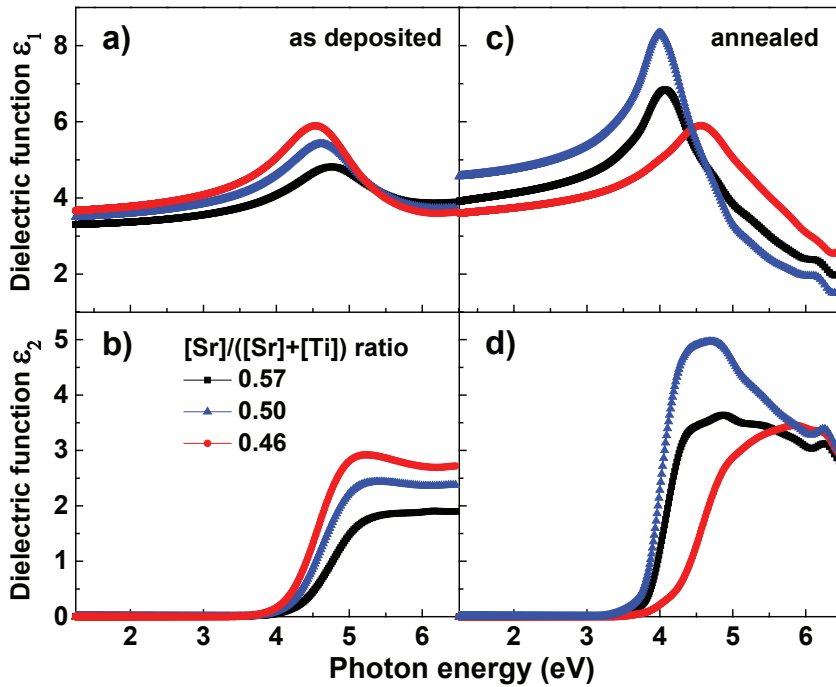
Figure 7.1: Optical dielectric functions (ϵ_1 and ϵ_2) of the stoichiometry series of about 30 nm thick $Sr_xTi_yO_z$ thin films grown at 350 $^{\circ}$C on Pt coated Si substrate by plasma-assisted ALD (a,b) and after annealing at 650 $^{\circ}$C for 10 min in N_2 (c,d).
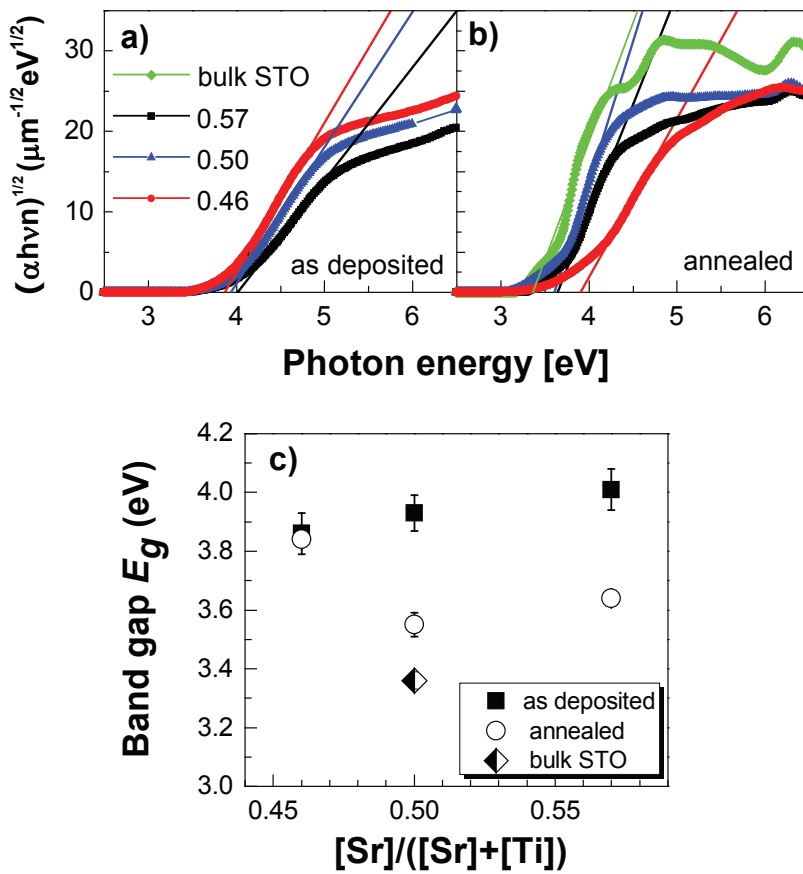
Figure 7.2: Determination and values of the optical band gap E_g of (a) as deposited (amorphous) and (b) 650 °C annealed films as a function of the $Sr_xTi_yO_z$ stoichiometry. Data point of a $SrTiO_3$ single crystal is added as a reference.

The change in dielectric function corresponds to crystallization into the perovskite structure. We note here that the stoichiometric and Sr-rich films were fully crystallized while the Ti-rich STO film remained amorphous or exhibited only partial crystallization [17].

The optical constants of the films have been determined from the dielectric function values through the relations:

$$\epsilon_1 = n^2 - k^2 \; and \; \epsilon_2 = 2nk, \tag{7.1}$$

where n is the refractive index and k is the extinction coefficient. The band gap values E_g of as-deposited and annealed films, both ~ 30 nm thick (see Figure 7.2.c) were determined from the plot $(\alpha h \nu n)^{1/2}$ versus $h\nu$, shown in Figure 7.2.a and b, respectively, where $h\nu$ is the energy of incident photons and α the absorption coefficient. The linear parts of these curves were fitted with a straight line. The band gap values correspond to the intercept of these lines with the horizontal axis. The band gap for bulk single crystalline (100) STO (Crystal GmbH) is also determined as a reference. The band gap values for as-deposited and annealed films, and bulk STO are reported in Figure 7.2.c. The band gap values of the as-deposited films increase with increasing Sr-content as previously reported [17]. For the annealed Ti-rich film no remarkable change compared to the as-grown state was recorded in agreement with the fact that this film remained amorphous. Due to the crystallization into the perovskite phase the stoichiometric and Sr-rich film showed a decrease in band gap after the RTA step. Also for the crystallized films an increased Sr-content resulted in a higher band gap. The band gap values obtained for the crystallized films were higher than the bulk value 3.35 eV, also shown in Figure 7.2.c. Higher band gap values for nanocrystalline STO thin films compared to the bulk have been reported in the literature [21]. The "optical shift of the band gap"-effect has been attributed to quantum-size effects due to the nanoscale crystallites' dimension [22, 23].

7.3.2   X-ray Diffraction

Figure 7.3 shows the GI-XRD spectra of the $Sr_xTi_yO_z$ films with different compositions. Except the Ti-rich film (0.46), which was found to be mainly amorphous, the other layers show a strong (220) peak at 2θ-value of 67.8 °. The other peaks corresponding to the perovskite structure are not observed or have very limited intensities. The broad peak at $2\theta \sim 30$ ° for the stoichiometric sample is imputed to amorphous or nanocrystalline STO indicating that this film was not fully crystalline after RTA at 600 °C for 10 min. The high relative intensity of the (220) peak for the stoichiometric and Sr-rich films could
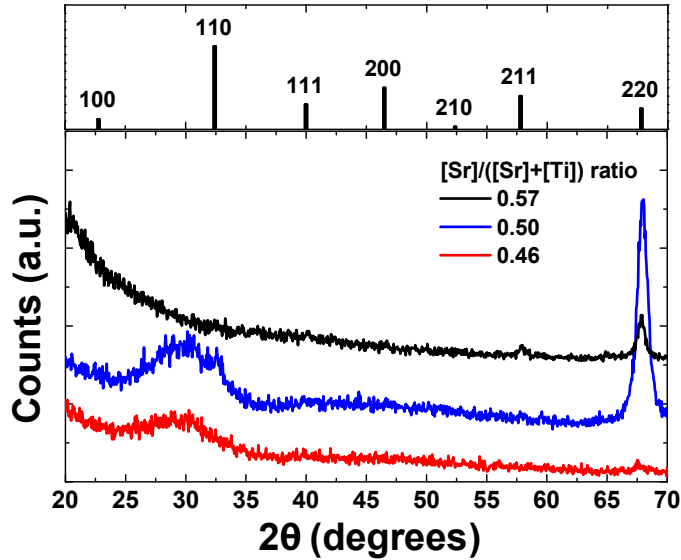
Figure 7.3: GI-XRD scans of $Sr_xTi_yO_z$ thin films after RTA at 600 $^\circ$C for 10 min under N_2.

be explained by a (111) preferential orientation of the STO grains perpendicular to the substrate surface.

The angle of incidence of the X-ray radiation was θ_{in} = 0.324 $^\circ$, and the angle between the (111) and (220) directions is about 35.26 $^\circ$. Therefore, the mismatch between the (220) direction and the bi-sector when 2θ = 67.8 $^\circ$ is only 1.684 $^\circ$. This means that the (220) planes could still satisfy Bragg's law for these conditions and the (220) reflection could be detected. To confirm this hypothesis ψ-scans were performed to detect the STO (110) diffraction peak (Figure 7.4). For this measurement 2θ was kept constant in diffraction conditions for the STO (110) planes ($\sim$ 32.4 $^\circ$). Peaks corresponding to (110) planes were detected for $\psi \pm 35.26$ $^\circ$ confirming the (111) preferred orientation of the STO grains. The sharp peak at $\sim$ 0 $^\circ$ in Figure 7.4 is caused by the Si substrate. The width of the (110) peaks suggest that the texture is limited to some extent with bending of the lattice plane. This is in agreement with our previous observations that the STO crystals grow in a transrotational fashion with the lattice plane bending due to the densification of the film upon the amorphous-crystalline transition [18, 24].
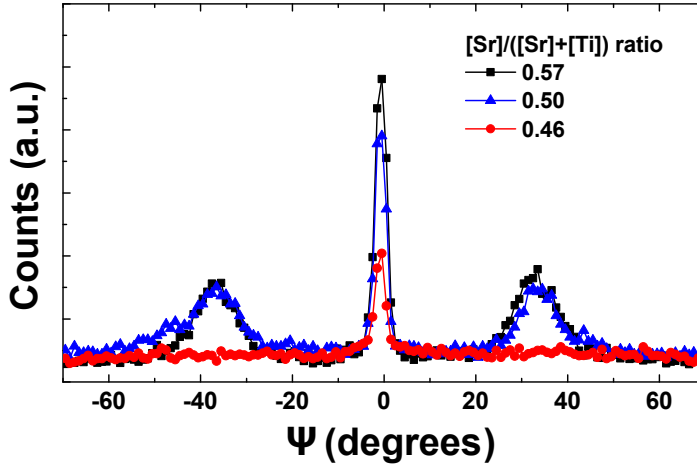
Figure 7.4: ψ-scans of $Sr_xTi_yO_z$ thin films after RTA at $650\,°C$ for 10 min under N_2 gas.

7.4 Results on Performances of MIM Capacitors

MIM capacitors were fabricated by conventional photolithography and lift-off processes. The annealing of the $Sr_xTi_yO_z$ at $600\,°C$ was done before the top electrode was deposited and no post-deposition annealing was performed after this. A schematic of the MIM capacitors is given in the left picture of Figure 7.5, and an optical micrograph of functional MIM capacitors is shown on the right picture of Figure 7.5.

For the electrical measurements the voltage signal was always applied on the Pt top electrode of the $Pt/Sr_xTi_yO_z/Pt$ capacitor while the Pt bottom electrode was grounded.

7.4.1 Current-Voltage Characteristics

For MIM capacitors used in integrated circuits rather strict limits are defined for the acceptable leakage currents which are in the range of 10^{-7} A cm^{-2} at 1.0 V [10]. Therefore, the influence of the crystallinity and of the stoichiometry on the leakage current densities of the Pt/30 nm $Sr_xTi_yO_z$/Pt structures was analyzed. Representative *I(V)* characteristics measured at room temperature are depicted in Figure 7.6. Lower leakage current densities are achieved for the as-deposited films (Figure 7.6.a) than for the annealed ones (Figure 7.6.b). A clear influence of the stoichiometry is also observed showing that $Pt/Sr_xTi_yO_z/Pt$ capacitors made from Sr-rich STO films exhibited the lowest leakage current densities from all STO samples investigated. These observations are in accordance
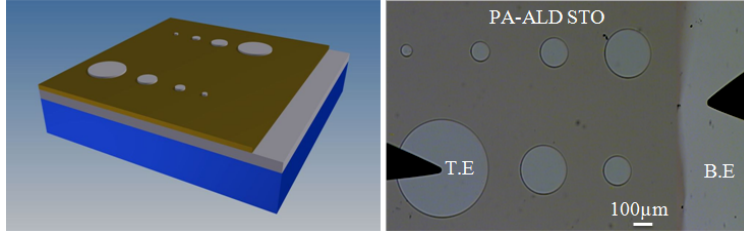
Figure 7.5: Pt/Sr$_x$Ti$_y$O$_z$/Pt capacitors: schematic (left) and optical micrograph of MIM capacitors of different pad sizes (right). TE and BE are top and bottom electrode, respectively.

to the results on TiN/STO/Pt structures recently reported by Menou et al. [19]. Two contributions to the leakage current density have to be considered. First is the effect of the stoichiometry on the band gap as is shown in Figure 7.2.c. Second is the effect of the film microstructures as has been studied on comparable samples by transmission electron microscopy (TEM). A related, recently published study [18] clearly revealed a change of the films' microstructure with varying stoichiometry.

The films show a high density in as-deposited state which is obvious from the high refractive index of about 1.95 for the stoichiometric composition which is comparable to literature results for STO films grown by high-temperature thermal ALD [14]. Upon crystallization by RTA at 600-650 °C the films showed a decrease in thickness of $\sim 15\%$ which is consistent with the development of nano-crack formation at the grain boundaries as previously reported [16,18]. However, a clear increase in the density of grains and reduction of nanocracks with increasing Sr-excess was obtained [18]. At a typical voltage of 1.0 V current density values of about 2×10^{-8} and 5×10^{-6} A cm^{-2} were achieved for the as-deposited and for the crystallized Sr-rich STO films, respectively.

7.4.2 Capacitance-Voltage Characteristics

Relevant parameters describing the performance of MIM-capacitors in charge based memory or on-board integrated decoupling devices are:

- the capacitance density at small voltages (C_0/A), where C_0 is the measured capacitance close to 0 V, and A is the area of the plate capacitor. The effective permittivity at technical frequencies is determined by

$$\epsilon_{eff} = (t_{phys}/\epsilon_0) \cdot C_0/A, \tag{7.2}$$

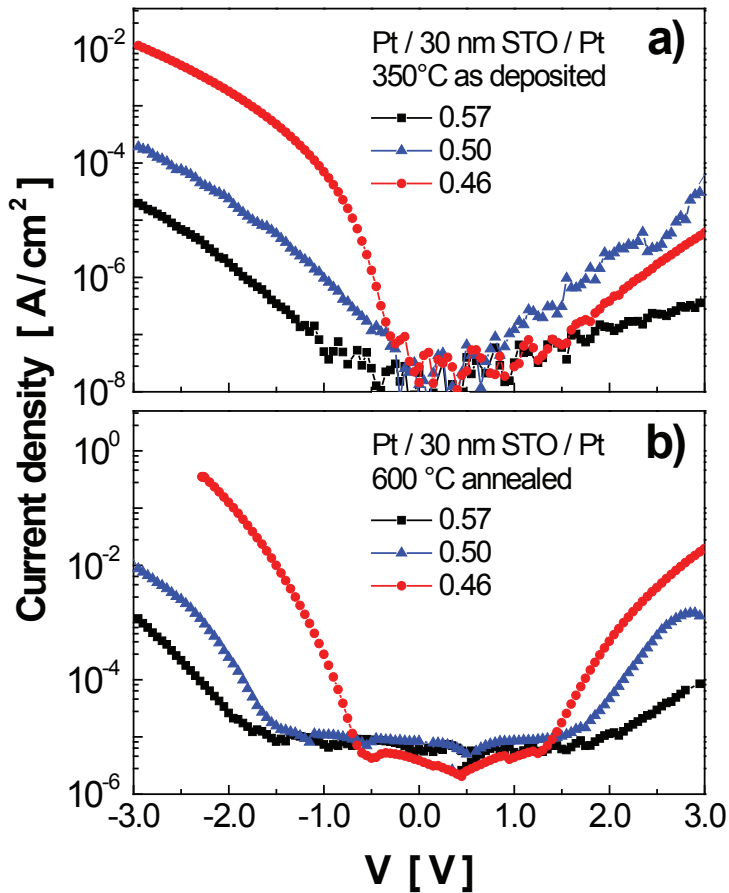**Figure 7.6:** Leakage current densities for Pt/Sr$_x$Ti$_y$O$_z$/Pt structures with STO films ($\sim$ 30 nm) with three different [Sr]/([Sr]+[Ti]) compositions for (a) as-deposited films and (b) 600 °C 10 min N$_2$ annealed films.

where t_{phys} is the physical thickness of the dielectric and ϵ_0 is the permittivity of free space.

- the capacitance equivalent thickness (CET) with respect to SiO$_2$, given by

$$CET = \epsilon_0 \cdot \epsilon_{SiO_2} \cdot A/C_0, \tag{7.3}$$

where $\epsilon_{SiO_2} \approx 3.9$ is the relative permittivity of SiO$_2$.

- and the capacitance-voltage nonlinearity factor α, which is defined by the following relation [25]:

$$C(V) = C_0(\alpha V^2 + \beta V + 1), \tag{7.4}$$

where V is the applied bias voltage, and α and β are the quadratic and linear coefficients, respectively.

For integrated passive devices a capacitor's performance of $C_0/A > 10$ nF mm^{-2} and $\alpha < 100$ ppm V^{-2} is required, while memory applications target values of CET < 0.5 nm. Nonlinearity coefficients α [6] and CET values [19] achieved for SrTiO$_3$-based capacitors have recently been reported. In order to investigate the dependency of the characteristic capacitor's properties on the stoichiometry and microstructure of the utilized Sr$_x$Ti$_y$O$_z$ we present the full set of data determined for the various Pt/Sr$_x$Ti$_y$O$_z$/Pt capacitors. Figure 7.7 summarizes the effects of the different film microstructures, compositions ([Sr]/([Sr]+[Ti]) and thickness (30 and 15 nm) on the capacitance versus bias voltage characteristics. The nonlinearity coefficient α is obtained from the data in Figure 7.7 by applying a polynomial fitting procedure according to Equation 7.4. The extracted α-values as a function of the film compositions are plotted in Figure 7.8.c. For the Pt/Sr$_x$Ti$_y$O$_z$/Pt structures based on as-deposited amorphous films positive α-values of about 400-440 ppm V^{-2} were determined, rather independent of the film stoichiometry. In contrast, the (C/C_0) versus V plots of the Pt/Sr$_x$Ti$_y$O$_z$/Pt capacitors from annealed (polycrystalline) oxides (Figs. 7.7.b and c) show a strong downward bending of the curves which results in negative α-values.

7.4.3 Performance of Pt/STO/Pt Capacitors

Figure 7.8 gives the dielectric properties of capacitor structures built from plasma-assisted ALD Sr$_x$Ti$_y$O$_z$ thin films with different composition, microstructure, and thickness. Figure 7.8.a shows the capacitance densities C_0/A of the Pt/Sr$_x$Ti$_y$O$_z$/Pt devices at zero bias voltage, Figure 7.8.b gives the derived CET values, and the capacitance-voltage nonlinearity factors α, determined for a bias voltage range of $\pm$ 2.0 V, are plotted in Figure
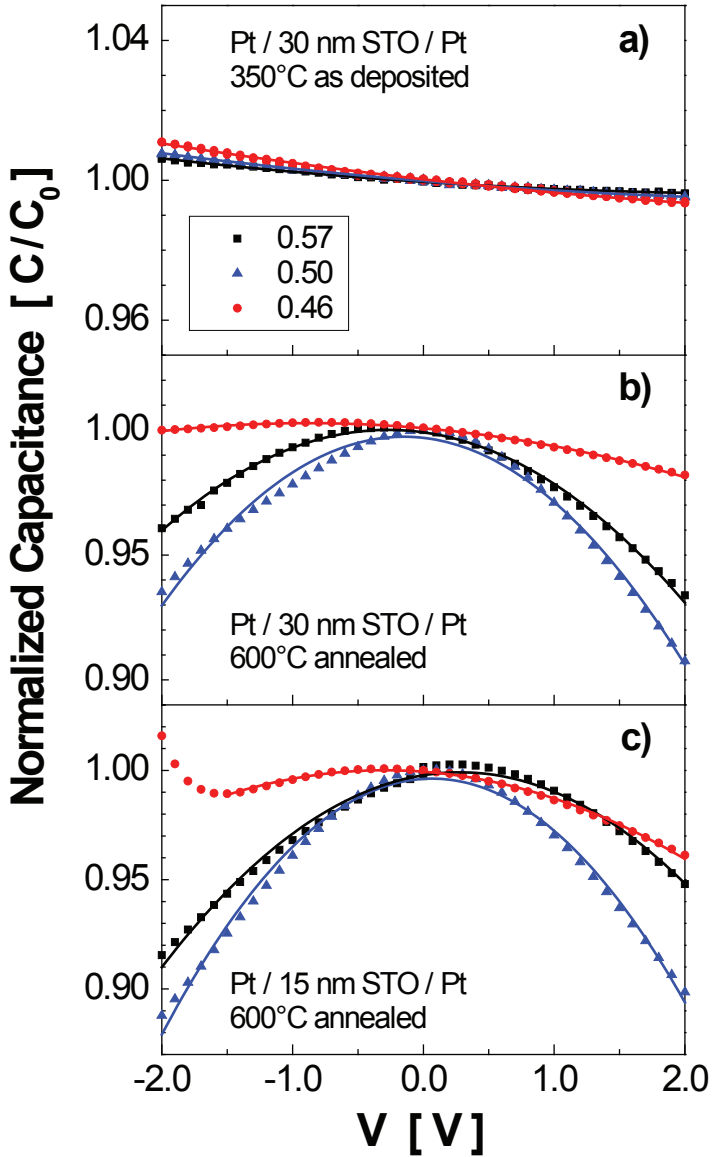
Figure 7.7: Normalized capacitance C/C_0 versus bias voltage for Pt/$Sr_xTi_yO_z$/Pt capacitors. Data are presented for films of various [Sr]/([Sr]+[Ti]) compositions from 0.46 to 0.57: (a) $\sim$ 30 nm as deposited STO; (b) $\sim$ 30 nm, and (c) $\sim$ 15 nm STO films annealed at 600 °C 10 min under N_2. The corresponding absolute values (C_0/A) are given in Figure 7.8.a.

7.8.c.

The capacitors with about 30 nm thick as deposited STO films exhibit low capacitance densities of about 5-8 fF μm^{-2} resulting in CET values between 4 and 6 nm.

Determined effective permittivity values ϵ_{eff} are in the range of 17-27, respectively. The composition effect is not very pronounced but as a tendency one could observe that the STO which is closest to stoichiometry exhibits a slightly higher *C_0/A* value and corresponding lower CET value as compared to the Ti- or Sr-rich films. As mentioned earlier, the capacitance voltage nonlinearity factors α of the amorphous films are positive with values of about 400-440ppm V^{-2}. The characteristic data for capacitors obtained from as deposited STO films agree well with the results which were obtained for medium-permittivity dielectrics as for example HfO_2. Jorel et al. [6] introduced the ratio $\alpha/(C_0/A)^2$ to quantify the difficulty to obtain both a high capacitance density *(C_0/A)* and a low α-value for integrated capacitor applications. For an ideal capacitor the ratio $\alpha/(C_0/A)^2$ should be independent of the oxide's thickness t_{phys} if the electrical field inside the capacitor is constant. Jorel et al. summarized the data for different HfO_2 based capacitors, which all fitted to a value of $\alpha/(C_0/A)^2 \approx 10$ (ppm μm^2 V^{-2} fF^{-2}). For our as-deposited STO films the respective values of $\alpha/(C_0/A)^2$ in units of (ppm μm^2 V^{-2} fF^{-2}) are in between $\sim$ 15 and 7 for the nonstoichiometric and for the stoichiometric STO films, respectively. Taking into account that the α-values differ over several orders of magnitude the abovementioned ratios for the as deposited STO layers show a good agreement with the data from HfO_2-based capacitors [6].

The capacitors derived from $Sr_xTi_yO_z$ layers annealed at $600\,^{\circ}C$ for 10 min under N_2 showed a stoichiometry dependence of the dielectric properties, an increased capacitance density and a reduction of the CET values. Negative α-values were obtained for all $Pt/Sr_xTi_yO_z/Pt$ structures with annealed films. For most of the $Sr_xTi_yO_z$ films we found a polycrystalline perovskite structure after annealing at 600-$650\,^{\circ}C$ for 10 min. While the crystallization effect was strong for the Sr-rich and stoichiometric STO films, Ti-rich films remained in an amorphous to nanocrystalline state. Consequently, for an annealed stoichiometric STO film of 15 nm thickness the capacitance density could be increased up to $C_0/A \approx 50$ fF μm^{-2} corresponding to a CET value of about 0.7 nm and to an effective permittivity of $\epsilon_{eff} \approx 85$, while the capacitance voltage nonlinearity factor α reaches highly negative values of (-20000 ppm V^{-2}). Crystalline stoichiometric $SrTiO_3$ is a high-permittivity paraelectric perovskite type material which is known to display negative nonlinearity factors α [26]. For capacitors from stoichiometric $SrTiO_3$ films the transition from positive α-values for amorphous films to negative α-values for the perovskite phase has also been reported by Jorel et al. [6]. The authors discuss two possible
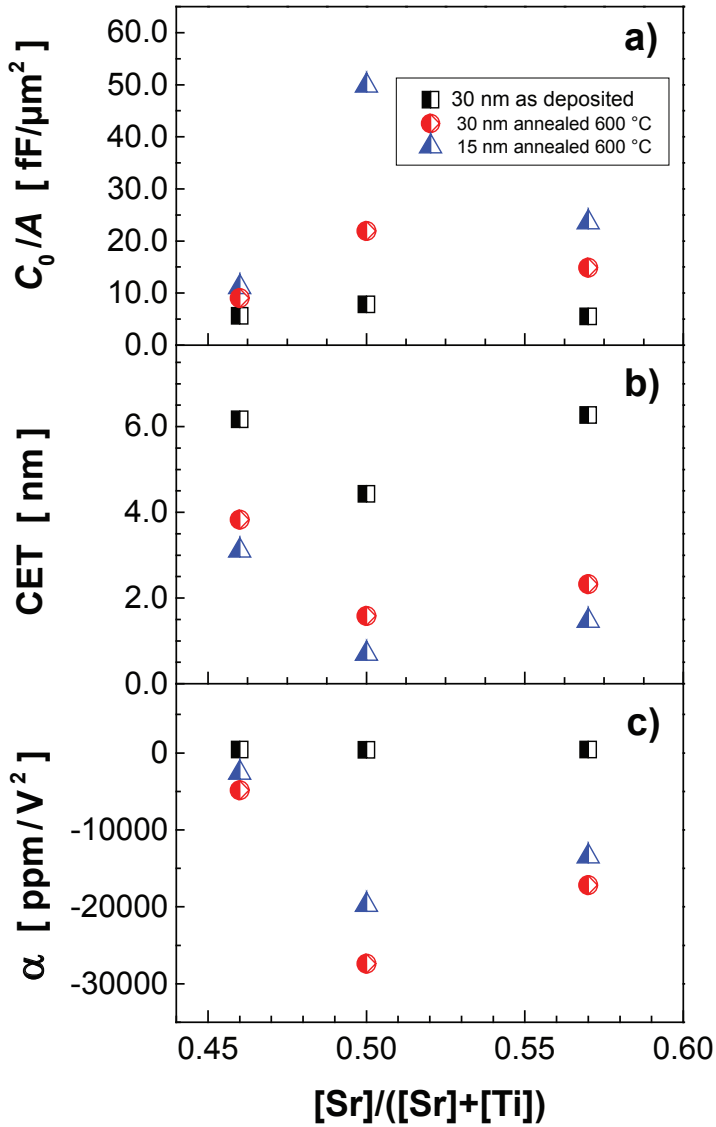
Figure 7.8: Composition dependence of the performance of Pt/$Sr_xTi_yO_z$/Pt capacitors determined at 100 kHz: (a) average capacitance density values *(C_0/A)* at zero bias; (b) calculated CET values at zero bias; and (c) capacitance-voltage nonlinearity factor α determined from the fittings shown in Figure 7.7 for a bias voltage range of $\pm$ 2.0 V.
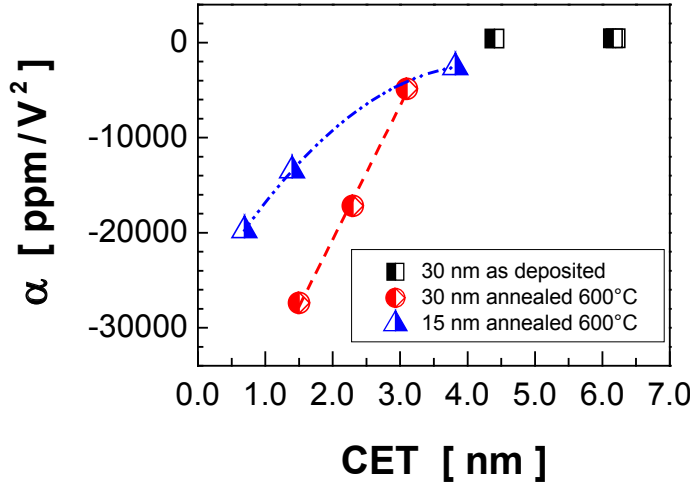
Figure 7.9: Capacitance-voltage nonlinearity factor α versus capacitance equivalent thickness CET of Pt/Sr$_x$Ti$_y$O$_z$/Pt capacitors derived from plasma-assisted ALD STO films with different microstructures: 30 nm thick 350 °C as-deposited films (black squares) and 600 °C annealed films of different thickness, 30 nm (red circles) and 15 nm (blue triangles). Within the three series (black, red, blue) the sequence from lower to higher CET values maps the different stoichiometries, i.e., stoichiometric STO, Sr-rich STO, and Ti-rich STO, while for the amorphous films the values for the nonstoichiometric films coincide.

origins for the positive α-values in amorphous films. These are the absence of crystals and a certain degree of oxygen deficiency in the amorphous phase. Wenger et al. [25] presented a microscopic model for the nonlinear behavior of MIM structures with positive α-values applicable to medium permittivity materials like HfO$_2$ and to amorphous high permittivity materials. This model is based on fundamental physical mechanisms, such as electrostriction, Coulomb interaction between electrodes, and nonlinear optical effects. The authors address the differences in electrostrictive coefficients of isotropic amorphous materials and nonisotropic crystalline material as the main origin for the change of the sign of the α-values. Thus, the observations for the Pt/Sr$_x$Ti$_y$O$_z$/Pt capacitors are consistent with existing models for medium and high permittivity dielectric capacitors.

Furthermore, our study demonstrates that the composition and the closely related microstructure of nonstoichiometric films have an additional effect on the performance of

Pt/$Sr_xTi_yO_z$/Pt capacitors. For the Ti-rich STO films, CET values of about 3 nm were obtained with a rather small negative nonlinearity factor ($\alpha \approx$ -3000 ppm V^{-2}). This agrees with the amorphous to nanocrystalline microstructure of these films. For Sr-rich STO films annealed at 600 °C CET values below 2 nm were achieved with medium nonlinearity coefficients ($\alpha \approx$ -15000 ppm V^{-2}). The influences of $Sr_xTi_yO_z$ film microstructure, composition and thickness are summarized in the α versus CET plot which is shown in Figure 7.9. The capacitors derived from as-deposited, amorphous STO films show a lower CET value for the stoichiometric composition while no significant effect of the composition on the capacitance-voltage nonlinearity factor α is found. Capacitor structures obtained from annealed STO films show a linear relationship between α and CET for films of different compositions but with the same thickness. A change of the slope in the (α vs. CET) plot is observed for annealed STO films of different thicknesses, namely 15 and 30 nm. The variation of a with a change in CET is less pronounced in the thinner films as compared to the thicker ones.

On the one side, Figure 7.9 illustrates how important an understanding and control of the high permittivity films with respect to microstructure, composition and thickness is. On the other side, Figure 7.9 clearly demonstrates the variability of STO derived capacitors structures which can be utilized to tune the performance of integrated capacitors once the complex relationships are controlled.

7.5 Summary

In this work, a comprehensive study on the optical and electrical properties of $Sr_xTi_yO_z$ thin films deposited by means of plasma-assisted ALD on Pt-coated Si-substrates is presented. We discussed the effect of the composition of as-deposited films on the microstructure after annealing under nitrogen at 600-650 °C, and the influence of the composition on the optical properties of the films in amorphous and in polycrystalline state. Additionally, the influence of the stoichiometry of the plasma-assisted ALD $Sr_xTi_yO_z$ films on the electrical performance of integrated Pt/$Sr_xTi_yO_z$/Pt capacitors was investigated. The comprehensive analysis of the films' optical properties and microstructures together with the leakage currents and the dielectric properties of derived capacitor structures enabled a better understanding of the complex relationship between film stoichiometry, crystallization behavior, and electrical performance under DC and AC applied field. The performance of Pt/STO/Pt capacitors could be varied between high-k applications (CET $\approx$ 0.7 nm) and integrated capacitor applications ($\alpha \rightarrow$ 0 ppm V^{-2}) by choosing tailored compositions and microstructures of the plasma-assisted ALD $Sr_xTi_yO_z$ films. A type of

capacitors design map is suggested which comprises data obtained for the capacitance voltage nonlinearity factor (α) versus the CETs.

Acknowledgments

7.6   References

1. R. McKee, F. Walker and M. Chisholm, *Science*, 293, 468 (2001).

2. M.A. Pawlak, M. Popovici, J. Swerts, K. Tomida, M. Kim, B. Kaczer, K. Opsomer, M. Schaekers, P. Favia, H. Bender, C. Vrancken, B. Govoreanu, C. Demeurisse, W. Wang, V.V. Afanas'ev, I. Debusschere, L. Altimime and J. A. Kittl, *IEDM 2010, Technical Digest*, (2010).

3. J.H. Ahn, J.Y. Kim, J.H. Kim, J.S. Roh and S.W. Kang, *Electrochem. Solid State Lett.*, 12, G5 (2009).

4. S.K. Kim, S.W. Lee, J.H. Han, B. Lee, S. Han and C.S. Hwang, *Adv. Funct. Mater.*, 20, 2989 (2010).

5. S. Schmelzer, D. Braeuhaus, S. Hoffmann-Eifert, P. Meuffels, U. Boettger, L. Oberbeck, P. Reinig, U. Schroeder and R. Waser, *Appl. Phys. Lett.*, 97, 132907 (2010).

6. C. Jorel, C. Valle, P. Gonon, E. Gourvest, C. Dubarry and E. Defay, *Appl. Phys. Lett.*, 94, 253502 (2009).

7. M. Lukosius, C. Wenger, T. Blomberg and G. Ruhl, *J. Vac. Sci. Technol. B*, 31, 1A102 (2013).

8. K. Chiang, C. Huang, G. Chen, W. Chen, H. Kao, Y. Wu, A. Chin and S. McAlister, *IEEE Trans. Electron Devices*, 53, 2312 (2006).

9. D.R. Chase, L.Y. Chen and R.A. York, *IEEE Trans. Microw. Theory Technol.*, 53, 3215 (2005).

10. Radio Frequency and Analog/Mixed-Signal Technologies for Wireless Communications, International Technology Roadmap for Semiconductors (Semiconductor Industry Association, Palo Alto, 2011 update).

11. U. Schroeder, H. Schroeder, A. Kingon, S. Summerfelt, C.S. Hwang and U. Boettger, in: "Nanoelectronics and Information Technology: Advanced Electronic Materials and Novel Devices", 3rd ed., edited by R. Waser (Wiley-VCH, Weinheim, Germany, 2012), Chap. 27.

12. M. Vehkamäki, T. Hanninen, M. Ritala, M. Leskelä, T. Sajavaara, E. Rauhala and J. Keinonen, *Chem. Vapor Depos.*, 7, 75 (2001).

13. T. Blomberg, J.Anttila, S.Haukka, M. Tuominen, M. Lukosius, C. Wenger and T. Saukkonen, *Thin Solid Films*, 520, 6535 (2012).

14. S.W. Lee, O.S. Kwon, J.H. Han and C.S. Hwang, *Appl. Phys. Lett.*, 92, 222903 (2008).

15. S.W. Lee, J.H. Han, W. Jeon, Y.W. Yoo, S.W. Lee, S.K. Kim, C.H. Ko, C. Lansalot-Matras and C. S. Hwang, *Chem. Mater.*, 25, 953 (2013).

16. M. Popovici, S. Van Elshocht, N. Menou, P. Favia, H. Bender, E. Rosseel, J. Swerts, C. Adelmann, C. Vrancken, A. Moussa, H. Tielens, K. Tomida, M. Pawlak, B. Kaczer, G. Schoofs, W. Vandervorst, D. Wouters and J. Kittl, *J. Vac. Sci. Technol. B*, 29, 01A3041 (2011).

17. V. Longo, N. Leick, F. Roozeboom, and W.M.M. Kessels, *ECS J. Solid State Sci. Technol.*, 2, N15 (2013).

18. V. Longo, M.A. Verheijen, F. Roozeboom and W.M.M. Kessels, *ECS J. Solid State Sci. Technol.*, 2, N120 (2013).

19. N. Menou, M. Popovici, S. Clima, K. Opsomer, W. Polspoel, B. Kaczer, G. Rampelberg, K. Tomida, M. Pawlak, C. Detavernier, D. Pierreux, J. Swerts, J. Maes, D. Manger, M. Badylevich, V. Afanasiev, T. Conard, P. Favia, H. Bender, B. Brijs, W. Vandervorst, S. Van Elshocht, G. Pourtois, D. Wouters, S. Biesemans and J. Kittl, *J. Appl. Phys.*, 106, 094101 (2009).

20. M. Lukosius, T. Blomberg, D. Walczyk, G. Ruhl and C. Wenger, *IOP Conf. Ser.: Mater. Sci. Eng.*, 41, 12015 (2012).

21. D. Bao, X. Yao, N. Wakiya, K. Shinozaki and N. Mizutani, *Appl. Phys. Lett.*, 79, 3767 (2001).

22. Y. Wang and N. Herron, *J. Phys. Chem.*, 95, 525 (1991).

23. G. Hodes, A. Albuyaron, F. Decker and P. Motisuke, *Phys. Rev. B*, 36, 4215 (1987).

24. V.Y. Kolosov and A.R. Thölén, *Acta Mater.*, 48, 1829 (2000).

25. C. Wenger, G. Lupina, M. Lukosius, O. Seifarth, H.J. Muessig, S. Pasko and C. Lohe, *J. Appl. Phys.*, 103, 104103 (2008).

26. C. Ang and Z. Yu, *Phys. Rev. B*, 69, 174109 (2004).

Chapter 8

Impact of composition and crystallization behavior of ALD strontium titanate films on the resistive switching of Pt/STO/TiN devices[*]

Abstract   The resistive switching (RS) properties of strontium titanate ($Sr_{1+x}Ti_{1+y}O_{3+(x+2y)}$, STO) based metal-oxide-metal structures prepared from industrial compatible processes have been investigated focusing on the effects of composition, microstructure and device size. Metastable per-ovskite STO films were prepared on Pt-coated Si substrates utilizing plasma-assisted atomic layer deposition (ALD) from cyclopentadienyl-based metal precursors and oxygen plasma at $350\,^{\circ}\mathrm{C}$, and a subsequent annealing at $600\,^{\circ}\mathrm{C}$ in nitrogen. Films of 15 nm and 12 nm thickness with three different compositions ([Sr]/([Sr]+[Ti]) of 0.57 (Sr-rich STO), 0.50 (stoichiometric STO) and 0.46 (Ti-rich STO) were integrated into Pt/STO/TiN crossbar structures with sizes ranging from 100 μm^2 to 0.01 μm^2. Nano-structural characterizations revealed a clear effect of the composition of the as-deposited STO films on their crystallization behavior and thus on the final microstructures. Local current maps obtained by local-conductivity atomic force microscopy were in good agreement with local changes of the films' microstructures. Correspondingly, also the initial leakage currents of the Pt/STO/TiN devices were affected by the STO compositions and by the films' microstructures. An electroforming process set the Pt/STO/TiN devices into the ON-state, while

---

the forming voltage decreased with increasing initial leakage current. After a reset process under opposite voltage has been performed, the Pt/STO/TiN devices showed a stable bipolar RS behavior with non-linear current-voltage characteristics for the high (HRS) and the low (LRS) resistance states. The obtained switching polarity and nearly area independent LRS values agree with a filamentary character of the RS behavior according to the valence change mechanism. The devices of 0.01 μm^2 size with a 12 nm polycrystalline stoichiometric STO film were switched at a current compliance of 50 μA with voltages of about $\pm$ 1.0 V between resistance states of about 40 kΩ (LRS) and 1 MΩ (HRS). After identification of the influences of the films' microstructures, i.e. grain boundaries and small cracks, the remaining RS properties could be ascribed to the effect of the ([Sr]/([Sr]+[Ti]) composition of the ALD STO thin films.

8.1   Introduction

The increasing importance of advanced information technology drives the searching for an energy-efficient, non-volatile memory device with high integration density, fast access time, high endurance, and sufficient data retention. Among alternative concepts which are discussed for future replacement of today's dynamic random access memory (DRAM) and Flash memory, the redox-based memristive device (ReRAM) is one of the most promising concepts [1]. ReRAM basically consists of an insulator (e.g. a metal oxide) sandwiched between two metal electrodes (MOM stacks), and the information is stored in form of at least two or even multilevel resistance states [2]. The reversible switching between the different resistance states is induced by a certain voltage signal; V_{set}, which sets the device to the low resistance state (LRS, or ON-state) and V_{reset} which resets the device to the high resistance state (HRS, or OFF-state). For ReRAM applications a resistance ratio $R_{off}/R_{on} > 10$ is required, while absolute values in the MΩ range guarantee low power operation. Among the class of resistive switching (RS) materials transition metal oxides are attracting increasing interest [3,4].

For a wide range of metal oxides the valence change memory effect (VCM) occurs characterized by a migration of oxygen anions (or corresponding oxygen vacancies), typically over a length of a few nanometers. The local change of the metal to oxygen stoichiometry results in a nanoionic redox reaction and a valence change of the cation sublattice leading to a change in the electronic conductivity. The VCM effect is a bipolar-type RS where the polarity of the applied voltage determines the direction of the redox reaction, i.e. reduction (set) or oxidation (reset) [5]. Basically, VCM cells consist of an active electrode, at which the RS takes place, a mixed ionic-electronic conducting (MIEC) layer, and an ohmic reference electrode from a material of higher oxygen affinity as compared to the active electrode. The active (switching) interface will form between the MIEC layer and the active electrode with the low oxygen affinity and high work function. In most M/O/M' stacks with a single oxide layer an electroforming (EF) process at higher voltages V_{EF} is required before stable bipolar RS can be obtained. In today's understanding of the VCM-type RS phenomena, the electroforming process locally removes oxygen ions from the insulating oxide lattice providing semiconducting filamentary type paths which allow the high current flow [5]. High forming voltages are undesirable because they are not applicable to integrated devices [6] and because of the large material reconstruction which is induced by the high power applied to the device [7]. The RS behavior of a device under study depends strongly on the performed EF procedure which needs therefore to be discussed along with the RS characteristics them-

selves.

Towards the industrial application of ReRAM devices vertical cross point architectures (VCPA) are intensively discussed for reaching the extreme high integration density required for future memory devices. Therefore, atomic layer deposition (ALD) will be the preferred deposition technique for the preparation of thin films on such 3-dimensional structures. The utilization of ALD processes for ReRAM fabrication so far is basically limited to a few binary oxides, like HfO_2 [8,9], Al_2O_3 [10], and TiO_2 [11,12] grown in amorphous or nano-crystalline form. While only a few studies deal with binary oxide single crystalline material, for example in refs. [13,14].

In this work the use of ALD for ReRAM is extended to STO, a ternary oxide, where the composition of the films can be tuned by the ALD processing parameters. Main focus was on the effect of the cation ratio [Sr]/([Sr]+[Ti]) on the RS performance, because of two reasons. First, the STO composition has a significant effect on the leakage current properties of metal/STO/metal capacitors [15]. Second, stoichiometry effects in the RS phenomena of epitaxial STO structures grown by pulsed laser deposition (PLD) at temperatures of typically $700\,^{\circ}C$ to $800\,^{\circ}C$ have been intensively studied [16] and might serve as a good comparison and therefore give insights on the RS of ALD STO films [17].

The bipolar RS in epitaxial $SrTiO_3$ thin film devices is basically attributed to an electric field and temperature-enhanced drift of oxygen vacancies along filaments that induces a metal-to-insulator transition in the $SrTiO_3$ material [5,18,19]. The confined nature of the conductive filaments in single-crystalline $SrTiO_3$ has been shown by Szot et al. [20] using local-conductivity atomic force microscopy (LC-AFM) with nanometer resolution. In addition to the filamentary-type RS an area-dependent type of RS has been reported for epitaxial $SrTiO_3$ films by Muenstermann et al. [21]. The corresponding I-V switching curves reveal two main differences regarding the switching polarity and the electrode area scaling behavior. It should be noted that the RS polarity is defined for a "standard" M/O/M' configuration, when the voltage of the active electrode is displayed in the I-V curve [5]. With this definition, the "filamentary" type of RS is characterized by a "counter-eightwise" I-V characteristic, and it shows no significant contact area dependence while the "homogeneous" RS effect exhibits an "eightwise" switching polarity and a clear pad size dependence of the conducting LRS state. According to Muenstermann et al. [21], both types of RS, filamentary and area switching, can coexist in the same epitaxial $SrTiO_3$ thin film, depending on the local defect density in the active switching regime. For PLD STO films effects on the RS behavior by growth induced structural defects [22] and by variations in the cation stoichiometry [23] were reported. The stud-

ies on epitaxial STO thin films already showed that the control of the density and the distribution of defects are of utmost importance for the fabrication of reproducible and scalable resistive switching devices. An obstacle for the use of epitaxial STO layers is that they are grown by high temperature PLD processes on single crystalline oxide substrates. Both requirements are not compatible with high-density large-scale integration of up-to-date memory technologies.

In contrast, industrially relevant RS devices need to be integrated onto complementary metal oxide semiconductor (CMOS) chips in analogy to today's production of high-k layers in dynamic random access memories (DRAMs) [24,25] and in analog circuit applications [26-28]. The microstructure of integrated STO thin films is therefore expected to be amorphous, nano-crystalline, or even a mixture of the two. For the conformal growth on three dimensional (3D) structured devices with high integration density, chemical vapor deposition techniques [29,30] and in particular atomic layer deposition (ALD) techniques [15,31-32] were utilized. Although the requirements on the aspect ratio of 3D structures for ReRAM applications are still moderate, the future of high-density ReRAM will also be defined by more challenging 3D topologies [33].

In this study we attempt to link fundamental knowledge about resistive switching mechanisms in single crystalline material with the same material grown in high quality by means of the ALD technique in order to identify key factors in the transfer from the "ideal" system design to the design of "real" structures. According to the previous works, thin film STO is a predestined material for this study. Therefore, a comprehensive analysis of the RS performance of capacitors built from ALD STO thin films was performed with a focus on the effects of films cation composition, microstructure, and morphology. While the [Sr]/([Sr]+[Ti]) ratio in the as-deposited amorphous films could be well controlled by means of the ALD pulsing sequence, the microstructure and morphology of the polycrystalline STO thin films was found to depend in a complex manner on various external parameters, like the substrate material, the cation stoichiometry, the film thickness, and the annealing conditions [15,34]. We will show that, in addition, the RS behavior of the ALD STO based device is affected by the [Sr]/([Sr]+[Ti]) composition and by the thin film's microstructure and morphology.

8.2   Experimental Section

12 and 15 nm thick $Sr_{1+x}Ti_{1+y}O_{3+(x+2y)}$ films with various compositions, [Sr]/([Sr]+[Ti]) of 0.57 (Sr-rich), 0.50 (stoichiometric) and 0.46 (Ti-rich), were deposited by means of plasma-assisted atomic layer deposition (ALD) at 350 °C in an Oxford Instruments Fl-
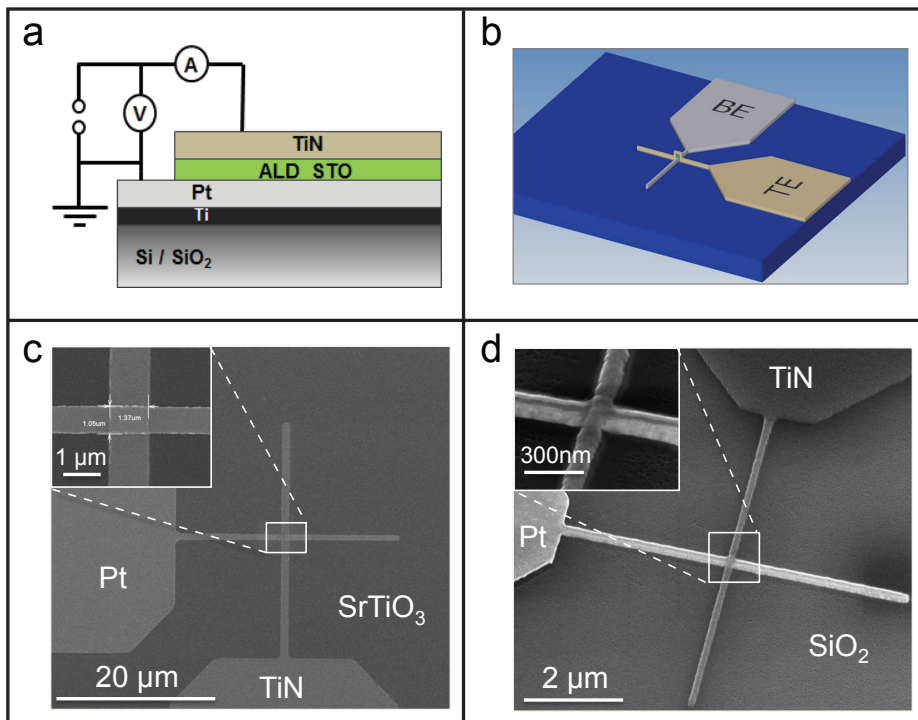
Figure 8.1: (a) Stack sequence and electrical measurement setup of the Pt/STO/TiN devices. (b) Schematic picture of the nano-crossbar structures with the bottom (BE) and the top electrode (TE). In the "top-down" approach the switching oxide layer only remained under the TE. (c) SEM micrographs of a micro-crossbar Pt/STO/TiN structure. In the "bottom-up" approach the TiN TE is structured by a lift-off technique. (d) SEM micrographs of a nano-crossbar Pt/STO/TiN structure; the TiN and the STO underneath are structured by RIBE.

exAL reactor. Platinum coated silicon wafers with a layer stack of Si/SiO$_2$ (430nm)/Ti (5nm)/Pt (30nm) were used as substrates with the Pt bottom electrode in planar or bar-structured configuration. Cyclopentadienyl-based precurors from AirLiquide, namely, Ti-Star, (pentamethylcyclopenta-dienyl) tri-methoxy-titanium, CpMe$_5$Ti(OMe)$_3$, and Hyper-Sr, bis(tri-isopropylcyclopentadienyl)-strontium with a 1,2-dimethoxy-ethane adduct, Sr(^{i}Pr$_3$Cp)$_2$DME, were used in sequence with oxygen plasma as the co-reactant. The [Sr]/([Sr]+[Ti]) ratios of the films were adjusted by tuning the [SrO]/[TiO$_2$] ALD cycle ratio while the film thicknesses were controlled by the numbers of executed ALD cycles. Details on the growth process can be found in a recent publication [35]. For the determination of the thickness, and the optical properties of the films grown on planar Si/Pt substrates, ex-situ spectroscopic ellipsometry (SE) measurements were performed on a J.A. Woollam/M2000D system (1.25-6.5 eV). The [Sr]/([Sr]+[Ti]) content of the as-deposited STO films was estimated from the optical properties of the thin films determined by SE employing a library calibrated by Rutherford back-scattering measurements [35]. Additionally, the composition was determined from X-ray photoelectron spectroscopy (XPS) data taken with a Thermo Scientific K-Alpha spectrometer using monochromatic Al Kα X-ray radiation ($h\nu$ = 1486.6 eV). Charge correction was performed by setting the C1s signal at a binding energy of 284.8 eV [36]. A post-deposition rapid thermal annealing (RTA) of the films at 600 °C in nitrogen atmosphere was performed for crystallization of the layers into the perovskite structure. The chemical and structural properties of the annealed films grown on planar Pt substrates were analyzed by means of XPS and by grazing-incidence X-ray diffractometry (GI-XRD) using a Panalytical X'Pert PRO MRD with Cu Kα radiation. In addition, the morphology of the annealed films was studied by scanning electron microscopy (SEM) using a Hitachi SU 8000 system. Local-conductivity atomic force microscopy (LC-AFM) analyses were done with a Pt/Ir coated tip on a JEOL JSPM-5200 scanning probe microscope to record topography and current maps under UHV conditions at 200 °C. For the resistive switching characterization, similar STO thin films were integrated into Pt/STO/TiN crossbar devices on Si/SiO$_2$ substrates. Schematics of the stack sequence and of the lateral structure together with two representative electron micrographs are shown in Figures 8.1.a-d. The fabrication of the bottom electrodes (BE) on (25×25 mm^2) silicon substrates with about 430 nm thermal oxide started by sputtering of 5 nm Ti and 30 nm Pt. A conventional photolithography process using a Mask Aligner MA6, Karl Suess combined with reactive ion beam etching (RIBE) with argon plasma in an Oxford Ionfab 300 Plus system to pattern the micro-sized BE. For the nano-sized Pt BE a structuring process was performed by UV nanoimprint lithography (NIL) using a Nanonex NX 2000 nanoimprinter and RIBE. In

analogy to the planar structures, the STO thin films were grown by plasma-assisted ALD and subsequently annealed at $600\,^\circ$C in flowing nitrogen for 10 min (15 nm) and 5 min (12 nm). The top electrodes (TE) of the micro-crossbar cells were prepared in a "bottom-up" approach as follows. First, the electrode structures were defined by photolithography. Then, a 30 nm thick TiN film was deposited by sputtering, and the TE was structured by a lift-off process. Last, the platinum bottom electrode (BE) of each device was opened for making an external electrical contact, again by means of photolithography and RIBE. A top-view SEM micrograph of the micro-crossbar structure is shown in Figure 8.1.c. The TEs of the nano-crossbar cells were prepared in a "top-down" approach. First, 30 nm thick TiN was deposited by sputtering, second, the TE structures were defined by means of e-beam lithography using a Vistec EBPG 5000 plus system. Next, the TiN layer and the STO films underneath were patterned by means of reactive ion beam etching (RIBE) with CF_4 plasma. A schematic and a scanning electron micrograph are given in Figures 8.1.b and d. For both types of cross bar structures the final stack sequence in the cross junction area consisted of the BE (5nm Ti/30 nm Pt), the functional STO film of (15 or 12 nm), and the TE (30 nm TiN) as depicted in Figure 8.1.a. The lateral dimensions of the active device areas ranged from (10×10) μm^2 to (1×1) μm^2, and (100×100) nm^2, for the micro- and nano-crosspoint junctions, respectively. The current-voltage (I-V) characteristics were recorded in a quasi-static mode under ambient conditions using an Agilent B1500A semiconductor analyzer combined with a Suess Microtec PA-200 probe station. In the used configuration the current-resolution of the setup was in the range of 1 pA. In the measurements of the Pt/STO/TiN crossbar devices the voltage signal was always applied to the top electrode (TiN) while the bottom electrode (Pt) was grounded.

8.3   Results and Discussion

8.3.1   Physical and Chemical Properties of STO Films

The chemical composition and the thickness of as-deposited STO films on planar Si/Pt structures were characterized by means of spectroscopic ellipsometry (SE) and X-ray photoelectron spectroscopy (XPS). Further details on the characterization methods applied to comparable STO films grown on different substrates have been reported in references [34,35,37]. Table 8.1 comprises the properties of the STO films which were used in this study. It should be mentioned that the planar Pt layers were deposited in exactly the same manner as the Pt bottom electrodes of the crossbar structures in order to assure identical ALD growth behavior of the STO films. Films of three different compositions

Table 8.1: Cation stoichiometry of the STO films as-deposited on planar Si/Ti/Pt substrates given as a function of the ALD process parameters. The [Sr]/([Sr]+[Ti]) content ratios were determined by SE and cross-checked by XPS. The relative errors in the [Sr]/([Sr]+[Ti]) ratios from SE and XPS are ± 0.03 and ± 0.02, respectively.

STO composition	[SrO]/[TiO$_2$] ALD cycle ratio	[Sr]/([Sr]+[Ti]) ratio from SE	[Sr]/([Sr]+[Ti]) ratio from XPS
Ti-rich	1:4	0.46	0.46
Stoichiometric	1:3	0.50	0.50
Sr-rich	1:2	0.57	0.58

were obtained, Ti-rich STO, stoichiometric STO, and Sr-rich STO with [Sr]/([Sr]+[Ti]) ratios of 0.46, 0.50, and 0.57, respectively.

The as-deposited amorphous films underwent a rapid thermal annealing (RTA) step at $600\,^\circ$C to achieve crystallization where the film thickness is decreased of about 10-15 % of the initial value. Although variations of the cation composition in the as-deposited amorphous films can be easily adjusted in ALD, induced effects on the film crystallization behavior might result in different microstructures for films of various compositions after crystallization. In addition, the incorporation of excess strontium or titanium oxide into the SrTiO$_3$ thin films is an issue.

High quality SrTiO$_3$ single crystals exhibit a rather low solubility limit for either excess SrO or excess TiO$_2$. Witek et al. [38] found for STO ceramics that a Ti excess of only 0.5 at% is sufficient to start the segregation of TiO$_2$. Depending on the oxygen content, not only TiO$_2$ but also various titanium suboxides might form [39]. In consequence, intergrowth of SrO layers or TiO$_2$ layers and the perovskite-type SrTiO$_3$ might occur. The intergrowth leads to the formation of either Ruddelsden-Popper phases for the Sr-rich STO material (Sr$_{n+1}$Ti$_n$O$_{3n+1}$) [40,41] or Magneli type-phases for the Ti-rich STO films (Ti$_n$O$_{2n-1}$)(SrTiO$_3$) [42,43].

Depending on the growth or annealing temperature the mean free path of cations is limited, and therefore in the STO thin films the ordered-fashion-type intergrowth might only happen on a local scale leading to micro-regions of slightly different composition [41]. The incorporation of cations in excess of the stoichiometric SrTiO$_3$ composition has been investigated for different ALD STO thin films used as high-k material [15]. Clima et al. [44] and Popovici et al. [32] studied the crystallization behavior of Sr-rich STO films grown by thermal ALD from Sr(^{t}Bu$_3$Cp)$_2$ and Ti(OMe)$_4$. After RTA at $600\,^\circ$C the films showed perovskite-type reflections in XRD while the peaks of the Sr-rich film are slightly shifted towards lower angle as compared to the stoichiometric film. This "low temperature metastable crystalline" state was transferred into a Ruddlesden-Popper
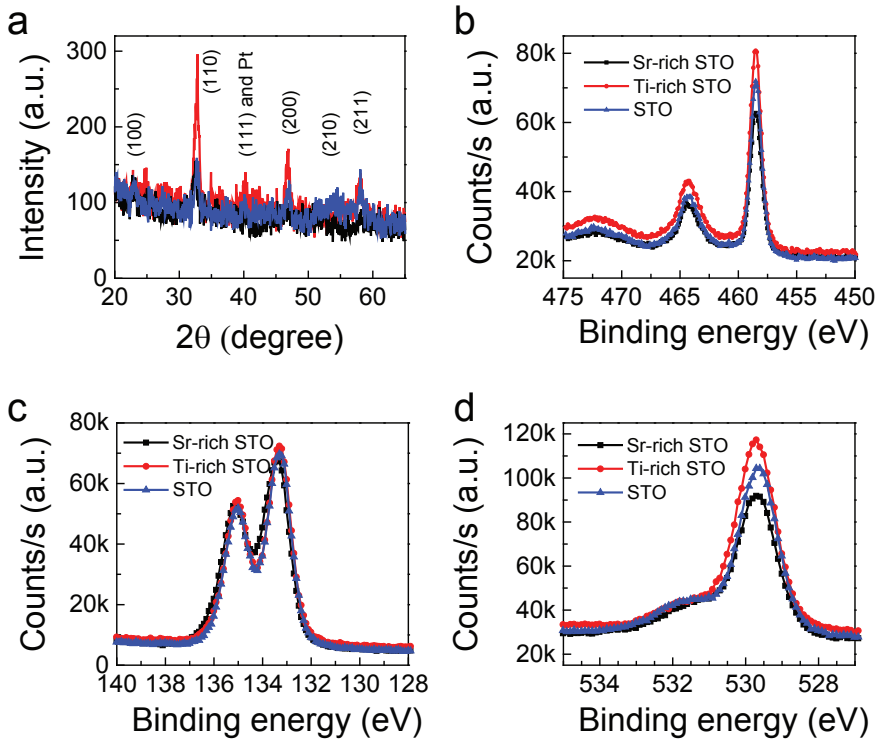
Figure 8.2: Structural and chemical characterization of 12 nm thick STO films with different [Sr]/([Sr]+[Ti]) compositions according to Table 8.1. The films were grown on planar Pt/Si substrates and annealed at $600\,^{\circ}$C in nitrogen for 5 minutes, analog to the crossbar structures; (a) GI-XRD scans, (b-d) XPS spectra of the Ti2p lines (b), the Sr3d lines (c), and the O1s lines (d).

(RP)-type crystalline structure, $SrO(SrTiO_3)_n$, after annealing at about $1000\,°C$ [44]. A similar result was reported by Shibuya et al. [45] showing that PLD grown Sr_2TiO_4 films exhibit a distribution of extended defects or a regular RP-phase structure depending on the growth temperature. In the resistive switching behavior of oxide devices local imperfections and inhomogeneities in the thin film structure and morphology can play an important role. Therefore the micro-structural properties of the $600\,°C$ annealed ALD STO thin films were carefully analyzed.

Figure 8.2.a shows the GI-XRD scans of 12 nm thick STO films of the three compositions annealed at $600\,°C$ for 5 minutes. The spectra clearly show that despite of the non-stoichiometry, all STO films appeared to crystallize into the metastable perovskite phase. The results are comparable to the previous reports on the micro-structural evolution of annealed ALD STO films [15,27,32,35]. For the metastable crystalline Sr-rich STO films it is suggested that the excess SrO could be distributed randomly and in a disordered manner in the $SrTiO_3$ matrix. This picture might also apply to the metastable crystalline STO thin films of different stoichiometry investigated in this study.

Detailed photoelectron spectra of the Ti2p, Sr3d, and O1s signals taken for the 12 nm thick STO films after annealing at $600\,°C$ are shown in Figures 8.2.b-d, respectively. The binding energies of $Ti2p_{3/2}$ of ≈ 458.5 eV, and of $Sr3d_{5/2}$ of ≈ 133.3 eV found for all the three samples with different compositions are in good agreement to bulk reference data [46]. For a comparative analysis of the chemical states of the constitutive cations in the stoichiometric, Ti-rich and Sr-rich STO films, the photoelectron spectra for the Ti2p and Sr3d signals were normalized to the maximum intensity of the $Ti2p_{3/2}$ and $Sr3d_{5/2}$, respectively. The normalized patterns are given in the insets of the figures. The Ti2p lines show the same valence states and FWHM values for all three STO compositions, while in general the thin film signals reveal a broadening as compared to single crystal reference data indicating a higher degree of lattice disorder. The Sr3d lines of the stoichiometric and the Ti-rich STO film are nearly identical, while for the Sr-rich STO a broadening of the lines towards higher binding energies is observed, which indicates the formation of a Sr-carbonate compound in the near surface region. In addition, the O1s signals show two features, a broad shoulder originating from carbonyl-adsorbates on the surface and the O1s peak at ≈ 529.8 eV attributed to $SrTiO_3$. The intensity ratio of surface oxygen to bulk oxygen increases with increasing [Sr]/([Sr]+[Ti]) content. The formation of a strontium carbonate compound on the surface of the Sr-rich STO film agrees to a microscopic model of an intergrowth of SrO and $SrTiO_3$ layers in the Sr-rich STO films (0.57), where SrO in the near surface region will react to form $SrCO_3$ based compounds.

XRD and XPS analyses of the $600\,°C$ annealed STO films revealed perovskite-type
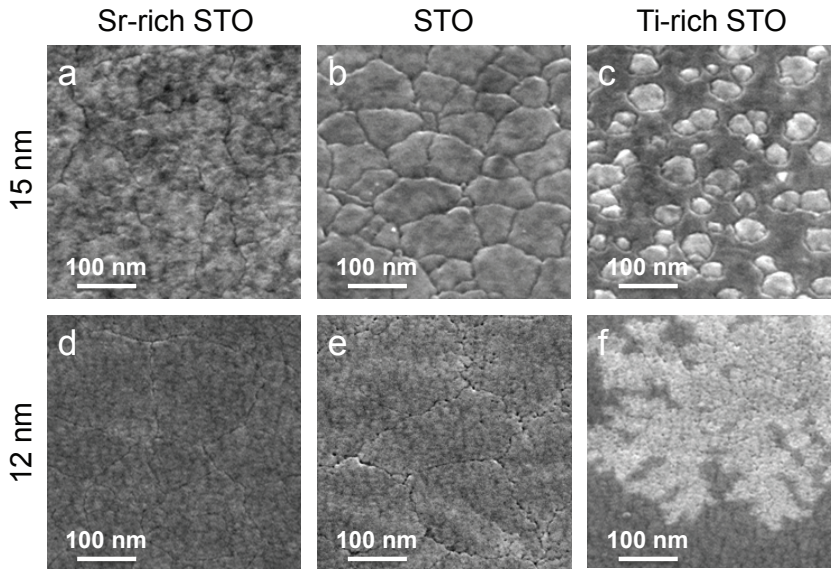
Figure 8.3: SEM top view micrographs of STO thin films of different [Sr]/([Sr]+[Ti]) compositions grown on planar Si/Pt substrates after annealing at 600 °C in nitrogen; (a-c) 15 nm films annealed for 10 min, (d-f) 12 nm films annealed for 5 min; the STO compositions are arranged from the left to the right Sr-rich (a,d), stoichiometric (b,e), and Ti-rich (c,f).

crystalline phases with contributions from intergrowth of excess-cation oxide. XPS data suggests the possibility of SrO intergrowth in the Sr-rich STO films. Although defined signals originating from TiO_{2-x} intergrowth in the Ti-rich STO films were not observed, the broadening of the Ti2p lines might indicate additional Ti oxidation states.

8.3.2   Thin film microstructure and morphology

The microstructure and the morphology of the plasma-assisted ALD STO thin films after annealing at 600 °C were analyzed with respect to the different compositions and film thickness. The thin film crystallization is controlled by the kinetics of nucleation and grain growth. On similar thin films deposited on Si_3N_4 grids Longo et al. [34] showed by means of transmission electron microscopy (TEM) that the crystallization of the films yielded transrotational perovskite-type crystals. In addition, the important effect of the STO composition and the annealing temperature on the final grain size, the crack and the void formation has been demonstrated. In particular, the regular small-grain morphology

of the crystalline Sr-rich STO films was imputed to a high nucleation probability at the onset of crystallization process.

The microstructural characterizations were performed on STO thin films of Sr-rich (0.57), stoichiometric (0.50) and Ti-rich (0.46) composition deposited on planar Si/Pt substrates after annealing at 600 °C in nitrogen for about 5 min (12 nm) and 10 min (15 nm). Figure 8.3 displays the plan-view high resolution SEM top view micrographs of the annealed STO thin films. The graphs of the 15 nm thick STO films are shown in Figures 8.3.a-c and those of the 12 nm films are given in Figures 8.3.d-e. The micrographs are arranged from left to right with respect to a decreasing Sr-content, in particular Sr-rich STO (0.57), stoichiometric STO (0.50), and Ti-rich STO (0.46). The Sr-rich and the stoichiometric composition each show a comparable surface morphology for the films of different thickness, while grain boundaries appear more pronounced in the 15 nm thick STO films as compared to 12 nm thick films. The Sr-rich STO films (Figures 8.3.a, d) exhibit a finer grained structure with a more uniform morphology compared to the stoichiometric films (see Figures 8.3.b, e) where grid-patterns indicate small cracks formed at the grain boundaries upon crystallization and consequent densification (see also [34]). The cracks seem less pronounced for the Sr-rich films. This is consistent with the previous TEM study [34] which revealed an increased nucleation density leading to a higher density of smaller grains for the Sr-rich films as compared to the stoichiometric STO films. The Ti-rich STO films showed altogether a different surface morphology. Regimes of different contrast with a lateral extension of about 100 nm-500 nm are revealed in the SEM micrographs (Figures 8.3.c, f). Referring to previous crystallization studies [34], the morphological differences were explained by a locally incomplete crystallization process. In particular, additional AFM analyses (see Figure 8.4.c) revealed the brighter contrast regions being about 10 % thinner compared to the surrounding darker regions. The reduced thickness is related to a densification process due to the crystallization. The different shapes of the crystallites between the films of 12 nm and 15 nm in thickness might relate to a thickness effect on the crystallization or to slight differences in composition. It has been shown that Ti-rich STO thin films require an increased thermal budget to achieve crystallization compared to stoichiometric and Sr-rich films [34]. Hence, slight differences in composition can lead to pronounced changes in the crystallization behavior of the Ti-rich films.
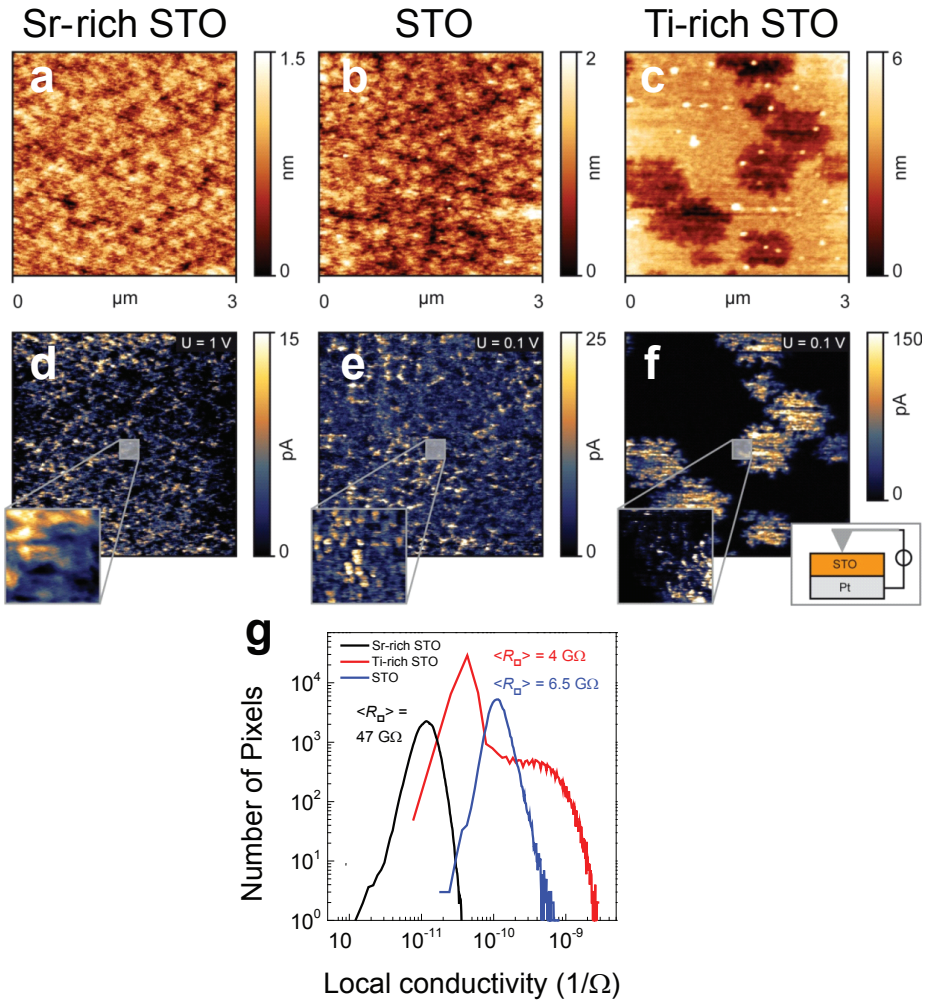
Figure 8.4: (a-c) AFM and (d-f) LC-AFM pictures showing the topography and the corresponding current maps, respectively, of the 12 nm STO thin films grown on planarSi/Pt substrates and annealed for 5 minutes. at 600 °C in nitrogen; the STO compositions are arranged from the left to the right Sr-rich (a,d), stoichiometric (b,e), and Ti-rich (c,f). The LC-AFM measurements were performed at 200 °C under UHV conditions with the voltage applied to the AFM tip. (g) Histogram of the local conductivity values shown in pictures (d-f). Average resistance values <R$_\square$> refer to the measured areas of (3 × 3) μm^2.

8.3.3 Local conductivity probed by LC-AFM

Morphological atomic force microscopy (AFM) and local-conductivity atomic force microscopy (LC-AFM) studies were performed in order to analyze local conducting paths along grains and grain boundaries. For this, the films' surface topography was recorded in parallel to a laterally resolved current mapping for the 12 nm thick STO films annealed for 5 min. at 600 °C. The measurements were performed under ultra-high vacuum (UHV) conditions at 200 °C while a constant voltage was applied to the sample via a conducting Pt/Ir-coated AFM tip. The AFM results shown in Figures 8.4.a-c reveal distinct topographical differences between the three samples, with the surface of the Sr-rich (a) and the stoichiometric STO (b) film being rather flat and consisting of grains separated by grain boundaries. The corresponding current maps (Figures 8.4.d-f) show an inhomogeneous distribution of differently conducting regimes. Although the averaged conductivity of the Sr-rich sample (Figure 8.4.d) was significantly lower than that of the stoichiometric STO (Figure 8.4.e), both films reveal conducting paths along grain boundaries. Small cracks in the stoichiometric STO film which appear in the topography map (Figure 8.4.b) as darker lines show up as slightly brighter lines in the LC-AFM map (Figure 8.4.e). The degree by which the nano- or microcracks contribute to the total leakage current of a device might depend on the dimensions of the cracks for each individual case. Comparable results on local leakage non-uniformity in ALD STO thin films have been reported by Menou et al. [15] who also attributed the higher leakage paths to micro-cracks in their films. The topography map of the partly crystallized Ti-rich STO film (([Sr]/([Sr]+[Ti])=0.46) in Figure 8.4.c looks completely different as for the other STO compositions. The corresponding current map in Figure 8.4.f shows that the thinner areas of the material exhibit increased conductivity indicating that semiconducting phases are formed locally in the Ti-rich STO films. One might notice the remarkable accordance between the AFM, LC-AFM and SEM images with respect to the areas of reduced film thickness in Figure 8.4.c and these with enhanced conductivity in Figure 8.4.f. Therefore, these regimes might be described by being large crystal plates of Ti-rich STO phase embedded in an insulating matrix of amorphous material. The assumption of partial crystallization is in qualitative agreement with the results of a recently performed TEM study [34], while slight variations in the film growth might arise from the different substrates.

The LC-AFM results clearly reveal locally inhomogeneous current spots which relate to the thin film's microstructure being influenced by the film's composition as the result of a stoichiometry-affected nucleation and crystallization behavior. Thus, in or-

der to interpret the electrical properties of the RS devices properly, both, the influence of the [Sr]/([Sr]+[Ti]) composition as well as the microstructure of the ALD STO thin films after annealing have to be considered. It should be mentioned that the above de-scribed microstructural phenomena particular appear on a length scale of a few hundred nanometers. Therefore the electrical properties of the micro-crossbar structures present average thin film properties, whereas for the nano-crossbar devices with the pad size ap-proaching the grain size one would expect a slight statistical change in the electrical data. In the 100 nm regime the pad might either cover a single grain or two grains with a grain boundary in between or, alternatively for the Ti-rich STO films the pad could either sit on the amorphous, less conducting matrix or on a semiconducting grain. In addition, the presence of a current inhomogeneity on the smaller scale could be observed by LC-AFM at higher resolution. The grains of the Sr-rich and stoichiometric STO (see Figure 8.4.d,e) revealed additional local conductivity spots with a diameter of 10 nm to 30 nm inside the grains. This observation agrees with the evidence of voids with diameter of a few nano-meters within single STO grains found by TEM in our previous study [34]. Since the stoichiometry range of $SrTiO_3$ is very small, a phase separation in non-stoichiometric parts could also evolve. Hence, one possible explanation of the locally different con-ductivity observed by LC-AFM could be that in the investigated Ti-rich STO thin films TiO_x-phases [47] were present influencing the local conductivity.

In the histogram in Figure 8.4.g, the distribution of the local conductivity as measured by the LC-AFM scans in Figure 8.4.d-f over an area of $3 \times 3 \ \mu m^2$ is shown. The num-ber of pixels is plotted logarithmically versus the local conductivity calculated from the measured current and the applied voltage, $\sigma_{loc} = I_{loc}/V_{tip}$. This allows a semi-quantitative discussion of the mean thin film resistance values $<R_\square>$. It can be seen that the average conductivity of the Sr-rich STO film was the lowest ($<R_\square>$ = 47 GΩ) although a relat-ively high voltage of 1.0 V was applied to the sample, whereas for the stoichiometric STO film a higher average conductivity was determined ($<R_\square>$ = 6.5 GΩ) at a lower applied voltage of 0.1 V. The Sr-rich and the stoichiometric STO thin film both exhibit comparable unimodal conductivity distributions indicating that the distribution of con-ducting grains is similar in both cases despite of the overall difference in conductivity. The histogram of the Ti-rich STO film instead shows a bimodal distribution relating to the two regions with different local conductivities. While a large part of the scanned area revealed a low local conductivity resulting in the appearance of the maximum peak in the histogram, the highly conducting areas in Figure 8.4.f are reflected by the tail of the distribution at higher conductivities. The width of the local conductivity distribution in the histogram is the highest for the Ti-rich sample due to the inhomogeneous distribution

of conducting grains, while the mean value of the thin film resistance $<R_\square> = 4$ GΩ is only slightly smaller than the value of the stoichiometric STO film.

8.3.4 Electrical properties of MOM devices in the initial state

The effect of the [Sr]/([Sr]+[Ti]) composition on the dielectric properties of MOM based devices obtained from 15 nm thick films annealed at 600 °C has been investigated in a previous study [50]. Mean values of the capacitance density were about 50 $fF/\mu m^2$, 25 $fF/\mu m^2$, and 10 $fF/\mu m^2$ for the stoichiometric, the Sr-rich and the Ti-rich composition, respectively. Considering the identical device geometry and the same film thickness the differences were addressed to the different microstructures and different bulk properties of the STO layers. The high effective dielectric permittivity of $\epsilon_{eff} \approx 85$ was attributed to a higher degree of crystallization in the stoichiometric STO film as compared to nanocrystalline Sr-rich STO ($\epsilon_{eff} \approx 42$) and partly amorphous Ti-rich STO film ($\epsilon_{eff} \approx 17$).

Figures 8.5.a and b show representative current-voltage (I-V) characteristics of the pristine Pt/STO/TiN crossbar devices measured in the range of ± 2.0 V with the voltage signal always applied to the TiN top electrode. A statistical analysis from 30 devices for each sample is shown in Figures 8.5.c and d, respectively, showing the cumulative distribution function (CDF) for the leakage current of the stoichiometric and Ti-rich STO samples measured at +1.0 V and of the higher insulating Sr-rich STO devices measured at +2.0 V.

Micro-crossbar devices. Figure 8.5.a shows the I-V plots for micro-crossbar cells of about 1 μm^2 size made from the Sr-rich, stoichiometric, and Ti-rich STO films of about 15 nm thickness annealed at 600 °C for 10 minutes. The slight asymmetry of the current values with respect to the voltage polarity is attributed to the difference in the work functions of the respective electrode metals, Pt and TiN, thus giving rise to different Schottky barrier heights of the respective metal/STO interfaces. Although well-defined data for ALD STO/metal interfaces are not available from the literature, the ALD HfO$_2$/metal system might serve as a reference here. For these interfaces effective metal work functions of 5.15 eV for Pt [48] and (4.56 ± 0.35) eV for TiN [49] in contact to ALD HfO$_2$ have been determined revealing a barrier offset of roughly 0.5 eV. From the 50% values of the CDF functions (Figure 8.5.c) mean initial resistances of the micro-crossbar devices were determined being about 5 GΩ for Sr-rich STO, 4 MΩ for Ti-rich STO and 25 kΩ for the stoichiometric STO. The surprisingly high values of the leakage current in the stoichiometric STO devices contradict the findings reported by other groups [15,31].
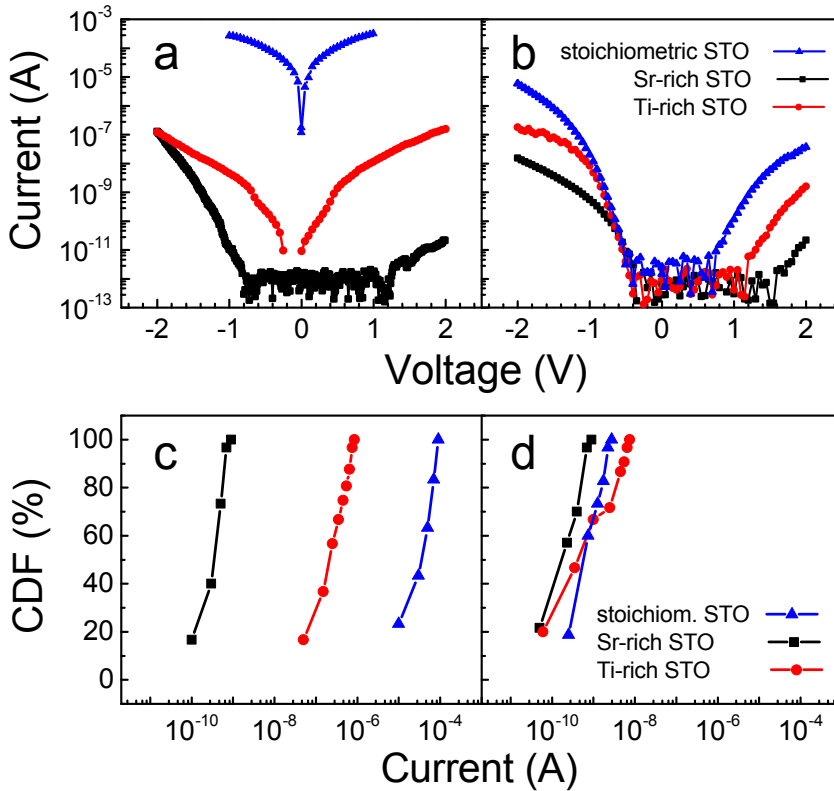
Figure 8.5: Current-voltage (I-V) characteristics as a function of the STO composition (see Table 8.1) of Pt/STO/TiN devices in pristine state measured at room temperature with the voltage applied to the TiN top electrode. (a) Micro-crossbar devices of 1 μm^2 size made from 15 nm thick polycrystalline STO films, and (b) 0.01 μm^2 size nano-crossbar structures with 12 nm thick STO integrated. And cumulative distribution functions (CDF) representing the leakage current variations of the (c) micro-crossbar and (d) nano-crossbar devices. The current for the Sr-rich STO films is measured at +2.0 V, for the stoichiometric and Ti-rich films the current values are determined at +1.0 V.

This might be attributed to the formation of micro-cracks allowing an enhanced current flow. The insulating behavior of the Sr-rich devices is in line with the regular dense morphology of the fine-grained films and with the slightly increased band gap found for the Sr-rich STO [50].

Nano-crossbar devices. Figure 8.5.b shows the I-V plots for the nano-crossbar devices of 0.01 μm^2 size built from the STO films of different compositions which were annealed at 600 °C for 5 minutes. For the small pad sizes the current-resolution of the setup of about 1 pA was easily reached at low voltages. The leakage current data of the 12 nm polycrystalline STO films at higher voltages are in reasonable agreement with results reported for high-k STO thin films [15,31]. Apparently, the leakage current for the stoichiometric STO films of 12 nm thickness was considerably reduced as compared to the 15 nm thick films (see Figure 8.5.a). This behavior might be attributed to the different microstructures of the films. The SEM micrographs in Figures 8.3.b and e clearly show that micro-cracks are more pronounced in the 15 nm as compared to the 12 nm film. This might originate either from the variation of the film thickness or the slightly different annealing times, or both. This comparison further supports the assumption that the enhanced current flow in the devices containing stoichiometric STO films was mainly along nano- or micro-cracks rather than along grain boundaries. A statistical analysis of the mean leakage currents of the STO nano-crossbar devices is given in Figure 8.5.d. The data for the Sr-rich and stoichiometric STO devices are based on a yield of > 90%. Thus mean resistance values of about few 10 GΩ for Sr-rich STO and few GΩ for the stoichiometric STO devices are determined as representative values. The Ti-rich STO nano-crossbar devices show a bigger spread in their initial resistance values ranging from about several GΩ to about 100 MΩ. The type of bimodal device distribution (see Figure 8.5.d) is consistent with the local conductivity distribution determined by LC-AFM (see Figure 8.4.g). Thus for the case of the partly crystallized 12 nm Ti-rich STO films the nano-crossbar devices might cover different areas of crystalline and amorphous material which results in a larger spread of the initial resistances. For the RS study we comprised the data of all devices which were formed into the ON state by a positive voltage signal and which were successfully reset to the OFF state by a negative voltage applied to the top electrode.

8.3.5 Electroforming of the MOM devices

The voltage controlled electroforming process [51] was performed for the Pt/STO/TiN diodes by applying a positive voltage ramp to the TiN TE, with the Pt BE being groun-
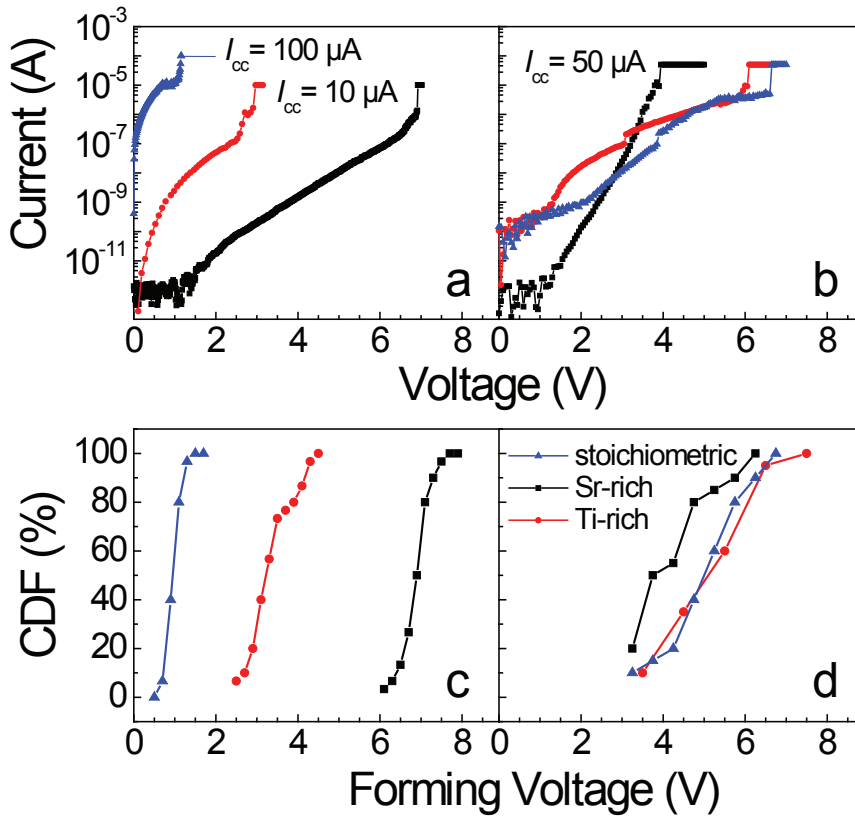
Figure 8.6: Representative electroforming I-V curves for the (a) micro-crossbar (1 μm^2, 15 nm STO) and (b) nano-crossbar (0.01 μm^2, 12 nm STO) Pt/STO/TiN devices. A positive voltage ramp applied to the TiN top electrode initiated a soft-breakdown event while the devices were protected by a current compliance I_{cc}. Each cumulative distribution function (CDF) was derived from thirty electro-formed (c) micro- and (d) nano-crossbar devices.

ded. To protect the device from hard breakdown a current compliance I_{cc} for the electroforming procedure was set with values between 10 μA and 100 μA, depending on the leakage current behavior of the investigated cell. Representative electroforming curves for devices of different STO compositions and for two different pad sizes, explicitly 1 μm^2 and 0.01 μm^2, are shown in Figures 8.6.a and b, respectively. The voltage at which the abrupt increase in current, the soft breakdown, occurred was identified as the electroforming voltage V_{EF}. Thus, the initially insulating MOM structure changed into a higher conducting state, which represents voltage-induced electroforming into the ON state. The application of a voltage ramp of opposite polarity resulted in a partial recovery of a high resistivity, thus the device was reset into the OFF state. For the micro-crossbar devices from STO films of different compositions (see Figure 8.6.a) a clear trend of decreasing electroforming voltage with increasing leakage current of the MOM structure is observed. This trend was not explicitly repeated in the electroforming behavior of the nano-crossbar devices (Figure 8.6.b), which nevertheless reproduce well the I-V curves of the pristine devices for voltages below +2.0 V (see Figure 8.5.b). This observation is attributed to differences in the conduction mechanisms at high fields for the devices built from STO thin films of different compositions and vairous microstructures.

In summary, all different Pt/STO/TiN devices were electroformed into the ON state when a voltage ramp of positive polarity was applied to the TiN TE. If the samples were afterwards polarized with a negative voltage of about -3.0 V, the high current through the devices was reduced significant, the devices were reset into a higher resistance state, the OFF state. Under subsequent cycling of the voltage signal, the devices showed a hysteretic I-V characteristic, i.e. switching between low (LRS = ON) and high resistance (HRS = OFF) state. For each STO thin film sample statistical analysis for an average of 30 devices formed into the ON state was performed with respect to the electroforming and the RS behavior. Figures 8.6.c and d show the cumulative probability plots of the electroforming voltages (V_{EF}) as a function of the STO composition for 1 μm^2 devices with 15 nm thick STO and 0.01 μm^2 cells with 12 nm thick STO, respectively. For the micro-crossbar cells (Figure 8.6.c) a clear dependency of the films composition on the V_{EF} value is found, with very little variation in V_{EF} for different devices. The mean values were for Sr-rich STO V_{EF} = 7.0 $\pm$ 1.0 V, for Ti-rich STO V_{EF} = 3.5 $\pm$ 1.0 V, and for stoichiometric STO V_{EF} = 1.0 $\pm$ 0.5 V. The electroforming voltages are higher for devices with lower initial leakage currents. Interestingly, for the nano-crossbar devices a similar effect of the different STO composition on the electroforming voltage was not observed. However, in comparison to the micro-crossbars the device-to-device variations in electroforming voltage increased considerably as demonstrated by the non-steep CDF-

characteristics in Figure 8.6.d. Mean values determined for the various compositions were for Sr-rich STO $V_{EF} = 4.5 \pm 1.5$ V, and for stoichiometric and Ti-rich STO $V_{EF} = 5.0 \pm 2.0$ V. Considering the LC-AFM current maps (see Figure 8.4) these larger variation of the V_{EF} values for the nano-crossbar structures might be attributed to a device scenario where the contact pad sizes approach the lateral dimensions of the local conductivity changes of the thin films. This "lateral parameter" can be either the grain size, the distance between small cracks for the Sr-rich and stoichiometric STO films, or the distance between the grains for the Ti-rich STO films. From the apparent changes in the CDF-characteristics of V_{EF} (see Figures 8.6.c, d) which are observed upon changing the crossbar size from "micro" to "nano", we can determine a characteristic length of about a few 100 nm as the distance between local weak spots in the annealed STO thin films. This is in good agreement with the dimensions of the local changes observed in LC-AFM. In summary, the electroforming voltage of M/STO/M devices is affected by the STO composition in two different ways. The change of the material's stoichiometry affects, intrinsically, the conduction mechanism in the STO film and, extrinsically, the thin film's microstructure and morphology.

8.3.6   Resistive switching of Pt/STO/TiN devices

After the electroforming and reset procedures had been carried out, all devices studied exhibited bipolar resistive switching (RS) behavior. Exemplary, Figures 8.7.a-c show the quasi-static I-V sweeps obtained for the Pt/STO/TiN nano-crossbar structures with STO films of different compositions. The nano-crossbar devices could be stable switched at a current compliance of $I_{cc} = 50$ μA with a resistance ratio of $R_{off}/R_{on} > 10$, fulfilling the requirement for ReRAM operation [19]. In addition, Figure 8.7.d shows the endurance plot for the Ti-rich STO nano-crossbar device obtained by repeating 1000 quasistatic switching cycles taking. At a read voltage of $V_{read} = +0.3$V the mean resistance values are 15 kΩ for LRS and > 3 MΩ for HRS. The micro-crossbar devices showed similar RS characteristics although higher I_{cc} values were required.

All the Pt/STO/TiN crossbar devices exhibited the same polarity of the bipolar switching characteristic. For the I-V curves shown in Figures 8.7.a-c the current is plotted against the voltage signal applied to the TiN top electrode. For discussing the polarity in respect of a switching model, the I-V hysteresis needs to be referred to the voltage signal at the active switching interface, which for the crossbar cells is the Pt/STO interface. Exemplary, the inset in Figure 8.7.c shows the corresponding I-V_{Pt} switching curve with the voltage V_{Pt} applied to the Pt electrode given on the abscissa. Thus, the Pt/STO/TiN
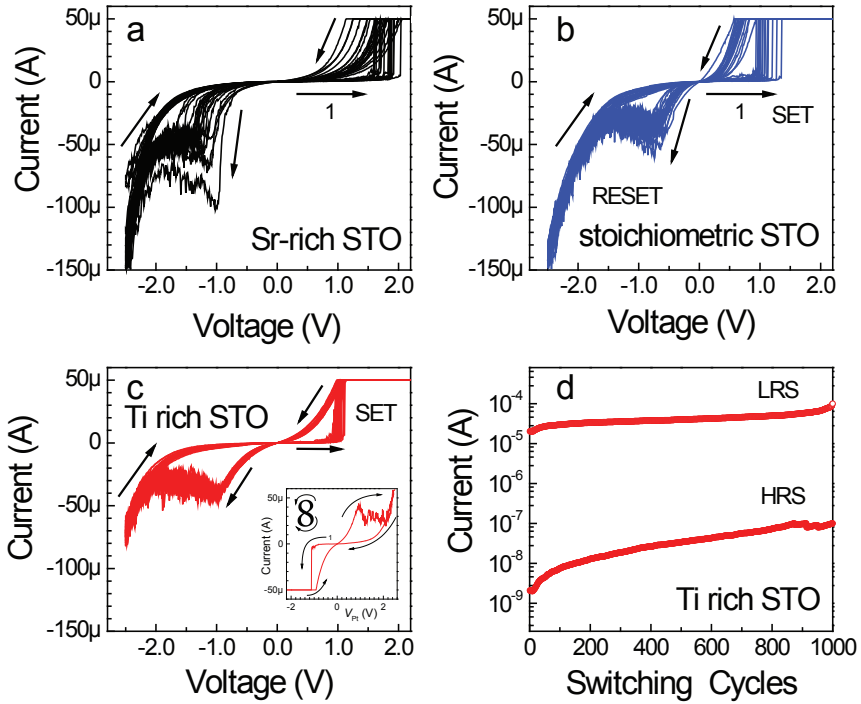
Figure 8.7: (a-c) I-V hysteresis of nano-crossbar Pt/STO/TiN devices of 0.01 μm^2 size with 12 nm polycrystalline STO thin films of different compositions listed in Table 8.1. The voltage signal was applied to the TiN top electrode. All devices reveal a stable bipolar RS at a current compliance of 50 μA. The inset in (c) shows the "counter-eight-wise" RS with respect to the actively switching Pt/STO contact. (d) Endurance plot over 1000 quasistatic switching cycles (I_{cc} = 100 μA) for a Pt/Ti-rich STO/TiN device at V_{read} = +0.3 V.

crossbar devices exhibit a typical "counter-eightwise" bipolar RS [21] which is characteristic for valence change memories [5,52]. A conspicuous difference in the continuous I-V characteristics of the different STO samples appears in the non-linearity of the LRS current response. While the I-V nonlinearity for the stoichiometric and the Ti-rich STO devices (see Figures 8.7.b and c) is comparable, the Sr-rich STO nano-crossbar LRS characteristic shows an enhanced nonlinearity (see Figure 8.7.a). A quantitative value for the LRS-nonlinearity is in general defined by the non-linearity factor NL which is calculated from the reset characteristic of the continuous I-V curve according to $NL =$ $\mid I(V_{reset}) \mid$ / $\mid I(V_{reset}/2) \mid$ [53]. For the RS characteristics of the STO nano-crossbar structures show in Figures 8.7.a-c, we calculated values of the NL-factor of about 18 for the Sr-rich STO device in comparison to 6.5 and 4 for the stoichiometric and Ti-rich STO films, respectively.

The RS characteristics of the various STO devices have been analyzed in a statistical manner for two device sizes, i.e. 1 μm^2 and 0.01 μm^2, and three STO compositions, i.e. [Sr]/([Sr]+[Ti]) ratios of 0.57 (Sr-rich), 0.50 (stoichiometric) and 0.46 (Ti-rich). The variation of the data determined from about 20 devices and 30 switching cycles per device is described by means of the cumulative distribution function (CDF). Characteristic values of the I-V hysteresis (see Figures 8.7.a-c) to be discussed are: 1) the set-voltage V_{set}, determined as the voltage where the current compliance is reached during the (abrupt) set-process, 2) the reset-voltage V_{reset}, determined as the voltage where the negative current reaches a local maximum during reset-process and 3) the resistance values R_{on} (LRS) and R_{off} (HRS) determined at a read voltage V_{read} = +0.3 V.

Figure 8.8 shows the CDF of the set- and reset-voltages of the STO based RS devices for (a) the 1 μm^2 micro-crossbars, and (b) the 0.01 μm^2 nano-crossbars. The three STO compositions are again encoded by colors (see Figure 8.7). The micro-crossbar cells reveal rather narrow distributions of the switching voltages and quite symmetric values for V_{set} and V_{reset}, in contrast to the nano-crossbar devices. The micro-crossbar devices with non-stoichiometric STO films show a slightly larger set-voltage compared to the value of the reset-voltage. For the Ti-rich STO mean values were $V_{set} \approx 0.85 \pm 0.1$ V and $|V_{reset}| \approx$ 0.65 $\pm$ 0.15 V, and for the Sr-rich STO we obtain $V_{set} \approx 1.0 \pm 0.15$ V and $|V_{reset}| \approx 0.9 \pm$ 0.1 V. In contrast, the switching voltages of the stoichiometric STO cells are nearly symmetric with absolute values of $V_{set} \approx |V_{reset}| \approx (0.9 \pm 0.1)$ V. Remarkably, the switching voltages of the different micro-crossbar devices are very close in contrast to the forming voltages which differ significantly for the various STO compositions (see Figure 8.6.c). Additionally, it is found that the stoichiometric STO devices with the highest leakage current in the initial state (see Figure 8.5.a) show a nearly forming-free RS behavior, i.e.
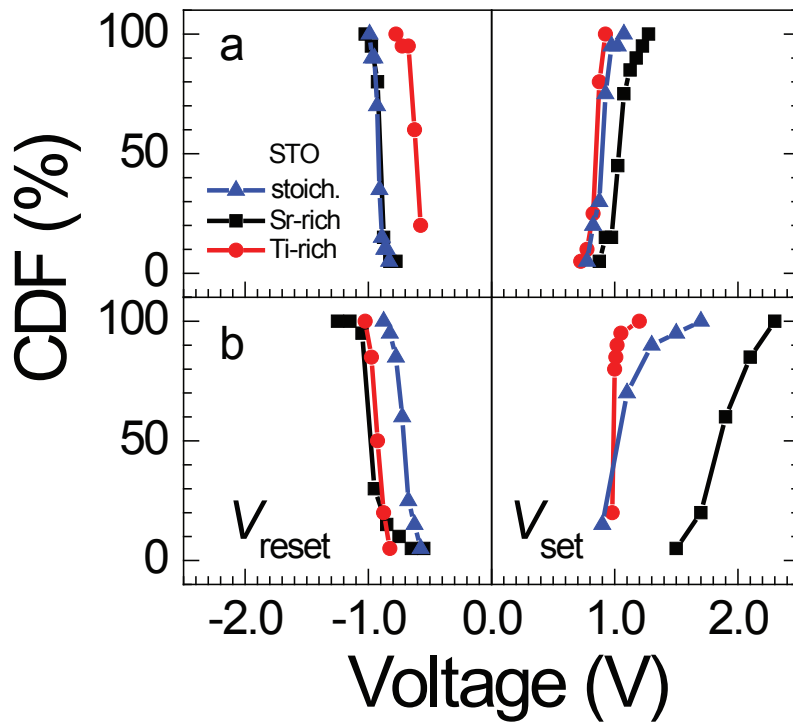
Figure 8.8: Cumulative distribution functions of the set- and reset-voltages of the quasi-static I-V hystereses for (a) micro-crossbar (1 μm^2 size, 15 nm thick STO) and (b) nano-crossbar (0.01 μm^2 size, 12 nm thick STO) Pt/STO/TiN devices of different compositions listed in Table 8.1.

$V_{EF} \approx V_{set} \approx 1$ V.

A relation between higher initial leakage and lower forming voltage has also been reported for HfO$_2$-based RS devices [9]. From the correlation of morphological and LC-AFM studies we suggest that the RS switching in the polycrystalline STO films might dominantly appear at weak points like, for example, the observed micro-cracks. This brings up the question whether the RS in the ALD STO based devices is a filamentary-type phenomenon or somehow relates to the density of micro-cracks in the thin films. This point will be further addressed at the end of the section.

For the nano-crossbar cells shown in Figure 8.8.b, in general, the set-voltages $|V_{set}|$ were higher than the corresponding $|V_{reset}|$ reset-voltages. Here, the Ti-rich STO films show the most symmetric RS curves with $V_{set} \approx 1.0 \pm 0.15$ V and $|V_{reset}| \approx 0.95 \pm 0.1$ V. In contrast, the stoichiometric STO devices with $V_{set} \approx 1.1 \pm 0.4$ V and $|V_{reset}| \approx 0.7 \pm 0.15$ V, and the Sr-rich STO with $V_{set} \approx 1.9 \pm 0.4$ V and $|V_{reset}| \approx 1.0 \pm 0.2$ V exhibit a significant asymmetry in the RS behavior. Notable for the nano-crossbars are the quite broad distributions of the set-voltages observed for all three STO compositions. In addition, the RS voltages of the nano-crossbar devices are significantly lower than the respective forming voltages of about +5.0 V (see Figure 8.6.d). The higher set-voltage of the Sr-rich STO nano-crossbar might indicate that setting these devices into the highly conductive ON-state is more difficult to achieve than in case of the Ti-rich and stoichiometric STO devices.

An increase of the set- and reset-voltages with decreasing size of the RS devices has also been reported for HfO$_2$-based RS devices by Chen et al. [8], who addressed this effect to the lower total number of defects in the smaller devices compared to the larger ones. This scenario might also apply to the STO based RS devices in this study. Interestingly, the analysis of the influence of the [Sr]/([Sr]+[Ti]) composition on the switching voltages revealed the same trends for the micro- and nano-crossbar cells, i.e. an increase of the mean switching voltage with increasing Sr-content in the thin films. This stoichiometry effect is especially pronounced in the nano-crossbar cells which were electroformed at comparable voltages.

Figure 8.9 shows the CDF plots of the ON-state (LRS) and OFF-state (HRS) resistance values for the STO based RS devices as determined from the continuous I-V switching cycles at a read voltage of $V_{read} = +0.3$ V. Again, the three STO compositions are encoded by colors and the data for the micro- and nano-crossbars are shown in Figures 8.9.a and b, respectively. General trends which can be identified are, first, that smaller devices exhibit higher LRS- and HRS-values, and second, that the data spread as a function of the [Sr]/([Sr]+[Ti]) composition is larger for the LRS values as compared
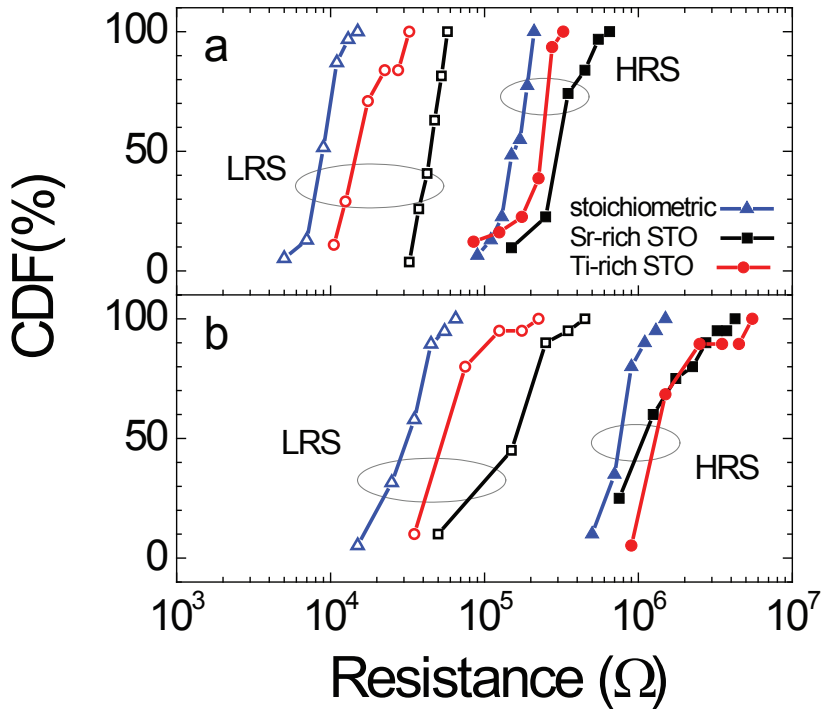
Figure 8.9: Cumulative distribution functions of the resistance values derived from the quasistatic I-V hystereses for (a) micro-crossbar (1 μm^2 size, 15 nm thick STO) and (b) nano-crossbar (0.01 μm^2 size, 12 nm thick STO) Pt/STO/TiN devices of different compositions (see Table 8.1).
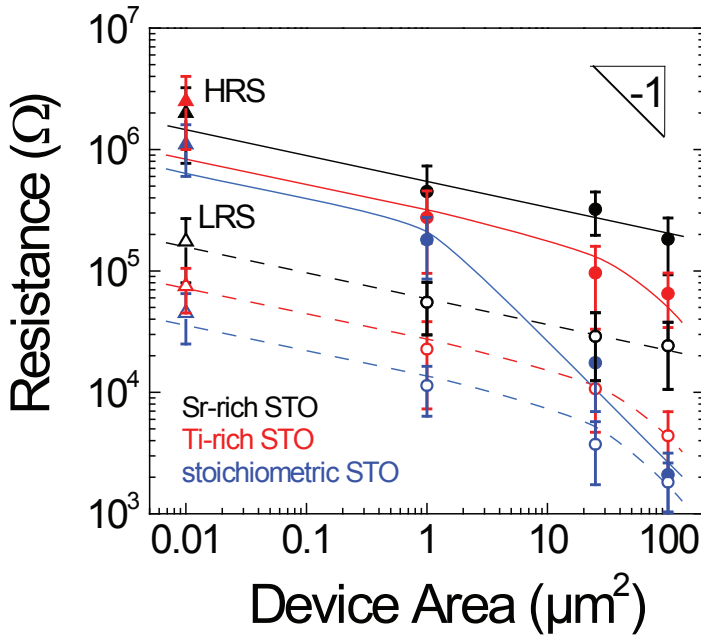
Figure 8.10: Area dependency of the resistance states of the Pt/STO/TiN devices determined at V_{read} = +0.3 V from stable, quasistatic I-V hystereses. The colors encode the films composition, Sr-rich (black), Ti-rich (red), and stoichiometric STO (blue) values (see Table 8.1), resistance values of LRS/HRS are given in open/filled symbols. The symbols stand for the different structures, circles for micro- and triangles for nano-crossbars. The slope of (-1) is plotted for easy identification of area-scaling.

to the HRS values. In addition, for each device size, the STO cells show the lowest resistance values in ON- and OFF-state compared to the values of the non-stoichiometric STO devices, while in general an increase in the resistance ratio R_{off}/R_{on} with decreasing device size is observed.

In order to assess the influence of the device size, the area dependency of the resistance values for the devices of different STO compositions has been analyzed. The graph in Figure 8.10 comprises mean values of the HRS (filled symbols) and the LRS (open symbols) for four different device sizes, i.e. 0.01 μm^2, 1 μm^2, 25 μm^2, and 100 μm^2. The micro-crossbar devices (> 1μm^2) were fabricated from STO films of about 15 nm thickness, while for the nano-crossbar devices (0.01 μm^2) films of about 12 nm were integrated. The different STO compositions are again encoded by the colors. Despite

the different film thicknesses, a consistent trend in the resistance values as a function of the device size is obtained for the devices of different STO compositions. The area-dependency can be summarized as follows: the Sr-rich STO devices (black) show a very weak area dependency for the LRS and HRS values which change roughly by a factor of ten when the cell area is varied by a factor of 10^4. A resistance ratio $R_{off}^{Sr-STO}/R_{on}^{Sr-STO}$ ≈ 10 independent of the device area was determined which is addressed to the high insulating properties of the annealed Sr-rich STO thin films. The Ti-rich STO devices also show a weak area-dependency of the LRS similar to that of the Sr-rich STO devices, while the value is reduced to about one third, $R_{on}^{Ti-STO}/R_{on}^{Sr-STO} \approx 0.3$. The HRS values of the Ti-rich STO reveal an enhanced dependency on the cell area which is attributed the higher leakage currents becoming significant for larger devices. Thus a mean resistance ratio $R_{off}^{Ti-STO}/R_{on}^{Ti-STO} \approx 20$ is obtained for the smaller devices. For small area cells ($< 1~\mu m^2$) the stoichiometric STO devices show a weak area dependence for the LRS and HRS values with a resistance ratio $R_{off}^{Stoi-STO}/R_{on}^{Stoi-STO} \approx 25$, while for device sizes $> 1~\mu m^2$ the HRS values show a strong area dependence with a proportionality factor of approximately one. This clearly demonstrates that the effect of leakage current through the micro-cracks (see Figure 8.3.b) dominates the total current for large pad sizes, thus for large stoichiometric STO devices any RS effect is completely obscured by the high leakage current contribution from the non-switching area of the device. As a consequence, reliable information on the compositional effect of the ALD STO films on the RS properties can only be obtained from device structures with reasonably small sizes.

In LRS, all STO devices of the three compositions show a considerably weak area-dependency of their resistance values. This is interpreted in the way that the area-independent VCM-type filamentary mechanism dominates the RS characteristics of the Pt/STO/TiN devices after electroforming. The area-dependency of the HRS values demonstrates the significant effect of the films microstructure and morphology on the RS properties. Overlying the area-dependency, also an effect of the STO thin film composition is observed, predominantly for the LRS states. Considering devices of the same size, smaller than $10~\mu m^2$, the ON-state resistance values increase from stoichiometric to Ti-rich to Sr-rich STO films resulting in a ratio of the LRS values $R_{on}^{Sr-STO}/R_{on}^{Stoi-STO} \approx$ 6. Although the HRS states of the smaller devices are not too much affected by an area dependent leakage current parallel to the filament current, the dependence of the HRS states on the composition of the STO films is less pronounced. Especially when the RS cell is in insulating state defects in the MOM device might have a considerable influence on the total (HRS) resistance. However, the highest resistance ratio R_{off}/R_{on} of about

25 was obtained for stoichiometric STO and the lowest value of about 10 for the Sr-rich STO films. The lowest values of LRS were found for the stoichiometric STO films, while either Sr- or Ti-excess result in higher R_{on} values. This scenario is more pronounced for the Sr-rich STO than for the Ti-rich devices.

In addition to the significant influence of the STO thin films microstructure on the RS characteristics of respective Pt/STO/TiN devices also a composition effect was observed. While micro-structural effects (e.g. micro-cracks and grain sizes) dominate the resistance states for larger cell areas, the HRS states of the nano-crossbar cells might still be affected by varying defect densities in the films induced by differences in the films crystallization behavior. However, the LRS values of the Pt/STO/TiN devices show a reproducible tendency with variation of the STO film composition: $R_{on}^{Sr-STO} > R_{on}^{Ti-STO} > R_{on}^{Stoi-STO}$, for different device sizes, film thicknesses and microstructures. This finding might indicate a compositional dependence of the local defect states of the conducting filaments RS devices from polycrystalline ALD STO thin films with various ([Sr]/([Sr]+[Ti]) contents.

8.4   Conclusions

In this study, we investigated the resistive switching (RS) properties of Pt/STO/TiN devices from ALD derived $Sr_{1+x}Ti_{1+y}O_{3+(x+2y)}$ thin films of various compositions. Meta-stable perovskite STO films were grown on platinum coated silicon substrates by ALD at 350 °C using cyclopentadienyl-based metal precursors and oxygen plasma and a subsequent annealing at 600 °C in N_2. STO films of 15 nm and 12 nm thickness and with three different compositions ([Sr]/([Sr]+[Ti]) of 0.57 (Sr-rich), 0.50 (stoichiometric) and 0.46 (Ti-rich) were integrated into crossbar-devices with lateral dimensions varied from (10×10) μm^2 to (100×100) nm^2. Nano-structural characterizations by means of SEM and LC-AFM revealed a significant influence of the STO cation composition on the crystallization behavior and, thus, on the resulting morphologies of the ALD films. Local defects in the films' microstructure dominantly affect the leakage current behavior of pristine MOM cells and their soft-breakdown or electroforming voltages. For cell sizes > 1 μm^2 also the HRS of the RS characteristics is superimposed by residual cell conductivity. The polarity dependence of the RS curves and the area-independent LRS values serve as a direct proof of VCM-type filamentary RS taking place in the Pt/STO/TiN devices under study. Once the microstructural effects of the polycrystalline thin films have been assessed, a clear effect of the STO composition on the RS behavior was observed. Nano-crossbar devices from stoichiometric STO films could be switched at lowest voltages of

about 1.0 V between the lowest LRS values of $R_{on} \approx 40$ kΩ, and reasonable HRS values of $R_{off} \approx 1$ MΩ determined at +0.3 V. Non-stoichiometry in the ALD STO films, Ti-rich or Sr-rich, predominantly increases the RS devices R_{on} values, i.e. result in LRS of lower conductance.

Acknowledgments

References

1. ITRS, http://www.itrs.net/ (2012).
2. S. Yu, B. Gao, Z. Fang, H. Yu, J.F. Kang and H.S. P. Wong, *Adv. Mater.*, 25, 1774 (2013).
3. R. Bruchhaus, R. Muenstermann, T. Menke, C. Hermes, F. Lentz, R. Weng, R. Dittmann and R. Waser, *Curr. Appl. Phys.*, 11, E75 (2011).
4. H.D. Lee, S.G. Kim, K. Cho, H. Hwang, H. Choi, J. Lee, S.H. Lee, H.J. Lee, J. Suh, S. Chung, Y.S. Kim, K.S. Kim, W.S. Nam, J.T. Cheong, J.T. Kim, S. Chae, E. Hwang, S. N. Park, Y.S. Sohn, C.G. Lee, H.S. Shin, K.J. Lee, K. Hong, H.G. Jeong, K.M. Rho, Y.K. Kim, S. Chung, J. Nickel, J.J. Yang, H.S. Cho, F. Perner, R.S. Williams, J.H. Lee, S.K. Park and S. Hong, *VLSI Tech. Dig.*, 151 (2012).
5. R. Waser, R. Bruchhaus and S. Menzel, in R. Waser (ed.) Nanoelectronics and Information Technology (3rd edition), Wiley-VCH, 683 (2012).
6. Y. Chen, B. Govoreanu, L. Goux, R. Degraeve, A. Fantini, G. Kar, D. Wouters, G. Groeseneken, J. Kittl, M. Jurczak and L. Altimime, *IEEE Trans. Electron Devices*, 59, 3243 (2012).
7. S. Stille, C. Lenser, R. Dittmann, A. Koehl, I. Krug, R. Muenstermann, J. Perlich, C.M. Schneider, U. Klemradt and R. Waser, *Appl. Phys. Lett.*, 100, 223503/1 (2012).
8. Y.Y. Chen, L. Goux, L. Pantisano, J. Swerts, C. Adelmann, S. Mertens, V.V. Afanas'ev, X.P. Wang, B. Govoreanu, R. Degraeve, S. Kubicek, V. Paraschiv, B.

Verbrugge, N. Jossart, L. Altimime, M. Jurczak, J. Kittl, G. Groeseneken and D.J. Wouters, *Microelectron. Eng.*, 112, 92 (2013).

9. M. Lanza, G. Bersuker, M. Porti, E. Miranda, M. Nafria and X. Aymerich, *Appl. Phys. Lett.*, 101, 193502 (2012).

10. Y. Wu, S. Yu, B. Lee and P. Wong, *J. Appl. Phys.*, 110, 94104/1 (2011).

11. K. Kim, S. Han and C. Hwang, *Nanotechnology*, 23, 035201 (2012).

12. S.J. Park, J.P. Lee, J.S. Jang, H. Rhu, H. Yu, B.Y. You, C.S. Kim, K.J. Kim, Y.J. Cho, S. Baik and W. Lee, *Nanotechnology*, 24, 295202/1 (2013).

13. K. Szot, M. Rogala, W. Speier, Z. Klusek, A. Besmehn and R. Waser, *Nanotechnology*, 22, 254001/1 (2011).

14. M. Rogala, Z. Klusek, C. Rodenbücher, R. Waser and K. Szot, *Appl. Phys. Lett.*, 102, 131604 (2013).

15. N. Menou, M. Popovici, S. Clima, K. Opsomer, W. Polspoel, B. Kaczer, G. Rampelberg, K. Tomida, M.A. Pawlak, C. Detavernier, D. Pierreux, J. Swerts, J.W. Maes, D. Manger, M. Badylevich, V.V. Afanas'ev, T. Conard, P. Favia, H. Bender, B. Brijs, W. Vandervorst, S. Van Elshocht, G. Pourtois, D.J. Wouters, S. Biesemans and J.A. Kittl, *J. Appl. Phys.*, 106, 94101/1 (2009).

16. R. Waser, R. Dittmann, G. Staikov and K. Szot, *Adv. Mater.*, 21, 2632 (2009).

17. R. Muenstermann, T. Menke, R. Dittmann, S. Mi, C.L. Jia, D. Park and J. Mayer, *J. Appl. Phys.*, 108, 124504/1 (2010).

18. S. Menzel, M. Waters, A. Marchewka, U. Böttger, R: Dittmann and R. Waser, *Adv. Funct. Mater.*, 21, 4487 (2011).

19. R. Waser and M. Aono, *Nat. Mater.*, 6, 833 (2007).

20. K. Szot, W. Speier, G. Bihlmayer and R. Waser, *Nat. Mater.*, 5, 312 (2006).

21. R. Muenstermann, T. Menke, R. Dittmann and R. Waser, *Adv. Mat.*, 22, 4819 (2010).

22. A. Koehl, D. Kajewski, J. Kubacki, C. Lenser, R. Dittmann, P. Meuffels, K. Szot, R. Waser and J. Szade, *Physical Chemistry Chemical Physics*, 15, 8311 (2013).

23. K. Shibuya, S. Mi, C.L. Jia, P. Meuffels and R. Dittmann, *Appl. Phys. Lett.*, 92, 241918 (2008).

24. U. Schroeder, H. Schroeder, A. Kingon, S. Summerfelt, C.S. Hwang, and U. Böttger, in R. Waser (ed.), Nanoelectronics and Information Technology (3rd edition), Wiley-VCH, 635 (2012).

25. S.K. Kim, S.W. Lee, J H. Han, B. Lee, S. Han and C.S. Hwang, *Adv. Funct. Mater.*, 20, 2989 (2010).

26. M. Lukosius, T. Blomberg, D. Walczyk, G. Ruhl and Ch. Wenger, *IOP Conf. Ser.: Mater. Sci. Eng.*, 41, 12015/1 (2012).

27. T. Blomberg, J. Anttila, S. Haukka, M. Tuominen, M. Lukosius, Ch. Wenger and T. Saukkonen, *Thin Solid Films*, 520, 6535 (2012).

28. C. Jorel, C. Valle, P. Gonon, E. Gourvest, C. Dubarry and E. Defay, *Appl. Phys. Lett.*, 94, 253502 (2009).

29. M. Lukosius, C. Wenger, T. Blomberg and G. Ruhl, *J. Vac. Sci. Technol. B*, 31, 1A102/1 (2013).

30. C.S. Hwang, *Mater. Sci. Eng. B*, 56, 178 (1998).

31. W. Lee, J.H. Han, W. Jeon, Y.W. Yoo, S.W. Lee, S.K. Kim, C.H. Ko, C. Lansalot-Matras and C.S. Hwang, *Chem. Mater.*, 25, 953 (2013).

32. M. Popovici, S. Van Elshocht, N. Menou, P. Favia, H. Bender, E. Rosseel, J. Swerts, C. Adelmann, C. Vrancken, A. Moussa, H. Tielens, K. Tomida, M. Pawlak, B. Kaczer, G. Schoofs, W. Vandervorst, D. Wouters and J. Kittl, *J. Vac. Sci. Technol. B*, 29, 01A3041 (2011).

33. S. Yu, H.Y. Chen, B. Gao, J. Kang and H.S.P. Wong, *Acs Nano*, 7, 2320 (2013).

34. V. Longo, M.A. Verheijen, F. Roozeboom, and W.M.M. Kessels, *ECS J. Solid State Sci. Technol.*, 2, N120 (2013).

35. V. Longo, N. Leick, F. Roozeboom, and W.M.M. Kessels, *ECS J. Solid State Sci. Technol.*, 2, N15 (2013).

36. D. Briggs and M.P. Seah, John Wiley & Sons New York (1990).

37. V. Longo, F. Roozeboom, W.M.M. Kessels and M.A. Verheijen, *ECS Transactions*, 58, 153 (2013).

38. S. Witek, D.M. Smyth and H. Pickup, *J. Am. Ceram. Soc.*, 67, 372 (1984).

39. G.J. McCarthy, W.B. White and R. Roy, *J. Am. Ceram. Soc.*, 52, 463 (1969).

40. R. Tilley, *J. Solid State Chem.*, 21, 293 (1977).

41. K. Szot and W. Speier, *Phys. Rev. B: Condens. Matter*, 60, 5909 (1999).

42. M. Fujimoto and M. Watanabe, *J. Mater. Sci.*, 20, 3683 (1985).

43. N.A. Benedek, C. Elsaesser and M.W. Finnis, *Journal of Physics: Conference Series*, 94, 12005 (2008).

44. S. Clima, G. Pourtois, N. Menou, M. Popovici, A. Rothschild, B. Kaczer, S. Van Elshocht, X.P. Wang, J. Swerts, D. Pierreux, S. DeGendt, D.J. Wouters and J.A. Kittl, *Microelectron. Eng.*, 86, 1936 (2009).

45. K. Shibuya, R. Dittmann, S. Mi and R. Waser, *Adv. Mater.*, 22, 411 (2010).

46. B. Psiuk, J. Szade, H. Schroeder, H. Haselier, M. Mlynarczyk, R. Waser and K. Szot, . *Phys. A-Mater. Sci. Process.*, 89, 451 (2007).

47. D. Kajewski, R. Wrzalik, M. Wojtyniak, M. Pilch, J. Szade, K. Szot, Ch. Lenser, R. Dittmann and R. Waser, *Phase Transit.*, 84, 483 (2011).

48. D. Gu, S. K. Dey and P. Majhi, *Appl. Phys. Lett.*, 89, 82907/1 (2006).

49. R.K. Pandey, R. Sathiyanarayanan, U. Kwon, V. Narayanan, and K.V.R. M. Murali, *J. Appl. Phys.*, 114, 34505/1 (2013).

50. N. Aslam, V. Longo, W. Keuning, F. Roozeboom, W.M.M. Kessels, R. Waser and S. Hoffmann-Eifert, *Phys. Status Solidi*, 211, 389 (2014).

51. D.S. Jeong, H. Schroeder, U. Breuer and R. Waser, *J. Appl. Phys.*, 104, 123716/1 (2008).

52. D. Jeong, R. Thomas, R. Katiyar, J. Scott, H. Kohlstedt, A. Petraru and C. Hwang, *Rep. Prog. Phys.*, 75 (2012).

53. F. Lentz, B. Roesgen, V. Rana, D.J. Wouters and R. Waser, *IEEE Electron Device Lett.*, 34, 996 (2013).

Chapter 9

General Conclusions and Outlook

In this dissertation work the control and the tailoring of the material properties of STO thin films by optimization of the processing steps, in particular atomic layer deposition (ALD) and rapid thermal annealing (RTA), have been studied. Furthermore, the ALD STO thin films were implemented in functional MIM structures in order to study the influence of the thin film properties on the performance of capacitor-based and resistive switching devices. From this work the following conclusions could be drawn:

- ALD, besides being a deposition technique which gives accurate thickness control in the preparation of ultra-thin films, allows to carefully control the composition of ternary compounds such as STO. In this work the cation ratio [Sr]/([Sr]+[Ti]) could be controlled by tuning the ALD cycle ratio between TiO_2 and SrO ALD cycles. Therefore, the STO thin film stoichiometry is a process parameter which can be tuned by ALD in a versatile way.

- Spectroscopic ellipsometry (SE) is a non-intrusive characterization technique which can be effectively used to determine the thickness and the optical properties of STO thin films. More importantly, SE can be employed to determine the STO film composition without recurring to other time-consuming techniques such as XPS or RBS. Therefore, SE offers the possibility to determine the STO film composition in a fast measurement which can also be performed in-situ allowing the real-time monitoring of the film thickness and composition during the deposition process.

- The crystallization behavior of STO strongly depends on the thermal budget ap-

plied and on the film composition. By tuning the composition through the control of the ALD conditions and by controlling the temperature and duration of the RTA treatment, it is possible to achieve a wide set of film microstructures and morphologies. In particular, Sr-rich STO thin films show an enhanced nucleation probability at the onset of crystallization leading to a reduced average grain size compared to more stoichiometric films. Furthermore, the presence and distribution of nanocracks and voids also show a composition dependence with a more uniform microstructure for Sr-rich films. Moreover, the nucleation probability and therefore the grain density show a clear trend with the temperature of the annealing. At lower RTA temperatures a low nucleation probability results in a low density of grains which expand in lateral dimension over annealing time, i.e. the crystallization behavior is growth-dominated, while at higher RTA temperatures a high nucleation probability results in a high grain density with reduced average grain size, i.e. the crystallization behavior is nucleation-dominated.

- When manufacturing a multi-layered structure such as the Pt/STO/Pt MIM stacks studied in this work, the interplay of the different steps involved in the preparation of the structure has to be taken into account. During the RTA step applied to the STO/Pt stack, intended to crystallize the STO film, the Pt bottom electrode shows microstructural changes. In particular, during RTA the ALD deposited Pt bottom electrode undergoes a solid-state crystallization process which results in an increased average grain density and a higher degree of texture in the Pt film. Furthermore, the texture of the STO films in STO/Pt stacks depends on the degree of texture of the Pt bottom electrode before the RTA step. Despite the fact that the ALD deposited Pt undergoes a recrystallization process during RTA, the STO films seem unaffected by this process and show a random orientation of the grains, while STO films deposited on highly textured PVD deposited Pt bottom electrodes show a preferred orientation.

- The performance of the STO thin films for the applications studied in this work strongly depend on the film composition, microstructure and morphology. Therefore, the appropriate processing conditions employed in the deposition and crystallization of STO films need to be chosen to optimize such performances. In the case of Pt/STO/Pt capacitors the achieved capacitance values (and, consequently, the EOT values) are determined by the composition and crystalline phase of the STO films. While amorphous as-deposited STO films showed relatively low permittivities, high capacitance values can be achieved with crystallized perovskite

STO films, with the highest permittivity obtained for the near-stoichiometric STO. The leakage current of the high-k crystallized films shows an indirect dependence on the STO film composition. Despite the fact that the optical band gap is increased for Sr-rich films the reduced leakage current recorded for this composition is mainly imputed to a more regular morphology compared to the more stoichiometric films. Similarly, in the case of Pt/STO/TiN micro- and nano-crossbar devices for resistive switching (RS) applications, working parameters such as the electroforming voltage are dependent on the morphology of the film studied. In particular, the leakage current values, related to the amount of cracks at the grain boundaries, determines the electroforming process of the devices. Moreover, the lateral size of the crossbar structures has an important influence on determining RS parameters such as the SET and the RESET voltages and the values of the low and high resistance states (LRS and HRS, respectively).

For the employment of ALD STO thin films in industrial applications different technical issues should be solved. For example, the implementation of STO films in MIM DRAM capacitors with high aspect ratio structures is not trivial. Despite the fact that capacitance and leakage current values satisfying the DRAM requirements have been obtained in the literature for planar capacitors, the achievement of the same performance on 3D structure is challenging. Furthermore, due to compatibility issues reduced thermal budgets are preferred in the manufacturing process. Therefore, optimization of the thermal treatment or alternative solutions should be further investigated in order to minimize the thermal budget during the STO crystallization process. From these considerations the findings reported in this dissertation call for further research in the following directions:

- Only preliminary results on the conformality of STO thin films deposited by plasma-assisted ALD have been reported. However, the achieved results are not satisfactory for the applications in which the employment of STO is envisioned on stringent 3D structures. Furthermore, conformality in terms of material composition on 3D structures have not been reported in this thesis. Therefore, further research should focus on the optimization of the deposition conditions in order to achieve the required conformality. Efforts should be oriented in order to optimize the dosing of the precursors and the plasma conditions (i.e. pressure and plasma power) to achieve excellent thickness and composition conformality on high aspect ratio structures. The outcome of this research would also give valuable insight into the conformal deposition of other multi-component compounds.

- The crystallization behavior of STO thin films on 3D structures has not been ad-

dressed in the literature. Gradients over 3D structures in terms of film composition could lead to differences in morphology and microstructure along the structure profile. A similar effect can occur due to gradients in temperature during the annealing step. Therefore, determining the influence of these parameters on the crystallization behavior of STO film deposited on 3D topologies is vital from an application point of view.

- The crystallization study of STO thin films could be extended to STO seed-layers employed to achieve in-situ crystallization of STO films as described in Section 2.3.3. Determining the crystallization behavior of ultrathin (~ 3 nm) STO with different compositions and by applying different thermal budgets would give insight into the in-situ crystallization process of STO films. In particular, the influence of different seed-layer microstructures on the final STO film morphology should be addressed.

- The influence of ion bombardment on the crystallizion process of the STO films should be investigated. By treating the STO films with a plasma (i.e. oxygen plasma) energetic ions could induce displacement of atoms and, therefore, initiate the crystallization process. Thus, the combination of a thermal and a plasma treatment could lead to crystallization of the films with a reduced thermal budget.

Summary

Atomic Layer Deposition of Strontium Titanate from material control to nanoscale devices

With the scaling of advanced microelectronics approaching its physical limits new technological solutions are needed. In particular innovative 3D-structures are being investigated with an increasing number of functional layers containing novel and more complex materials. To fulfill the strict requirements for future nanoscale devices the properties of the materials to be employed are of crucial importance. Hence, the thickness, the composition and the interfaces of the deposited thin films need to be carefully tailored also when deposited in the 3D-structures. In addition, the morphological and microstructural changes in the materials induced during the entire process flowchart need to be taken into account and controlled.

To meet these challenging requirements atomic layer deposition (ALD) is increasingly used as an ultrathin-film deposition technique. It enables superior thickness control and film conformality and also enables the control of the film composition of multicomponent compounds. A technologically relevant example of a material for which the properties can be tailored by ALD and the subsequent processing steps is strontium titanate ($SrTiO_3$, STO). STO represents a class of multicomponent oxides with their dielectric properties and morphology strongly depending on the cation stoichiometry and on the thermal treatments they undergo. Due to their high permittivity STO thin films find their main application as the *ultrahigh-k* dielectric layer in metal-insulator-metal (MIM)-based memory devices. Also they show other interesting properties for application in, for instance, resistive switching valence change memories. In all of these applications the tailoring of the material properties is vital to achieve the targeted performances.

This thesis work focuses on the control of the material properties of ALD STO thin films. The plasma-assisted ALD processes for TiO_2 and SrO were developed using cyclopentadienyl-based precursors and an O_2 plasma. By combining the ALD cycles of the two binary oxides with different ratios it was possible to accurately control the stoichiometry of the films over a wide range of [Sr]/([Sr]+[Ti]) ratios. By using Rutherford backscattering spectrometry (RBS) and X-ray diffraction (XRD) data a method was established to determine stoichiometry and crystallinity of the films by means of spectroscopic ellipsometry (SE).

The as-deposited STO films are amorphous, and rapid thermal annealing was used

to achieve crystallization into the desired *ultrahigh-k perovskite* structure. Transmission electron microscopy (TEM) was used to study the influence of the film stoichiometry and of the thermal budget applied on the crystallization behavior of STO films deposited on Si_3N_4 and Al_2O_3. It was shown that the lattice planes of the STO crystallites bent due to film densification upon the amorphous-crystalline transformation. Furthermore, it was found that film composition and annealing conditions strongly influenced the nucleation probability and the final morphology of the crystalline films, with a smaller grain size and reduced crack formation at the grain boundaries for Sr-rich films.

In the aforementioned applications STO is used in metal MIM structures. Therefore Pt/STO/Pt stacks were fabricated by ALD with the aim of studying the growth, the crystallization behavior and the interplay of the processing steps involved in the fabrication of the structures. Results evidenced that not only crystalline STO is obtained after the RTA step but that the Pt bottom electrode also undergoes a re-crystallization process upon annealing which results in an increased Pt texture. Structural analysis showed that the morphology of the STO crystals was comparable to those obtained on Si_3N_4 and Al_2O_3 substrates.

The STO thin films were also studied as functional layers in electronic device structures. First, Pt/STO/Pt structures were investigated to determine the dielectric properties of the STO films. *Ultrahigh-k* STO thin films were obtained with their permittivity depending on the film composition. While higher capacitance values were achieved for the stoichiometric STO films, Sr-rich films showed the lowest leakage current values. This was ascribed not only to the higher band gap values but also to the more compact morphology of Sr-rich films compared to near-stoichiometric STO films.

Furthermore, the influence of the STO film composition on the resistive switching behavior of Pt/STO/TiN MIM micro- and nano-crossbar structures was addressed. Results showed that the filamentary-type resistive switching behavior was predominantly governed by the morphology of the STO film after the RTA step, which is controlled by the composition of the film. Therefore, the lateral size of the crossbars structure employed in this study showed to be of critical importance on the working parameters of the device.

In conclusion, this research work provides deeper insight into the tailoring of STO thin films prepared by ALD from the level of material properties up to the device level. It serves as a valuable example on how to finely tune multi-component oxides employed in the fabrication of nanoscale devices by accurate control and optimization of the processing conditions.

List of publications related to this work

1. V. Longo, N. Leick, F. Roozeboom, and W.M.M. Kessels, *ECS Trans.*, 41 (2), (2011). *This work has been presented at the 220th meeting of The Electrochemical Society (Boston, Massachusetts, U.S.A., October 2011).*

2. V. Longo, N. Leick, F. Roozeboom, and W.M.M. Kessels, *ECS J. Solid State Sci. Technol.*, 2 (1), N15 (2013).

3. V. Longo, F. Roozeboom, W.M.M. Kessels and M.A. Verheijen, *ECS Trans.*, 50 (13), (2012). *This work has been presented at the 222nd meeting of The Electrochemical Society (Honolulu, Hawaii, U.S.A., October 2012).*

4. V. Longo, N. Leick, F. Roozeboom, and W.M.M. Kessels, *ECS J. Solid State Sci. Technol.*, 2 (5), N120 (2013).

5. V. Longo, F. Roozeboom, M.A. Verheijen and W.M.M. Kessels, *ECS Trans.*, 58 (10), (2013). *This work has been presented at the 224th meeting of The Electrochemical Society (San Francisco, California, U.S.A., October 2013).*

6. N. Aslam, V. Longo, W. Keuning, F. Roozeboom, W.M.M. Kessels, R. Waser, and S. Hoffmann-Eifert, *Phys. Status Solidi A*, 211, 389 (2014).[*]

7. N. Aslam, V. Longo, C. Rodenbücher, F. Roozeboom, W.M.M. Kessels, K. Szot, R. Waser and S. Hoffmann-Eifert, submitted for publication to *J. Appl. Phys.*[*]

---

[*]N.A. and V.L. contributed equally to this work.

Acknowledgements

During my PhD I have met many people that I would like to thank for helping me reach this point, the end of my PhD, both in a professional way, as friends, or simply for being there for me at the right moment.

I would like to thank my supervisor, **Erwin**, for giving me the opportunity to carry out my PhD research at PMP and for helping me throughout these four years to improve as a scientist, researcher, writer and presenter. His critical comments and observations on papers, presentations and results have certainly helped me achieve this goal in my life. I would also like to express my heartfelt gratitude to **Fred**. During these four years he has not only been my supervisor but also a good friend. I'm going to miss our discussions, not necessarily work-related, which have led to new experimental ideas during my PhD but that also have helped me overcome the hardest times of my PhD. Moreover, I would like to thank my co-supervisor, **Marcel**. I still remember when after my first year of PhD I was thinking in which direction I should have "steered" my future experimental work. I then thought to myself: "Why don't you try to give a few samples to Marcel to see if we get something nice out by putting them under the TEM?". "Something nice" did come out and I'm grateful to him for all the work and effort he has put in to analyze my samples but also for teaching me and helping me to understand the results.

My next thanks go to the technicians, in particular, **Cristian** and **Wytze**. **Cristian**, for assisting me and helping me to solve the problems with the systems in the cleanroom (and for forgiving me when I forgot to fill in the logbook). You have truly witnessed my "love and hate" relationship with FlexAL. **Wytze**, thanks for the XRD measurements, for the help with the XPS and for the many discussions on the results (food, whiskey, holiday destinations etc.).

At this moment I still don't know what the future holds for me but of one thing I am sure: I'm going to miss **PMP** and my colleagues. I would like to thank **Noemi** for her support at the beginning of my PhD. I would also like to acknowledge **Florian**, **Ilker**, **Stephen**, **Harm**, **Adrie** for sharing with me either their scientific knowledge or good times together in Eindhoven and at conferences. Thanks also to **Jeanne** and **Lianne** for the funny conversations and for coping with me with all the bureaucratic paperwork. *Grazie anche a **Valerio**, **Alberto**, e **Ben** (you should be fluent in Italian by now) per tutti i coffee break, le serate fuori, i pranzi, le cene, le partite giocate con PEST e i bei momenti passati assieme.* A special thank goes to **Matthieu** with whom I shared my four years of PhD. Together, we have traveled a lot in Europe (thanks to *Enhance*), but also in US and the Dominican Republic. We have shared a lot of good times during these trips but

have also experienced the same "painful" moments during our PhDs. At the end we both made it!

Despite the many injuries, one of the things I'm going to miss the most about PMP is our football team: **PEST**. I would like to thank all the players I had the pleasure to play with in these years, for the great times together (and all the assists). I'm going to miss you guys, especially now that we made it to the third league.

During the first three years of my PhD project I was involved in the *Enhance* Marie-Curie project. Thanks to this, I have had the chance to travel all over Europe for workshops and summer-schools. These have been occasions to share great times (and great food) with great people: **Tim**, **Yoann**, **Nabeel**, the amazing **Bruno**, **Marco**, **Daniela**, **Babu**, **Manish**, **Quentin** and of course, **Matthieu**. Within the *Enhance* network I had the chance to establish fruitful collaborations. For this I would like to thank **Susanne** and **Nabeel** (Forschungszentrum Jülich) and **Tim** (University of Helsinki).

A particular thank goes to my friends **Fons**, **Sareh**, **Alma**, **Paty**, **Elisabeth**, **Ozan**, **Ariel**, **Han**, **Chrystal**, **Eszther** and **Thomaz** for the fun we had together during all the movie nights, barbeques, parties, nights out and dinners.

*Un ringraziamento speciale va a tutta la mia famiglia e in particolare ai miei genitori **Ornella** e **Silvano** e a mia sorella **Erika**. Grazie per il sostegno che mi avete dato e per avere resistito ad avermi lontano. Un pensiero particolare va anche alle mie nonne, **Antonietta** e **Eufemia**. Anche se relativamente lontani siete sempre stati comunque sempre un po' qui con me.*

*Infine, un grazie molto speciale va a **Gloria** per avermi sopportato durante questi tre anni passati assieme e sopattutto durante la scrittura della tesi. Senza di te sarebbe stato tutto molto piu' difficile. Grazie di esserci per me!*

Curriculum Vitae

3rd November 1982

Born in Montebelluna, Italy

July 2001

Technical Institute Diploma
Istituto Tecnico Industriale "G. Galilei", Conegliano, Italy

September 2001 - October 2005

Bachelor of Science Degree in Electronic Engineering (*cum laude*)
Università degli Studi di Udine, Udine, Italy

November 2005 - March 2009

Master of Science Degree in Electronic Engineering (*cum laude*)
Università degli Studi di Udine, Udine, Italy

Six months Erasmus student exchange program
INPG/Minatec, Grenoble, France

Six months traineeship and master thesis project
LCN, London Centre for Nanotechnology, London, UK

July 2009 - January 2010

Researcher in the AFM/Raman spectroscopy characterization laboratory
CBM, Centre for Molecular Biomedicine, Area Science Park, Trieste, Italy

February 2010 - May 2014

PhD candidate in the group Plasma and Materials Processing,
Department of Applied Physics
Eindhoven University of Technology, Eindhoven, The Netherlands